Aus dem Max-Planck-Institut für Kolloid- und Grenzflächenforschung

Strings and Filaments: From Vortices to Biopolymers

Habilitationsschrift

zur Erlangung des akademischen Grades
Doktor rerum naturalium habilitatus
(Dr. rer. nat. habil.)
in der Wissenschaftsdisziplin Theoretische Physik

eingereicht an der
Mathematisch-Naturwissenschaftlichen Fakultät
der Universität Potsdam

von
Dr. Jan Kierfeld
geboren am 31.1.1969 in Essen

Potsdam im Januar 2006

Contents

Chapter 1

Strings and Filaments

The description of soft and condensed matter systems usually starts on the atomic or molecular scale and typical models involve positional degrees of freedom of electrons, ions, atoms, or molecules in a material. Many material properties are related to the thermal and quantum fluctuations of such *point* particles. On the other hand, there are numerous examples where the relevant degrees of freedom are *lines*, i.e., objects with one internal dimension. The most important example for applied physics are *linear macromolecules* or linear assemblies of molecules, i.e., polymers, filaments and fibers in chemical and biological physics and materials science. Polymeric materials play a central role in today's materials science because of their versatile chemical properties that can be tailored by varying the degree of polymerization or functionalizing side groups. Moreover, polymers provide the physical basis of cell biology and biological physics as the three most important molecules of life, DNA, RNA, and proteins, are polymeric.

Apart from polymeric lines there are also numerous other examples of fluctuating lines throughout physics. The path-integral representation of the wave function of a quantum particle shows that its state can be described as a superposition of paths or *world-lines.* This establishes a description by world-lines, i.e., lines in the higher-dimensional space of positions *and* time, which applies to any quantum particle. Also in condensed matter physics various *defect lines* and *line-like excitations* play an important role. Topological defect lines in three dimensional materials include dislocations, magnetic vortex lines, or flux-lines in a type-II superconductor. Other line-like defect structures are steps on crystal surfaces. There are also strongly correlated condensed matter materials such as certain high-temperature superconducting materials, which exhibit "striped" phases at low temperatures. Finally, in particle physics "string theory" interprets elementary particles in terms of excitations of strings. In all of these different systems fluctuations of line-like objects play a central role.

In this thesis, we consider fluctuation phenomena of two different types of lines, stiff biopolymers such as cytoskeletal filaments, on the one hand, and vortices or flux-lines in type-II superconductors, on the other hand. Both line systems have in common that assemblies of such lines represent *soft matter* in the sense that typical elastic deformation energies are in the range of $1k_BT$. This holds although the relevant temperature scales are rather different: For cytoskeletal filaments the relevant temperature range is $T \sim 300\mathrm{K}$, i.e., room temperature, whereas even high-temperature superconductors become superconducting only below temperatures in the range of $T \sim 100\text{K}$.

The fluctuations of lines are determined by their elastic properties. We will restrict ourselves to fluctuations of the line *contour* and neglect possible internal deformations related, for example, to twist or torsion of the lines. Contour fluctuations can be governed either by *tension* or by the *bending energy* of the line. We will call lines that are governed by tension "strings" and lines that are governed by bending rigidity "filaments" in the following. Stiff polymers such as cytoskeletal filaments can be modeled as thermally fluctuating elastic rods with a bending rigidity and are an example for filaments. Flux-lines in type-II superconductors, on the other hand, are an example for strings as it is energetically favorable for them to align to the applied magnetic field, which thus exerts a tension.

Both for biopolymers and vortices *assemblies* of lines play an important role since new material properties emerge in this "line matter". In type-II superconductors the fluctuations of a vortex lattice are qualitatively different from fluctuations of isolated lines and the destruction of the lattice order plays an essential role for the phase behavior and possible technical applications of these materials. The elastic properties of filament assemblies such as filament bundles are also qualitatively different from those of isolated filaments. The increased stiffness of bundles makes them important structural elements of the cytoskeleton.

As the stability of any state of matter is one of the central questions of physics, the *stability* and mechanisms of *disassembly* are also for line assemblies important issues. The stability is governed by the interplay of interaction forces, external forces, thermal and eventually disorder-induced fluctuations, which lead to a variety of *phase transitions* in these line systems: melting, disorder-induced melting, delocalization, unbinding, unzipping, desorption, and force-induced desorption are among the examples treated within this thesis but this list is far from being complete. Because line-like objects are inherently *macroscopic*, i.e., already a single line has a macroscopic number of deformation degrees of freedom, also single-line phenomena such as delocalization represent genuine phase transitions and can be described with methods from statistical physics. This also establishes close links in the theoretical treatments of the phase transitions of the different line assemblies despite all experimental differences.

Besides the issue of stability, the other aspect of general interest is the *manipulation* of single lines and line assemblies, i.e., their response to external forces. Several experimental breakthroughs in manipulation and visualization techniques have taken place in polymer and biological physics during the last decade. Using micromanipulation techniques, such as the atomic force microscope with suitably functionalized tips, it has become possible to manipulate single polymers and characterize their mechanical properties by force spectroscopy. Properties of larger assemblies can be probed by microrheology techniques which have also been considerably refined.

In flux-line lattices, forces are provided by pinning and Lorentz forces. Pinning centers of various geometry and concentration can be generated experimentally, ranging from point-like pinning centers to columnar pins, and pinning planes. The Lorentz-force is controlled by transport currents in the sample. Apart from an improved experimental control of pinning structure, the field of vortex physics has benefitted over the last decade from the development of *local* probes to measure magnetic fields and, thus, local flux-line concentrations. With increasing progress in experimental techniques on the nano-scale we may eventually witness revolutionizing experiments analogous to single molecule experiments in biological physics also in the field of vortex physics in the near future, e.g., single vortex manipulation experiments using magnetic force microscopes instead of atomic force microscopes. Also new materials and systems, such as vortex lattices in Bose-Einstein condensates, may pave the way for a new generation of manipulation experiments as they operate on experimentally more accessible length scales.

Part I

Strings and Vortex Phases

Chapter 2

Introduction

Since the discovery of high-T_c superconductors in 1986 [1] the behavior of fluctuating "vortex matter" in the mixed phase of type-II superconductors has shifted into the focus of theory and experiment, as it is essential for any application of these promising materials. As predicted by Abrikosov in his seminal work [2], magnetic flux can penetrate a type-II superconductor in the mixed phase in the form of vortex or flux-lines, each carrying a magnetic flux quantum $\Phi_0 = hc/2e$, see Fig. 2.1. This happens below the critical temperature T_c and between the lower and upper critical fields, $H_{c1} < H < H_{c2}$. In the absence of any fluctuations, the vortex lines form a hexagonal Abrikosov lattice as predicted by Abrikosov in Ginzburg-Landau mean-field theory and indicated in Fig. 2.1. Already within mean-field theory several important properties of this line lattice or "vortex matter" can be established. Flux-line elements have pairwise interactions over a range λ given by the magnetic penetration depth. In type-II superconductors, this length scale exceeds the size ξ of the normal conducting core region of the vortex lines. The third important length scale is the lattice constant a of the flux-line lattice (FLL), which is given by the magnetic induction $B = \Phi_0 a^2 \sqrt{3}/2$. As both the penetration depth $\lambda \propto (1 - T/T_c)^{-1/2}$ and the lattice constant a can be tuned by changing the temperature and the magnetic field, respectively, we can easily tune both density and interaction range of vortex matter experimentally, which opens unique possibilities for the study of structural properties of this line lattice.

It has proven to be an extremely fruitful approach to describe the energetics of the low-lying phononic deformations of the vortex lattice in terms of an elasticity theory [5, 6], where the only degrees of freedom are the positions of the vortex cores. Such a description can be based either on Ginzburg-Landau or on London theory and can be justified over a wide range of magnetic fields if one allows for a dispersion of elastic moduli due to the non-local nature of vortex interactions. Each vortex line tends to align with the applied magnetic field in its ground state. Deviations from this preferred direction cost an energy, which is proportional to the length of the vortex line. For a single vortex line this gives rise to a line *tension* or a tilt modulus. We want to call lines, whose elasticity is governed by tension, *strings*. Arrays of interacting vortex strings also acquire shear and compression moduli. This elastic behavior determines the deformations of vortex lines if they are subject to forces. Typical shear energies of a vortex lattice can easily become of the order of $1 k_B T$,

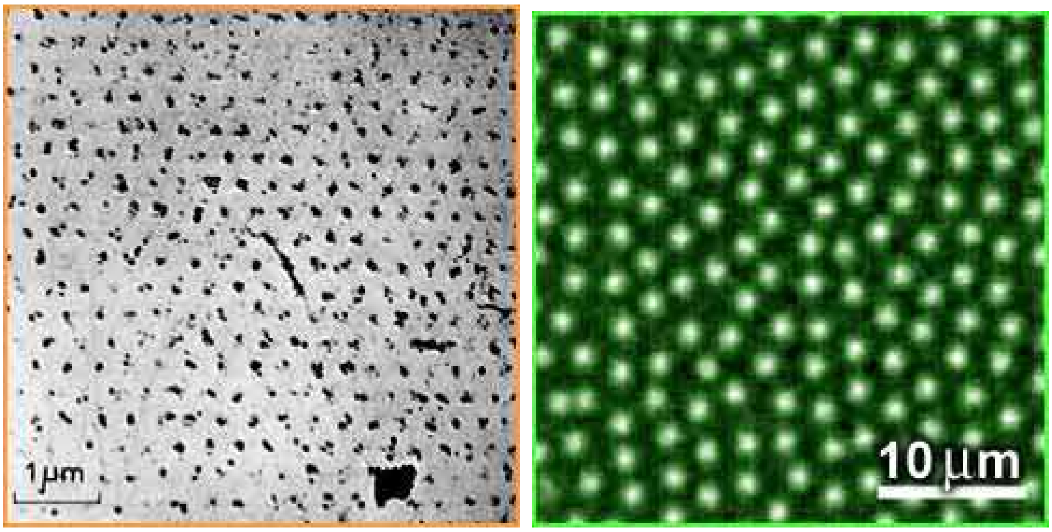

Figure 2.1: Left: First imaging of the Abrikosov lattice by Bitter Decoration in Pb (1967) [3]. Right: Magnetooptical image of the Abrikosov lattice in $NbSe_2$ (2001) [4]. .

in particular close to the lower critical field H_{c1}, where the vortex interaction becomes exponentially small, or close the upper critical field H_{c2}, where vortex cores start to become very large. One example is seen in Fig. 2.1 on the right, where the vortex lattice in the low-T_c material 2H-$NbSe_2$ close to the lower critical field exhibits considerable deformations as compared to the perfect hexagonal Abrikosov lattice.

The vortex line lattice is subject to a variety of forces giving rise to fluctuations: (i) In the presence of a transport current $\mathbf{j}$ a flux-line experiences a Lorentz force $\mathbf{f} = \mathbf{j} \times \mathbf{n}\Phi_0/c$, which leads to a dissipative, overdamped flux-line motion. The resulting flux-flow destroys the superconducting property of the material. (ii) Pinning forces from quenched random heterogeneities in the material can anchor flux-lines against these driving forces and re-establish superconductivity. (iii) Finally, flux-lines are subject to thermal fluctuations. The combined effect of all of these forces gives rise to a variety of different fluctuation dominated “vortex phases”. This is particularly pronounced in the novel high-T_c superconductors, such as $Bi_2Sr_2CaCu_2O_{8+x}$ (BSCCO) or $YBa_2Cu_3O_{7-x}$ (YBCO), which are extremely susceptible to thermal and disorder-induced fluctuations due to the interplay of several material parameters, such as high transition temperatures T_c, large magnetic penetration depths λ and short coherence lengths ξ, and strong anisotropies of the material. But also in low-T_c materials like 2H-$NbSe_2$ (NbSe) structural instabilities of the vortex lattice produce analogous effects in the critical current, however, in much closer vicinity to the upper critical field H_{c2} as compared to high-T_c materials.

In equilibrium, i.e., in the absence of transport currents and at low temperatures, pinning forces can give rise to vortex glass (VG) phases. These VG phases are one of the central topics of this thesis. The important questions are how many VG phases exist, how they

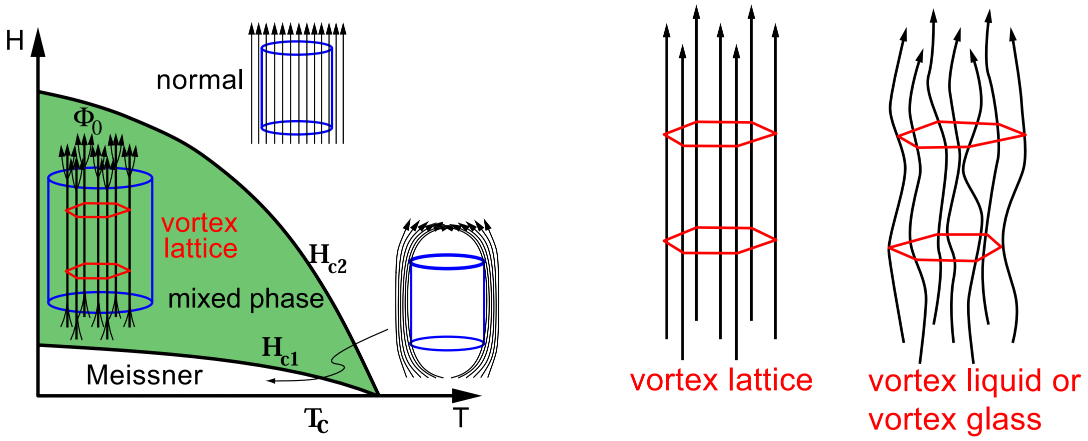

Figure 2.2: Left: Schematic mean-field phase diagram of a type-II superconductor according Abrikosov [2]. In the mixed phase, i.e., below the upper critical field H_{c2} and above the lower critical field H_{c1}, the hexagonal Abrikosov lattice of magnetic flux-lines forms. In the Meissner phase below H_{c1}, the magnetic field is completely excluded. Right: Thermal or disorder-induced fluctuations lead to positional fluctuations of vortex lines and the destruction of the vortex lattice.

can be characterized in terms of suitable order parameters, how they can be experimentally distinguished by their transport properties, and how we can describe the phase transitions between different VG phases. There are distinct VG phases for point-like pinning centers, as they are always present in high-T_c superconductors due to stoichiometric disorder, i.e., the doping parameter x in their chemical composition $Bi_2Sr_2CaCu_2O_{8+x}$ (BSCCO) or $YBa_2Cu_3O_{7-x}$ (YBCO), and for columnar pins, as they can be generated by heavy ion irradiation of samples. Upon increasing the temperature the vortex matter can melt into a vortex liquid (VL). The description of this phase transition is another central topic of this thesis. Finally, in the presence of a transport current, the pinned vortex matter eventually starts to move above a threshold current if the Lorentz forces are sufficient to overcome the collective pinning forces in the vortex lattice. The thermally activated creep motion below this threshold is also subject of this thesis. Eventually the vortex lattice starts to move with finite velocity in the so-called flux-flow regime. Then, depending on the velocity, distinct moving vortex lattice phases, which are separated by dynamic phase transitions, can be observed.

The details of this picture of fluctuating vortex matter phases in high-T_c materials have been established over the past 20 years. The theory of vortex pinning by point defects is much older and dates back to the 1970s, when Larkin established important ideas about the collective pinning of the vortex lattice. Almost exhausting reviews on the subject of pinning are Refs. [7, 6, 8]. We want to start the first part of this thesis by a short overview of these developments. Before the discovery of high-T_c materials, thermal fluctuations only played a minor role in vortex physics. Pinning, which is necessary for all technological applications, was in the focus of interest. Larkin and Ovchinnikov [9] were the first to show that pinning forces from point defects will destroy the translational order of the vortex lattice below four spatial dimensions. The treatment of Larkin and Ovchinnikov gave for the first time a systematic summation of pinning forces in the vortex lattice but it was based on a perturbative description using random forces, not taking into account the global features of the complicated energy landscape arising from the pinning potentials. Building on ideas from spin glass theory, it was Fisher [10] to propose that the phase that results from the instability as found by Larkin could be characterized as a glassy phase, the so-called vortex glass. This idea was further elaborated in Ref. [11] by Fisher, Fisher, and Huse. They argued that the vortex lattice order is completely lost in the VG phase due to the proliferation of topological defects such as dislocations. Therefore, they based their description of VG properties on superconducting phase correlations. Experimental support for the VG hypothesis came from transport measurements [12] where some of the scaling predictions could be confirmed.

In a parallel development, it was first established by Nelson and coworkers that in the high-T_c materials, where high temperatures of vortex matter are accessible, thermal fluctuations can give rise to a vortex lattice melting into a vortex liquid [13, 14]. (The idea of vortex lattice melting has been pioneered very early on by Eilenberger [15], but could not be tested experimentally at that time and was not further investigated.) The phenomenological Lindemann criterion has been employed successfully then to calculate the locus of the melting line [16, 17]. With regard to melting, the analogy with atomic crystals and the description of their deformations by elasticity theory proved fruitful, as it allows to draw on the vast amount of literature and ideas on melting of atomic crystals. Lindemann criteria are one such idea originating from this analogy. Experimentally, it was later firmly established that the vortex lattice melting transition is a first order melting transition with discontinuities in the magnetization [18, 19, 20] and a latent heat [21, 22]. Yet, as also for crystals the exact melting mechanism is still controversial, also for the vortex lattice the melting mechanism remains a subject of current research. In this context, it is a very puzzling detail (which is still not completely understood from the theoretical perspective) that the vortex lattice melts similar to ice as the magnetization or flux-line density *increases* during melting. In this thesis, we approach the melting transition from the phenomenological site with a detailed Lindemann analysis for a variety of materials, and we propose and elaborate a dislocation-mediated melting mechanism. Recently, also other melting theories going beyond the Lindemann analysis have been proposed. For example, a self-consistent analysis in Ref. [23] shows how anharmonicities beyond the elastic deformation of the FLL give rise to a melting instability in a layered superconductor.

Regarding the issue of the nature of the VG phase in the presence of point disorder, a paradigm shift took place during the last 10 years. The arguments given in Ref. [11] for the proliferation of dislocations in the vortex glass phase do not take into account that the results of Larkin and Ovchinnikov for the pinned elastic vortex lattice get strongly modified for displacements exceeding the coherence length ξ. Then, perturbation theory breaks down and the growth of relative displacements in a dislocation-free pinned vortex lattice is slowed down considerably. This has been established first in Ref. [24] and, since then, further elaborated in the framework of the theory of pinned elastic manifolds. This approach starts from an elastic vortex lattice, from which dislocations are explicitly excluded. If flux-line displacements exceed the coherence length ξ, which is also the natural scale of pinning energy variations, a perturbative expansion of the pinning potential energy in terms of vortex displacements breaks down, and one is forced to consider the competition of competing energy minima in the random pinning energy landscape. These minima correspond to the optimally pinned elastic vortex lattice configurations in the absence of topological defects. Depending on the length scales considered, the behavior of the relative displacements of flux-lines, which can be characterized by a roughness exponent ζ, then shows several crossovers. In perturbation theory on small length scales, the classic perturbation theory result of Larkin and Ovchinnikov is $\zeta = (4 - d)/2$ for a d-dimensional pinned FLL [9]. This behavior first crosses over to a power law with a somewhat smaller ζ [24], before a very slow *logarithmic* growth sets in on the largest scales, which has been established first by Nattermann [25] and later by Giamarchi and Le Doussal [26]. In the absence of dislocations this leads to a VG phase, which maintains quasi-long-range translational order with power-law Bragg singularities in the structure factor and, therefore, has been called elastic VG or "Bragg glass" (BrG) [26]. If the issue of stability against dislocations is re-addressed taking this scaling of displacements into account it has been argued that the elastic BrG phase is stable with respect to dislocation proliferation, at least for weak disorder or at small magnetic fields [26, 27, 28].

The existence of an elastic "Bragg glass" phase was confirmed by a number of experiments, most impressively by neutron scattering experiments by Cubitt et al. [29] on BSCCO, which clearly showed the existence of power-law Bragg peaks at low magnetic fields in complete agreement with theory. However, in this experiment it was also seen that the BrG is destroyed at higher magnetic fields, where the Bragg peaks vanish, suggesting a field-driven transition to a more disordered VG phase, which we also want to refer to as "amorphous VG" (AVG) phase in the following. The neutron experiment thus suggested the existence of an order-disorder transition between two glassy phases, the elastic BrG with quasi-long-range order and the topologically disordered amorphous VG. Transport measurements on YBCO [30] also indicated a crossover from the first-order melting at low magnetic fields to a continuous VG-VL transition at higher magnetic fields. This provides another hint that at some critical field strength there might be a corresponding order-disorder transition within the regime of the VG phases at lower temperatures. The results in Ref. [30] also suggested for the first time the existence of a critical point where the melting line ends. Such a critical point has later been found also for BSCCO [20] by magnetization measurements. Since then other groups [31, 32] have reported measurements on YBCO showing a critical point terminating the melting line. The "puzzle" of the critical point [33] is one of the main subjects of this thesis, and we try to deliver a consistent theoretical explanation of this phenomenon. The phenomenon of a critical point is particularly puzzling because in "clean" FLLs, i.e., in the absence of point disorder, no critical point is possible as the vortex-vortex interaction is purely repulsive and, thus, two fluid phases cannot coexist. Therefore, the existence of the critical point must be a disorder-induced phenomenon [33]. In chapter 4, we will present an explanation of the critical point based on a dislocation theory, which characterizes all vortex phases – a quasi-ordered elastic BrG at low temperatures and weak point disorder, the thermally disordered VL, and the amorphous VG at strong disorder – by their dislocation density and which describes all vortex phase transitions in terms of the dislocation free energy. The approach takes into account both thermal and disorder-induced fluctuations of dislocations in the FLL.

For atomic lattices the idea of a *defect-mediated melting* has been brought forward as early as in the thirties by Mott and Gurney [34] and has been elaborated since then (for reviews see Refs.[35, 36, 37]). Defect-mediated melting theories are based on the observation that the liquid phase might be interpreted as a solid containing a macroscopic number of topological defects leading to the destruction of the lattice symmetries. Bragg [38] and Shockley [39] were the first to establish the idea that the liquid state can be seen as a solid saturated with dislocations. Early theories for dislocation-mediated melting have been formulated by Mizushima [40] and Ookawa [41]. Edwards and Warner [42] obtained a first order transition for a dislocation-loop mediated melting neglecting the hard-core repulsion between dislocations. In Ref. [36], Kleinert elaborates a theory of defect-mediated melting in three dimensions, which is based on an artistic treatment of the statistical physics of dislocation *and* disclination loops in three dimensions. A slightly different avenue has been taken by Yamamoto and Izuyama [43] who considered an ensemble of *directed* dislocation lines threading the whole sample instead of closed loops. Within a transfer-matrix treatment they find a first order melting for atomic crystals, however, at much higher temperatures as experimentally observed. A more recent work on dislocation-mediated melting along the same lines was presented in [44]. For the FLL, it was first noted by Labusch [45] that it may contain dislocations which were observed and classified for the first time in Bitter decoration experiments on conventional type-II superconductors by Träuble and Essmann [46]. The dislocation theory of vortex lattice phase transition presented in chapter 4 builds on these relatively old works and extends them to the FLL, which is a *line* lattice. Furthermore, the dislocation-mediated melting theory is extended to disordered systems, i.e., the pinned FLL, which is an aspect that is absent for atomic lattices.

If one is not interested in the exact mechanism of vortex phase transitions Lindemann criteria can be used to predict the *locus* of the phase transition lines. In a Lindemann criterion, one calculates the root-mean-square displacement of vortex lines and uses the empirical fact that lattice order is lost if the displacement fluctuations of flux-lines exceed a certain fraction of the lattice spacing between the lines. This fraction is often in the range $c_L \sim 0.15 - 0.2$ and called the *Lindemann number*.

Lindemann criteria have been successfully applied to the thermal melting of atomic solids. They can be applied (i) to calculate the locus of the melting line for a single material using one particular Lindemann number, which is independent of the thermodynamic control parameters such as temperature or pressure, and (ii) to compare the melting lines of different materials with eventually different microscopic interactions by comparing their Lindemann numbers. In its first function (i), the Lindemann criterion relates points on the melting line of a single material in a universal manner to each other; in its second function (ii), it eventually establishes connections between different materials regarding their melting mechanism. When Lindemann first introduced the criterion in 1910 [47], he considered the locus of the melting line for an atomic solid. Later on, the Lindemann criterion was also used in its second function to compare the melting lines of different atomic solids and also other systems, such as colloidal systems with a variety of different microscopic interactions (see Ref. [48] for a review). Apart from the Lindemann criterion there are other phenomenological criteria, such as the Hansen-Verlet criterion for the structure factor [49], all of which are based on the concept of seeking for certain universal values in a dimensionless number, which can characterize the strength of fluctuations independently of thermodynamic control parameters.

By applying the Lindemann criterion to the FLL we can also infer information of two different types according to the two above functions (i) and (ii) of the Lindemann criterion. In its original function (i), the Lindemann criterion can be used to obtain the melting line of the FLL for a particular type-II material in the parameter plane of magnetic fields and temperatures. Changing magnetic fields is similar to changing the density in an atomic solid but the FLL differs from an atomic solid because interactions are tunable. Varying the penetration depth λ versus the lattice spacing a the interaction changes from a logarithmic 2D Coulomb-like long-ranged interaction for large $\lambda/a \gg 1$ to an exponentially decaying interaction of range λ for small $\lambda/a \ll 1$. Because λ is a function of the temperature and diverges upon approaching the critical temperature T_c, the nature of vortex interactions changes along the melting line for the same material. Therefore, it is a remarkable fact that it is usually possible to describe the melting line of a material using a single Lindemann number. Furthermore, the FLL is a *line* lattice rather than a lattice of point particles. At high magnetic fields above the decoupling field the line lattice eventually disintegrates into weakly coupled pancake vortices. Therefore, it represents a different type of matter as compared to atomic solids. Using the Lindemann criterion in its function (ii), the melting mechanisms of these different types of lattices can be compared using their Lindemann numbers.

Another interesting question is whether the Lindemann criterion can also be applied to the vortex glass states of the pinned FLL. By considering suitably generalized mean square displacements, which include not only thermal but also disorder-induced positional fluctuations, modified Lindemann criteria have been proposed to predict the locus of the melting line from a vortex solid or VG into a VL upon increasing the temperature as well as the locus of the order-disorder transition line for the disorder-induced transition from an elastic BrG into the amorphous VG. A detailed discussion of such Lindemann criteria will be given in chapter 3. There, we will both motivate different forms of modified Lindemann criteria to describe disorder-induced vortex phase transformations and perform a detailed Lindemann analysis for three type-II materials representative for the most important classes of type-II superconductors used in experimental studies of the vortex phase diagram. The phase diagrams obtained from the Lindemann analysis agree remarkably well with the experimental results. However, one should always bear in mind that the purely phenomenological Lindemann criterion is not able to give a mechanism for the vortex phase transitions and, thus, it gives no hint towards a thermodynamic characterization of the different vortex phases. For this purpose, one has to consider more advanced theoretical approaches, such as the dislocation theory presented in chapter 4. On the other hand, we will be able to *derive* modified Lindemann criteria from the dislocation theory of melting and establish a connection between the two descriptions: The dislocation theory gives a consistent *mechanism* of the vortex phase transformations and allows to derive Lindemann criteria, which, in turn, allow to calculate concrete phase diagrams which can be compared to experiments as shown in chapter 3.

In the beginning of the 90s, one main goal of experiments was to optimize pinning in order to achieve high critical currents. A breakthrough was made with the discovery that pinning is much more effective if columnar defects are brought into the material. This has been first shown for heavy ion irradiated YBCO samples [50, 51], where the ion irradiation leaves long columnar tracks of damaged material behind. But these systems were not only interesting from the applied point of view but also extremely interesting from the theoretical point of view, because the three-dimensional line lattice in the presence of columnar pins can be treated by a mapping to a two-dimensional quantum system of bosons with point disorder [52, 53]. In this mapping, quantum fluctuations of bosons play the role of thermal fluctuations of the flux-lines, and the thermodynamic limit of long flux-lines corresponds to the low temperature limit in the bosonic system. This opens the possibility to study quantum mechanical localization phenomena using vortex systems. Localization of bosons at point defects corresponds to the formation of a strongly pinned “Bose glass” (BoG) phase in the flux-line system. For the system with columnar defects, the magnetic field strength where the density of defects matches the density of flux-lines, the so-called matching field B_Φ, plays an important role. Below the matching field, the physics is dominated by individual vortices searching for their optimal pinning column, which leads to a localization of vortices and a very effective pinning. Above the matching field, on the other hand, several vortices are competing for a single pinning column, and pinning becomes much weaker. The competition for pinning sites leads to frustration in the system, which, in turn, can give rise to interesting delocalization transitions.

This part of the thesis is structured as follows. In chapter 3, which is based on Refs. [54, 55], we give a detailed discussion of the phenomenological approach to the vortex phase diagram using Lindemann criteria. We present different possible generalizations of the conventional Lindemann criterion, which allow to treat also disorder-induced fluctuations and, thus, transitions involving vortex glass phases. In chapter 4, which is based on Refs. [56, 57], a deeper theoretical approach to the vortex phase diagram is presented, which is no longer phenomenological but based on dislocation-mediated phase transitions [56]. This approach allows to characterize all vortex phases by their dislocation density and to describe all vortex phase transitions in terms of the dislocation free energy. Moreover, the treatment of pinned dislocations in the FLL can be extended to dynamics. In this way, plastic creep phenomena in the topologically disordered vortex glass can be described, which might explain the origin of the so-called second peak effect [57]. Finally, in the last chapter 5, which is based on Ref. [58], we consider melting in the presence of dilute columnar defects. Here, we establish a distinct melting mechanism, which is a delocalization melting mechanism.

Chapter 3

Lindemann Analysis of the Vortex Phase Diagram

We discuss the destruction of vortex lattice order in type-II superconductors by random point pinning and thermal fluctuations based on Lindemann criteria. The location of the melting line and the order-disorder transition, which marks the destruction of the topologically ordered Bragg glass phase and is the reason for the second peak effect, is calculated. We focus on a comparative discussion of different versions of Lindemann criteria and, with regard to experiment, on a comparative discussion of three classes of type-II superconductors – low-T_c, anisotropic high-T_c, and layered high-T_c materials. Specific attention is paid to the role of nonlocal magnetic interlayer couplings and the softening of elastic moduli at high magnetic fields, which is crucial for low-T_c materials. We also discuss in detail the competing mechanisms of thermal depinning and temperature dependence of the pinning strength through microscopic parameters as well as the crossover between single-vortex and bundle pinning for low-T_c materials.

3.1 Introduction

In high-T_c superconductors (HTSC's) such as $\mathrm{Bi_2Sr_2CaCu_2O_{8+x}}$ (BSCCO) or $\mathrm{YBa_2Cu_3O_{7-x}}$ (YBCO) the flux-line array is extremely susceptible to thermal and disorder-induced fluctuations due to the interplay of several parameters such as high transition temperature T_c, large magnetic penetration depth λ and short coherence length ξ, and a strong anisotropy of the material. This leads to the existence of a variety of fluctuation dominated phases of the flux-line array and very rich phase diagrams for the HTSC materials [7, 6, 8]. But also in low-T_c materials such as 2H-$\mathrm{NbSe_2}$ (NbSe) structural instabilities of the vortex lattice produce analogous effects in the critical current, however, in much closer vicinity to the upper critical field H_{c2} as compared to high-T_c materials.

Upon increasing the temperature the flux-line lattice (FLL) melts into an entangled vortex liquid (VL) as first proposed by Nelson [14]. Calculations for the locus of the melting line have been mainly based on the Lindemann criterion $\langle u^2\rangle_T = c_L^2 a^2$, which estimates the root-mean-square thermal displacement fluctuations $(\langle u^2\rangle_T)^{1/2}$ of a vortex element at the melting transition as a fraction $c_L a$ of the FLL spacing a with a Lindemann number $c_L \approx 0.2$.

The phenomenological Lindemann criterion has proven very successful in describing experimental melting curves, and refined theoretical evaluations of $\langle u^2 \rangle_T$ have been presented for anisotropic [16, 17] and strongly layered [59] HTSC materials. Recently, different melting theories going beyond the Lindemann analysis have been proposed. In Ref. [23], a self-consistent analysis of anharmonicities beyond the elastic deformation of the FLL leads to a melting instability. In chapter 4, we will present a theory of dislocation-mediated vortex lattice melting.

Since the work of Larkin and Ovchinnikov [9], the influence of quenched pointlike pinning centers on the vortex lattice and the nature of the collectively pinned FLL have been subject of intense theoretical interest. It was argued in Refs. [10] and [24] that weak point disorder drives the vortex lattice into a vortex glass (VG) state with zero linear resistivity. In weak collective pinning theory according to Ref. [9], disorder-induced relative displacements grow as $\overline{\langle [u(\mathbf{r}) - u(0)] \rangle^2} \sim r^{4-d}$ in d-dimensional space, i.e., the pinned FLL is described by the roughness exponent $\zeta = (4-d)/2$. This would lead to an instability with respect to the proliferation of topological defects such as dislocations in the FLL (Ref. [11]) such that weak point disorder was believed to destroy the crystal order of the FLL. However, the argument does not take into account that the results of Ref. [9] get modified for displacements exceeding the coherence length ξ. On larger length scales the growth of relative displacements first crosses over to a power law with a somewhat smaller ζ [24], before a very slow *logarithmic* growth sets in on the largest scales [25, 26]. In the absence of dislocations this leads to a VG phase that maintains quasi-long-range translational order with power-law Bragg singularities in the structure factor and has thus been called “Bragg glass” (BrG) [26]. In Refs. [26, 27, 28] it has been argued that the elastic BrG is stable against dislocation formation at low magnetic fields.

Upon increasing the magnetic field the vortex lattice softens and the point disorder strength effectively increases. At sufficiently high magnetic fields the BrG becomes unstable and dislocations proliferate [27, 28, 56]. Various experimental signatures can be attributed to the resulting order-disorder or amorphization transition into a high-field *amorphous* VG. Neutron-diffraction measurements on BSCCO (Ref. [29]) show a destruction of the characteristic power-law Bragg peaks at higher fields. Also transport measurements on YBCO (Ref. [30]) indicate a crossover from the first-order melting at low magnetic fields to a continuous VG-VL transition that can be related to the order-disorder transition within the vortex solid. The occurrence of a very sharp second peak in magnetic hysteresis measurements on BSCCO [60], YBCO [61], or NbSe (Ref. [62]) at a well-defined second peak field can be interpreted as another hallmark of the order-disorder transition from a low-field elastic BrG to the high-field amorphous VG. The second peak is associated with a rise of the critical current across this transition which is due to an onset of plastic deformation as we will show in chapter 4. This corresponds to the intuitive picture that the additional plastic deformation allows better adjustment of the pinned FLL configuration thus leading to larger critical currents.

Analogously to the case of thermal melting, progress in predicting the locus of the order-disorder or amorphization transition has mainly been made by using generalized phenomenological Lindemann criteria [63, 64, 65, 66, 67, 68, 69, 70]. Derivations of Lindemann criteria have been given in Refs. [27] and will be presented in chapter 4 by studying the onset of the instability of the BrG with respect to spontaneous generation of disorder-induced dislocations. Whereas Refs. [63, 64, 65, 66, 67, 68] and [70] focus on high-T_c materials such as BSCCO or YBCO, Ref. [69] addresses also low-T_c materials such as NbSe. In this chapter we want to critically review the Lindemann analysis for the three representative materials BSCCO, YBCO, and NbSe with BSCCO as a typical strongly layered high-T_c compound with weak Josephson coupling, YBCO as a typical moderately anisotropic high-T_c, and NbSe as a typical weakly anisotropic low-T_c type-II superconductor. On the one hand, we want to emphasize the common approach via the Lindemann analysis; on the other hand, the comparative study will show that each of the three mentioned classes of superconductors exhibit peculiarities that have to be taken into account in the analysis. At low magnetic fields, when the vortex spacing a becomes larger than the magnetic penetration depth λ, we have to pay specific attention to the role of nonlocal electromagnetic couplings. This becomes particularly important for BSCCO. In low-T_c materials, on the other hand, the softening of elastic moduli at high magnetic fields is particularly relevant because both melting line and the order-disorder transition are located close to the upper critical field H_{c2}. An important point in interpreting experiments is also a detailed knowledge of the temperature dependence of the order-disorder transition line, which is determined by an interplay between the temperature dependence of microscopic parameters entering the pinning strength and the effective weakening of the pinning potential by "thermal smearing" due to thermal motion of the vortices which can give rise to thermal depinning [7]. Often one or the other source of temperature dependence can be neglected. For example, in low-T_c materials depinning temperatures are very close to T_c and the temperature dependence through microscopic parameters is more important whereas in high-T_c materials thermal depinning is the dominating effect.

This chapter is organized as follows. First we will discuss the Lindemann criteria for thermal and disorder-induced melting transitions in Sec. 3.2. In a system subject to quenched disorder the Lindemann criterion can be formulated in two slightly different versions both of which can be interpreted in terms of the underlying melting mechanism: Thermal and quenched fluctuations can act *independently* from each other in destroying the lattice order or they can act *cooperatively*. In Sec. 3.3 we will show how the Lindemann criterion for melting of the vortex lattice can be reformulated in terms of fluctuations of *single* vortices of a certain length, the *single-vortex length* L_0, that is set by the interactions within the FLL. In Sec. 3.4 we discuss how the properties of single-vortex fluctuations are strongly modified if the nonlocal electromagnetic coupling cannot be neglected. In Sec. 3.5 we present the Lindemann analysis for thermal melting in the absence of quenched disorder for YBCO, NbSe, and BSCCO. In order to study the order-disorder or amorphization transition that is caused by quenched point disorder employing the single-vortex Lindemann criterion we have to discuss the pinning of single vortices which is done in Sec. 3.6. Within weak collective pinning theory the characteristic length scale set by the frozen-in point disorder is the *collective pinning* or *Larkin length* L_c. We have to distinguish several pinning regimes depending on the size of the pinning length L_c in comparison to the single-vortex length L_0 and the layer spacing d in a layered material. We have *bundle pinning* for $L_c > L_0$ and *single-vortex pinning* for $L_c < L_0$. For $L_c < d$ the layered structure becomes relevant for the pinning, and there is a crossover from weak collective pinning to *strong pinning* of pancake vortices. The Lindemann analysis is complicated by the fact that the pinning strength is temperature dependent through two different mechanisms. We have a temperature dependence of the pinning strength through the microscopic parameters (such as λ or ξ) but we also have smearing or weakening of disorder by thermal fluctuations above the *depinning temperature* T_{dp}. Therefore we have to carefully discuss the temperature dependence of the crossover between the different pinning regimes for the three exemplary materials throughout Sec. 3.6. Having clarified the different pinning regimes we can perform the Lindemann analysis for the order-disorder or amorphization transition driven by the quenched point disorder. This task is split into two parts. In Sec. 3.7 we discuss the analysis for $T = 0$ depending on magnetic fields and pinning strength. Finally, in Sec. 3.8, we discuss the influence of thermal fluctuations and perform the Lindemann analysis for $T > 0$, i.e., in the familiar B-T plane.

3.2 Lindemann criterion

In its conventional form for thermal fluctuations the Lindemann criterion is formulated as

$$\langle u^2 \rangle_T = c_L^2 a^2 \ , \tag{3.1}$$

where $\mathbf{u}$ is the displacement of vortex elements and $\langle \ldots \rangle_T$ the purely thermal average in the *absence* of quenched disorder. The Lindemann number c_L is introduced here as a phenomenological parameter that is supposed to depend only weakly on the specific lattice parameters of the solid phase, in particular it is assumed to be independent of the magnetic field. In principle its value can be determined by *ab initio* melting theories going beyond a Lindemann analysis, for example, in the next chapter 4 we find a value $c_L \approx 0.2$ for dislocation-mediated vortex lattice melting. The Lindemann number c_L can also be determined from simulations of the vortex lattice melting transition. Early Monte Carlo studies of an interacting line model [71] find a melting transition with a Lindemann number that depends weakly on the magnetic field with values $c_L \approx 0.2$ over a wide field range. Path integral Monte Carlo simulations of the corresponding lattice to superfluid transition of two-dimensional (2D) bosons [72] give a Lindemann number $c_L \approx 0.25$. Finally, Monte Carlo simulations of the three-dimensional uniformly frustrated, anisotropic XY model [73] give a value of $c_L \approx 0.18$. All these findings suggest that a Lindemann number $c_L \approx 0.2$ is appropriate for the thermal vortex lattice melting. For the disorder-induced transition we will assume similar values of the Lindemann number.

For thermal fluctuations the main contribution to the mean-square displacement comes from fluctuations with the shortest wavelength of the order of the vortex spacing a. Therefore one can rewrite the Lindemann criterion for thermal melting (3.1) as

$$\langle \Delta u^2(a,0) \rangle_T = \langle [u(\mathbf{a},0) - u(\mathbf{0},0)]^2 \rangle_T = c_L^2 a^2 \ , \tag{3.2}$$

where $\mathbf{u}(\mathbf{R},z)$ is the displacement of the vortex element at $\mathbf{r} = (\mathbf{R},z)$, and $\mathbf{a}$ is a unit vector of the hexagonal Abrikosov lattice. z is the coordinate parallel to the magnetic field

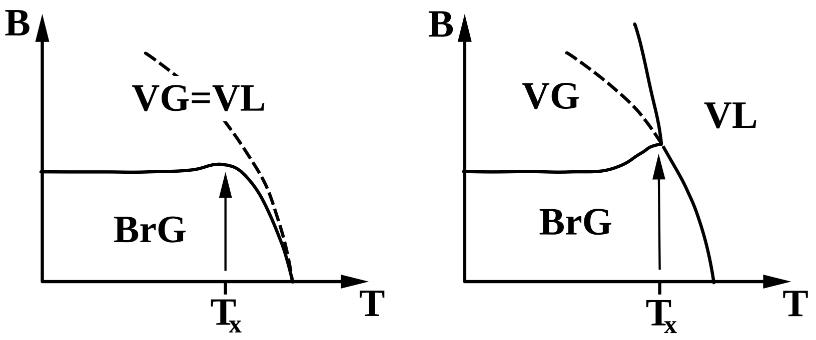

Figure 3.1: Schematic phase diagram (neglecting reentrance at low fields) illustrating the two scenarios corresponding to the two possible generalizations of the Lindemann criterion. Left: According to eq. (3.3) if temperature and point disorder act cooperatively. Right: According to eqs. (3.2), (3.4), and (3.5) if temperature and point disorder cause distinct phase transitions. The dashed line is the thermal melting line in the absence of quenched disorder according to eq. (3.2). The temperature T_x is defined by $\langle \Delta u^2(a,0)\rangle_T = \overline{\langle \Delta u(a,0)\rangle^2} = c_L^2 a^2$.

H which is directed along the c axis of the anisotropic type-II superconductor in the usual experimental situation, $\mathbf{H}||\mathbf{c}$. In the form (3.2), the Lindemann criterion is a *local* criterion where thermal fluctuations in the bond length $a + \Delta u(a,0)$ connecting nearest neighbors are used to indicate the loss of *global* positional order of the FLL. In the form (3.2) the Lindemann criterion can also be applied to situations where $\langle u^2\rangle_T$ is formally diverging as, for example, in the thermal melting of a two-dimensional lattice and to the order-disorder transition due to quenched point disorder that we will discuss now.

There are two possibilities to generalize the criterion (3.2) in order to include phenomenologically the disorder-induced quenched displacement fluctuations as possible cause for the destruction of the vortex crystal. To see this we first note that at finite temperatures and in the presence of quenched point disorder the displacement has two parts $\mathbf{u} = \mathbf{u}_p + \mathbf{u}_{th}$. The quenched part $\mathbf{u}_p$ is due to pinning and does not average to zero upon performing the thermal average: $\mathbf{u}_p = \langle \mathbf{u}\rangle$. The part $\mathbf{u}_{th} = \mathbf{u} - \langle \mathbf{u}\rangle$ describes thermal fluctuations around the pinning part. Thus $\overline{\langle u_{th}^2\rangle} = \overline{\langle u^2\rangle} - \overline{\langle u\rangle^2}$ is the thermal part and $\overline{u_p^2} = \overline{\langle u\rangle^2}$ the disorder part of the mean-square fluctuations. By using a tilt symmetry of the vortex system [74] one can establish that $\overline{\langle u_{th}^2\rangle}$ is unchanged by the quenched disorder, i.e., $\overline{\langle u_{th}^2\rangle} = \langle u^2\rangle_T$. However, u_{th} is *not* Gaussian distributed as in the absence of quenched disorder [75].

The first possibility to generalize criterion (3.2) is to replace $\langle \Delta u^2(a,0)\rangle_T = \overline{\langle \Delta u_{th}^2(a,0)\rangle}$ by the *full* mean-square displacement $\overline{\langle \Delta u^2(a,0)\rangle} = \overline{\langle \Delta u_{th}^2(a,0)\rangle} + \overline{\langle \Delta u_p^2(a,0)\rangle}$ in eq. (3.1):

$$\overline{\langle \Delta u^2(a,0)\rangle} = \langle \Delta u^2(a,0)\rangle_T + \overline{\langle \Delta u(a,0)\rangle^2} = c_L^2 a^2 \ . \tag{3.3}$$

This procedure is suitable if temperature (or entropy) and quenched disorder act *cooperatively* in generating topological defects in the FLL. It corresponds to a scenario where there is only *one* topologically disordered phase beyond the BrG instability, and the VL phase and the amorphous VG are thermodynamically identical phases. A criterion such as eq. (3.3) would shift the thermal melting line to lower fields and lead to a *crossover* of the thermal melting line into the amorphization transition line as soon as $\langle \Delta u^2(a,0)\rangle_T = \overline{\langle \Delta u(a,0)\rangle^2} = c_L^2 a^2$ at a temperature T_x, see Fig. 3.1. A Lindemann criterion of the form (3.3) has been assumed in almost all previous Lindemann analysis of the BrG stability [63, 64, 65, 66, 68, 69, 70]. It can also be formulated in terms of three characteristic energies of a vortex lattice unit cell [67, 70], the temperature T, a characteristic energy $E_{pl} \propto c_L^2$ necessary for plastic deformation of the FLL, and a characteristic pinning energy E_{pin} (equations for E_{pl} and E_{pin} will be given below) as $T + E_{pin} = E_{pl}$.

A different possibility to generalize criterion (3.2) is based on a mechanism where temperature and quenched disorder do not act cooperatively but lead to two *distinct* instabilities of the BrG, for example instabilities with respect to dislocation loops on two different length scales. Such a mechanism will be presented in the next chapter 4, where temperature leads to an instability with respect to a dislocation array of high (areal) dislocation density $\rho \sim a^{-2}$, which can be interpreted as a VL phase saturated with small dislocation loops. On the other hand, quenched disorder leads to an instability with respect to a much smaller dislocation density that is essentially set by a large pinning length (the positional correlation length, see chapter 4) and characterizing the amorphous VG. Having such a scenario in mind one would rather generalize eq. (3.1) by introducing a second criterion which considers only the pinning-induced displacements

$$\overline{\langle \Delta u(a,0)\rangle^2} = c_L^2 a^2 \;, \tag{3.4}$$

giving the locus of the disorder-induced or amorphization transition line. The locus of the thermal melting line is still given by eq. (3.1) or (3.2) and unchanged by quenched disorder.

Within the scenario where quenched disorder and thermal fluctuations act independently, one consequently argues for *two* distinct topologically disordered phases, the VL and the amorphous VG (at least close to the stability region of the quasiordered BrG, where we expect Lindemann criteria to work, at higher fields a critical end point can occur, see chapter 4). This suggests that the locus of the VG-VL transition is given by a third Lindemann-like criterion

$$\langle \Delta u^2(a,0)\rangle_T = \overline{\langle \Delta u(a,0)\rangle^2} \;, \tag{3.5}$$

and we have three-phase coexistence for $\langle \Delta u^2(a,0)\rangle_T = \overline{\langle \Delta u(a,0)\rangle^2} = c_L^2 a^2$ at the temperature T_x, see Fig. 3.1. Only in the Lindemann analysis of Ref. [67] this second generalization of the Lindemann criterion has been employed consistently although in Ref. [63] a criterion equivalent to eq. (3.5) is applied to calculate the irreversibility line [but the BrG phase boundary is calculated using eq. (3.3) in Ref. [63]]. In Ref. [67] the two Lindemann criteria were formulated in terms of the three characteristic energies that we introduced above. We can write $T = E_{pl}$ equivalent to eq. (3.1) as criterion for thermal melting, the BrG-VL transition. $E_{pin} = E_{pl}$ corresponding to eq. (3.4) is the criterion for the order-disorder transition line between VL and amorphous VG. Finally $T = E_{pin}$ equivalent to eq. (3.5) is the criterion for the VG-VL transition.

Within a dislocation-mediated melting theory it is indeed possible to give some qualitative arguments supporting the view that quenched disorder and thermal fluctuations act *independently* rather than cooperatively in destroying the lattice order. For dislocation-mediated melting it is expected that a first-order transition into a VL phase without any short-scale translational order has to correspond to a phase transition where a dense array of dislocations ($\rho \sim a^{-2}$) enters the sample. On the other hand, in the presence of quenched disorder dislocation lines gain disorder energy by optimizing their position and shape. However, in a dense dislocation array with dislocation distances or dislocation loop sizes of the order of the lattice spacing a also the optimization of position and shape can only take place over distances of the order of a, and thus give only small additional disorder energy gains compared to the entropic terms. This suggests that quenched disorder is an irrelevant perturbation and that thermal fluctuations $\overline{\langle u_{th}^2 \rangle}$ alone should be considered in the Lindemann criterion, as in eq. (3.1). On the other hand, for the melting induced by quenched disorder, thermal fluctuations are irrelevant because in the three-dimensional FLL $\overline{\langle u_{th}^2 \rangle}$ is independent of system size and thus not diverging in the thermodynamic limit. Therefore we expect temperature to be an irrelevant perturbation at this order-disorder or amorphization transition that causes only thermal smearing of the disorder but does not change the nature of the transition [7]. This suggests that as in eq. (3.4) disorder-induced fluctuations $\overline{\langle u \rangle^2}$ alone should be considered in the Lindemann criterion.

Based on these arguments we will employ the approach of *independently* acting quenched and thermal fluctuations, i.e., the criteria (3.2), (3.4), and (3.5) throughout this chapter which have also been used in Ref. [67] for BSCCO and which are supported by the melting theory presented in the next chapter 4.

3.3 Single-vortex length and Lindemann criterion

Local Lindemann criteria of the form (3.2)–(3.5), which are probing fluctuations of changes in bond length $\Delta u(a,0)$ between nearest neighbors, can be reformulated in terms of the fluctuations of a *single* vortex line of a certain length which is set by the interactions with its nearest neighbors. This length scale is the so-called *single-vortex length* L_0 (in the notation of Ref. [7]), which can be obtained within the elastic description of the FLL with an elastic Hamiltonian that contains tilt, shear, and compression modes and associated elastic moduli c_{44}, c_{66}, and c_{11}, see for example Refs. [7] and [6]. Over a wide range of parameters the vortex lattice is practically incompressible, $c_{11} \gg c_{66}$. Therefore, we can neglect the longitudinal displacement modes for what follows, and we consider a vortex line participating in a shear deformation on the scale of the vortex lattice unit cell $R = a$ perpendicular to the vortex line and on a scale L along the vortex line (we denote perpendicular scales by R and scales parallel to the vortex line by L). The single-vortex scale L_0 is determined by optimizing the sum of the tilt and shear energy of the vortex lattice unit cell with respect to the length L which gives

$$L_0 \simeq a \left(\frac{c_{44}(1/a, 1/L_0)}{c_{66}} \right)^{1/2} \sim \left(\frac{\varepsilon_l(1/L_0)}{c_{66}} \right)^{1/2}, \tag{3.6}$$

where we have to take into account the dispersion of the tilt modulus $c_{44} = c_{44}(K,q)$ whereas the shear modulus is approximately dispersion-free. Because $K \simeq 1/a$ represents the shortest wavelength $c_{44}(1/a,q) \simeq \varepsilon_l(q)/a^2$ is given by the single-vortex line tension $\varepsilon_l(q)$. The length scale L_0 sets the typical scale along the vortex line over which a single vortex can freely fluctuate in the "cage" created by its neighbors.

As the vortex lattice is essentially incompressible the elastic vortex lattice fluctuations are dominated by transversal shear and tilt modes which are described by the transversal part $G_T(\mathbf{K},q)$ of the elastic vortex lattice Green's function $G_T(\mathbf{K},q) = c_{66}K^2 + c_{44}(K,q)q^2$. Tilt and shear contributions always enter the final results for thermal and disorder-induced displacement fluctuations through this elastic Green's function. Therefore we can rewrite the Lindemann criteria (3.2)–(3.5) using

$$\langle \Delta u^2(a,0)\rangle_T = \langle \Delta u^2(0,L_0)\rangle_T \ , \qquad \overline{\langle \Delta u^2(a,0)\rangle} = \overline{\langle \Delta u^2(0,L_0)\rangle}. \tag{3.7}$$

To calculate mean values of $\Delta u(L_0) = u(\mathbf{0},L_0) - u(\mathbf{0},0)$, however, we only need to know single-vortex properties on scales $L < L_0$ [the relative fluctuations of $\Delta u(L_0)$ are also identical to the total fluctuations u of a vortex of length $L = L_0$]. Hence, fluctuations of a *single* vortex up to the scale of the cage length are identical to relative fluctuations of two neighboring vortices. The local character of the Lindemann criteria (3.2)–(3.5) becomes even more obvious.

If the Lindemann criterion is formulated in terms of three characteristic energies as in Refs. [67] and [70] they also refer to the energies of a vortex fluctuation of wavelength L_0 parallel and wavelength a perpendicular to the vortex line. The typical thermal energy of such a fluctuation is T. The typical energy for a plastic deformation can be estimated by the elastic energy corresponding to a deformation with $u = c_L a$ which is $E_{pl} \simeq \varepsilon_l(1/L_0)c_L^2a^2/L_0$. The typical pinning energy is estimated by the elastic energy corresponding to the typical pinning-induced displacement $u = \overline{\langle \Delta u(a,0)\rangle^2}$ which is $E_{pin} \simeq \varepsilon_l(1/L_0)\overline{\langle \Delta u(a,0)\rangle^2}/L_0$. It becomes clear that the criteria $T = E_{pl}$, $T + E_{pin} = E_{pl}$, $E_{pin} = E_{pl}$, and $T = E_{pin}$ are equivalent to the Lindemann criteria (3.2)–(3.5).

Using eq. (3.6), we can calculate the single-vortex length L_0, for which we find

$$L_0 \simeq \begin{cases} \varepsilon a(1-b)^{-1/2} & \text{for } a < \lambda_{ab} \\ a\,(a/\lambda_{ab})^{-3/4}\, e^{a/2\lambda_{ab}} & \text{for } a > \lambda_{ab} \ , \end{cases} \tag{3.8}$$

where $b \equiv B/B_{c2} = 2\pi\xi_{ab}^2/a^2$ is the reduced magnetic induction, λ_{ab} is the magnetic penetration depth, and

$$\varepsilon \equiv \lambda_{ab}/\lambda_c \tag{3.9}$$

the anisotropy ratio of the type-II superconductor. Small logarithmic corrections are neglected in eq. (3.8). In the dilute limit ($a > \lambda_{ab}$) and in the dense limit ($a < \lambda_{ab}$) very close to the upper critical field $1 - b \ll 1$ the single-vortex length becomes very large. In both cases this is due to a softening of the lattice and a corresponding decrease in c_{66}, however for slightly different reasons. At low fields the vortex interaction decreases exponentially with increasing a/λ_{ab} leading to a softening, at extremely high fields softening is due to the effective increase of the magnetic penetration depth $\tilde{\lambda}_{ab} \equiv \lambda_{ab}(1-b)^{-1/2}$ by the large normal cores of the vortices [6] and an effective decrease of the vortex-vortex interaction by a factor $(1-b)$ [5]. In low-T_c materials such as NbSe this effect becomes very important because melting and amorphization transition lines are both located in the vicinity of the upper critical field.

Using the result (3.8) we can also derive a simple expressions for the line stiffness which is justified if prefactors and logarithmic corrections are not crucial and valid only for the relevant fluctuations $q < 1/L_0$ which are not suppressed by the cage effect:

$$\varepsilon_l(q) \simeq \begin{cases} a < \lambda_{ab}: & \varepsilon_0(1-b)\varepsilon^2 \\ a > \lambda_{ab}: & \begin{cases} \varepsilon_0 & \text{for } q < \lambda_{ab}^{-1} \\ \varepsilon_0/q^2\lambda_{ab}^2 & \text{for } \lambda_{ab}^{-1} < q < (\varepsilon\lambda_{ab})^{-1} \\ \varepsilon_0\varepsilon^2 & \text{for } q > (\varepsilon\lambda_{ab})^{-1} \end{cases} \end{cases} \tag{3.10}$$

where $\varepsilon_0 \equiv (\Phi_0/4\pi\lambda_{ab})^2$ is the characteristic line energy of a vortex, and ξ_{ab} is the coherence length. The results for the dense limit $a < \lambda_{ab}$ and the regime $q > 1/\varepsilon\lambda_{ab}$ in the dilute limit $a > \lambda_{ab}$ are due to the Josephson coupling, whereas tin remaining limits the results originate from the electromagnetic interaction of line elements, which gives rise to the strong non-locality.

3.4 Single-vortex fluctuations and electromagnetic coupling

As already pointed out we can use eq. (3.7) to calculate the averages in the Lindemann criteria (3.2)–(3.5) by considering *single*-vortex fluctuations up to the scale L_0 set by the vortex interaction. As the simplified expression (3.10) shows there are no further complications from nonlocal couplings in the dense regime $a < \lambda_{ab}$ because the essentially nondispersive Josephson coupling governs the behavior up to the scale L_0 in this regime.

This, however, changes if the dilute limit $a > \lambda_{ab}$ is considered where competing effects of Josephson and electromagnetic coupling between vortex elements have to be taken into account as eq. (3.10) shows. The effects for single-vortex fluctuations due to temperature and quenched disorder are discussed in detail elsewhere [55]. For a self-contained discussion we will present here the main results.

Due to the competing nonlocal electromagnetic and local Josephson coupling there is a window of wave vectors $1/\lambda_{ab} < q < 1/\varepsilon\lambda_{ab}$ in the dilute limit $a > \lambda_{ab}$ where the line stiffness is strongly dispersive with $\varepsilon_l(q) \propto q^{-2}$, see eq. (3.10). In the limit of a very weak Josephson coupling $\varepsilon \approx 0$ the dispersion of the electromagnetic contribution persists down to the shortest length scale, which is then set by the layer distance d. For the fluctuation behavior in the dilute limit the largest possible wave vector showing q^{-2} dispersion is important. In a layered material this is $q_d \simeq 1/\max\{d, \varepsilon\lambda_{ab}\}$ and we introduce a corresponding *dispersion length scale*

$$L_d = \max\{d, \varepsilon\lambda_{ab}\} = \lambda_{ab}\max\{\varepsilon_d, \varepsilon\}\ , \tag{3.11}$$

where

$$\varepsilon_d \equiv d/\lambda_{ab} \tag{3.12}$$

is an effective *layered anisotropy* of the material. For the short-scale fluctuations it is important to distinguish between two classes of superconductors depending on the strength of the Josephson coupling or the size of ε. Superconductors with a *strong* Josephson coupling $\varepsilon > \varepsilon_d$ have $L_d \simeq \varepsilon\lambda_{ab}$; YBCO falls into this class and of course all low-T_c materials such as NbSe without layered structures. On the other hand, superconductors with a *weak* Josephson coupling $\varepsilon < \varepsilon_d$ have $L_d \simeq d$. But it has to be noted that even if $\varepsilon < \varepsilon_d$ at $T = 0$ the Josephson coupling becomes strong above a temperature

$$t_d = 1 - (\varepsilon/\varepsilon_d)^2 \tag{3.13}$$

because $\varepsilon_d \propto (1-t)$, where $t = T/T_c$ is the reduced temperature. For typical parameters for BSCCO, $\varepsilon \approx 1/200$, $d \approx 15$ Å, $\lambda_{ab} \approx 2000$ Å, and $T_c \approx 100$ K one finds that BSCCO has a weak Josephson coupling at low temperatures but the Josephson coupling becomes strong above $T_d \approx 55$ K.

Considering only fluctuations with wave vectors $1/\lambda_{ab} < q < q_d$ one can show that due to the predominantly electromagnetic coupling each vortex segment of length λ_{ab} effectively *decouples* into small segments of length L_d that fluctuate independently in a harmonic potential [76]. Therefore, the vortex line becomes very soft with respect to fluctuations on the short scale L_d. This holds for thermal fluctuations as well as for fluctuations due to pinning. In particular, this leads both for thermal and for fluctuations from quenched point disorder to a breakdown of scaling in the displacement correlations. Specifically, we find for $L = L_0$ (the following equation holds analogously for thermal averages $\langle \ldots \rangle_T$)

$$\overline{\langle \Delta u^2(L_0)\rangle} \simeq \begin{cases} \overline{\langle \Delta u^2(L_0)\rangle_\varepsilon} & \text{for } d < L_0 < \varepsilon\lambda_{ab} \\ \overline{\langle \Delta u^2(L_d)\rangle} & \text{for } L_d < L_0 < \lambda_{ab} \\ \overline{\langle \Delta u^2(L_0)\rangle_i} + \overline{\langle \Delta u^2(L_d)\rangle} & \text{for } L_0 > \lambda_{ab}\ , \end{cases} \tag{3.14}$$

where the subscript "ε" implies that only large wave vectors $q > \varepsilon\lambda_{ab}$ are integrated over and thus the average is performed using the anisotropic stiffness $\varepsilon_l(q) \simeq \varepsilon_0\varepsilon^2$ and analogously the subscript "i" implies that only small wave vectors $q < \lambda_{ab}$ are integrated over and thus the average is performed using the local limit of eq. (3.10) where the stiffness is isotropic $\varepsilon_l \simeq \varepsilon_0$.

According to the Lindemann criteria (3.2)–(3.5) in conjunction with eq. (3.7) the vortex phase diagram is determined by the displacement fluctuations of a single vortex on scales $L < L_0$. From eq. (3.14), the structure of the phase diagram with regard to the dominant scale of these single-vortex fluctuations becomes clear, see Fig. 3.2. In the dense regime $a < \lambda_{ab}$ the essentially nondispersive anisotropic Josephson part of $\varepsilon_l(q)$ is always dominating. Then the largest scale L_0 in the cage model is the dominant scale of fluctuations as in the first line of eq. (3.14) but we have to include possible high-field corrections and use $\varepsilon_l(q) \simeq \varepsilon_0(1-b)\varepsilon^2$ in the dense limit. Evaluation of the Lindemann criteria will show that this produces the upper branches of both the melting and the amorphization transition line in the regime $a < \lambda_{ab}$ of the B-T plane, see Fig. 3.2.

In the dilute limit $a > \lambda_{ab}$ the situation becomes more complicated because L_0 grows exponentially with a, see eq. (3.8), and thus $L_0 > \lambda_{ab}$ essentially in the whole dilute limit.

Then effects from the nonlocal electromagnetic coupling become relevant and according to eq. (3.14) fluctuations from two scales – L_0 and $L_d = \max\{d, \varepsilon\lambda_{ab}\}$ – are dominant. Evaluation of the Lindemann criteria shows that fluctuations on the scale L_d give the continuation of the upper branch of both the melting and the amorphization transition line into the dilute regime whereas fluctuations on the exponentially large scale L_0 give the lower branches of both transition lines, see Fig. 3.2. Thus the nonlocal electromagnetic coupling is responsible for the typical phase diagrams with reentrant liquid or amorphous vortex phases, see Figs. 3.3, 3.6, and 3.7. Experimentally, lower branches of neither the melting nor the order-disorder transition line could be observed so far in the dilute regime. Therefore we will focus on the upper branches throughout this chapter.

As the previous discussion showed, only for the upper branch of the transition lines in the dilute limit for BSCCO with a weak Josephson coupling dispersion becomes crucial, and we have to take into account fluctuations on the scale of the layer spacing $L_d = d$. This means we have to consider fluctuations of a single pancake vortex relative to its neighbors in adjacent layers.

Quasi-2D behavior of the vortex lattices becomes relevant for melting processes as soon as $L_0 < d$ when the tilt energy can be neglected against the shear energy on the scale of one layer spacing d. The crossover condition $L_0 < d$ is fulfilled for $b > b_{2D}$ above the *2D crossover field*

$$b_{2D} \simeq \frac{2\pi}{\kappa^2} \max\left\{\frac{\varepsilon^2}{\varepsilon_d^2}(1-b)^{-1}, 1\right\} \ , \tag{3.15}$$

where we used eq. (3.8) and neglected a logarithmic correction [7]. $\kappa \equiv \lambda_{ab}/\xi_{ab}$ is the Ginzburg-Landau parameter. For a strong Josephson coupling $\varepsilon > \varepsilon_d$ the crossover field is in the dense regime and has a temperature dependence $b_{2D}(1 - b_{2D}) \propto (1-t)^{-1}$. From eq. (3.8) one derives that for $\varepsilon > d/5\xi_{ab}$ we *always* have $L_0 > d$ and there is no crossover to quasi-2D behavior. This condition is actually fulfilled for YBCO with typical parameters $\varepsilon \approx 1/5$, $d \approx 12$ Å, and $\xi_{ab} \approx 15$ Å. Therefore we will exclude the possibility of 2D behavior for YBCO in our subsequent discussions of melting and order-disorder transitions. For a weak Josephson coupling $\varepsilon < \varepsilon_d$ the 2D crossover field is approximately equal to (actually slightly below) the field $b = 2\pi/\kappa^2$ at which $a = \lambda_{ab}$, i.e., the boundary between the dilute and dense regime. This means for a weak Josephson coupling, e.g., in BSCCO below $T_d \approx 55$ K, the vortex lattice melting shows quasi-2D behavior in the whole dense limit. It is expected that as soon as the melting or the amorphization transition line intersects the line $b_{2D}(t)$ the character of the melting or amorphization process changes from 3D linelike to quasi-2D and decoupling of the FLL happens prior to the melting, which is then a 2D melting transition. A two-dimensional BrG phase has been shown to be *always* unstable with respect to dislocation formation in the presence of disorder [77] such that the decoupling transition leads directly to a 2D amorphous VG if amorphization does not happen prior to decoupling [1].

---

[1] At this point it should be noted that a Lindemann-like criterion analogous to eq. (3.4) would give the incorrect result regarding the instability of the 2D BrG phase as it would predict the existence of an amorphization transition and thus of a quasiordered 2D BrG phase below a critical disorder strength.

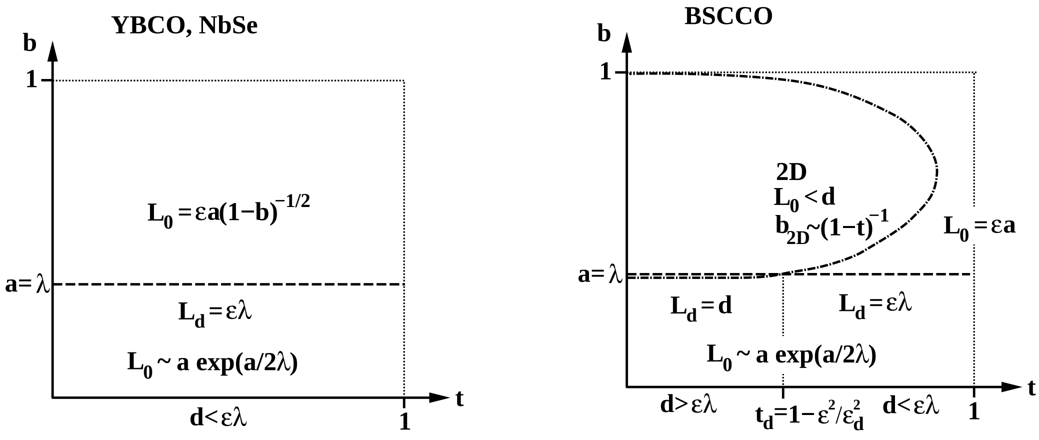

Figure 3.2: Schematic diagrams in the b-t plane (the dilute regime is enlarged) showing the dominant scales for displacement fluctuations of a single vortex of length L_0. For YBCO and NbSe fluctuations on the largest scale L_0 dominate in the dense regime and determine the upper branches of the melting and order-disorder transition lines. BSCCO exhibits quasi-2D behavior in large parts of the dense regime. Fluctuations on the exponentially large scale L_0 also determine the lower branches of transition lines deep in the dilute regime for YBCO, NbSe, and BSCCO. The continuation of the upper branches of the transition lines into the dilute regime, however, is determined by fluctuations on the scale L_d; for YBCO and NbSe $L_d = \varepsilon\lambda_{ab}$ whereas for BSCCO $L_d = d$ at low temperatures.

Figure 3.2 summarizes the findings of this section regarding the relevant length scales for the fluctuations causing melting or amorphization for the three exemplary materials we want to study in this chapter. YBCO has a strong Josephson coupling and $L_d = \varepsilon\lambda_{ab}$, BSCCO a weak Josephson coupling and thus $L_d = d$ for temperatures $T < T_d$, and in the low-T_c material NbSe there is no layered structure at all (formally corresponding to $\varepsilon_d \approx 0$) and $L_d = \varepsilon\lambda_{ab}$.

3.5 Thermal melting

First we want to briefly recapitulate the calculation of thermal melting curves in the absence of disorder according to the Lindemann criterion (3.2) or the equivalent criterion

$$\langle \Delta u^2(L_0) \rangle_T = c_L^2 a^2 \tag{3.16}$$

formulated in terms of displacement fluctuations of a single vortex on scales $L < L_0$ using eq. (3.7), to which we apply our results of the preceding section for the length scales of the relevant fluctuations causing melting. The results are summarized in Fig. 3.3 for NbSe, YBCO, and BSCCO.

YBCO and NbSe

YBCO and NbSe are both anisotropic type-II superconductors and have qualitatively similar melting curves as long as the layered structure of YBCO can be neglected. Fluctuations are larger in the high-T_c material YBCO due to the increased transition temperatures ($T_c \approx 90$ K for YBCO and $T_c \approx 6$ K for NbSe) and lower coherence lengths ($\xi_{ab} \approx 20$ Å in YBCO and $\xi_{ab} \approx 100$ Å in NbSe) which lead to a *Ginzburg number* $\mathrm{Gi} \equiv (T_c/\varepsilon\varepsilon_0\xi_{ab})^2/8$ [7] with $\mathrm{Gi} \approx 1.5 \times 10^{-2}$ for YBCO but much smaller $\mathrm{Gi} \approx 1.7 \times 10^{-6}$ in NbSe. Therefore, the vortex lattice melting in the low-T_c material NbSe takes place only at high fields in the vicinity of H_{c2}, see Fig. 3.3.

As pointed out in Sec. 3.4, the Josephson coupling dominates throughout the dense regime $a < \lambda_{ab}$ and thus we use the anisotropic line stiffness $\varepsilon_l(1/L_0) \simeq \varepsilon_0(1-b)\varepsilon^2$ and $L_0 \simeq \varepsilon a(1-b)^{-1/2}$ from eq. (3.8) to obtain $\langle\Delta u^2(L_0)\rangle_T \simeq TL_0/\varepsilon_l$. With the Lindemann criterion (3.16) this gives for the upper branch $b_m(t)$ of the melting line the well-known result [17, 7]

$$\frac{b_m}{(1-b_m)^3} \simeq \frac{\pi}{4}c_L^4\mathrm{Gi}^{-1}(1-t)t^{-2} \; . \tag{3.17}$$

If the upper branch of the melting line is continued into the dilute limit $a > \lambda_{ab}$ fluctuations on the scale L_d dominate the expectation value in the Lindemann criterion (3.16), $\langle\Delta u^2(L_0)\rangle_T \simeq \langle\Delta u^2(L_d)\rangle_T$. YBCO and NbSe have a strong Josephson coupling and thus $L_d = \varepsilon\lambda_{ab}$. On the scale $\varepsilon\lambda_{ab}$, we use again the anisotropic line stiffness $\varepsilon_l(1/\varepsilon\lambda_{ab}) \simeq \varepsilon_0\varepsilon^2$ to get $\langle\Delta u^2(\varepsilon\lambda_{ab})\rangle_T \simeq T\varepsilon\lambda_{ab}/\varepsilon_l$. Then the Lindemann criterion gives the upper branch $b_m(t)$ of the melting line in the dilute limit as [59]

$$b_m \simeq \frac{\pi}{\sqrt{2}}c_L^2\kappa^{-1}\mathrm{Gi}^{-1/2}(1-t)^{1/2}t^{-1}. \tag{3.18}$$

BSCCO

The strongly layered BSCCO has a weak Josephson coupling at temperatures below $T_d \approx 55$ K. The upper branch of the melting line should intersect the 2D crossover line $b_{2D}(t)$ around the 2D melting temperature of a superconducting layer $T_m^{2D} \approx d\varepsilon_0/70$ [7]. Taking again $d \approx 15$ Å and $\lambda_{ab} \approx 2000$ Å as typical parameters for BSCCO, one finds $T_m^{2D} \approx 10$ K which is well below T_d. This means that at the temperature T_m^{2D} the 2D crossover line is at the boundary to the dense regime, see eq. (3.15), such that the upper branch of the 3D melting line lies entirely in the dilute regime, see Fig. 3.3. For clarity of presentation we will limit the discussion here to phase diagrams for the situation $T_m^{2D} < T_d$ that arises for a realistic choice of parameters for the BSCCO material.

In the dilute regime, BSCCO exhibits a behavior distinct from YBCO or NbSe due to its weak Josephson coupling or $L_d = d$. At the upper branch of the melting line fluctuations on the scale of the layer spacing $L_d = d$ dominate the mean-square displacement in eq. (3.16) due to the nonlocal electromagnetic coupling as discussed in Sec. 3.4, i.e., $\langle\Delta u^2(L_0)\rangle_T \simeq \langle\Delta u^2(d)\rangle_T$. To calculate $\langle\Delta u^2(d)\rangle_T$ on the scale of the layer distance, we can consider a single pancake coupled to the pancakes in adjacent layers by a harmonic potential $\varepsilon_l(1/d)\Delta u^2/d$, and use $\varepsilon_l(1/d) \simeq \varepsilon_0\varepsilon_d^2$ from eq. (3.10) in $\langle\Delta u^2(d)\rangle_T \simeq Td/\varepsilon_l(1/d)$. Then the Lindemann criterion gives the upper branch $b_m(t)$ of the melting line for BSCCO in the dilute limit as [59]

$$b_m(t) \simeq \sqrt{2}\pi c_L^2\kappa^{-2}\mathrm{Gi}_{2D}^{-1}(1-t)t^{-1}, \tag{3.19}$$

where we used the 2D Ginzburg number $\mathrm{Gi}_{2D} \equiv 2\mathrm{Gi}^{1/2}\kappa^{-1}\varepsilon/\varepsilon_d \approx T_c/100T_m^{2D}$ [7]. For BSCCO with $T_c \approx 100$ K the 2D Ginzburg number is $\mathrm{Gi}_{2D} \approx 0.096$. For low temperatures $t \ll 1$, the transition approaches the 2D melting transition of a layer upon intersecting $b_{2D} \approx 2\pi/\kappa^2$ (if we choose $c_L \approx 1/\sqrt{70}$), see Fig. 3.3.

For temperatures $T < T_m^{2D}$ the 3D vortex solid first undergoes a decoupling transition at a field b_{dc} into a 2D vortex solid which undergoes a 2D melting transition at T_m^{2D}. If this decoupling transition is also described by a Lindemann criterion of the form $\langle\Delta u^2(0,d)\rangle_T = c_L^2a^2$ as suggested in Refs. [78] and [59], we will get the same formula (3.19) for the decoupling transition line $b_{dc}(t)$, which is thus the continuation of the 3D melting line into the 2D regime, see Fig. 3.3.

3.6 Pinning of single vortices

Before addressing the BrG stability boundaries by using the Lindemann criterion (3.4) we want to discuss different pinning regimes depending on the strength of the frozen disorder. We consider a single elastic vortex line with stiffness $\varepsilon_l(q)$ in a quenched disorder potential $V(z,\mathbf{u})$ with a Gaussian distribution, zero mean, and short-range correlations in all directions,

$$\overline{V(z,\mathbf{u})V(z',\mathbf{u}')} = \gamma\xi_{ab}^4\delta(z-z')\Delta_{\xi_{ab}}(\mathbf{u}-\mathbf{u}') \; . \tag{3.20}$$

The parameter γ gives the strength of the quenched disorder and is temperature dependent [7]. This temperature dependence due to the microscopic pinning mechanism will be discussed further below. Usually, we consider point disorder correlations of a short range ξ_{ab} given by the size of the vortex cores with and an integrable disorder correlator that we approximate by $\Delta_{\xi_{ab}}(\mathbf{u}) \approx \delta_{\xi_{ab}}(\mathbf{u})$, i.e., a δ function of range ξ_{ab}.

A convenient *pinning strength parameter* δ (see Ref. [7]) is defined by the ratio of the mean-square pinning energy $E_{pin}^2(\xi_c) \simeq \gamma\xi_{ab}^2\xi_c$ for a small line element of length $L \simeq \xi_c$ and with typical displacement $u \simeq \xi_{ab}$ and the square of the corresponding tilt energy $E_{tilt}(\xi_c) \simeq \varepsilon_0\varepsilon^2\xi_{ab}^2/\xi_c \simeq \varepsilon_0\xi_c$ [2]

$$\frac{\delta}{\varepsilon} \equiv \frac{\gamma\xi_{ab}^2\xi_c}{(\varepsilon_0\xi_c)^2} \; . \tag{3.21}$$

In a layered material one can consider the analogous energies for a segment of length $L \simeq d$, i.e., the mean-square pinning energy $E_{pin}^2(d) \simeq U_p^2$ with the *pancake pinning energy*

---

[2] It should be noted that this expression has *no* correction factors $(1-b)$ at high fields because $\gamma \propto f_{pin}^2 \propto \varepsilon_0^2$ where f_{pin} is the pinning force exerted by a single point defect [7, 69]; therefore corrections due to the replacement $\varepsilon_0 \to \tilde{\varepsilon}_0 = \varepsilon_0(1-b)$ in eq. (3.21) cancel.

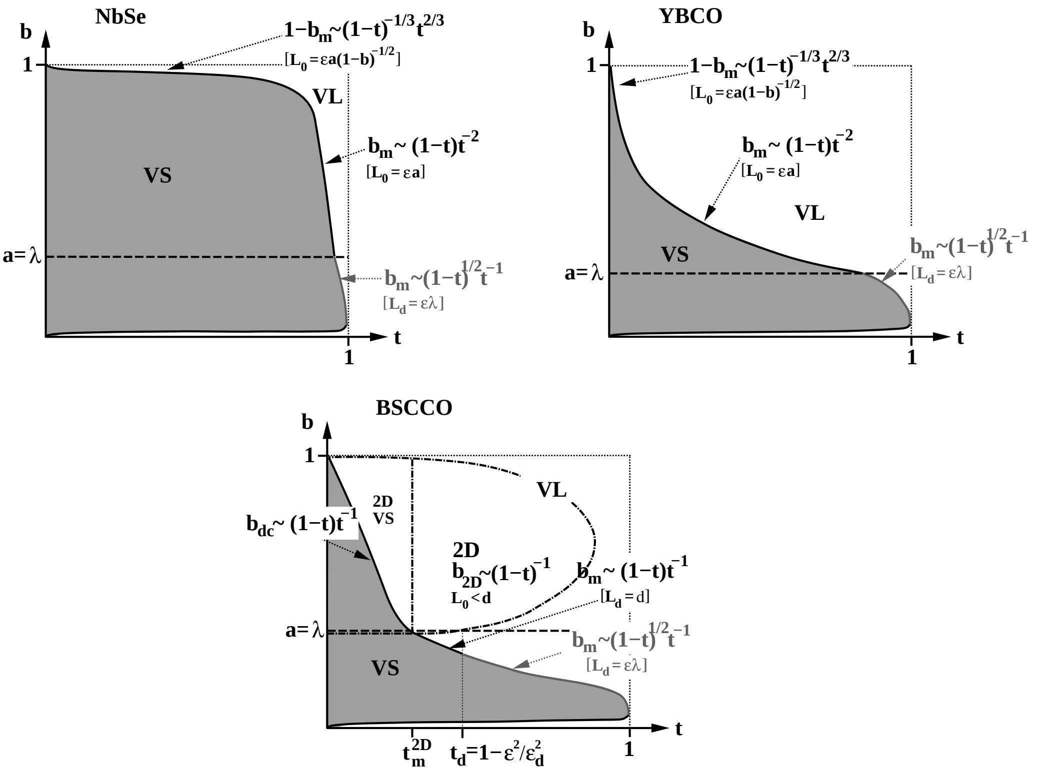

Figure 3.3: Schematic phase diagrams for thermal melting of the vortex solid (VS) into a vortex liquid (VL) in the absence of quenched disorder for NbSe, YBCO, and BSCCO. For BSCCO above the crossover field b_{2D} there is a decoupling into a 2D VS prior to melting. (The dilute regime is enlarged, the reentrance at very low fields is shown for completeness but not discussed in the text.)

$U_p = (\gamma \xi_{ab}^2 d)^{1/2}$ and the square of the corresponding tilt energy $E_{tilt}(d) \simeq \varepsilon_l(1/d)\xi_{ab}^2/d \simeq \varepsilon_0(\varepsilon^2 + \varepsilon_d^2)\xi_{ab}^2/d$, see eq. (3.10). Using this we define an analogous *layered pinning strength parameter* δ_d as

$$\delta_d \equiv \frac{U_p^2}{[\varepsilon_0(\varepsilon^2 + \varepsilon_d^2)\xi_{ab}^2/d]^2} \ . \tag{3.22}$$

From the definitions (3.21) and (3.22) it is clear that collective pinning theory applies to weak pinning $\delta/\varepsilon \ll 1$ and $\delta_d \ll 1$. Whereas the former condition is usually fulfilled both in low-T_c materials such as NbSe and anisotropic HTSC's such as YBCO, the latter condition is violated in layered HTSC's with strong disorder, e.g., in BSCCO. We will call pinning with $\delta_d > 1$ *strong pinning*. Experimental estimates for the pinning strength can be obtained from measurements of the (single-vortex) critical current j_c using the relation $j_c \simeq j_0\,(\delta/\varepsilon)^{2/3}$, where $j_0 \simeq c\varepsilon_0/\xi_{ab}\Phi_0$ is the depairing current [7]. Due to their larger anisotropy and the intrinsic doping typical values for the pinning parameter δ/ε are usually higher in the high-T_c materials YBCO and BSCCO. Throughout this chapter we assume values $\delta/\varepsilon \approx 10^{-2}$ for YBCO (corresponding to $j_c \approx 10^7$ A cm^{-2}). and much smaller values $\delta/\varepsilon \approx 10^{-9}$ for the low-T_c material NbSe (corresponding to $j_c/j_0 \sim 10^{-6}$, see Ref. [79]), both well in the weak pinning regime. For BSCCO we find indeed strong pinning $\delta_d \approx 10^4 \gg 1$ using an estimate $U_p \approx 10$ K (these values correspond to $\delta/\varepsilon \approx 0.03$).

There are two basic microscopic pinning mechanisms, δl pinning from variations in the mean free path and δT_c pinning from variations in T_c, which give rise to a different temperature dependence of δ/ε. Without going into details here it is found [7, 69] that

$$\delta \;\propto\; (1-t)^{3/2} \quad (\delta l \text{ pinning}) \;, \tag{3.23}$$
$$\delta \;\propto\; (1-t)^{-1/2} \quad (\delta T_c \text{ pinning}) \;. \tag{3.24}$$

Whereas for high-T_c materials (YBCO, BSCCO) the thermal smearing of the pinning energy landscape above the depinning temperature T_{dp} is much more important because it sets in at much lower temperatures ($T_{dp} \ll T_c$), the temperature dependence through the microscopic parameters of δ plays an important role in low-T_c materials (NbSe) where the depinning temperature essentially coincides with T_c.

Weak collective pinning

Within weak collective pinning theory the central crossover length for a single vortex is the *collective pinning or Larkin length* L_c which is defined as the length scale at which $\overline{\langle \Delta u(L_c)\rangle^2} = \xi_{ab}^2$ at low temperatures. On smaller scales perturbation theory applies and the disorder potential can be expanded into random forces (RF). In this regime the roughness exponent is $\zeta_{RF} = 3/2$, i.e., $\overline{\langle \Delta u(L)\rangle^2} \propto L^3$. Segments longer than L_c, on the other hand, explore many almost degenerate minima of the pinning energy landscape. In this so-called random manifold (RM) regime we use the estimate $\zeta_{RM} \approx 5/8$ for the roughness exponent [80, 81]. As pointed out in Sec. 3.4 we only need to consider single-vortex fluctuations with the nondispersive anisotropic Josephson stiffness and fluctuations of single pancakes on the scale d if we are only interested in the upper branch of the order-disorder transition between BrG and amorphous VG phase.

For pinned single vortex lines with the anisotropic Josephson stiffness we have at low temperatures the usual anisotropic collective pinning length [7]

$$L_c \simeq \varepsilon \xi_{ab} \left(\delta/\varepsilon\right)^{-1/3} \tag{3.25}$$

which has *no* correction factors $(1-b)$ at high fields exactly like δ/ε. The displacement fluctuations are given by

$$\overline{\langle \Delta u(L)\rangle^2} \;\simeq\; \xi_{ab}^2 \left(L/L_c\right)^3 \quad \text{for } L < L_c \;, \tag{3.26}$$
$$\overline{\langle \Delta u(L)\rangle^2} \;\simeq\; \xi_{ab}^2 \left(L/L_c\right)^{5/4} \quad \text{for } L > L_c \;. \tag{3.27}$$

There are two important crossovers upon increasing the disorder strength, the crossover from bundle pinning to single-vortex pinning [7] if L_c decreases below the single-vortex length L_0 set by the interaction between vortices and the crossover from weak collective to strong pinning if L_c drops below the layer spacing d and we have to consider the strong pinning of individual pancake vortices [55].

At higher temperatures the disorder gets effectively weakened by thermal fluctuations within the pinning energy landscape as soon as $\langle\Delta u^2(L_c)\rangle_T = \xi_{ab}^2$. This happens at the anisotropic depinning temperature

$$T_{dp} \simeq \varepsilon\varepsilon_0\xi_{ab}\,(\delta/\varepsilon)^{1/3} \tag{3.28}$$

above which an exponential increase of the pinning length sets in [7, 82]

$$L_c(T) \simeq L_c\frac{T_{dp}}{T}e^{C(T/T_{dp})^\alpha} \tag{3.29}$$

with a numerical factor C and an exponent α. For point disorder with an integrable disorder correlation function $\Delta_{\xi_{ab}}(\mathbf{u})$ one finds $\alpha = 3$ [7, 82], and the numerical factor $C = 32/\pi$ has been determined in Ref. [83]. The displacement fluctuations for $L > L_c(T)$ become

$$\overline{\langle\Delta u(L)\rangle^2} \;\simeq\; \xi_{ab}^2\left(1+\frac{T}{T_{dp}}\frac{L_c(T)}{L_c(0)}\right)\left(\frac{L}{L_c(T)}\right)^{5/4}. \tag{3.30}$$

Note that thermal depinning plays no role in low-T_c materials where $\varepsilon\varepsilon_0\xi_{ab} \sim 1000$ K at $T = 0$, and the depinning temperature practically coincides with T_c if the temperature dependence of the microscopic parameters λ_{ab} and ξ_{ab} is taken into account and T_{dp} is calculated self-consistently from eq. (3.28).

Single-vortex versus bundle pinning

For $L_0 < L_c$ pinned vortices on the scale of the pinning length are already interacting and the collectively pinned objects are vortex bundles rather than single vortices [7]. The regime $L_0 < L_c$ is called *bundle pinning* regime. For our purposes bundle pinning simply means that on the scale of the single-vortex length, single-vortex displacements are still treated correctly by the perturbative RF regime (3.26). On the other hand, for $L_0 > L_c$ the pinned objects on the scale of the pinning length are single vortex lines rather than bundles. The regime $L_0 > L_c$ is therefore called *single-vortex pinning* regime. In this regime the RF regime does no longer apply on the single-vortex scale L_0 but we rather have to apply the findings (3.27) for the RM regime. For the following discussion of different materials it is crucial to know the *single-vortex pinning field* b_{sv} where the crossover between single-vortex and bundle pinning happens within the pinning diagram in the b-δ plane. For our purposes, we can focus the discussion on the dense regime $a < \lambda_{ab}$, in the dilute regime single-vortex pinning is dominant because interactions become exponentially weak. At $T = 0$ the condition $L_0 = L_c$ for b_{sv} gives

$$b_{sv}(1-b_{sv}) \simeq 2\pi\,(\delta/\varepsilon)^{2/3} \tag{3.31}$$

using eqs. (3.8) and (3.25). This equation produces two branches for the single-vortex pinning field b_{sv}. For $b \ll 1$, we find for the lower branch $b_{sv}^l \propto (\delta/\varepsilon)^{2/3}$ and close to the

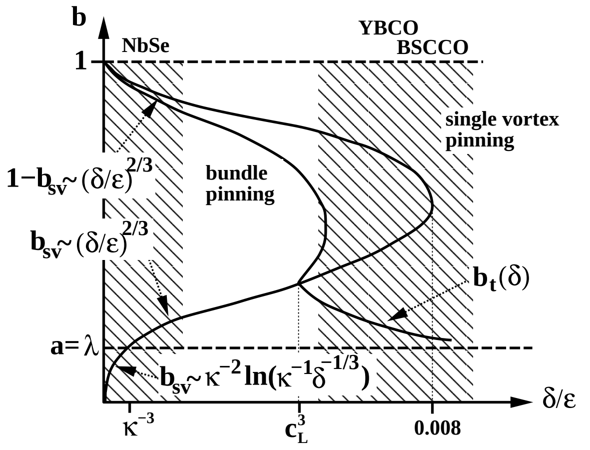

Figure 3.4: Schematic pinning diagram in the b-δ plane showing the single-vortex pinning field b_{sv} at low temperatures (the dilute regime is enlarged). Due to their larger anisotropy typical values for the pinning parameter δ/ε are usually higher in the high-T_c materials YBCO and BSCCO and lie in the single-vortex pinning regime (right hatched region). They are lower in the low-T_c materials such as NbSe and lie typically in the bundle pinning regime (left hatched region). The line $b_t(\delta)$ shows the amorphization transition line in the dense regime as described by eq. (3.40) for bundle pinning and eq. (3.42) for single-vortex pinning. For very weak pinning $\delta/\varepsilon < c_L^3$ as in NbSe this line is in the bulk pinning regime, for stronger disorder as in YBCO and BSCCO it lies in the single-vortex regime.

upper critical field $1-b \ll 1$, an upper branch $1-b_{sv}^u \propto (\delta/\varepsilon)^{2/3}$, see Fig. 3.4. For $\delta/\varepsilon < \kappa^{-3}$ the lower branch enters the dilute regime $a > \lambda_{ab}$ where $b_{sv}^l \propto \kappa^{-2}\ln^{-2}\left(\kappa^{-1}\delta^{-1/3}\right)$; this is the generic situation for NbSe, see Fig. 3.4. For $\delta/\varepsilon > (8\pi)^{-3/2} \approx 0.008$ there is only single-vortex pinning; typical disorder strengths for YBCO and BSCCO have such values as shown in Fig. 3.4. For low-T_c materials the lower branch of the single-vortex pinning boundary b_{sv}^l is usually in the dilute regime $a > \lambda_{ab}$ due to the small disorder strength whereas in the high-T_c materials it is in the dense regime $a < \lambda_{ab}$. This is the experimental situation that we will assume throughout the following discussion of the different materials and that is sketched in Fig. 3.4.

The temperature dependence of the lines b_{sv} is rather different depending on whether the depinning temperature T_{dp} is much smaller then the critical temperature T_c as in the high-T_c materials YBCO and BSCCO or whether it practically coincides with T_c as in the low-T_c superconductor NbSe, see Fig. 3.5. Therefore the thermal weakening of disorder above the depinning temperature, which gives an exponential increase of the pinning length, is the dominant effect for high-T_c superconductors. The temperature dependence through the microscopic parameters (3.23) or (3.24) can be neglected for these materials as long as T_{dp}/T_c is small. In this situation we have to use the condition $L_0 = L_c(T)$ with $L_c(T)$ from eq. (3.29) above the depinning temperature T_{dp}. This gives in the dense regime

$$b_{sv}(1-b_{sv}) \simeq 2\pi\,(\delta/\varepsilon)^{2/3}\,(T_{dp}/T)^2\,e^{-2C(T/T_{dp})^3} \tag{3.32}$$

from which we derive an exponentially decreasing lower branch an exponentially increasing

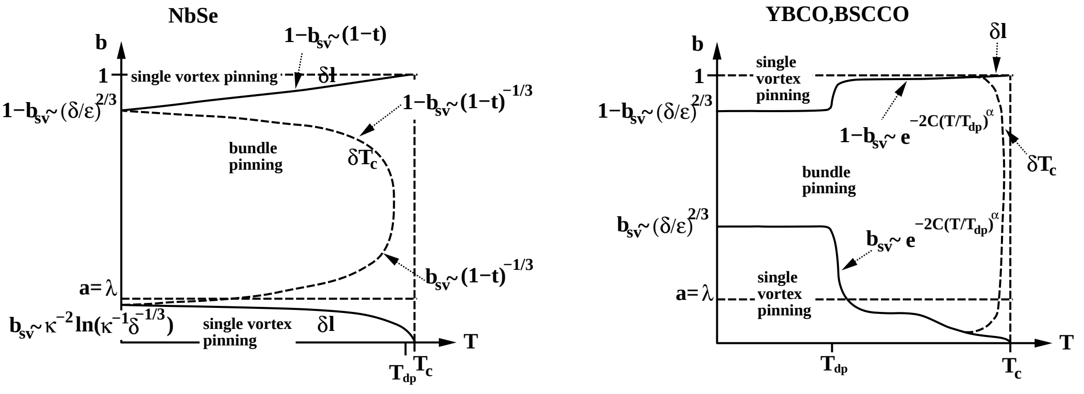

Figure 3.5: Schematic pinning diagram in the b-t plane showing the temperature dependence of the single-vortex pinning field b_{sv} for δl pinning (solid lines) and δT_c pinning (dashed lines). For the high-T_c materials YBCO and BSCCO thermal smoothing above the depinning temperature T_{dp} governs the temperature dependence of b_{sv}. For the low-T_c material NbSe the temperature dependence of the pinning parameter $\delta(t)$ itself [eqs. (3.23) and (3.24)] is most relevant.

upper branch as shown in Fig. 3.5. At temperatures slightly above T_{dp} the lower branch enters the dilute regime $a > \lambda_{ab}$. Note that for high-T_c materials $b_{sv}^l(T)$ typically starts out in the dense regime for $T = 0$. The thermal weakening of disorder above T_{dp} has been neglected in Ref. [70] although high-T_c materials with potentially rather low T_{dp} have been considered.

On the other hand, T_{dp}/T_c is no longer small for the low-T_c superconductors where $T_{dp}/T_c \approx 1$, and in these materials the temperature dependence of the pinning length comes exclusively through the temperature dependence of the pinning strength (3.23) or (3.24). Using this in eq. (3.31) we find $b_{sv}^l(t) \propto (1-t)$ and $1 - b_{sv}^l(t) \propto (1-t)$ for δl pinning and $b_{sv}^l(t) \propto (1-t)^{-1/3}$ and $1 - b_{sv}^l(t) \propto (1-t)^{-1/3}$ for δT_c pinning in the dense regime. If $b_{sv}^l(T)$ starts out in the dilute regime for $T = 0$ the lower branch for δl pinning is $b_{sv}^l(T) \propto \kappa^{-2} \ln^{-2}\left[\kappa^{-1}\delta^{-1/3}(1-t)^{-1/2}\right]$ and stays in the dilute regime, see Fig. 3.5. For δT_c pinning the lower branch will enter into the dense regime at a temperature $1 - t \simeq (\delta/\varepsilon)^2\kappa^6$ in this case, see Fig. 3.5. Note that these results are different from what has been obtained in Ref. [69] where factors $(1 - b)$ in the expression for L_0 have been neglected.

Pinning of pancake vortices

On the smallest scale in a layered superconductor $L = d$ we can no longer discuss fluctuations of vortex *lines*. Then we have to consider the relative displacements $\mathbf{u} \equiv \Delta\mathbf{u}(d)$ between single pancake segments of the vortex line in two neighboring layers and discuss the pinning of single pancake vortices [84, 66, 85, 55]. For large disorder strength and weak Josephson coupling as it occurs typically in BSCCO, it is possible that $\delta_d > 1$, which is equivalent to $L_c < d$ as becomes clear from the definition (3.22) of δ_d. In this case the pinning of pancake vortices becomes particularly interesting because we cross over to a regime where pinning is no longer a small perturbation but we have *strong pinning* of pointlike pancake vortices. To calculate $\langle \Delta u^2(d)\rangle_T$ on the scale of the layer distance, we consider as in Sec. 3.5 a single pancake with displacement $\mathbf{u}$ coupled to the pancakes in adjacent layers by a harmonic potential $\varepsilon_l(1/d)u^2/d$, but with an additional pinning potential $V_d(\mathbf{u}) = dV(0,\mathbf{u})$.

Using an Imry-Ma argument [84, 66, 85, 55] one can estimate $\overline{\langle u\rangle^2}$ for strong pinning ($\delta_d > 1$) at low temperatures,

$$\overline{\langle u\rangle^2} \simeq \xi_{ab}^2 \delta_d^{1/2} \ln^{-1/2}(\delta_d^{1/2}) \; . \tag{3.33}$$

The corresponding ground-state energy $E_0 \simeq E_{pin}(u)$ is

$$E_0 \simeq -U_p \ln^{1/2}(\delta_d^{1/2}) \tag{3.34}$$

whereas the typical elastic energy sets an energy scale

$$U^* \simeq U_p \ln^{-1/2}(\delta_d^{1/2}) \tag{3.35}$$

which is the typical size of elastic energy barriers between different metastable states.

Equation (3.33) is a non-perturbative result which holds for $\overline{\langle u\rangle^2} > \xi_{ab}^2$, which is exactly the condition $\delta_d > 1$ for strong pinning. Otherwise perturbation theory applies and one finds

$$\overline{\langle u\rangle^2}_{RF} \simeq \xi_{ab}^2 \delta_d \; . \tag{3.36}$$

which is the perturbative RF result for weakly pinned pancake vortices.

Thermal fluctuations weaken the pinning and lead to thermal depinning of pinned pancakes. The characteristic depinning temperatures, however, are different for the cases of strong pinning ($\delta_d > 1$) and weak pinning ($\delta_d < 1$). For strong pinning the relevant depinning temperature is set by the typical barrier height U^*, and the depinning happens in the temperature interval $U^* < T < |E_0|$ [55, 85].

What remains to be considered for strong pinning are the displacements on scales larger than d, i.e., the case $L > d > L_c$. At low temperatures, we are in the RM regime at all scales $L > d$ such that

$$\overline{\langle \Delta u\rangle^2}(L) \simeq \overline{\langle \Delta u\rangle^2}(d)\,(L/d)^{2\zeta_{RM}} \quad , \tag{3.37}$$

where $\overline{\langle \Delta u^2\rangle}(d)$ is given by eq. (3.33), and $\zeta_{RM} \approx 5/8$. This result stays valid up to temperatures U^* where the strongly pinned pancakes thermally depin. At this temperature the thermally increased pinning length grows beyond the layer spacing $L_c(U^*) = d$, increases (double) exponentially for $U^* < T < |E_0|$, and crosses over to the weak pinning result (3.29) for $T > |E_0|$. The details of the (double-) exponential increase of $L_c(T)$ in the temperature interval $U^* < T < |E_0|$ for strong pinning are given in Ref. [55].

3.7 Order-disorder transition at $T = 0$

In the presence of quenched point disorder the Lindemann criterion (3.4) for the stability of the BrG and thus the location of the order-disorder transition can be written as

$$\overline{\langle \Delta u(L_0)\rangle^2} = c_L^2 a^2 \; , \tag{3.38}$$

where we used eq. (3.7). As for thermal fluctuations we only need to consider displacement fluctuations of single vortices on scales $L < L_0$ using the results for pinned single vortices introduced in the preceding Sec. 3.6. In this section we want to consider the case $T = 0$ and study the order-disorder or amorphization transition line $b_t(\delta)$ as function of the pinning strength only. The resulting phase diagrams in the b-δ plane are shown in Fig. 3.6 for NbSe, YBCO, and BSCCO.

NbSe, YBCO

At $T = 0$ the anisotropic type-II superconductors YBCO and NbSe have essentially identical phase diagrams in the b-δ plane if pinning is weak enough that a vortex is collectively pinned over distances $L_c > d$ and the layered structure of YBCO can be neglected.

For weak pinning in the dense regime $a < \lambda_{ab}$ we use the weak collective pinning theory and the anisotropic stiffness from the Josephson coupling, i.e., eq. (3.26) for bundle pinning or eq. (3.27) for single-vortex pinning to evaluate the left-hand side (lhs) $\overline{\langle \Delta u(L_0)\rangle^2}$ of the above Lindemann criterion. For very weak pinning the transition line will be in the bundle pinning regime where we use $L_0 \simeq \varepsilon a(1-b)^{-1/2}$ from eqs. (3.8) and (3.26) to obtain

$$\overline{\langle \Delta u(L_0)\rangle^2} \simeq \xi_{ab}^2 \,(L_0/L_c)^3 \simeq a^2\,(b/2\pi)^{-1/2}\,(1-b)^{-3/2}\delta/\varepsilon \ . \tag{3.39}$$

This result is interesting because it means that the Lindemann criterion (3.38) gives a order-disorder transition line $b_t(\delta)$ leading to a *reentrance* of the amorphous VG within the dense regime $a < \lambda_{ab}$ as long as we have bundle pinning. We find upper and lower branches of the reentrant transition line $b_t(\delta)$,

$$\begin{aligned} 1 - b_t^u &\simeq (2\pi)^{1/3} c_L^{-4/3}\,(\delta/\varepsilon)^{2/3} \ , \\ b_t^l &\simeq 2\pi c_L^{-4}\,(\delta/\varepsilon)^2 \ . \end{aligned} \tag{3.40}$$

which meet at $b_t = 1/4$ such that there is no transition line in the bundle pinning regime for disorders $\delta/\varepsilon > 0.13 c_L^2$, see Fig. 3.6. Using the condition $L_0 = L_c$ for b_{sv}, one finds that the order-disorder transition line $b_t(\delta)$ intersects the single-vortex pinning line $b_{sv}(\delta)$ for $c_L^2 a^2 = \overline{\langle \Delta u(L_c)\rangle^2} = \xi_{ab}^2$ and thus leaves the bundle pinning regime at a field $b_t = 2\pi c_L^2$ and a disorder strength $\delta/\varepsilon \approx c_L^3$, see also Fig. 3.4. Therefore, the peculiar reentrant behavior can only be found for $b_t = 2\pi c_L^2 < 1/4$ or Lindemann numbers $c_L < (8\pi)^{-1/2} \approx 0.2$. As indicated in Fig. 3.6, NbSe typically has a very small pinning parameter such that the upper order-disorder transition field is given by the bundle pinning result (3.40). The lower transition field is then located within the dilute regime $a > \lambda_{ab}$, and not given by eq. (3.40).

For stronger disorder $\delta/\varepsilon > c_L^3$, as it is typical for YBCO, there will be another transition line in the dense regime, which lies in the single-vortex pinning regime at magnetic fields $b_t < 2\pi c_L^2$, see Fig. 3.6. This part is found from eqs. (3.27) and (3.8),

$$\overline{\langle \Delta u(L_0)\rangle^2} \simeq \xi_{ab}^2\,(L_0/L_c)^{5/4} \simeq a^2\,(b/2\pi)^{3/8}\,(1-b)^{-5/8}\,(\delta/\varepsilon)^{5/12} . \tag{3.41}$$

For single-vortex pinning, the Lindemann criterion (3.38) only gives an upper branch of the order-disorder transition line $b_t(\delta)$ at

$$b_t^u \simeq 2\pi c_L^{16/3}\,(\delta/\varepsilon)^{-10/9} \ , \tag{3.42}$$

where we used $1-b \ll 1$ because $b_t^l < 2\pi c_L^2 \ll 1$ in the single-vortex regime. We conclude that there will be a reentrance of the amorphous VG and the BrG as function of the magnetic field for disorder strengths $c_L^3 < \delta/\varepsilon < 0.13 c_L^2$, see Fig. 3.6, if the Lindemann number c_L is sufficiently small. Only the result (3.42) for the order-disorder transition line in the single-vortex pinning regime, which can be more generally written as

$$b_t^u \sim c_L^{2/(1-\zeta_{RM})} \left(\delta/\varepsilon\right)^{-2\zeta_{RM}/3(1-\zeta_{RM})} , \tag{3.43}$$

has been obtained in all previous Lindemann analysis [63, 64, 65, 66, 67, 68, 69, 70] which differ only in the estimates used for ζ_{RM}.

On the continuation of the upper branch of the order-disorder transition line into the dilute limit $a > \lambda_{ab}$ fluctuations on the scale $L_d = \varepsilon\lambda_{ab}$ govern the displacement fluctuations in the Lindemann criterion (3.38), i.e., $\overline{\langle \Delta u(L_0)\rangle^2} \simeq \overline{\langle \Delta u(\varepsilon\lambda_{ab})\rangle^2}$. Only for single-vortex pinning disorder is strong enough ($\delta/\varepsilon > c_L^{24/5}\kappa^{9/5}$) that the upper branch of the amorphization line lies in the dilute regime. Thus we use eqs. (3.27) and (3.8) to obtain

$$\overline{\langle \Delta u(\varepsilon\lambda_{ab})\rangle^2} \simeq \xi_{ab}^2 \left(\frac{\varepsilon\lambda_{ab}}{L_c}\right)^{5/4} \simeq a^2 \frac{b}{2\pi} \kappa^{-5/4} \left(\delta/\varepsilon\right)^{5/12} , \tag{3.44}$$

which gives with the Lindemann criterion the upper branch of the order-disorder transition in the dilute regime,

$$b_t^u \simeq 2\pi c_L^2 \kappa^{-5/4} \left(\delta/\varepsilon\right)^{-5/12} . \tag{3.45}$$

YBCO

The YBCO phase diagram in the b-δ plane is qualitatively different from the NbSe diagram only for such strong disorder that the collective pinning length drops below the layer spacing $L_c < d$, see Fig. 3.6. This happens for $\delta/\varepsilon > (\varepsilon\xi/d)^3 = (\varepsilon/\varepsilon_d\kappa)^3$ [or $\delta_d = (\delta/\varepsilon)(\kappa\varepsilon_d/\varepsilon)^3 > 1$, see eqs. (3.21) and (3.22)] in the single vortex pinning regime; for generic disorder strengths in YBCO this also happens before the order-disorder transition line enters the dilute regime as indicated in Fig. 3.6. For $L_c < d$ we have to use our results about strongly pinned pancake vortices from Sec. 3.6). In particular, we have to use eq. (3.37) together with eq. (3.33) to calculate the lhs $\overline{\langle \Delta u(L_0)\rangle^2}$ in the Lindemann criterion (3.38).

In the dense limit $a < \lambda_{ab}$ the Josephson coupling and thus fluctuations on the scale L_0 dominate the displacements. Neglecting logarithmic corrections we find from eqs. (3.37) and (3.33)

$$\overline{\langle \Delta u(L_0)\rangle^2} \simeq \xi_{ab}^2 \delta_d^{1/2} \left(\frac{L_0}{d}\right)^{5/4} \simeq a^2 \left(\frac{b}{2\pi}\right)^{3/8} \left(\frac{\varepsilon_d}{\varepsilon}\kappa\right)^{1/4} \left(\frac{\delta}{\varepsilon}\right)^{1/2} , \tag{3.46}$$

which gives for the upper branch of the order-disorder transition in the dense limit [68]

$$b_t^u \simeq 2\pi c_L^{16/3} \left(\varepsilon_d\kappa/\varepsilon\right)^{-2/3} \left(\delta/\varepsilon\right)^{-4/3} . \tag{3.47}$$

Upon increasing the disorder strength, the order-disorder transition line enters the dilute limit [for $\delta/\varepsilon > c_L^4(\varepsilon/\varepsilon_d\kappa)^{1/2}\kappa^{3/2}$], see Fig. 3.6. In the dilute limit, fluctuations on the scale $L_d = \varepsilon\lambda_{ab}$ cause the strongest displacements, for which eqs. (3.37) and (3.33) yield

$$\overline{\langle\Delta u(\varepsilon\lambda_{ab})\rangle^2} \simeq \xi_{ab}^2\delta_d^{1/2}\left(\frac{\varepsilon\lambda_{ab}}{d}\right)^{5/4} \simeq a^2\frac{b}{2\pi}\left(\frac{\varepsilon_d}{\varepsilon}\kappa\right)^{1/4}\kappa^{5/4}\left(\frac{\delta}{\varepsilon}\right)^{1/2} \tag{3.48}$$

and hence for the upper branch of the order-disorder transition line in the dilute limit

$$b_t^u \simeq 2\pi c_L^2\left(\varepsilon_d\kappa/\varepsilon\right)^{-1/4}\kappa^{-5/4}\left(\delta/\varepsilon\right)^{-1/2} \ . \tag{3.49}$$

This case has been previously studied in Ref. [66], the results of which agree with eq. (3.49).

BSCCO

The strongly layered BSCCO has a weak Josephson coupling at low temperatures, and the 2D crossover field b_{2D} is slightly below the boundary to the dense regime according to eq. (3.15). Consequently, the upper branch of the 3D amorphization transition line lies entirely in the dilute regime where fluctuations on the scale $L_d = d$ dominate on the lhs of the Lindemann criterion (3.38), $\overline{\langle\Delta u(L_0)\rangle^2} \simeq \overline{\langle\Delta u(d)\rangle^2}$.

In a strongly layered material such as BSCCO it is more convenient to use the parameter δ_d, see eq. (3.22), for the disorder strength and discuss the order-disorder transition line in the b-δ_d plane. For weak pinning ($\delta_d < 1$) we use eq. (3.36) to calculate for the upper branch of the order-disorder transition line in the dilute limit

$$b_t^u \ \simeq \ 2\pi c_L^2\delta_d^{-1} \ . \tag{3.50}$$

On the other hand, for strong pinning ($\delta_d > 1$) we use eq. (3.33) to obtain

$$b_t^u \ \simeq \ 2\pi c_L^2\delta_d^{-1/2} \ , \tag{3.51}$$

which agrees with the corresponding result of Ref. [66]. For typical values $\kappa \approx 200$ for BSCCO it is clear that the order-disorder transition line intersects the 2D crossover field $b_{2D} \simeq 2\pi\kappa^{-2}$ in the strong pinning regime for $\delta_d \simeq c_L^4\kappa^4$ (which usually entails $\delta_d \gg 1$). Note that typical pinning strengths for BSCCO have similar values, as indicated in Fig. 3.6. At smaller disorder strengths the BrG phase will be stable up to a decoupling field $b_{dc}(\delta_d)$ where the FLL decouples into 2D pancake lattices. As already mentioned there is no stable 2D BrG phase and we thus conclude that at the decoupling field also the in-plane topological order is lost and we have a direct transition into a 2D amorphous VG. If the decoupling transition is also described by a Lindemann criterion of the form $\overline{\langle\Delta u(0,d)\rangle^2} = c_L^2a^2$ as proposed in Ref. [84] the same formulas (3.50) and (3.51) apply to the decoupling transition line $b_{dc}(\delta_d)$, which is the continuation of the order-disorder transition line into the regime above the 2D crossover field b_{2D}, see Fig. 3.6. It should be stressed that the phase diagram of BSCCO in the b-δ plane looks qualitatively different from those of YBCO and NbSe in the dense regime $a < \lambda_{ab}$ at higher fields as the peculiar reentrance of the amorphous VG phase is absent for BSCCO because fluctuations on the scale of the layer spacing d are dominating for this material.

3.8 Order-disorder transition at $T > 0$

In this section we discuss the influence of thermal fluctuations on the phase diagrams we derived in the preceding section for $T = 0$. To do so we choose a realistic $T = 0$ value for the disorder strength δ/ε or δ_d somewhere in the hatched regions of Fig. 3.6. The results for the phase diagrams of NbSe, YBCO, and BSCCO in the b-t plane are summarized in Fig. 3.7. Similar to what we found already for the single-vortex pinning field b_{sv} there are essential differences in the temperature dependence of the order-disorder transition line $b_t(t)$ depending on whether the depinning temperature T_{dp} is much smaller than the critical temperature T_c as in the high-T_c materials YBCO and BSCCO or whether it practically coincides with T_c as in the low-T_c superconductor NbSe. In the high-T_c materials the thermal weakening of the disorder is by far the dominant effect. On the other hand, in the low-T_c materials T_{dp} is very close to T_c and the temperature dependence through the microscopic pinning parameters (3.23) or (3.24) is most important.

NbSe

In a low-T_c such as NbSe we typically have weak bundle pinning at the order-disorder transition at $T = 0$, and the order-disorder transition fields $b_t^{u,l}$ are given by eq. (3.40). Thermal depinning from disorder can be neglected, and the temperature dependence of the order-disorder transition line comes exclusively from the temperature dependence through the microscopic parameters entering the pinning strength δ, i.e., eq. (3.23) or (3.24). Then, the order-disorder transition line in the b-t plane is obtained from eqs. (3.40), (3.42), and (3.45) simply by substituting the correct $\delta(t)$.

For δl pinning the disorder strength $\propto (1-t)^{3/2}$ gives together with eq. (3.40) an upper branch of the order-disorder transition line which stays in the bundle pinning regime and has a temperature dependence $1 - b_t^u(t) \propto (1-t)$. Therefore, the order-disorder transition line approaches $b = 1$ with increasing temperature and has to intersect the melting line $b_m(t)$ where it terminates, see Fig. 3.7. Because we used here the Lindemann criterion based on the scenario of two distinct instabilities for thermal and quenched fluctuations the phase diagram looks qualitatively as in Fig. 3.1 on the right. For a cooperative mechanism the transition line will be lower and *not* intersect the melting line as on the left in Fig. 3.1.

For δT_c pinning the situation is rather different because the disorder strength increases with temperature $\propto (1-t)^{-1/2}$ such that the BrG becomes always unstable sufficiently close to T_c and the order-disorder transition line does not intersect the melting line. Because the disorder strength increases with temperature for δT_c pinning the topology of the phase diagram in the b-t plane is the same as that in the b-δ plane, as can be seen in Figs. 3.6 and 3.7. In particular the amorphous VG and the BrG are reentrant as a function of the magnetic field in the dense regime also in the b-t plane. Using eq. (3.40) we find within the bundle pinning regime the two branches $1 - b_t^u(t) \propto (1-t)^{-1/3}$ and $b_t^l(t) \propto (1-t)^{-1}$. In the single-vortex pinning regime (3.42) gives $b_t^u(t) \propto (1-t)^{5/9}$. These results are summarized in Fig. 3.7.

Our results for the case of δT_c pinning might give an explanation for the experimental phase diagram measured in Ref. [62] where a reentrant amorphous VG phase was found in the dense regime which does not intersect with the melting line. This is exactly what we find for δT_c pinning in the bundle pinning regime, see Fig. 3.7.

YBCO

For the high-T_c materials YBCO and BSCCO the thermal smearing plays a much bigger role than the temperature dependence through the microscopic parameters contained in the pinning strength δ. For YBCO effects from the layered structure can be neglected unless at rather high disorder strength $\delta/\varepsilon > (\varepsilon\xi/d)^3$ or $\delta_d > 1$ where $L_c(0) < d$. However, typical disorder strengths δ/ε for YBCO are bigger than for NbSe (due to the intrinsic doping of HTSC and the increased anisotropy) and the order-disorder transition field b_t^u is located within the single-vortex pinning regime at low temperatures.

For $L_c(0) > d$ collective pinning theory applies and the thermal smearing sets in above the depinning temperature T_{dp}. For $T < T_{dp}$ the order-disorder transition line $b_t^u(t)$ is horizontal and given by eq. (3.42), see Fig. 3.7. In high-T_c materials T_{dp} is typically well below T_c. Taking typical values for YBCO as an anisotropic high-T_c superconductor with strong Josephson coupling, $\lambda_{ab} \approx 1500$ Å, $\varepsilon \approx 1/5$, $d \approx 12$ Å and a disorder strength $\delta/\varepsilon \approx 10^{-2}$ (corresponding to a critical current $j_c \simeq j_0(\delta/\varepsilon)^{2/3} \simeq 10^7$ Acm^{-2}), we have weak pinning $[L_c(0) > d]$ and find $T_{dp} \simeq 40$ K for the depinning temperature, which is indeed well below $T_c \approx 90$ K. For $T > T_{dp}$ we have to use (3.30) to evaluate the lhs of the Lindemann criterion (3.38) and obtain

$$\overline{\langle\Delta u(L_0)\rangle^2} \simeq \xi_{ab}^2 \, (L_0/L_c(0))^{5/4} \, (T/T_{dp})^{5/4} \, e^{-(C/4)(T/T_{dp})^3} \, . \tag{3.52}$$

Pinning-induced displacements drop exponentially above T_{dp}, therefore the thermal smearing is by far the most important effect of thermal fluctuations. The Lindemann criterion (3.38) yields an exponentially increasing upper branch of the order-disorder transition line

$$b_t^u \simeq 2\pi c_L^{16/3} \, (\delta/\varepsilon)^{-10/9} \, (T/T_{dp})^{-10/3} \, e^{(2C/3)(T/T_{dp})^3}, \tag{3.53}$$

which will intersect the melting line at a temperature T_x, which can be determined from a simple argument as follows. According to the scenario where thermal and quenched fluctuations cause independently instabilities of the BrG, thermal displacements should be of the *same* size as disorder-induced fluctuations at T_x, i.e., $\langle\Delta u^2(L_0)\rangle_T = \overline{\langle\Delta u(L_0)\rangle^2}$. However, this is exactly the definition of the pinning length $L_c(T)$ above the temperature T_{dp} from which we conclude that T_x is determined by the additional condition $L_c(T_x) = L_0$. This also means that the amorphization transition line $b_t^u(t)$ does not leave the single vortex pinning regime for thermally weakened disorder above T_{dp} until it intersects also with the single-vortex pinning boundary $b_{sv}(t)$ (3.32) at T_x, see Fig. 3.7. For the temperature T_x and the field $b_x \equiv b_m(t_x) = b_t^u(t_x) = b_{sv}(t_x)$ we find

$$T_x \simeq T_{dp} \left([2/C] \ln \left[(\delta/\varepsilon)^{1/3} c_L^{-1} \right] \right)^{1/3} , \tag{3.54}$$

$$b_x \simeq 2\pi c_L^4 \, (\delta/\varepsilon)^{-2/3} \, (T_x/T_{dp})^{-2} \, . \tag{3.55}$$

The temperature T_x is only slightly above T_{dp} due to the exponential increase of the upper branch of the order-disorder transition line. Using a disorder strength $\delta/\varepsilon \approx 10^{-2}$ and $c_L \approx 0.15$ we obtain $B_x \approx 5.6$ T for the intersection field in good agreement with experimental phase diagrams for YBCO [61]. The characteristic exponentially increasing upper branch of the order-disorder transition line (3.53) above the depinning temperature T_{dp} has also been obtained in Refs. [63], [65], and [68].

For $L_c(0) < d$ pancake vortices are strongly pinned at low temperatures and the thermal smearing of the pinning potential sets in at the higher temperature U^* (3.35) which is the characteristic depinning temperature for strong pinning. For $T < U^*$ the order-disorder transition line $b_t^u(t)$ is horizontal and given by eq. (3.47), see Fig. 3.7. At the temperature U^* we find $L_c(U^*) = d$, and in the temperature interval $U^* < T < |E_0|$ pinning-induced displacements decrease (double-)exponentially with increasing temperature. For $T > |E_0|$ the results cross over to the above formula (3.53). The details of the (double-)exponential increase of the order-disorder transition line $b_t^u(t)$ for $U^* < T < |E_0|$ can be easily obtained using the results of Ref. [55] but will not be presented here. The resulting phase diagram looks qualitatively as for weak pinning with the slightly higher $t^* = U^*/T_c$ replacing the depinning temperature t_{dp}, see Fig. 3.7.

Regardless of whether we have strong disorder with $L_c(0) < d$ or weak collective pinning, we find a remarkable reentrant non-monotonic BrG instability line if we follow the order-disorder transition line $b_t^u(t)$ and after the intersection further on the thermal melting line $b_m(t)$, see Fig. 3.7. This is in agreement with experiments [61] where a non-monotonic BrG instability line is clearly seen for YBCO. Because we used here the Lindemann criterion based on the scenario of two distinct instabilities for thermal and quenched fluctuations the phase diagram of YBCO in Fig. 3.7 looks qualitatively as in Fig. 3.1 on the right. For a cooperative mechanism the transition line $b_t^u(t)$ will be lower and *not* intersect the melting line as on the left in Fig. 3.1. However, also in this scenario a reentrant non-monotonic behavior of the resulting curve $b_t^u(t)$ is found.

BSCCO

For the strongly layered BSCCO several phase diagrams in the b-t plane are possible depending on the three temperatures T_d, below which BSCCO has a weak Josephson coupling, the 2D melting temperature T_m^{2D}, and finally the characteristic depinning temperature U^*. For pancake pinning energies U_p between $U_p \approx 10$ K and $U_p \approx 20$ K one finds values between $U^* \approx 5$ K and $U^* \approx 10$ K for the depinning temperature U^*.

As for the thermal melting we will focus on the situation $T_m^{2D} < T_d$ that occurs for a realistic choice of material parameters for BSCCO; in Sec. 3.5) we found estimates $T_d \approx 55$ K and $T_m^{2D} \approx 10$ K. Then the upper branch of the 3D melting line lies entirely in the dilute regime as in Fig. 3.3. Typical disorder strengths for BSCCO are such that we are in the strong pinning regime $\delta_d > 1$. For sufficiently strong disorder $\delta_d > c_L^4 \kappa^4$ ($\gg 1$), which corresponds to $U^* > T_m^{2D}$, there is a genuine 3D amorphization transition at $T = 0$ whereas for smaller disorder $1 < \delta_d < c_L^4 \kappa^4$, corresponding to $U^* < T_m^{2D}$, we have found a decoupling transition that simultaneously destroys topological in-plane order.

For strong disorder $\delta_d > c_L^4 \kappa^4$ or $U^* > T_m^{2D}$ the 3D amorphization transition field b_t^u lies in the dilute regime at low temperatures and its disorder dependence is given by eq. (3.51). Thermal fluctuations lead to a depinning of strongly pinned pancake vortices only above the temperature U^* at which $\overline{\langle \Delta u(d) \rangle^2} \simeq \langle \Delta u(d)^2 \rangle_T$ [55]. Therefore U^* is also the temperature where the amorphization transition line $b_t^u(t)$ intersects the melting line, i.e., $T_x = U^*$. For all $T < U^*$ the amorphization transition line runs horizontally, see Fig. 3.7. In particular, this excludes a reentrant behavior. The horizontal order-disorder transition line $b_t^u(t)$ and, after intersecting, the thermal melting line $b_m(t)$ are monotonously decreasing with increasing temperature. This is unchanged also if we use the slightly different Lindemann criterion based on a cooperative mechanism of thermal and quenched fluctuations. Indeed, experimental signs for a non-monotonic BrG instability line are much weaker for the BSCCO compound [60], and only recently a small "inverse melting" effect has been confirmed experimentally [86]. Because the non-monotony is much smaller in BSCCO than in YBCO this effect might be beyond the scope of the Lindemann criterion for BSCCO. Above the order-disorder transition line $b_t^u(t)$ we can speculate that a 3D amorphous VG phase will be stable up to the thermal decoupling field $b_{dc}(t)$ that we discussed in Sec. 3.5. At $b_{dc}(t)$ the FLL decouples by thermal fluctuations into 2D pancake lattices which are in a 2D amorphous VG phase as there is no stable 2D BrG phase. The 2D amorphous VG phase might be separated by another dynamical crossover, in which the dislocation mobility increases by thermal fluctuations, from the 2D VL phase but both phases have no in-plane topological order.

For somewhat weaker disorder $1 < \delta_d < c_L^4 \kappa^4$ or $U^* < T_m^{2D}$ a slightly different sequence of transitions occurs as at low temperatures the BrG phase is stable up to a decoupling field b_{dc}, which lies in the dense regime and the disorder dependence of which is also given by the right-hand side of eq. (3.51). As there is no stable 2D BrG phase the FLL decouples directly into the 2D amorphous VG at b_{dc}. If the locus of this line is as well determined by a Lindemann criterion $\overline{\langle \Delta u(0,d) \rangle^2} = c_L^2 a^2$, we obtain as for the amorphization transition line a temperature-independent, horizontal transition line $b_{dc}(t)$ that intersects the thermal melting line at a temperature $T_x = U^*$, see Fig. 3.7. However, there will be no subsequent thermal decoupling in this case but eventually another temperature-driven crossover to the 2D VL phase.

3.9 Conclusion

In conclusion, we have presented a comparative and comprehensive Lindemann analysis of the melting line and the stability boundaries of the Bragg glass phase, i.e., the amorphization transition line for the three superconducting materials of most intense experimental interest: the high-T_c materials YBCO and BSCCO and the low-T_c superconductor NbSe. We find that it is important to distinguish between slightly different versions of the Lindemann criterion depending on whether quenched disorder-induced and thermal fluctuations act cooperatively or independently in destroying the lattice order. The two versions can actually be linked to different scenarios for the proliferation of topological defects in the destruction of the Bragg glass phase.

Special attention is paid to the role of the electromagnetic coupling for the strongly layered compound BSCCO and to the different mechanism of temperature dependence in the pinning strength. We find that in high-T_c materials thermal smearing of the pinning potential is most important whereas in the low-T_c material NbSe the temperature dependence through the microscopics of the pinning mechanism determines the phase behavior. Taking also into account high-field corrections to the elastic moduli we obtain results regarding the phase diagram of the low-T_c material NbSe which are different from earlier findings [69] and which give a reentrant amorphous VG phase in the dense regime very similar to what has been observed in recent experiments [62].

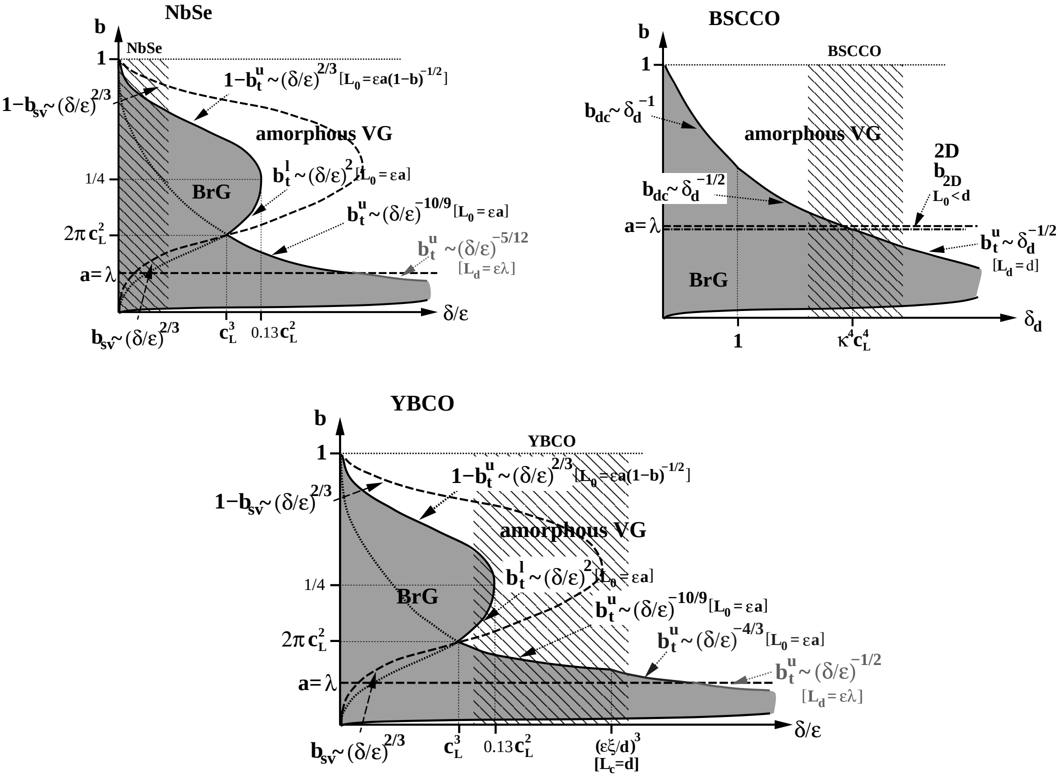

Figure 3.6: Schematic phase diagram for NbSe and YBCO in the b-δ/ε plane, and for BSCCO in the b-δ_d plane (the dilute regime is enlarged, the reentrance of the amorphous VG at very low fields is shown for completeness but not discussed in the text). The diagram also contains the single-vortex pinning field b_{sv} marking the boundary between single-vortex pinning and bundle pinning, cf. Fig. 3.4. The hatched regions indicate a range of realistic disorder strengths for each material, cf. Fig. 3.4. The BrG is stable in the dark shaded regions. For NbSe and YBCO the order-disorder transition line b_t is given by eq. (3.40) for bundle pinning and eq. (3.42) for single-vortex pinning. Note that in the bundle pinning regime there can be an upper and lower branch leading to a reentrant amorphous VG phase. For YBCO with strong disorder we have $L_c < d$, and the upper branch of the order-disorder transition line in the single-vortex regime is given by eqs. (3.47) and (3.49). For BSCCO the order-disorder transition is given by eqs. (3.50) and (3.51). The decoupling transition line b_{dc}, which is the continuation of the order-disorder transition line above the 2D crossover field b_{2D}.

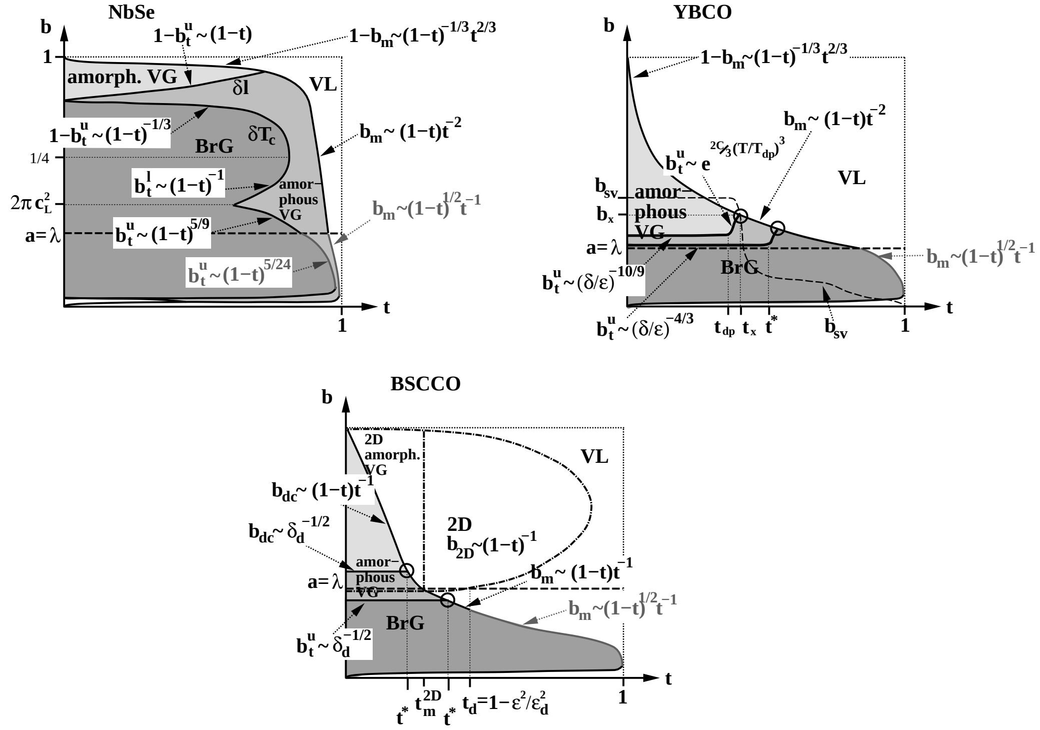

Figure 3.7: Schematic phase diagram for NbSe, YBCO, and BSCCO in the b-t plane. (The dilute regime is enlarged, the reentrance at very low fields is shown for completeness but not discussed in the text.) The BrG is stable in the dark shaded regions. The amorphous VG phase occurs in the light shaded regions. The diagrams contain both the thermal melting lines b_m from Fig. 3.3 and the order-disorder transition lines b_t. For YBCO and BSCCO the order-disorder transition line is shown for two different disorder strengths; for the smaller disorder strength the stable BrG phase extends into the lighter shaded region. For NbSe the temperature dependence of the order-disorder transition line stems from the temperature dependence through microscopic parameters. The stable BrG phase for δT_c pinning is indicated by the dark shaded region, for δl pinning it extends also into the lighter shaded region to the right. For YBCO and BSCCO the temperature dependence mainly stems from thermal smoothing above the depinning temperature T_{dp}. For YBCO the order-disorder transition line is temperature independent below T_{dp} and given by eq. (3.53) between T_{dp} and T_x, where it intersects the melting line and the single-vortex pinning line b_{sv}. For BSCCO the order-disorder transition line is generically temperature independent, i.e., horizontal and intersects the melting line at $T_x = U^*$ ($t^* \equiv U^*/T_c$).

Chapter 4

Dislocation Theory of the Vortex Phase Diagram

A theory for dislocation-mediated structural transitions in the vortex lattice in the presence of point defects is developed, which allows for a unified description of phase transitions between the three phases, the elastic Bragg glass, the amorphous vortex glass, and the vortex liquid, in terms of a free-energy functional for the dislocation density. The elastic Bragg glass is dislocation-free, whereas the amorphous glass contains pinned dislocations at low density, and the vortex liquid is saturated with a high density of unpinned dislocations. The theory explains the existence of a critical point, *in which the first-order melting line terminates at high magnetic fields and which has been observed in a number of experiments. Considering the driven thermally activated dynamics of dislocations we develop a theory for* plastic vortex creep *in the topologically disordered (dislocated) vortex glass phase. Plastic barriers for dislocations show a power-law divergence at small driving currents* j, $U_{pl}(j) \propto j^{-\mu}$, *with* $\mu = 1$ *for a single dislocation and* $\mu = 2/5$ *for creep of dislocation bundles. This implies a suppression of the creep rate at the transition from the ordered vortex phase* ($\mu = 2/11$) *to the dislocated glass and can manifest itself as an observed increase of the apparent critical current (second peak).*

4.1 Introduction

Since the pioneering work [14] where the first-order flux-line lattice (FLL) melting into an entangled vortex liquid (VL) was established, there has been a continuous development of our views of the vortex lattice phase diagram in high-T_c superconductors [7]. Weak point disorder was shown to drive the vortex lattice into a vortex glass (VG) state with zero linear resistivity [24, 10, 12]. Observations of hysteretic resistivity switching and magnetization measurements [18, 19] have supported the first-order melting of very clean lattices. A crossover from the first-order melting at low magnetic fields to a continuous VG-VL transition has been related to the structural transition within the vortex solid which is described as a topological transition between the low-field *elastic* VG [26], free from topological defects [26, 27, 28] and maintaining quasi long-range translational order [25, 26], and the high field *amorphous* VG, where disorder generates proliferation of dislocations [27, 28]. We have seen in the previous chapter 3 how a simple picture of the vortex phase diagram emerges from a Lindemann analysis [54]. In this picture the three generic phases – VL, the high field amorphous VG, and the low-field, low-temperature quasilattice or Bragg glass (BrG) (Ref. [26]) – are governed by the three basic energies: the energy of thermal fluctuations T, the pinning energy E_{pin}, and the typical energy E_{pl} for a plastic deformation. The Lindemann criterion can be applied to obtain the transition lines between these phases essentially by matching of any of the two basic energies and matching of all three energies marks the point of three-phase coexistence [67]. This suggests a naive phenomenological picture where it is tempting to identify the point of three-phase coexistence with the critical point of the melting lines that has been observed both for BSCCO by magnetization measurements [20] and YBCO by transport [31] and magnetization measurements [32]. While this naive phenomenological picture is supported by the observations on BSCCO [20], it fails to describe the YBCO phase diagram where the critical point of the first-order melting line appears to be *separated* from the point of three-phase coexistence where topological transition and melting line merge [30, 31, 32].

In this chapter, we present an explanation for the existence of a critical point of the first-order melting line in the presence of point disorder. Our argumentation is based on a unified description of the vortex lattice phases. We demonstrate that all phase transitions between vortex lattice phases can be described as *dislocation mediated* by deriving the free energy for an ensemble of directed dislocations as a function of the dislocation density in the presence of thermal *and* disorder.

Each of the experimentally observed phases is characterized by its inherent *dislocation density* or, equivalently, by the characteristic dislocation spacing R_D. The elastic VG is dislocation-free and has $R_D = \infty$. The VL can be viewed as a vortex array saturated with dislocations such that $R_D \sim a$, and in the amorphous VG, $R_D \sim R_a$, where R_a is the so-called positional correlation length on which typical vortex displacements are of the order of the lattice spacing a [7]. Within our approach each phase corresponds to one of the *local* minima in the dislocation ensemble free energy, and dislocation densities in these minima represent the *equilibrium* dislocation densities in the corresponding phases. The global minimum corresponds to the thermodynamically stable phase under the given conditions, phase transitions occur when two local minima exchange their role as global minimum. This mechanism for the transitions enables us to *derive* Lindemann-criteria both for the locations of the thermal melting line and for the disorder-induced instability line of the BrG. Furthermore, the characteristic scale set by the mean distance between free dislocations offers a natural explanation of the critical endpoint of the first-order melting line: While at low magnetic fields $R_a \gg a$ and the amorphous VG appears to contain significantly less dislocations than the VL, at higher field where $R_a = a$ the two phases become thermodynamically *equivalent* and the first-order melting line has to terminate.

One of the most fascinating dynamic phenomena of complex systems with internal degrees of freedom is the thermally activated motion of elastic media in a random environment (creep) characterized by a highly nonlinear response to a dc driving force, F [87]: $v \sim \exp(-\mathrm{const}/TF^{\mu})$, where v is the velocity, T is the temperature, and μ is the exponent depending on the geometry and the dimensionality of the driven medium. The concept of thermally activated creep is ubiquitous in disordered systems and describes a wealth of low temperature transport phenomena including the dynamics of dislocation and/or domain walls in inhomogeneous environments [87, 88], driven vortex lattices and charge density waves [24, 10, 25, 7]. The derivation of the fundamental creep feature, energy barriers $U(j) \sim j^{-\mu}$ diverging at small driving forces (currents j), was based on the *elastic* behavior of the pinned structures; thus in the common view creep behavior is implicitly attributed to the elastic medium free of topological defects.

The description of thermally activated dynamics of amorphous structures containing a large amount of topological defects is a long standing problem, that appeared first in the theory of work hardening and related relaxation processes in dislocated solids. In the context of vortex physics the quest for the description of creep in a topologically disordered medium is motivated by the observation of the disorder-induced transition between a low-field quasi-lattice or Bragg glass (BrG) [25, 26], the phase free of topological defects, and the high-field phase, characterized by an enhanced apparent critical current [89, 90, 91, 92, 93, 60], which we suggest to be a *topologically disordered*, dislocated vortex state or amorphous vortex glass (AVG). In a recent series of experiments [94, 95] the phase coexistence characteristic for a first-order transition was established, and creep barriers in the high-field vortex state were shown to diverge *faster* than creep barriers in the low-field elastic phase.

In this chapter, we also propose a quantitative description of plastic creep in terms of the dislocation degrees of freedom. We find a critical plastic current j_{pl} below which dislocations are *collectively pinned* and plastic creep occurs via the *activated* motion of collectively pinned dislocation lines. The critical plastic current is lower than the critical current for vortex depinning $j_{pl} < j_c$, hence plastic motion of depinned dislocations sets in before viscous flow of the entire vortex lattice can occur. We derive the associated *plastic* creep energy barriers $U_{pl}(j) \sim j^{-\mu_{pl}}$ diverging *infinitely* at $j \to 0$. We calculate the pinning force acting on dislocations from the Peach-Köhler force exerted on vortices by the pinning centers. We show that an external current sent through a dislocated vortex lattice generates a Peach-Köhler force with a component causing dislocation glide. The interplay of these two forces determines the glassy dislocation dynamics, in particular the depinning threshold for dislocation glide and the energy barriers for plastic creep below the depinning threshold.

4.2 Dislocations in the Vortex Lattice

As first observed by Labusch [45], the FLL can contain screw and edge dislocations with three possible Burger's vectors $\mathbf{b}$, identical to the three elementary lattice vectors of the hexagonal Abrikosov lattice. As also pointed out already by Labusch, dislocations can split into partials $\mathbf{b} = \frac{1}{2}\mathbf{b} + \frac{1}{2}\mathbf{b}$ connected by a stacking fault of rectangular lattice structure. This process is energetically not very costly in the FLL with the rectangular lattice having only a slightly increased free energy compared to the hexagonal lattice [2] and has been experimentally observed in [46]. Also reactions $\mathbf{b}_1 + \mathbf{b}_2 = \mathbf{b}_3$ of two different edge dislocations are possible (whereas a fusion is energetically possible, a dissociation is not because $b_1^2 < b_2^2 + b_3^2$ violates the Frank criterion [96]). It was pointed out by Labusch [45] and later by Nelson and Marchetti [97] that there is a crucial difference between dislocations in

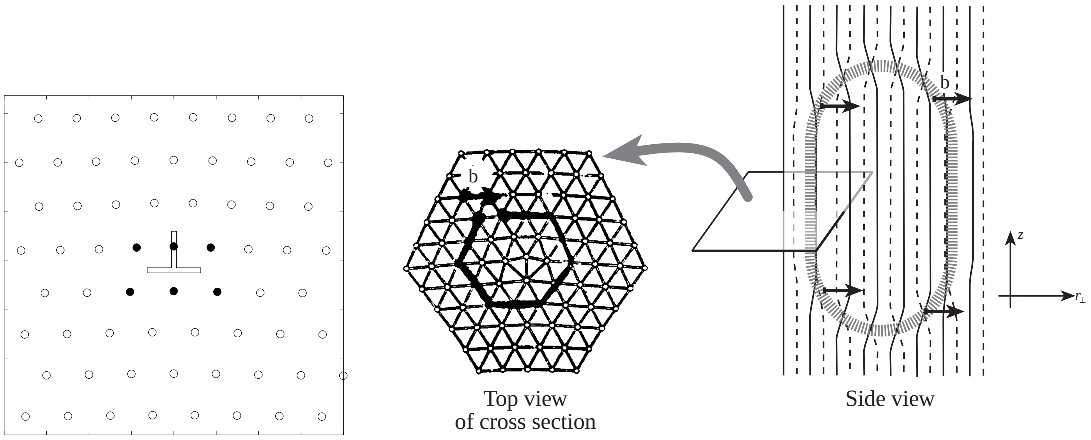

Figure 4.1: Left: A pair of edge dislocations in a lattice of straight flux-lines as obtained from numerical minimization of the interaction energies for $\lambda/a = 0.2$. Right: A schematic picture of a dislocation loop containing edge and screw parts (picture adapted from [63]).

a line lattice as opposed to the usual atomic point lattice: because a cutting of flux lines is not possible, edge dislocations cannot lie in the xy-plane. Therefore dislocations of the FLL have to lie in a plane spanned by the magnetic field $\mathbf{H}$ (parallel to the z-direction) and the Burger's vector $\mathbf{b}$ of the dislocation (which lies in the xy-plane). In other words, dislocations cannot climb but only glide. If $d\mathbf{s}$ is a dislocation line element the planarity constraint can also be written [97]

$$0 = d\mathbf{s} \cdot (\mathbf{H} \times \mathbf{b}) \ . \tag{4.1}$$

Therefore, pure edge dislocations are always parallel to the z axis of the magnetic field.

Starting from elasticity theory for the FLL [6, 98] the energetics of dislocations can be discussed in complete analogy to dislocations in atomic solids [99, 96]. The elastic properties of the hexagonal FLL with lattice spacing a are described by the shear modulus c_{66}, the compression modulus c_{11} and the tilt modulus c_{44}. Due to the interactions of range λ, c_{11} and c_{44} become strongly dispersive $\propto k^{-2}$ for phonons with wavevectors $k > 1/\lambda$ which leads to a considerable softening of the FLL for short wavelength deformations. Because shear modes are volume preserving they are not sensitive to the existence of a finite magnetic interaction range and c_{66} is essentially dispersion-free. In the local limit of small wave vectors $k \ll \lambda^{-2}$, the compression modulus is much larger than the shear modulus ($c_{11} = 3c_{66}$ close to H_{c1} and $c_{11}/c_{66} \propto \lambda^2/a^2 \gg 1$ for higher magnetic fields in the dense limit $a \ll \lambda$), and we can neglect longitudinal compression modes to a good approximation. The compressibility is characterized by Poisson's ratio ν, which is given by $1/(1-\nu) = 2(1 - c_{66}/c_{11})$ (for three spatial dimensions). As we are considering straight, rigid, parallel FLs, we can neglect tilt deformations in the following such that the FLL deformations are completely characterized by the two moduli c_{66} and c_{11}. In addition, the z-component of the wave vector of deformations is always zero, $k_z = 0$, for straight, rigid lines.

The energetics of dislocations in the FLL has been worked out in [97, 99]. As compared to the results for dislocations in atomic lattices [96] differences arise since FL displacements do *not* have a z-component. There are two contributions to the elastic energy of a dislocation, one from the core region of size $\sim b = a$ where the lattice structure is strongly distorted and displacement gradients of $\mathcal{O}(1)$ and one from the long-range elastic strains $\sim 1/r$. The elastic self-energy (per length) of straight edge and screw dislocations are

$$\begin{aligned} E_{s,\mathrm{edge}} &= \frac{c_{66}b^2}{4\pi(1-\nu)}\left(c_D + \ln\left(\frac{L}{a}\right)\right) \\ E_{s,\mathrm{screw}} &= \frac{\sqrt{c_{66}c_{44}}b^2}{4\pi}\left(c_D + \ln\left(\frac{L}{a}\right)\right) \end{aligned} \tag{4.2}$$

The short-scale cutoff in (4.2) is provided by an effective core radius ae^{-c_D} which has been rewritten in terms of a (dimensionless) core energy c_D. For large scales, the cutoff L will be provided by the system size perpendicular to the dislocation orientation for a *single* dislocation. In the presence of *many* dislocations L will be the distance to the next dislocation (of opposite Burger's vector) as we will see below. Whereas a pure edge dislocation involves only shearing of the vortex lattice and has thus a prefactor $\sim c_{66}b^2$, a screw dislocation involves also tilting and therefore has a prefactor $\sim \sqrt{c_{66}c_{44}}b^2$. Reasonable estimates for the core parameters are $c_D \simeq 1 \ldots 1.4$ [96]. Numerical values of these parameters for edge and screw dislocations are similar [96]. Therefore we take the same values in the following for simplicity. The spatial anisotropy in the dislocation line energies can be characterized by the parameter

$$\gamma_D = \frac{E_{s,\mathrm{screw}}}{E_{s,\mathrm{edge}}} = \frac{1}{2}\sqrt{\frac{c_{44}}{c_{66}}} \; . \tag{4.3}$$

It is important to note that the anisotropy γ_D is over a wide range of magnetic fields several orders of magnitude bigger in a FLL than in usual atomic lattices. In particular, this is the case in the high-T_c materials the layered structure of which leads to strongly anisotropic properties of the vortices, which are characterized by the ratio $\varepsilon = \lambda_{ab}/\lambda_c = \xi_c/\xi_{ab}$ of in-plane (ab) and out-of-plane (c) magnetic penetration depths and coherence lengths. Typical values are $\varepsilon \sim 1/5$ in YBCO and $\varepsilon \sim 1/100$ for BSCCO. The dislocations in the FLL "inherit" these anisotropy via the anisotropic properties of the elastic constants [7, 6] because $\gamma_D \propto \varepsilon$. In addition, the elastic constants in the FLL are strongly dependent on the magnetic field which changes the interaction between vortices. In atomic lattices the anisotropy is only $\gamma = 1 - \nu$ and is determined solely by Poisson's ratio ν, which is typically in a range of 0.07 (Diamond) – 0.4 (Au) for atomic solids. In FLLs, however, we find at low magnetic fields $\gamma_D \gg 1$ and at high fields $\gamma_D \ll 1$ due to the additional factor of $\sqrt{c_{44}/c_{66}}$ in (4.3). To make dislocation energies spatially isotropic for the following we rescale the z-coordinate according to

$$z = \tilde{z}\gamma_D = \tilde{z}\frac{1}{2}\sqrt{\frac{c_{44}}{c_{66}}} \; . \tag{4.4}$$

To a good approximation the dislocation energies become isotropic in the rescaled system with

$$\begin{aligned} E_s &= \frac{Kb^2}{4\pi}\left(c_D + \ln\left(\frac{L}{a}\right)\right) \\ &= E_D + \frac{Kb^2}{4\pi}\ln\left(\frac{L}{a}\right) \end{aligned} \tag{4.5}$$

where

$$K \equiv \sqrt{c_{44}c_{66}} \tag{4.6}$$

is the *isotropized elastic constant* and $E_D = c_D Kb^2/4\pi$ is the core energy per length of a straight edge dislocation and the second term the elastic self-energy screened for distances bigger than L form the dislocation core.

In a system with isotropic dislocation energies the energy cost of small deviations from the straight dislocation configuration is essentially given by the additional self energy cost due to the increase in the dislocation length. The dislocation has therefore an an elastic stiffness $\epsilon_D = E_s$ [96] and we can write down the dislocation Hamiltonian as function of its displacement u_D as [100]

$$\mathcal{H}_D[u_D] = \int dz \left(E_s + \frac{1}{2}\epsilon_D(\partial_z u_D)^2\right) \ . \tag{4.7}$$

Note that we consider in (4.7) a *directed* edge dislocation line configuration (i.e., without overhangs) running along the z-direction. Furthermore, The planarity constraint (4.1) actually reinforces a *one-component* dislocation displacement field $u_D(z)$ by constraining $\mathbf{u}_D$ to lie in the plane spanned by the Burger's vector $\mathbf{b}$ and the magnetic field $\mathbf{H}$.

In general, the stiffness ϵ_D in (4.7) will be non-local and depend on the wavenumber k of the dislocation line fluctuation which will set a large scale cutoff for the elastic strains involved in the distortion. With spatially isotropic dislocation energies the stiffness is given through the increased line length and the elastic self energy carried by the added line elements which has to be cut off at the scale $L = 2\pi/q$ set by the wavelength of the distortion:

$$\epsilon_D(q) = E_s(L = 2\pi/q) = E_D + \frac{Kb^2}{4\pi}\ln\left(\frac{2\pi}{qa}\right) \ . \tag{4.8}$$

which leads to a weak logarithmic dispersion. For thermal melting, the short-wavelength limit, $q \sim 1/a$, is relevant and distortions on the shortest scale give the main contribution to the free energy of the dislocation. Therefore we will use essentially a "core stiffness" given by

$$\epsilon_D = E_D = c_D\frac{Kb^2}{4\pi} \ . \tag{4.9}$$

4.3 Vortex Lattice Melting

Before addressing effects of disorder we need to revisit the dislocation-mediated thermal melting of the FLL [97]. A free energy for the dislocation degrees of freedom governing phase transitions is derived from vortex lattice elasticity theory. Accordingly, the dislocation ensemble can be modeled as an array of elastic lines with a long-range Coulomb-like interaction. Note that the Peierls barrier W_p and the associated "kinking" (Ref. [96]) of edge dislocation lines can be neglected near the melting transition. It can be shown that kinks are irrelevant above the temperature

$$T_k \sim a\sqrt{W_p \epsilon_D}. \tag{4.10}$$

Numerically, we find $W_p \lesssim 10^{-4} E_D$, such that T_k is much *lower* than T_m. Therefore, the basic length scale along the magnetic field is solely set by the competition of FL tilt and shear and given by $a_z \approx a\sqrt{c_{44}/c_{66}}/2$ ($a_z \approx a$ in the rescaled system). The free energy of a single dislocation can be readily calculated from the partition sum $Z_D = \int \mathcal{D}u_D \exp\left(-\beta \mathcal{H}_D[u_D]\right)$ by Gaussian functional integration and consists of the core energy, the long-range strains elastic energy, and the entropy term:

$$\frac{F_D(L)}{L_z} = E_D + \frac{Kb^2}{4\pi} \ln\left(\frac{L}{a}\right) - T\frac{1}{2a_z} \ln\left(1 + \frac{2\pi T a_z}{\epsilon_D a^2}\right). \tag{4.11}$$

The spontaneous formation of a single dislocation is prohibited by the logarithmic divergence of its elastic energy which has to be *screened* for a phase transition to occur. One possible mechanism is screening by dislocation *loops* on all length scales as in a second-order 3DXY-type phase transition [101], the other is a first-order phase transition where an ensemble of *unbound* dislocation lines with *finite* density threads the sample at the transition. Without loss of generality we can consider an ensemble of *directed* dislocation lines in this scenario. In the ensemble of unbound dislocations with a Coulomb-type interaction, the Debye-Hückel screening by *free* dislocations of opposite Burger's vector is by far more effective than the screening by small closed dislocation loops which we therefore neglect in this situation. The effective hard-core repulsion of dislocations with the *same* Burger's vectors, due to the energy penalty for Burger's vectors with $b > a$, also gives rise to screening. We find in the FLL that the planarity constraint favors such a first-order transition. Using the approach of Shenoy (Ref. [101]) we calculate the transition temperatures for a second order loop-mediated 3DXY-type transition and compare to our findings for the first order transition. In the absence of a planarity constraint, we find that the 3DXY-type transition has a *lower* transition temperature whereas it has a *higher* transition temperature when planarity is enforced. Taking screening into account and an additional entropy cost ($\propto \rho^3$) from the steric repulsion, we derive the following free-energy density for a (topologically neutral) dislocation ensemble of density 2ρ [1]:

$$\begin{aligned} f(\rho) &= 2\rho\left(E_D - T\frac{1}{2a_z}\ln\left(1 + \frac{2\pi T a_z}{\epsilon_D a^2}\right)\right) + \\ &\quad + 2\rho\frac{Kb^2}{4\pi} 0.3 \ln\left(\frac{1}{b(T)\, a^2 \rho}\right) + \rho^3 \frac{\pi^2}{3}\frac{T^2 a^2}{\epsilon_D}. \end{aligned} \tag{4.12}$$

---

[1] For simplicity we use a square lattice where Burger's vectors of different orientation are non-interacting, and we need to consider only one direction of Burger's vectors.

$f(\rho)$ can be obtained in a more rigorous manner by mapping dislocations onto a quantum system of 2D Fermions with Coulomb interaction [43]. This allows for the systematic calculation of screening effects in Eq. (4.12) through the Lindhard-Thomas-Fermi theory for Coulomb screening and exchange terms, and leads to a screening parameter $b(T_m) \approx 0.5$. It follows from Eq. (4.12) that a *first-order melting* occurs at $T_m \approx 1.57 E_D a_z \approx 0.15 K a^3$, which is equivalent to melting according to the Lindemann-criterion with a Lindemann-number $c_L \approx 0.2$, in good agreement with experimental and numerical results. At the melting transition dislocations proliferate with a *high* density $\rho_m \approx 0.2 a^{-2}$, hence the VL is saturated with dislocations.

4.4 Pinned Dislocations and Vortex Glass Phase

Now we are in the position to address the effect of a random pinning potential $V_{pin}(\mathbf{r})$, in the presence of which the *dislocation-free* vortex array is collectively pinned and exhibits three different spatial scaling regimes: (i) Small distances where vortex displacements u are smaller than the coherence length ξ and perturbation theory applies [9]. (ii) Intermediate scales where $\xi \lesssim u \lesssim a$ and disorder potentials seen by different FLs are effectively *uncorrelated.* This regime is captured in so-called random manifold (RM) models [7, 26], leading to a roughness $\tilde{G}(\mathbf{r}) = \overline{\langle(\mathbf{u}(\mathbf{r}) - \mathbf{u}(0))^2\rangle} \simeq a^2 (r/R_a)^{2\zeta_{RM}}$ where $\zeta_{RM} \approx 1/5$ for the $d = 3$ dimensional RM with two displacement components. The crossover scale to the asymptotic behavior is the *positional correlation length* R_a where the average displacement is of the order of the FL spacing: $u \approx a$. (iii) The asymptotic Bragg glass regime where the a-periodicity of the FL array becomes important for the coupling to the disorder and the array is effectively subject to a *periodic* pinning potential with period a [25]. Here the *logarithmic* roughness $\tilde{G}(\mathbf{r}) \approx (a/\pi)^2 \ln(er/R_a)$, i.e., $\zeta_{BrG} = \mathcal{O}(\log)$ [25, 26] takes over.

In a disordered system at $T = 0$ the mechanism for dislocation proliferation is fundamentally different from the thermal melting discussed before. While thermal melting is governed by the *entropy gain* due to unbinding dislocations pairs, the $T = 0$ transition is driven by FLL adjustment to disorder. Disorder distorts the FLL giving rise to significant elastic stresses; dislocation proliferation releases these stresses, and leads to energy gain through the dislocation degrees of freedom. It has been shown in Refs. [27, 28] that the three-dimensional (3D) BrG phase is *stable* with respect to dislocation formation. As we will show, instabilities arise from the subasymptotic regimes. To handle analytical difficulties and to provide a unified treatment through all scaling regimes, we develop an approach to the 3D problem based on an *effective random stress model* which has the same displacement correlations as the full non-linear disordered model but allows for a *separation* of dislocation and elastic degrees of freedom. This idea is motivated by the renormalization group (RG) for the two-dimensional (2D) BrG which explicitly shows it renormalizes asymptotically into a random stress model [102] and has been used in Ref. [103] to show the *instability* of the 2D BrG with respect to dislocations [26, 103]. For simplicity we consider a *uniaxial* FLL model (in the incompressible limit $c_{11} \gg c_{66}$) which yields the same dislocation energetics as the isotropized two-component model. The Hamiltonian is

$$\mathcal{H}[\mathbf{u}] = \int d\mathbf{r} \left\{ \frac{1}{2} K (\nabla u)^2 + \sigma \cdot \nabla u \right\}, \tag{4.13}$$

where $\sigma(\mathbf{r})$ is the *random stress field* which we assume to be Gaussian distributed with a second moment $\overline{\sigma_i(\mathbf{k})\sigma_j(\mathbf{k}')} = \delta_{ij}\Sigma(k)(2\pi)^3\delta(\mathbf{k}+\mathbf{k}')$ characterized by the function $\Sigma(k)$ in Fourier space. The effective random stresses causing displacements with the same (two-point) correlations as those for the RM or BrG regime are

$$\Sigma(k) \quad = \quad \begin{cases} \text{BrG:} & \frac{1}{2} K^2 k^{-1} a^2 \\ \text{RM:} & B_{RM} K^2 k^{-1} a^2 (kR_a)^{-2/5} \end{cases} \tag{4.14}$$

(the exact crossover determining the numerical constant B_{RM} is nontrivial [104]). The validity of the random stress model is well-established in 2D. Besides, the functional RG treatment of the BrG in $d = 4 - \epsilon$ dimensions shows that displacements asymptotically obey Gaussian statistics up to the first order in ϵ [105], which can always be modeled by an effective random stress field.

We calculate the free energy of an ensemble of dislocation lines $\mathbf{R}_i(s)$ with the density $\mathbf{b}(\mathbf{r}) = \sum_i b \int ds d\mathbf{R}_i/ds$ from the Hamiltonian (4.13) analogously to Ref. [106]. In the random stress model the Hamiltonian *decouples* into the elastic part and a dislocation part:

$$\mathcal{H}_D[\mathbf{b}] \quad = \quad \int d\mathbf{r} \int d\mathbf{r}' \frac{K}{2} \mathbf{b}(\mathbf{r}) \cdot \mathbf{b}(\mathbf{r}') G_0(\mathbf{r} - \mathbf{r}') + \int d\mathbf{r} \mathbf{b}(\mathbf{r}) \cdot \mathbf{g}(\mathbf{r}) \tag{4.15}$$

where $G_0(\mathbf{r}) = 1/(4\pi r)$ is the 3D Green's function. Here $\mathbf{g}(\mathbf{r})$ is an effective *random potential* for dislocation lines defined by the transversal part of σ through $\nabla \times \mathbf{g} = \sigma_T$ (cf. Ref. [103]). The energy Eq. (4.15) contains the long-range elastic energy E_s of dislocations in the first term and in the stochastic second term the disorder energy E_{dis} which allows dislocations to gain energy by optimizing their paths. The dislocation disorder energy is completely determined by the FL displacement correlations through $\overline{g_i(\mathbf{k})g_j(\mathbf{k}')} = \delta_{ij}\frac{1}{2}\Sigma(k)k^{-2}(2\pi)^3\delta(\mathbf{k}+\mathbf{k}')$ in the different regimes given by Eq. (4.14). For a single directed dislocation line, the Hamiltonian (4.15) reduces to the problem of a directed elastic line with a logarithmic dispersion in a random potential that is long-range correlated described by Eq. (4.14). For a directed dislocation of length L_z and confined in the transversal direction to a scale L, the mean-square disorder energy fluctuations are

$$\overline{E_{dis}^2(L_z, L)} \quad \sim \quad \begin{cases} \text{BrG:} & E_D^2 L_z L \\ \text{RM:} & E_D^2 L_z L \left(\dfrac{L}{R_a} \right)^{2/5} \end{cases} \quad . \tag{4.16}$$

These expressions give an estimate of the *typical* disorder energy a dislocation line can gain. They neglect *rare fluctuations* in the energy gain from optimally positioning the dislocation in the transversal plane which give logarithmic corrections $\sim \mathcal{O}(\ln L)$ [28]. The optimal path of the dislocation is *rough* $u_D \sim L_z^{\zeta_D}$ with an exponent ζ_D. The roughness can be obtained by a Flory argument equating the elastic energy from the deformation $\epsilon_D(L)u_D^2/L$ and the disorder energy $\overline{E_{dis}^2(L_z = L, u_D)}^{1/2}$ on *one* large length scale set by the fluctuation wavelength L. This yields $\zeta_D(BrG) = 1 - \mathcal{O}(\log^{2/3})$ and $\zeta_D(RM) = \frac{15}{13} - \mathcal{O}(\log^{10/13})$ where logarithmic corrections come from the dispersion of the stiffness and rare fluctuations. Since $\zeta_D(BrG) \leq 1$, the BrG is marginally *stable* against penetration of a *single* directed dislocation [27, 28] whereas $\zeta_D(RM) > 1$ such that the random manifold is clearly *unstable.* Note that the scaling arguments of Ref. [28] taking into account rare fluctuations give the same result regarding the stability of the BrG phase as our Flory argument.

Given the stability of the BrG against spontaneous formation of a *single* dislocation at weak disorder we present a mechanism for the destruction of the topologically ordered BrG phase at increased disorder strengths or magnetic fields. The mechanism is based on the above result that within domains of subasymptotic size $L < R_a$ the FLL is unstable to a spontaneous formation of dislocations. This can indeed lead to the proliferation of infinitely long dislocations in a *weak first-order* phase transition where dislocation elements are laterally confined by a *finite* dislocation density to scales $L < 1/\sqrt{\rho}$. Thus the characteristic dislocation density $\rho_c \sim R_a^{-2}$ at the transition is given just by the crossover scale R_a below which instabilities can occur. The discontinuities in this transition are small and may eventually disappear for weak disorder if the length scale R_a becomes of the order of typical sample dimensions. The random stress model enables us to quantify this idea by estimating typical free energy *minima* of the dislocation ensemble. The screened long-range elastic energy density and the core energy density for the (neutral) dislocation ensemble with density 2ρ are given by $e_D(\rho) = 2\rho\left(E_D + (Kb^2/4\pi)\ln\left(1/a\rho^{1/2}\right)\right)$ as in Eq. (4.12) at $T = 0$. Dislocations are confined to a transversal scale $R_D \simeq \rho^{-1/2}$ set by the distance to the next dislocation. The disorder energy gain is optimized against the elastic deformation on each longitudinal scale $L_p \simeq R_D(R_D/R_a)^{-2/15}$ (RM) or $L_p \simeq R_D$ (BrG) *independently.* L_p is the collective pinning length of the dislocation. Using Eq. (4.16) with $L_z = L_p$ and $L = \rho^{-1/2}$ for the *BrG* regime ($\rho < R_a^{-2}$) and the *RM* regime ($\rho > R_a^{-2}$), we can estimate the corresponding minimal free-energy densities

$$f(\rho) \approx e_D(\rho) - \left\{ \begin{array}{ll} \text{BrG:} & 2A_{BrG}E_D\rho \\ \text{RM:} & 2A_{RM}\dfrac{E_D}{a^2}(\rho a^2)^{13/15}\left(\dfrac{a}{R_a}\right)^{4/15} \end{array} \right. . \tag{4.17}$$

The prefactors $A \equiv A_{BrG} \simeq A_{RM}$ are related to B_{RM} and the exact crossover in Eq. (4.14) and are not known exactly; for $A \approx 8$ (corresponding to $B_{RM} \approx 7$), we obtain good agreement with experiments in estimates below. When both results in Eq. (4.17) are combined one indeed finds a local minimum in the free-energy density at $\rho = R_a^{-2}$ that characterizes an amorphous VG phase. Over a wide range of magnetic fields the dislocation density in the amorphous VG is much *lower* than in the VL for which we have found $\rho \approx 0.2a^{-2}$ above. The elastic BrG phase loses stability with respect to dislocation proliferation and a transition into an amorphous VG phase if the local minimum at $\rho = R_a^{-2}$ becomes the global free energy minimum. This occurs via a weak first-order transition above a magnetic field B_{BrG} given by a criterion $R_a/a = C$ with a "Lindemann-number" $C = \exp(A-1)$.

This is *identical* to the Lindemann criterion obtained in Refs. [27] and [68] and equivalent [68] to the more familiar form $\overline{\langle (u(a)-u(0))^2 \rangle} = c_L^2 a^2$ (see Refs. [63, 65, 66]) with $c_L \approx \exp\left((1-A)/5\right) \approx 0.25$ for $A \approx 8$.

So far, we have derived the free energies (4.12) and (4.17) and identified *three* possible characteristic minima: (i) The dislocation-free minimum at $\rho = 0$ which is stable in the elastic BrG phase at low T and low H. (ii) The minimum at $\rho \sim a^{-2}$ that becomes stable in the disorder-free case for high T in the VL. (iii) A minimum at $\rho \approx R_a^{-2}$ which is realized in the amorphous VG. Combining our results for the thermal melting and the disorder-induced "melting", we have obtained a qualitative theory for the *entire* phase diagram of the vortex matter.

4.5 Vortex Phase Diagram and Critical Point

Moreover, this provides a framework for a natural explanation of the experimentally observed *critical point* of the first-order melting line: At elevated fields the positional correlation length R_a *decreases* [68] and finally reaches $R_a \sim a$ such that the two free-energy minima of the VL and the amorphous VG must *merge.* Both these phases become thermodynamically indistinguishable and have identical *equilibrium* lattice order. Above the critical point there might still exist a *dynamic* transition (or crossover) which involves the thermal depinning of dislocations, similar to the well-known thermal depinning transition of, for example, a single pinned vortex line.

The exact location of the critical point, obtained from the condition that the amorphous VG minimum of Eq. (4.17) moves away from $\rho = R_a^{-2}$ to higher dislocation densities, is determined by the condition $R_a/a = \exp\left(-\frac{1}{2} + \frac{13A}{15}\right)$, which is again equivalent to a Lindemann criterion, with a slightly larger c_L. This gives an estimate $B_{BrG}/B_{cp} = \exp\left(-\frac{8}{15}\left(\frac{4A}{15} - 1\right)\right) \approx 0.6$ for $A \approx 8$, which is in qualitative agreement with the experiments [31, 30, 32]. B_{BrG} is the instability field of the BrG (see above) and thus the "coexistence point" where the topological transition line ends in the first-order melting line and all three phases – elastic BrG, amorphous VG, and VL – can coexist.

It is also instructive to consider the spinodal lines emerging from the critical points, where either the VL or the amorphous VG phase become thermodynamically *unstable.* The above condition $R_a/a = \exp\left(-\frac{1}{2} + \frac{13A}{15}\right)$ for the location of the critical point also specifies the location of the spinodal line where the amorphous VG phase becomes unstable. This spinodal is independent of temperature. $T_{in} \approx 1.47 E_D a_z \approx 0.15 K a^3$ with $T_{in} < T_m$ gives the temperature below which the VL becomes unstable. Therefore, also both spinodals are equivalent to Lindemann criteria.

4.6 Plastic Vortex Creep

First we find the driving force acting on an edge dislocation with $b||x$ when a transport current $j||y$ is sent through the sample. The driving current creates a magnetization gradient, determined by Maxwell's equation $\nabla \times B = \frac{4\pi}{c}\mathbf{j}$. This gradient, in turn, induces shear

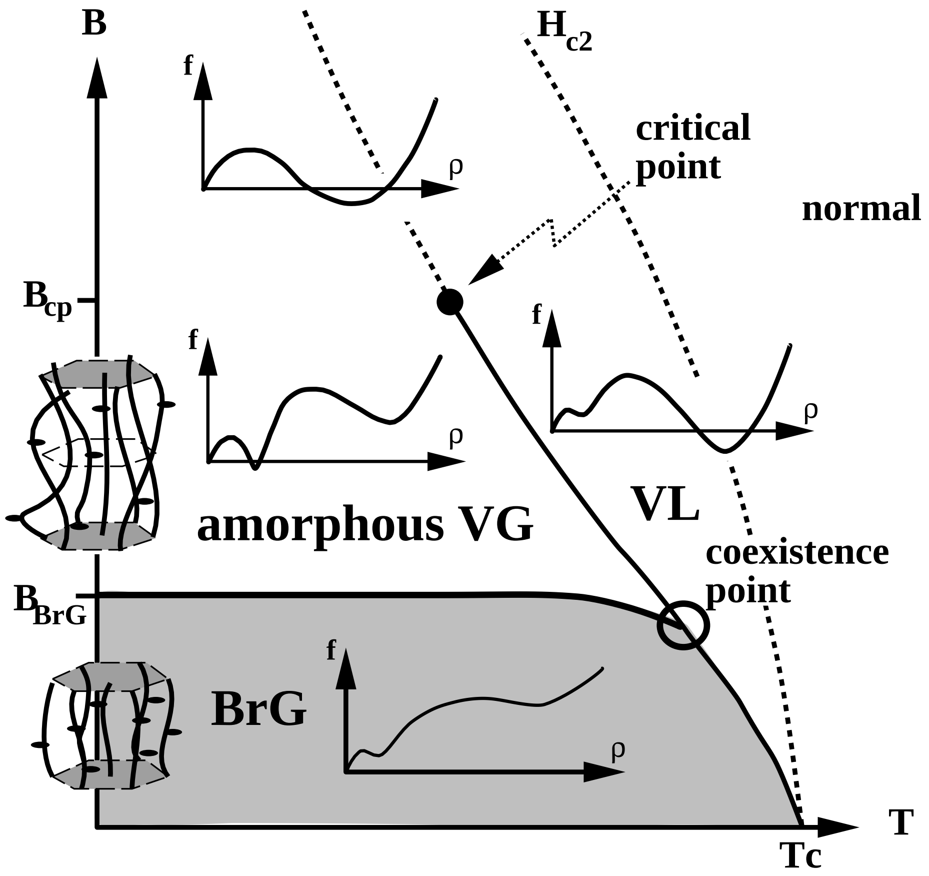

Figure 4.2: Schematic phase diagram of YBCO. Insets show typical free energy densities $f = f(\rho)$ of a dislocation ensemble as a function of the (areal) dislocation density ρ. In the BrG phase (shaded region) the dislocation-free BrG phase with a minimum of $f(\rho)$ at $\rho = 0$ is stable. The VL phase is saturated with dislocations an the stable minimum of $f(\rho)$ is at $\rho \sim a^{-2}$. In the amorphous VG phase we find the minimum at the characteristic density $\rho \sim R_a^{-2}$, which is set by the positional correlation length R_a, which is the crossover scale between the RM regime and the BrG regime.

strains in the vortex lattice: $\partial_x u_y = \partial_x a = a\frac{2\pi}{c}\frac{j}{B}$. The resulting shear stresses give rise to a glide-component of the driving Peach-Köhler force [96] (per dislocation length):

$$F_x^{drive} = \sigma_{yx} b = bKa\frac{2\pi}{c}\frac{j}{B}. \tag{4.18}$$

Note that compression stress leads only to dislocation climb, which can be neglected as slow process requiring diffusion of interstitials [97].

The displacements induced by the magnetization gradient can be accommodated only via the creation of a *stationary* superstructure of regularly spaced bands of dislocations with Burger's vectors having a y-component [107], see Fig. 4.3. Our representative "test"-dislocation moves through this superstructure, which is similar to grain boundaries ap-

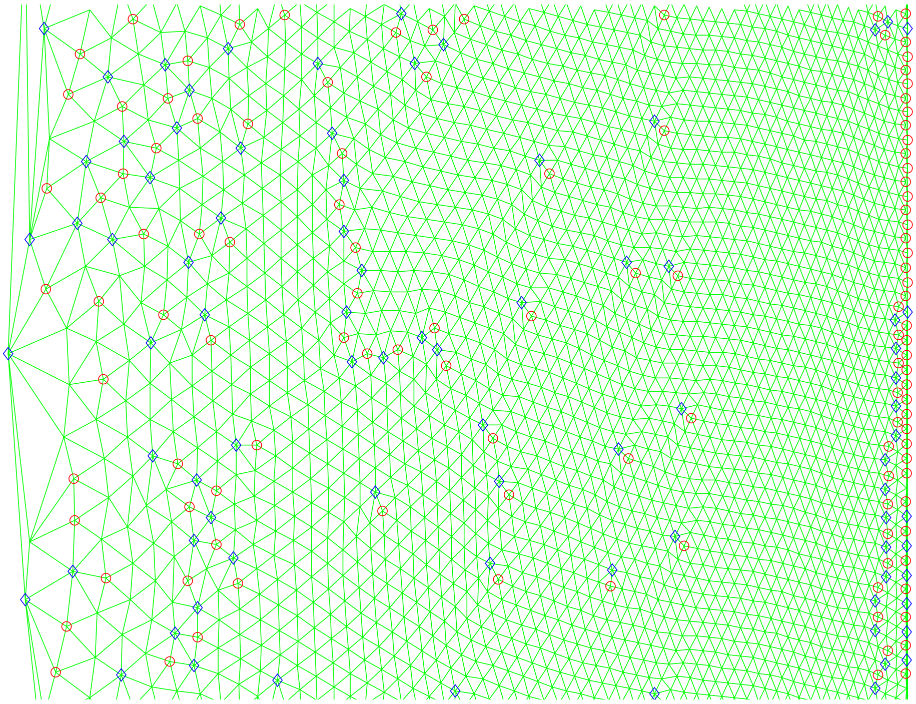

Figure 4.3: Dislocation bands obtained from numerical integration of the time-dependent Ginzburg-Landau equation with current $j||y$.

pearing in bent atomic crystals [96]. Since such dislocation bands are essentially free of shear stresses [96], they do not contribute to the bulk driving shear experienced by the test-dislocation (4.18) everywhere in between the bands, and, therefore, the superstructure does not affect the glide motion.

The random pinning potential $V_{pin}(\mathbf{r})$ "seen" by the vortex array also produces Peach-Köhler-type forces acting on dislocations. To find these pinning-induced Peach-Köhler forces we first have to determine the random stress exerted by the pinning potential on a frozen-in elastic displacement configuration $u_{el}(\mathbf{R}, z)$ of the vortex lattice: $V_{pin}(\mathbf{R}+\mathbf{u}_{el}, z) = \sigma_{ij}^{pin}(\mathbf{R}+\mathbf{u}_{el}, z)\nabla_i u_{el,j}$. The spatial distribution of the pinning stresses is thus governed by the quenched distribution of the elastic displacements u_{el} of the *dislocation-free* collectively pinned vortex array. The latter shows different scaling behaviors depending on the spatial regime in question: (i) Small distances where vortex displacements u are smaller than the coherence length ξ and perturbation theory applies [9]. (ii) The intermediate scales where $\xi \lesssim u \lesssim a$ and disorder potentials seen by different vortices are effectively *uncorrelated*. This regime is captured in so-called *random manifold* (RM) models [7, 26], leading to a roughness $\tilde{G}(\mathbf{r}) = \overline{\langle(\mathbf{u}_{el}(\mathbf{r}) - \mathbf{u}_{el}(0))^2\rangle} \simeq a^2(r/R_a)^{2\zeta_{RM}}$ where $\zeta_{RM} \approx 1/5$ for the $d = 3$ dimensional RM with two displacement components. The crossover scale to the asymptotic behavior is the *positional correlation length* R_a where the average displacement is of the order of the vortex spacing: $u \approx a$. (iii) The asymptotic *Bragg glass* regime where the

a-periodicity of the vortex lattice becomes important for the coupling to the disorder and the array is effectively subject to a *periodic* pinning potential with period a [25]. Here the *logarithmic* roughness $\tilde{G}(\mathbf{r}) \approx (a/\pi)^2 \ln(er/R_a)$, i.e., $\zeta_{BrG} = \mathcal{O}(\log)$ [25, 26] takes over.

For the physics of dislocations on scales $> a$ only the RM and BrG regimes are relevant. We obtain approximately Gaussian distributed quenched stresses with $\overline{\sigma_{ij}^{pin}} = 0$ and $\overline{\sigma_{ij}^{pin}(\mathbf{k})\sigma_{ij}^{pin}(\mathbf{k}')} = \Sigma^{pin}(k)(2\pi)^3\delta(\mathbf{k}+\mathbf{k}')$ with $\Sigma^{pin}(k) = K^2k^2G(k)$, i.e.,

$$\Sigma^{pin}(k) = K^2a^2k^{-1}\begin{cases} \text{BrG:} & 1 \\ \text{RM:} & B_{RM}(kR_a)^{-2\zeta_{RM}} \end{cases} \tag{4.19}$$

determined by the elastic correlations $G(k)$ with a numerical constant B_{RM}. The RM-result holds for $kR_a > 1$, while the BrG-behavior occurs for $kR_a < 1$.

To derive the correct Peach-Köhler pinning force it is crucial to take into account not only the "direct" quenched pinning stresses $\sigma_{ij}(\mathbf{r})$ but also the elastic stresses σ_{ij}^{el} themselves which are responding to the same pinning potential and hence tend to *relax* (longitudinal) components of the stress. A simple but lengthy calculation shows that the pinning Peach-Köhler force on a dislocation element $d\mathbf{R}$

$$dF_\alpha^{pin} = \epsilon_{\alpha\beta l}(\sigma_{\beta k}^{pin} + \sigma_{\beta k}^{el})b_k dR_l \tag{4.20}$$

is rotation-free $(\nabla \times d\mathbf{F}^{pin})_\gamma = 0$; the corresponding potential plays the role of the *pinning Hamiltonian*:

$$\begin{aligned} \mathcal{H}_D^{pin}[\mathbf{u}_D] &= \int dz \frac{d\mathbf{u}_{D,l}}{dz} b_k g_{kl}^{pin}(\mathbf{u}_D, z) \\ \overline{g_{kl}^{pin}(\mathbf{k})g_{k'l'}^{pin}(-\mathbf{k})} &\simeq k^{-2}\Sigma^{pin}(k)\delta_{kk'}\delta_{ll'} = K^2G(k)\delta_{kk'}\delta_{ll'} \end{aligned} \tag{4.21}$$

Combining (4.7), (4.18), and (4.21) one arrives at the free energy $\mathcal{H}_D[\mathbf{u}_D] + \mathcal{H}_D^{pin}[\mathbf{u}_D] - \int dz \mathbf{F}^{drive} \cdot \mathbf{u}_D$ giving an adequate description of an ensemble of pinned dislocations.

Starting with statics we discuss first roughening of the dislocation in the presence of disorder. The typical squared pinning energy fluctuations upon displacing a dislocation segment L over a distance u_D (in the xz glide plane) can be calculated from (4.21)

$$\begin{aligned} E_{pin}^2(L, u_D) &\simeq b^2K^2Lu_D \int_0^L dz \int_0^{u_D} dx \int \frac{d^3k}{(2\pi)^3} k^2G(k)e^{ik_zz+ik_xx} \\ &\simeq E_D^2Lu_D \begin{cases} \text{RM:} & (u_D/R_a)^{2\zeta_{RM}} \\ \text{BrG:} & 1 \end{cases} \end{aligned} \tag{4.22}$$

whereas, according to eq. (4.7), the corresponding elastic bending energy of the dislocation is

$$E_{el}(L, u_D) \simeq \frac{1}{2}E_D \ln(L/a)u_D^2/L\ . \tag{4.23}$$

Optimization gives a dislocation roughness as

$$u_D(L) \simeq L \begin{cases} \text{RM:} & (L/R_a)^{2\zeta_{RM}/(3-2\zeta_{RM})}\, \mathcal{O}(\log) \\ \text{BrG:} & \ln^{-2/3}(L/a) \end{cases} \tag{4.24}$$

i.e., exponents $\zeta_D \approx \frac{15}{13}$ for RM scaling ($L < R_a$) and $\zeta_D \approx 1 - log^{2/3}$ for BrG scaling. The instability with respect to dislocation proliferation is signaled by anomalous energy gains if $\zeta_D > 1$, i.e., in the RM-regime. In the BrG-regime the energy balance is more subtle and to conclude on the stability at $\zeta_D < 1$ one has to convert the result (4.24) into an approximate renormalization (RG) scheme: the energy gain due to roughening is $\Delta E \sim E_D L \ln^{-1/3}(L/a) \sim E_D L \tilde{\epsilon}_D(L)^{-1/3}$, where the logarithmic correction is identical to the dimensionless line tension $\tilde{\epsilon}_D = \epsilon_D/E_D$ on the scale L. Interpreting $\Delta E/(E_D L)$ as disorder correction to the line tension $\tilde{\epsilon}_D(L)$ on the scale L and summing these corrections up successively on each scale, together with the bare tension $\tilde{\epsilon}_D^0(L) = \ln(L/a)$, one obtains an integral RG equation

$$\tilde{\epsilon}_D(\ln L) = \int_0^{\ln L} d\ell (1 \pm \tilde{\epsilon}_D(\ell)^{-1/3}) \tag{4.25}$$

equivalent to the result of Ref. [28]. Integration shows that corrections to $\tilde{\epsilon}_D^0(L)$ are irrelevant and hence the BrG regime is stable with respect to dislocation formation [28]. The more detailed stability analysis for both regimes was given previously in this chapter: the BrG-AVG transition is weakly first-order, and dislocations proliferate with the density $\rho \simeq R_a^2$ defined by the scale R_a of crossover between the unstable RM and the stable BrG regimes.

Now we extend our scaling analysis to the dynamic behavior of the driven dislocation. A dislocation segment of length L ($< R_a$) and laterally displaced over u_D gains not only the energy (4.22) due to pinning potential but also an energy $Lu_D F^{drive}$ by the driving force (4.18) while it loses bending energy, and has thus a free energy:

$$\frac{F(u_D, L)}{E_D} \simeq \frac{u_D^2}{L} - (Lu_D)^{1/2} \left(\frac{u_D}{R_a}\right)^{\zeta_{RM}} - Lu_D \frac{8\pi^2}{c} \frac{j}{B} \tag{4.26}$$

Minima of the pinning potential are typically separated by distances $u_D \sim a$, determined by the core size of the dislocation. A dislocation confined within *one* such minimum is collectively pinned on a *plastic pinning length*

$$L_{pl} \simeq a \left(\frac{R_a}{a}\right)^{2\zeta_{RM}/3} < R_a \tag{4.27}$$

which is obtained by minimizing $F(u_D = a, L)$ with respect to L at zero current. This is the analogue of the Larkin pinning length $L_c \simeq \xi \delta^{-1/3}$ of the single vortex where δ is the dimensionless pinning strength of Ref. [7]. To depin the dislocation the driving force in (4.26) has to exceed the pinning force $F^{pin}(L_{pl}) \simeq \frac{E_D}{a} L_{pl} \left(a/R_a\right)^{4\zeta_{RM}/3}$ on a segment of length L_{pl}. This determines a *critical plastic current* j_{pl}

$$j_{pl} \simeq \frac{c}{8\pi^2} \frac{B}{a} \left(\frac{a}{R_a}\right)^{4\zeta_{RM}/3} \simeq j_0 \left(\frac{2\pi H_{c2}}{B}\right)^{-7/4} \delta^{5/18} \tag{4.28}$$

where $j_0 \simeq \frac{c}{6\sqrt{3}\pi} H_{c2}/\xi$ is the depairing current. Comparing this result to the depinning current $j_c \simeq j_0 \delta^{2/3}$ for a single vortex, one finds $j_{pl} < j_c$ for typical disorder strengths $\delta \sim 10^{-3}$, and the plastic motion of dislocations may occur even if the vortices themselves are still pinned. One concludes that at sufficient currents the plastic motion dominates transport in the dislocated AVG phase.

However, the existence of a current $j_{pl} > 0$ implies that dislocations are *pinned* at low currents and, therefore, the plastic motion for $j \ll j_{pl}$ occurs only via activation over *diverging* plastic energy barriers $U_{pl}(j) \sim j^{-\mu_{pl}}$ i.e as a *plastic creep*. The typical segment size $L(j)$ for activated motion at $j \ll j_{pl}$ is determined from (4.26) by balancing the energy gain due to the driving force $E_{drive} \simeq \frac{8\pi^2}{c} \frac{j}{B} L^{1+\zeta_D}$ against the pinning energy $E_{pin} \simeq E_D L^{2\zeta_D - 1}$ of a dislocation line roughened according to the above result (4.24). This yields

$$U_{pl}(j) \simeq E_D a \left(\frac{a}{R_a}\right)^{2\zeta_{RM}/3} \left(\frac{j_{pl}}{j}\right)^{(2\zeta_D-1)/(2-\zeta_D)} \tag{4.29}$$

and we obtain the scaling law $\mu_{pl} = (2\zeta_D - 1)/(2 - \zeta_D)$ (as for single vortex creep [7]) relating the plastic creep exponent μ_{pl} to the dislocation roughness. We find $\mu_{pl} = \frac{17}{11}$ in the RM-regime ($L(j) < R_a$) and $\mu_{pl} = 1$ in the BrG-regime ($L(j) > R_a$). Both exponents are considerably larger than their counterpart $\mu = 2/11$ for elastic single vortex creep showing that plastic creep rates are much smaller than elastic creep rates.

So far we focused on a *single* dislocation. Now we turn to an ensemble of interacting dislocations. On large scales exceeding the dislocation spacing R_D, which varies from $R_D \simeq R_a$ at the AVG-BrG transition to $R_D \simeq a$ at the critical point, interactions become essential and plastic creep is governed by the motion of dislocation *bundles* in a glide plane (xz-plane). Deformations $u_D(x,z)$ of such a 2D bundle can be described by an elastic Hamiltonian with tilt modulus $K_z \simeq E_D/R_D$ and the compression modulus $K_x \simeq R_D \partial^2_{R_D}(R_D^2 \tilde{f}(R_D))$ which can be calculated from the dislocation free energy for a dislocation density $\rho = 1/R_D^2$, $\tilde{f}(R_D) \equiv f(1/R_D^2)$, see eq. (4.17) (in the absence of disorder one finds $K_x \simeq E_D/R_D$). Including the pinning energies we obtain the Hamiltonian

$$\begin{aligned} \mathcal{H}[u_D(x,z)] &= \int dxdz \frac{1}{2} \left\{ K_x (\partial_x u_D)^2 + K_z (\partial_z u_D)^2 \right\} \\ &\quad + \sum_i \int dz \mathcal{H}_D^{pin}[\mathbf{b}_i, \mathbf{u}_D(iR_D, z)] \end{aligned} \tag{4.30}$$

The dislocation bundle contains dislocations of *opposite* signs with the same density to avoid the accumulation of stress. Hence the sum over the dislocation index i in (4.30) goes over *alternating* Burger's vectors $\mathbf{b}_i||x$. On scales $L_x \gg R_D$ dislocations couple effectively as dipoles to disorder and we obtain for the bundle disorder energy fluctuations $E^b_{dis}(L_z, L_x, u_D) \simeq E_{pin}(L_z, u_D)$ with $E_{pin}(L_z, u_D)$ from (4.22). This has to be balanced against the elastic energy $E_{el}(L_z, L_x, u_D) \simeq \sqrt{K_x K_y} u_D^2$ with $L_z \simeq \sqrt{K_z/K_x} L_x$ resulting in a roughness

$$u_D(L_z) \sim L_z^{1/3} R_D^{2/3} \begin{cases} \text{RM:} & \left(\dfrac{L_z^{1/3} R_D^{2/3}}{R_a} \right)^{\frac{2\zeta_{RM}}{3-2\zeta_{RM}}} \\ \text{BrG:} & 1 \end{cases} . \tag{4.31}$$

Note that the bundle roughness is *reduced* as compared to that of single dislocations: $\zeta_D \approx \frac{5}{13}$ for RM scaling ($L < R_a$) and $\zeta_D \approx \frac{1}{3}$ for BrG scaling. Analogously to the case of the single dislocation, one easily establishes the plastic creep exponents for bundle creep, in particular one finds the same scaling relation $\mu_{pl} = (2\zeta_D + d - 2)/(2 - \zeta_D)$ as for d-dimensional vortex bundles [7]. This gives $\mu_{pl} = \frac{10}{21}$ in the RM-regime and $\mu_{pl} = \frac{2}{5}$ in the BrG-regime. A crossover from the single dislocation- to the bundle scaling occurs at currents $j < j^b$ where $L(j^b) \simeq \sqrt{K_z/K_x} R_D$. For $R_D \simeq a$ one finds $j^b \simeq j_{pl}$, meaning that only plastic bundle creep can be measured above the critical point defined by $R_D \simeq a$.

By the spirit of the derivation our results seem to apply to superconductors with pronounced vortex lines (like YBCO) rather than to the layered BSCCO. Yet the creep exponent measured within the AVG phase in Ref. [94] is strikingly close to $\mu_{pl} = \frac{2}{5}$. In layered compounds such as BSCCO the vortex lattice consists of pancakes only weakly coupled across different layers by their magnetic interaction. Whereas the Bragg glass phase can persist at low magnetic fields due to the small interlayer coupling, the layers essentially decouple at higher fields, and the resulting two-dimensional (2D) pancake lattices are unstable with respect to dislocation formation in the presence of pinning by point defects [103]. Also the 2D dislocations exhibit plastic creep as can be seen from the following argument. Let us consider a pair of opposite edge dislocations a distance u_D apart with an interaction energy $E_{int}(u_D) = E_D \ln{(u/a))}$ where $E_D = c_{66} = b^2/2\pi$ in 2D. The typical energy gain from the disorder has been calculated in Ref. [103] to be $E_{pin}(u_D) \simeq E_D \ln^{3/2}{(u_D/R_a)}$. On the one hand the 2D Bragg glass is unstable to dislocation formation because the disorder-induced *valleys* exceed the interaction energy: $E_{pin}(u_D) \gg E_{int}(u_D)$ for $u_D \gg R_a$. Furthermore, $E_{pin}(u_D)$ also gives the typical size of the energy *barriers* between optimized dislocation positions, i.e., the barriers for plastic creep: $U_{pl} \simeq E_{pin}(u_D)$. In the presence of the driving current the dislocations will gain an energy $E_{drive} \simeq \frac{8\pi^2}{c} \frac{j}{B} u_D$ from the force (4.18) which can pull the dislocation pair apart over these energy barriers. Balancing both terms we find *logarithmically* diverging barriers for plastic creep in 2D:

$$U_{pl}(j) \sim E_D \ln^{3/2}{(1/j)} . \tag{4.32}$$

4.7 Conclusion

In conclusion, we have developed a dislocation theory which classifies all three phases – elastic BrG, amorphous VG, and VL – according to the (areal) density ρ of dislocations threading the system. The BrG phase is dislocation free with $\rho = 0$, the VL phase is saturated with dislocations, $\rho \sim a^{-2}$, and in the amorphous VG phase pinned dislocations enter the system at a characteristic low density $\rho \sim R_a^{-2}$.

Building on the ideas of pinned dislocations we went on to developed a theory of plastic creep in the amorphous VG phase in terms of the dislocation dynamics in the pinned vortex lattice. We have found diverging barriers for plastic vortex transport in agreement with the experimentally observed low creep rates or high apparent critical currents. The obtained results are relevant for other systems where glassy dynamics is controlled by topological defects, for example, charge density waves in disordered crystals and/or work-hardened solids.

Chapter 5

Competitive Localization of Vortex Lines

We present a theory for the localization of three-dimensional vortex lines or two-dimensional bosons with short-ranged repulsive interaction which are competing for a single *columnar defect or potential well. For two vortices we use a necklace model approach to find a new kind of delocalization transition between two different states with a single bound particle. This* exchange-delocalization *transition is characterized by the onset of vortex exchange on the defect for sufficiently weak vortex-vortex repulsion or sufficiently weak binding energy corresponding to high temperature. We calculate the transition point and order of the exchange-delocalization transition. A generalization of this transition to arbitrary vortex number is proposed.*

5.1 Introduction

Melting of the Bose glass, the low-temperature vortex phase in type-II superconductors with columnar defects, remains a subject of constant interest [108, 109]. The interest is motivated not only by the appeal and importance of understanding a basic phase transition of the vortex system, but, since the 3D vortex array is equivalent to a quantum 2D Bose system [52, 53], vortex melting also offers a unique experimentally accessible model to explore the interplay between disorder and interactions in the delocalization transition of the corresponding strongly correlated 2D quantum system.

Numerous experimental observations on Bose glass melting (see, for example, Refs. [110, 111, 109]) revealed a characteristic kink in the low-field segment of the melting line suggesting a change of the melting mechanism. A recent experimental study of BSCCO samples with a *very low* density of columnar pins [108] allowed one to identify the low-field part of the melting curve as depinning transition from a single columnar defect driven by vortex-vortex interactions. A theoretical study of the interacting boson system with a low density of strong defects [112] demonstrated the possibility of an intermediate superfluid state where condensate and localized bosons coexist. Furthermore, it was found in Ref. [112] that interactions suppress localization and the increase of the boson density results in a sharp *delocalization crossover* into a state where all bosons are delocalized.

The model that is conventionally used in studies of quantum localization can be viewed as an ensemble of (interacting) particles immersed in a random field that can, in principle, localize or accommodate all particles; in other words, there is a dense array of pinning centers struggling to localize dilute, but interacting, particles. Reference [112] proposed to take an alternative approach and consider quantum particles or vortex lines of high density competing for dilute traps or pinning sites. In this chapter, we extend this approach and explore the regime of low particle densities, i.e., a *finite* number of interacting quantum particles. A related quantum system that has been studied previously are two electrons interacting in the region of a short-range attractive potential [113].

In this chapter, we investigate the formation of bound states in an ensemble of N strongly repulsive particles competing for a single attractive potential well. In the related vortex system, this corresponds to N vortices competing for a single columnar defect, i.e., to a physical situation where vortices outnumber columnar defects (magnetic fields $B = NB_\Phi$ well exceed the matching field $B_\Phi = \Phi_0/a_D^2$ where a_D is the average defect spacing and Φ_0 the flux quantum). We focus on the situation where mutual repulsion is strong enough to suppress double-occupancy of the potential well and consider transversal dimensionalities $d_\perp \leq 2$, for which a bound state for a single particle in a symmetric potential well always exists (in the following, we use the language of either particles or vortex lines at our will). The main finding of this chapter is a new kind of delocalization phase transition driven by the *exchange* of the single bound particle with the $N-1$ unbound ones. We first derive this result for $N = 2$ and then propose a generalization for arbitrary N. Finally we obtain the transition temperature T_{de} for the exchange-delocalization transition in the vortex system and discuss the resulting phase diagram Fig. 5.2. Contrary to Ref. [112] where the boson (vortex) density was finite, we deal in this work with the genuine thermodynamic limit of *infinite* system size but *finite* particle (vortex) number N corresponding to $B, B_\Phi \approx 0$ with $N = B/B_\Phi$ finite. Thus the exchange-delocalization phase transition emerges in the limit $B \to 0$ and replaces the crossover that was found in Ref. [112] for macroscopic vortex density $B > 0$.

5.2 Model

We describe a single vortex line in a sample of thickness L interacting with an attractive columnar defect by the Hamiltonian

$$\mathcal{H}_1[\mathbf{r}(z)] = \int_0^L dz \left\{ \frac{1}{2}\varepsilon_l (\partial_z \mathbf{r})^2 + V_{cd}(\mathbf{r}(z)) \right\}, \tag{5.1}$$

where $(z, \mathbf{r}(z))$ is the vortex trajectory in $1 + d_\perp$ dimensions, the magnetic field aligned with the z axis, and ε_l is the stiffness or tilt modulus of a single vortex line; in an anisotropic superconductor $\varepsilon_l \approx \varepsilon^2 \varepsilon_0 \ln \kappa$ where $\varepsilon_0 = (\Phi_0/4\pi\lambda)^2$ is the characteristic vortex line energy, λ is the magnetic penetration depth, $\kappa = \lambda/\xi \gg 1$, ξ is the coherence length, and ε is the anisotropy parameter. $V_{cd}(r)$ is the pinning potential from a single columnar defect positioned at $\mathbf{r} = 0$. $V_{cd}(r)$ falls off exponentially for $r > \lambda$ [114] such that the large scale behavior of pinned vortex lines is well described using a cylindrical pinning potential well

$$V_{cd}(\mathbf{r}) = U_{cd} \;\text{ for }\; r < b_{cd}, \quad V_{cd}(\mathbf{r}) = 0 \;\text{ for }\; r > b_{cd} \tag{5.2}$$

with a potential depth $U_{cd} \equiv -\varepsilon_0 r_{cd}^2/4\xi^2$ and an effective radius $b_{cd} \equiv \sqrt{2\xi^2 + r_{cd}^2}$ where r_{cd} is the radius of the columnar defect [52, 53].

In $d_\perp \leq 2$ dimensions the line is *always* bound to the defect as can be seen via mapping onto the ground-state problem of a quantum particle in a potential $V_{cd}(\mathbf{r})$ for large L [115]. Choosing the energy scale such that the unpinned vortex line has a free energy $E_0 = 0$, the free energy per length $E_1 < 0$ of the bound vortex line is obtained as the ground state energy E_1 of the Schrödinger equation

$$\left[(T^2/2\varepsilon_l)\nabla_{\mathbf{r}}^2 - V_{cd}(\mathbf{r})\right]\psi(\mathbf{r}) = -E_1\psi(\mathbf{r}), \tag{5.3}$$

$$E_1 = U_{cd} f(T/T^*), \text{ where } \; T^* \equiv b_{cd}\sqrt{\varepsilon_l |U_{cd}|} \tag{5.4}$$

is a characteristic crossover energy, and $f(x)$ a scaling function. For $d_\perp = 2$ and the pinning potential (5.2), it has the asymptotic behavior $f(x) \approx 1 - \mathcal{O}(x^2)$ for $x \ll 1$ and $f(x) \approx x^2 \exp(-2x^2)/2$ for $x \gg 1$ [53].

For $N > 1$ we add the repulsive vortex interactions [7, 52, 53]

$$\mathcal{H}_N = \sum_{i=1}^{N} \mathcal{H}_1[\mathbf{r}_i(z)] + \sum_{i \neq j=1}^{N} \int_0^L dz V_r(|\mathbf{r}_i(z) - \mathbf{r}_j(z)|), \tag{5.5}$$

where $V_r(r) = 2\varepsilon_0 K_0(r/\lambda)$, and K_0 is the Bessel function. Double-occupancy of the defect over an extended length is energetically disfavored if $\varepsilon_0 \gg |E_1|$, which is always the case at high enough temperatures. We also focus on the regime of large vortex spacing $a \gg \lambda$.

5.3 Exchange-delocalization transition for N=2

We investigate the localization behavior for the case $N = 2$ making use of a *necklace model* approach [116]. As the double-occupancy of the defect is energetically unfavorable,

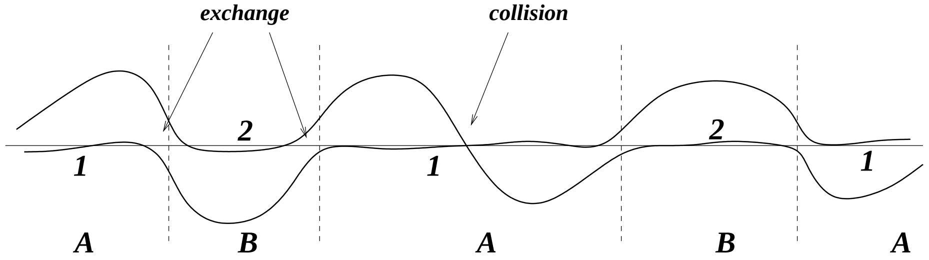

Figure 5.1: Two particles binding alternately to a single columnar defect. The particle binding to the defect can be exchanged in localized events and there are rare collisions between the free and the bound particle.

the accessible configurations of the vortex lines consist of a necklacelike succession of two possible configurations A and B, see Fig. 5.1. In the configuration A, the line 1 is bound to the defect with the binding free energy $E_1 < 0$ and the transversal localization length $\xi_\perp = T/\sqrt{|E_1|\varepsilon_l}$, whereas the line 2 is essentially in the unbound state with the free energy $E_0 = 0$ and experiences rare collisions with the bound line 1. As we assume $\lambda \ll a$, the unbound line is exploring the region $r > \lambda$ of exponentially weak repulsion, whereas collisions occur at $r < \lambda$. The configuration A ends in an exchange event where the endpoints of the unbound line 2 attach to the defect again; see Fig. 5.1. At these exchange points the configuration A can connect to the configuration B where the roles of the particles are exchanged.

First, we estimate the energy cost of the localized collision and exchange events. In the presence of the repulsion (5.5), each return of line 2 to the bound line 1 will cost an additional collision repulsion energy E_r which is determined by optimizing the sum of elastic and repulsive energies for a contact of length ℓ_r over which the typical line spacing is of the order $|\Delta\mathbf{r}| \simeq \lambda$, $E_r \simeq \varepsilon_l\lambda^2/\ell_r + \ell_r\varepsilon_0$:

$$\ell_r \simeq \lambda\sqrt{\varepsilon_l/\varepsilon_0}, \qquad E_r \simeq \lambda\sqrt{\varepsilon_l\varepsilon_0}, \tag{5.6}$$

and $v_r \equiv \exp(-E_r/T) < 1$ defines the Boltzmann-factor associated with each collision. Similarly, we estimate the energy cost E_{ex} of a localized exchange by optimizing the sum of the elastic energy and the loss of binding energy $|E_1|\ell_{ex}$ for a contact of length ℓ_{ex} over which the typical line spacing is of the order $|\Delta\mathbf{r}| \simeq \lambda$, $E_{ex} \simeq \varepsilon_l\lambda^2/\ell_{ex} + \ell_c|E_1|$. This gives

$$\ell_{ex} \simeq \lambda\sqrt{\varepsilon_l/|E_1|}, \qquad E_{ex} \simeq \lambda\sqrt{\varepsilon_l|E_1|}, \tag{5.7}$$

and $v_{ex} \equiv \exp(-E_{ex}/T) < 1$ is the Boltzmann-factor associated with each localized exchange.

Now we address the statistical mechanics problem of summing over all vortex line configurations. Adopting a coarse-grained description focusing on scales $r \gtrsim \lambda$ for transversal vortex fluctuations, we discretize the vortex system into segments of length $l = \lambda^2\varepsilon_l/T$ in the z-direction. In what follows, we calculate the grand-canonical partition sum $G(z) = \sum_n Z(n)z^n$ where $Z(n)$ is the partition sum for a system of length $L = nl$ and z is the fugacity. $\tilde{G}(E) = G(\exp{(lE/T)})$ is the Green's function at energy E for the corresponding two-particle quantum problem. The free energy density f of the system is determined by the real singularity z_0 of $G(z)$ closest to the origin by the relation $z_0 = \exp(lf/T)$. If $G_A(z)$ and $G_B(z)$ are the partition sums for configurations A and B, respectively, the full partition sum is obtained by summing over all alternating configurations G_A, G_B, $G_Av_{ex}G_B$, $G_Bv_{ex}G_A$, $G_Av_{ex}G_Bv_{ex}G_A$,…, separated by particle exchanges with Boltzmann-factor v_{ex}. Summing up the resulting geometric series we obtain

$$G(z) = \left.\frac{G_A + G_B + 2v_{ex}G_AG_B}{1 - v_{ex}^2G_AG_B}\right|_z = \frac{2G_A(z)}{1 - v_{ex}G_A(z)}, \tag{5.8}$$

where we used $G_A = G_B$ because both configurations are related by a mere particle exchange. [Boundary effects are irrelevant; we allow either A or B at the ends of the defect in (5.8)]. According to Eq. (5.8), the singularity determining the free energy of the system is given either by the singularity of $G_A(z)$ corresponding to the state where the *same* line is always bound or by the solution of $1 = v_{ex}G_A(z)$ corresponding to alternating bound particles. The *exchange-delocalization transition* between these two states occurs if both singularities occur at the same value of z.

To move further, we calculate the grand-canonical partition sum $G_A(z)$. In the absence of the interline repulsion, the canonical partition sum in configuration A, $Z_A(n) = Z_1(n)Z_2(n)$, is a product of the partition sum of the bound line 1, $Z_1(n) = \exp(-nlE_1/T)$ [see Eq. (5.4)], and of the free line 2, which is attached with its end-points to the defect. This restriction leads to $Z_2(n) = p_n \exp(-nlE_0/T)$ where p_n is the probability for the return of the unbound line to the defect and $E_0 = 0$ is its free energy per unit length. In the absence of the repulsion this return probability is given by the return probability of a random walk, $p_n \simeq n^{-d/2}$, for large n. Then the partition function $G_A(z)$ is related to the generating function $P(z) = \sum_n p_n z^n$ for these return probabilities by $G_A(z) = P(wz)$ where $w \equiv \exp(-lE_1/T) = \exp(-\lambda\varepsilon_l E_1/T^2)$. For $1-z \ll 1$, $P(z) \sim (1-z)^{d/2-1}$ for $d_\perp < 2$ and $P(z) \sim -\ln(1-z)$ for $d_\perp = 2$. Including the Boltzmann-factor v_r in the random walk of the unbound line for each collision with the repulsive bound line localized at the defect [see Eq. (5.6)] leads to a modified generating function $P_r(z)$:

$$P_r(z) = P(z) + P(z)v_r P_r(z) - P(z)P_r(z). \tag{5.9}$$

In this relation the contributions from the repulsion-free walks with Boltzmann-factor 1 are subtracted and the corresponding term with modified Boltzmann-factor v_r is added on the right hand side recursively for each collision. With this modification due to collisions, we finally obtain

$$G_A(z) = P_r(wz) = \frac{P(wz)}{1 + (1-v_r)P(wz)}, \ w \equiv e^{-lE_1/T} \tag{5.10}$$

for the grand-canonical partition function. $G_A(z)$ has a singularity at $z = 1/w$ corresponding to a free energy per length $f = E_1$ identical to that of a single bound particle because the second unbound particle has $E_0 = 0$. The function $P(wz)$ diverges upon approaching $z = 1/w$ and, thus, we find $G_A(1/w) = P_r(1) = (1-v_r)^{-1}$ at the singularity.

Now we turn to the exchange-delocalization transition determined by the singularities of (5.8). We have already found that the singularity of $G_A(z)$ (at $z = 1/w$ corresponding to the free energy $f = E_1$) describes, indeed, a single bound particle, i.e., a state with always the *same* line bound. We have argued above that there can be a real singularity closer to the real axis which is given by the solution of the equation $1 = v_{ex}G_A(z)$ and which corresponds to the phase with exchanging bound particle. From the functional form (5.10) of $G_A(z)$, one readily verifies that this singularity is indeed the one closer to the origin and therefore representing the thermodynamically stable phase provided

$$v_{ex} \geq v_{ex,c} = G_A^{-1}(1/w) = 1 - v_r \ . \tag{5.11}$$

According to (5.11), the exchange-delocalization phase transition occurs at the critical temperature T_{de} that is obtained from $\exp(-E_r/T_{de}) \approx E_{ex}/T_{de}$ where we assumed that

$E_{ex} \ll T_{de}$ because $T_{de} > T^*$. Using estimates (5.6) and (5.7), the asymptotics of the function $f(x)$ for $d_\perp = 2$, and $\lambda/b_D = \kappa/\sqrt{2}$, we arrive at

$$T_{de} \approx T^* \kappa^{1/3} \tag{5.12}$$

for the delocalization transition temperature T_{de} in the vortex system. The transition takes place in the regime $T > T^*$ where a single vortex is only weakly bound to the defect [52, 53]; see Fig. 5.2. Note that both Eqs. (5.4) and (5.12) are self-consistent equations for T^* and T_{de}, respectively, due to the temperature dependence of ξ and λ. Furthermore, it can be shown by expanding the equation $1 = v_{ex} G_A(z)$ about the transition point, that the exchange-delocalization transition is continuous for all $d_\perp \leq 2$ and of infinite order for $d_\perp = 2$.

We expect our results to apply to all short-ranged potential wells and particle interactions that decay faster than $1/r^2$ for large separations r [117]. More realistic pinning potentials contain an intermediate $1/r^2$-behavior on scales $\xi \ll r \ll \lambda$ [7, 112], which slightly changes the function $f(x)$ and thus the exact value of T_{de} but not the universal properties of the delocalization transition.

5.4 General N

We start from the exchange-delocalized state where all N vortices share the defect and consider the instability with respect to the exclusion of one of the vortices from the exchange. To this end we introduce N states (analogously to the states A and B for $N = 2$), where one vortex is unbound, i.e., excluded from the exchange, whereas the other $N-1$ vortices share the defect. Then the necklace is a succession of possible states $i = 1, ..., N$ each of which has a grand-canonical partition sum $G_i(z) = P(w_N z)/(1+[1-v_r(N)]P(w_N z))$ where $v_r(N) \equiv \exp(-\sqrt{N-1}E_r/T)$ is the Boltzmann-factor due to the enhanced repulsion from the $N-1$ vortices sharing the columnar defect. Similarly, $w_N \equiv \exp(-l f_{N-1}/T)$ is the Boltzmann-factor for the binding free energy of the $N-1$ vortices sharing the defect, which we approximate by $f_{N-1} \approx E_1$ or $w_N \approx w = \exp(-lE_1/T)$. Considering the generalized exchange between these N states and noting that exchange of the single bound particle is associated with the Boltzmann-factor v_{ex}, we arrive at the generalization of (5.8):

$$G(z) = \frac{N G_i(z)}{1-(N-1)v_{ex} G_i(z)} \ .$$

The transition point for the exclusion of one particle from the exchange is given by the relation $v_{ex,c}(N) = [1 - v_r(N)]/(N-1)$. As $v_{ex,c}(N)$ decreases for increasing N, also states with $N-1$ or less exchanging particles become unstable for $v_{ex} < v_{ex,c}(N)$. This leads to the conclusion that particle exchange entirely stops at this point, and we thus identify $v_{ex} = v_{ex,c}(N)$ as the exchange-delocalization transition point of the N-particle system. For $N = 2$ our result reduces to Eqs. (5.11) and (5.12), whereas we find

$$T_{de}(N) \approx \begin{cases} T^* \ln^{1/2}(\kappa/\ln N) & \text{for} \quad \ln N < \kappa \\ T^* \kappa/\ln N & \text{for} \quad \ln N > \kappa \end{cases} \tag{5.13}$$

for large $N = B/B_\Phi$. Note that our approach is limited to the regime of large vortex spacing $a \gg \lambda$ or $N \ll a_{cd}^2/\lambda^2$. The order of the transition is the same as for $N = 2$; i.e., the transition is of infinite order for $d_\perp = 2$.

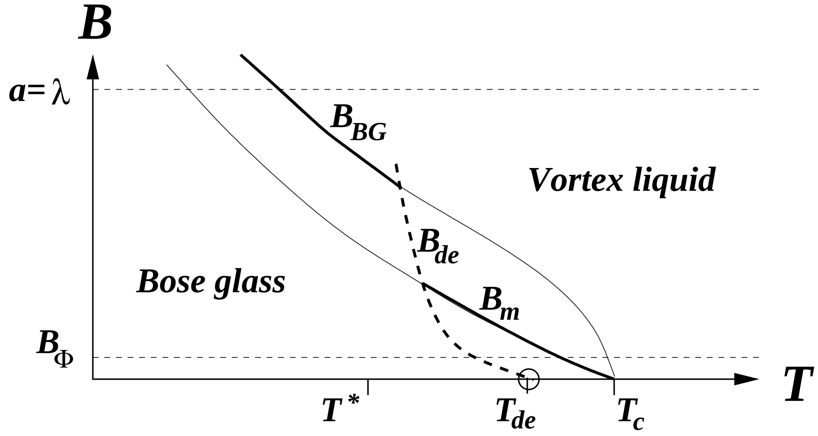

Figure 5.2: Schematic phase diagram in the B-T plane. B_m is the pristine melting line, B_{BG} the Bose glass melting line and B_{de} the exchange-delocalization crossover line which terminates at $B = 0$ in a genuine phase transition at temperature T_{de} (circle).

5.5 Phase diagram

In real vortex systems our results hold for the limit $B_\Phi \approx 0$. This implies also a vanishing vortex density $B \approx 0$ if $N = B/B_\Phi$ is fixed. A finite vortex density $\rho > 0$ corresponds to a system of the finite size $\propto 1/\rho^{1/2}$ which has no genuine phase transition. We thus conclude that the delocalization crossover line of Ref. [112] terminates in the genuine exchange-delocalization *transition point* at $B \approx 0$, which is given by Eqs. (5.12) or (5.13). For macroscopically large N the approximation of localized, well-separated exchange and repulsion events will break down and our low-density approach will become invalid whereas the description by a condensate of bosonic particles used in Ref. [112] works increasingly well in the high-density regime. The exact form of the crossover between both descriptions is an open question. In both descriptions the delocalization line $B_{de}(T)$ drops exponentially with temperature [see (5.13)] such that it intersects with both the pristine melting line $B_m(T)$ and the Bose glass melting line $B_{BG}(T)$; see Fig. 5.2. Beyond the delocalization line, vortex line exchange at the defects sets in, which leads to line wandering and a liquidlike behavior even in the presence of columnar defects, which become irrelevant. Therefore, the relevant melting line is the pristine melting line for $T > T_{de}(B)$ in the delocalized phase, whereas it is the Bose glass melting line in the localized phase. Therefore, there exists a range of magnetic fields where the vortex lattice melts by undergoing the delocalization transition [112] as shown in Fig. 5.2. The resulting phase diagram is in good agreement with the experimental results regarding the melting of "porous" vortex matter [108].

5.6 Conclusion

In conclusion, we have shown that the competitive localization of particles with mutual short-range repulsion by a short-range attractive defect leads to the existence of a genuine phase transition, the *exchange-delocalization transition*, which marks the onset of particle exchange at the defect. We have investigated the exchange-delocalization transition in a system of vortices with columnar defects or interacting bosons with localizing defects at low density. We expect exchange-localization transitions to play an important role in various other systems where competitive localization occurs. In the introduction, we have already mentioned the quantum mechanical system of two interacting electrons competing for an attractive potential [113] that could be realized by a quantum dot. We also expect competitive localization to be relevant for biopolymers, for example it applies to the competitive binding of two identical single strands of DNA to a single complementary DNA strand as it is important for DNA microarray engineering.

Chapter 6

Conclusion and Outlook

This part of the thesis has dealt with flux-lines in type-II superconductors, which are governed by their line *tension.* This tension is mainly created by the magnetic field whose energy is essentially proportional to the length of the line and, thus, gives rise to a tension which tends to align the flux-line with the applied magnetic field. We call lines governed by tension energy *strings.* Similar to vortex lines, also the topological defects in the flux-line lattice, i.e., dislocation lines, which have been discussed in chapter 4, and interstitial or vacancy lines [118] are governed by an energy cost associated with their length and, thus, are strings. In this context, it is useful to remember that also vortex lines are topological defects of the phase field in the underlying Ginzburg-Landau field theory describing superconductors, whereas dislocations are the analogous defects in the elasticity field theory of the flux-line lattice (FLL).

We have presented two complementary approaches to the phase diagram of vortex matter in the presence of point disorder or *point pinning centers.* In chapter 3, we applied *phenomenological* Lindemann criteria in order to calculate the loci of both the thermal melting transition into a vortex liquid and the amorphization transition between the topologically ordered, elastic Bragg glass and the disordered amorphous vortex glass phase. The results are in good agreement with existing experimental work.

Then, in chapter 4, we went on to develop a dislocation theory of these vortex phases, which goes beyond the phenomenological Lindemann analysis by putting forward a possible mechanism of the vortex phase transitions in terms of dislocation proliferation. Within this theory, it is possible to *derive* the phenomenologically successful Lindemann criteria, and we can make predictions regarding dynamic phenomena related to plastic creep, i.e., the motion of pinned dislocations in the presence of a driving current.

Finally in chapter 5, we studied a different melting mechanism that is effective in samples with a low concentration of *columnar pins* and is based on a delocalization of vortex lines from columnar pins by other vortex lines competing for the same columnar pin.

I want to conclude this part of the thesis giving an outlook and naming some of the important issues that are still unresolved regarding the vortex phase diagram. As far as thermal melting is concerned, a complete theoretical explanation of the “ice-like” first-order melting, i.e., the jump towards *increasing* magnetization or density at the first order melting transition [19] for a genuine vortex *line* lattice as in YBCO is still lacking. It is interesting to speculate to what extent this peculiarity might be connected to the fact that the vortex lattice is a line lattice in view of the results of Ref. [23] for layered superconductors. In comparison with known melting mechanisms of atomic solids, a systematic investigation of the possibility of surface melting of the vortex lattice is still missing. Regarding the vortex glass phases, the amorphous vortex glass phase, whose properties should be similar to the vortex glass phase originally proposed by Fisher, Fisher, and Huse [11] is still elusive. Starting from an elastic description of the FLL, this phase is inherently hard to describe due to the strong disorder, which allows for no obvious reference state to expand about. Closely connected is the question how many *thermodynamic* phases actually exist. The dislocation theory suggests that the amorphous vortex glass and the vortex liquid both have no positional order in the thermodynamic sense. Both phases only differ with respect to the dynamic properties of dislocations, which can be pinned and, thus, essentially immobile in the vortex glass phase at sufficiently low transport currents. However, it remains to be clarified whether orientational order is also lost in the amorphous vortex glass phase as in the vortex liquid or whether the orientational order is destroyed in a distinct transition at higher magnetic fields.

In the future, the field would certainly benefit from new types of *local* experiments. This development has begun in the last decade with the development of local magnetic field measurements using Hall probe arrays or magneto-optical techniques, which replaced simple bulk measurements and could elucidate the distribution of flux in the sample. One interesting possibility for the future would be the manipulation of *single* vortices, for example, using magnetic force microscopes, similar to single polymer manipulation techniques that have become available in chemical and biological physics over the past decade by atomic force microscopy techniques and will be discussed in the next part of this thesis. Another interesting route in this direction is provided by vortex lattices in Bose-Einstein condensates, which could be created only recently. These systems might also offer new possibilities of manipulation because the experimental length scales of vortices are more accessible to manipulation using optical techniques.

Regarding alternative applications of the vortex lattice dislocation theory, the vortex lattice with its tunable interactions and density can be used to test concepts for work-hardening, which is the very complex process of self-arrest in a crystal containing many dislocations and which is relevant for many materials science applications. Work-hardening can potentially stop dislocation motion and, in the FLL, eventually even vortex motion by effectively self-pinning the vortex lattice [119]. In the FLL dislocation core energies can be systematically tuned by changing interaction parameters and vortex density. Moreover, the sample geometry can be controlled, e.g., channel geometries can be fabricated in a controlled fashion [120]. This makes vortex matter an appealing laboratory system to develop a deeper theoretical and experimental understanding of the complex work-hardening process.

Part II

Filaments and Semiflexible Polymers

Chapter 7

Introduction

The previous part of this thesis has dealt with flux lines in type-II superconductors, which are governed by a line *tension* that is essentially due to the magnetic field energy. As a result, flux lines tend to align with the applied magnetic field. We call lines governed by such a tension *strings*. Whereas a line tension suppresses all local excursions from a straight configuration along a preferred direction, lines can also be governed by a *bending energy* which only penalizes local bending of the lines, regardless of an increase in length, see Fig. 7.1. We call lines governed by their bending energy *filaments*. Whereas the elastic material constant of strings is the line tension ε_l, the material constant of filaments is the bending rigidity κ [121]. Fluctuations of such filaments and cooperative phenomena displayed by fluctuating filaments will be the central subject of this part of the thesis.

Many polymers in chemical and biological physics are flexible and can be described as chains consisting of segments that can be freely rotated against each other. Such flexible polymers represent strings governed by an entropic tension, which tends to decrease the end-to-end distance to zero in order to maximize the number of possible chain conformations. Typical examples of flexible polymers are synthetic polymers with a carbon backbone, such as polyethylene, where the carbon-carbon bonds along the backbone can be easily rotated against each other. By now, there is a rather complete theoretical description of flexible polymers [122, 123, 124], which includes both statics and dynamics, effects from self-avoidance, and the cooperative behavior of flexible polymers in solutions or gels.

Apart from flexible polymers, there is another important class of more rigid polymers, which are governed by their bending energy rather than their entropic tension over a wide range of length scales. Thus, these polymers are filaments or *semiflexible* polymers. The competition between thermal energy and bending energy sets a characteristic length scale

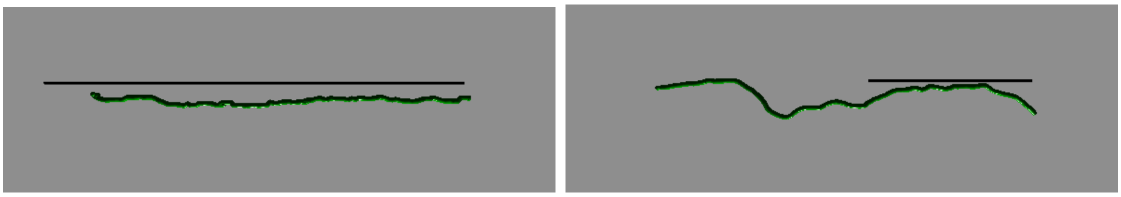

Figure 7.1: Monte Carlo simulation snapshots of a string governed by tension (left) and a filament governed by bending rigidity (right). The string has a preferred straight configuration, which is represented by the black bar. The filament exhibits larger excursions and appears straight over one persistence length L_p, see eq. (7.2), which is indicated by the black bar.

for semiflexible polymers, the *persistence length*[1]

$$L_p \equiv \frac{2\kappa}{T}. \tag{7.2}$$

The persistence length can also be characterized as the length scale above which tangent-tangent correlations decay exponentially, see eq. (7.5) below. On length scales larger than L_p, semiflexible polymers behave much like flexible polymers with a segment size of the order of L_p, i.e., the polymer decays into effectively independent segments of size L_p. In the limit of infinite persistence length it approaches a rigid rod, deformations of which are described by classical mechanics [121]. Semiflexible polymer models can thus describe various types of polymers ranging from flexible chains, which are recovered in the limit of small persistence length L_p, to rigid rods, which are obtained in the limit of large L_p. As compared to these to well-studied limits, new and interesting polymer physics emerges if the persistence length L_p is comparable to the contour length or the correlation length of the polymer. In this regime, neither the bending energy nor the thermal fluctuations can be neglected and semiflexible polymers exhibit distinct new properties, on which we want to focus in this thesis.

In biological and chemical physics one finds many examples of semiflexible polymers, some of which are shown in Fig. 7.2. Typically, these polymers are supramolecular assemblies with a relatively large diameter, i.e., they are much "thicker" than a flexible synthetic polymer with a carbon backbone. Such polymers are generically semiflexible because their large diameter leads to stronger entropic or enthalpic interactions along their backbones, which increases the bending rigidity. Often these thick supramolecular structures are the result of a rather complicated assembly process. Recent examples from chemical physics are provided by dendronized polymers [125], polyisocyanides (in particular,

---

[1] Alternative definitions of the persistence length can be found in the literature. Often a definition

$$\tilde{L}_p \equiv \frac{2}{d-1}\frac{\kappa}{T} \tag{7.1}$$

for a semiflexible polymer in d spatial dimensions is used, which includes the dimension-dependent factor and is motivated by the exponential decay of tangent correlations (7.5).

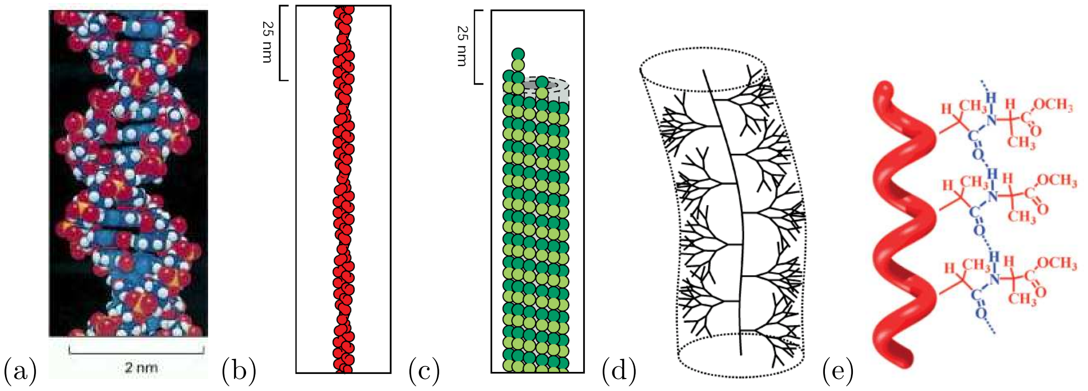

Figure 7.2: Examples of semiflexible polymers: a) DNA with a (mechanical) persistence length of $L_p = 2\kappa/T \simeq 100\text{nm} \simeq 320bp$ [135]. b) Actin filament with $L_p \simeq 34\mu\text{m}$ [132]. c) Microtubule with $L_p \sim$ mm [133] (Figs. a-c from Ref. [129]). d) Dendronized polymer [125]. e) Polyisocyanide with a persistence length $L_p \simeq 150\text{nm}$ [126].

polyisocanidepeptides [126]), and many supramolecular polymers [127], such as polyelectrolyte complexes [128]. Also cytoskeletal filaments, such as filamentous (F-) actin and microtubules, are supramolecular structures, which assemble spontaneously from globular protein monomers [129, 130, 131]. F-actin assembles from globular (G-) actin monomers, microtubules from tubulin monomers. These monomers bind by weak non-covalent bonds, typically each monomer binds by several hydrogen bonds. Therefore, cytoskeletal filaments can be viewed as "colloidal" polymers rather than genuine macromolecules (similar to the historic view of polymers as colloidal aggregates at the beginning of the 20th century). The persistence lengths of cytoskeletal filaments range from $30\mu\text{m}$ for F-actin [132, 133, 134] to the mm-range for microtubules [133] and becomes comparable to typical contour lengths of these polymers.

It is instructive to estimate the bending rigidity of large supramolecular filaments by modeling them in a simplified manner as an isotropic elastic rod made from an isotropic elastic material with Young's modulus E. For such rods, elasticity theory [121] gives a bending rigidity $\kappa = EI$, where I is the moment of inertia of the rod's cross section S_{cross}, $I \equiv \int_{S_{\text{cross}}} r^2 dS$, which is given by the surface integral over the square of the radius r. Therefore, $I \propto D^4$, where D is the filament diameter, and the persistence length $L_p \sim EI/T \propto D^4$ strongly increases with the filament diameter, i.e., thick filaments are much more rigid. For a filament diameter from 5 to 25nm and an elastic modulus $E \sim 1\,\text{GPa}$, persistence lengths $L_p \sim EI/T$ from 10 to $600\,\mu\text{m}$ are estimated. This simple model thus explains why thick filaments, such as microtubules with a diameter of 25 nm, are much stiffer than slender filaments like F-actin with a diameter of 8 nm. The elastic description works well for cytoskeletal filaments because they assemble from relatively large protein monomers. Globular (G-) actin, for example, has a molecular weight of 43kD.

Large supramolecular assemblies often form helices to optimize enthalpic interactions, which then also increases the rigidity. Filamentous actin, for example, assembles into a two-stranded helical structure. Another prominent example of a semiflexible helical polymer is DNA, which has a persistence length of 100nm [135]. The DNA helix forms as a result of the stacking interactions between planar nucleotide base pairs, which in turn arise from the hydrophobicity of the base pairs and electronic interactions. The helical structure allows base pairs to move closer and expel water from the space between bases. Both in F-actin and DNA the helical structure increases attractive interactions between monomers and increases the bending rigidity.

The bending rigidity of a polymer is also increased by repulsive electrostatic interactions between unscreened charges along the polymer backbone [136]. The simplest theory of electrostatic rigidity is due to Odijk, Skolnick, and Fixman [137, 138]. In the presence of charges the persistence length of a polyelectrolyte L_p^{PE} acquires an additional contribution from electrostatic interactions,

$$L_p^{PE} = L_p + L_{\mathrm{OSF}} = \frac{2\kappa}{T} + \frac{l_B}{2A^2 l_{DH}^2}, \tag{7.3}$$

where $l_B \equiv e^2/4\pi T\epsilon$ is the Bjerrum length, which denotes the distance at which two unit charges e in a dielectric medium with dielectric constant ϵ interact with the thermal energy T (T is the temperature in energy units). l_{DH} is the Debye-Hückel screening length, which is related to the salt concentration c_s by $l_{DH} = (8\pi q^2 l_B c_s)^{-1/2}$, where q is the valency of the screening salt ions. A is the distance between unit charges along the polymer backbone, i.e., $1/A$ is the charge density. The additional electrostatic contribution L_{OSF} to the persistence length leads to a stiffening of charged polymers at low salt concentrations. At physiological salt concentrations, the screening length is $l_{DH} \simeq$ 1nm so that we can usually neglect electrostatic interactions in modeling cytoskeletal filaments.

Typically, we are interested in fluctuations of semiflexible polymers on the scale of the persistence length such that molecular details are not relevant and a continuous description is justified. Moreover, many semiflexible polymers of interest, like F-actin, microtubules, or DNA, are inextensible to a good approximation. Then they can be modeled by the so-called *worm-like chain model* introduced by Kratky and Porod [139] to interpret X-ray scattering experiments on solutions of "filamentous" polymers ("Fadenmoleküle"), e.g., cellulose. Their worm-like chain model describes an inextensible continuous polymer governed by its bending energy

$$\mathcal{H}_{\mathrm{WLC}}[\mathbf{t}(s)] = \int_0^{L_c} ds \frac{\kappa}{2} (\partial_s \mathbf{t})^2. \tag{7.4}$$

Here, L_c is the contour length of the polymer, which is parameterized by its arc length s, and the polymer configuration is described by the unit tangent vectors $\mathbf{t}(s)$ so that $(\partial_s \mathbf{t})^2$ is the square of the local curvature. The statistical physics of the worm-like chain model is equivalent to the one-dimensional non-linear σ-model. Tangent correlations decay exponentially, and in d spatial dimensions one finds [139, 140, 141]

$$\langle \mathbf{t}(s) \cdot \mathbf{t}(s') \rangle = \exp\left(-(d-1) \frac{|s-s'|}{L_p} \right). \tag{7.5}$$

For $L_c \gg L_p$, the worm-like chain can then be described as an effective Gaussian chain with $N = L_c/L_p$ segments with Kuhn length $b = L_p$.

Beyond the inextensible, continuous worm-like chain model, more molecular details can be taken into account by considering discrete semiflexible harmonic chain models, which include the discrete molecular structure and the extensibility of molecular bonds. This is described in more detail in chapter 9. *Internal* interaction potentials, above all the excluded volume interaction between different parts of the chain, are neglected in the worm-like chain model. This approximation can be justified as long as the bending rigidity is sufficiently large such that the persistence length L_p is of the same order as the contour length L_c of the polymer. Then the bending energy is effectively preventing intrapolymer contacts.

With respect to an understanding of cooperative behavior of semiflexible polymers, i.e., association or ordering phase transitions, the coupling to *external* adsorption or interaction potentials represents a technical problem within the framework of the worm-like chain model because chain conformations are defined in the space of tangent vectors rather than positions of the polymers, whereas external potentials are a function of the local polymer segment positions. The position of the chain at arc length s can only be obtained by integration $\mathbf{r}(s) - \mathbf{r}(0) = \int_0^s d\tilde{s}\mathbf{t}(\tilde{s})$. On the other hand, for many important problems, such as the adsorption to an attractive planar surface, the binding to other polymers, or the confinement in channel-like geometries, the external potential gives rise to a preferred orientation and a straightening of the semiflexible polymer. Therefore, it is advantageous to parameterize semiflexible polymers in external potentials in a different manner, using the so-called Monge parameterization, which parameterizes contours explicitly in position space. The Monge parameterization is widely used for the description of fluctuating two-dimensional fluid membranes and has also been applied for the description of flux lines in the previous part of the thesis. The Monge parameterization is appropriate if the semiflexible polymer is only weakly bent, i.e., its persistence length is much larger than its contour length or the relevant correlation lengths along the polymer. Then the semiflexible polymer is oriented along a particular direction, say the x-direction, without overhangs, and it can be parameterized by the $d_\perp = d - 1$ dimensional displacement field $\mathbf{z}(x)$ perpendicular to the preferred x-direction. The Hamiltonian of a free semiflexible polymer in the Monge parameterization becomes

$$\mathcal{H}[\mathbf{z}(x)] = \int_0^L dx \left\{ \frac{\kappa}{2} (\partial_x^2 \mathbf{z})^2 \right\} \ , \tag{7.6}$$

where L is the projected length of the polymer in x-direction and where we neglected corrections of fourth and higher order in the displacement field, which can be justified for sufficiently small displacement gradients. In the remaining chapters we will often use this parameterization to describe semiflexible polymers subject to external potentials.

During the past decade single-molecule techniques, such as atomic force microscopy (AFM) [142], optical [143] and magnetic tweezers [144], have become available which allow to measure mechanical properties of *individual* molecules and polymers. These techniques give a force resolution in the pN-range and a spatial resolution in the nm-regime. Experiments on individual molecules allow to measure distribution functions of observables independent of the spatial averaging, which is always present in usual bulk measurements.

Other observables are not directly accessible in a bulk measurement, for example, the extension of a single polymer chain can only be deduced indirectly from scattering experiments in the bulk. Single-molecule techniques are also most suited to study dynamical fluctuations of individual molecules in or out of equilibrium. For example, they can access intermediate states and follow time-dependent pathways of chemical reactions that are difficult or even impossible to observe in an ensemble where they are hard to synchronize. Applied to polymers, these techniques permit quantitative experimental studies of single polymer deformations and, thus, provide the basis for a quantitative understanding of the mechanical properties of more complex polymer assemblies, such as polymer solutions, gels, or the cytoskeleton of a living cell.

A quantitative analysis of single polymer experiments requires theoretical models to extract the polymer properties. One prominent example are the first measurements of force-extension relations of single polymers such as DNA by stretching with magnetic beads [144, 145], which could only be properly interpreted based on theoretical results for the force-extension relation of the worm-like chain model [146]. Using the appropriate model, the persistence length of an individual DNA chain can be inferred from the single molecule experiment. In chapter 9, we present a theoretical model for stretching experiments on individual semiflexible polymers which goes beyond the inextensible and continuous worm-like chain model and takes into account effects from a discrete chain structure, extensibility effects, and finite size effects. Within this thesis, we also provide a theoretical description for a number of other manipulation experiments of single semiflexible polymers in chapters 8, 11, and 12. In general, semiflexible polymers are particularly suited for single polymer manipulation because they are typically "thicker" than flexible polymers, as explained above.

In chapter 8, we focus on cytoskeletal F-actin, which is manipulated by *confinement* to a microfluidic channel. Confinement effects are the most basic manipulation experiment and play an important role for fluctuating elastic manifolds throughout biological, soft matter, and condensed matter physics. The confinement of the filament in a channel gives rise to an entropy cost, and thus a confinement free energy or steric repulsion between filament and wall. Confinement has also important consequences for dynamic properties of semiflexible polymers as it gives rise to reptation dynamics [123]. It is relevant from the biological point of view because of crowding effects within the cytoplasm. Moreover, F-actin filaments in the living cell are confined within the filament meshwork in the cell cortex. In chapter 8, we focus specifically on the effects of confinement on the tangent correlations (7.5).

Similarly to an ideal gas that is confined to a container and therefore exerts pressure onto the confining walls, also confined polymers exert entropic forces onto the confining walls. Such entropic interactions have been studied first for flexible polymers [147, 148, 122, 123], which are governed by entropic tension, and are also well-known in the context of condensed matter theory for strings governed by tension since the seminal work of Prokovski and Talapov on incommensurate two-dimensional crystals [149]. They also play an important role for flux line lattices in confined geometries. For a two-dimensional flux line lattice in a planar superconductor with parallel magnetic field and point disorder, for example, the entropic interactions lead to a stabilization of the vortex glass phase at all temperatures

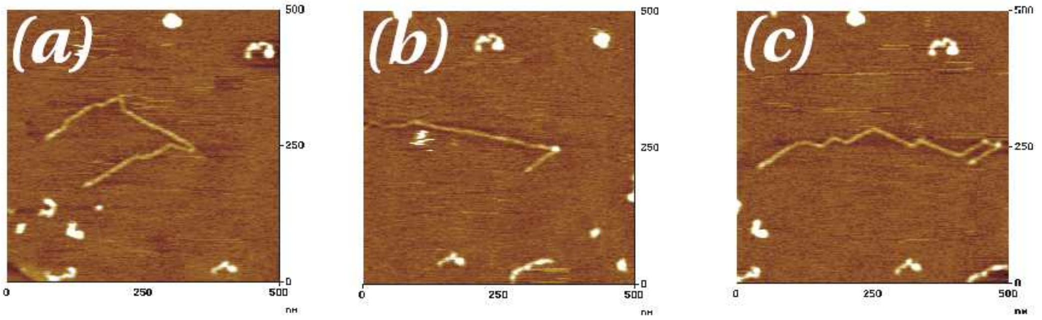

Figure 7.3: a) A single DNA molecule adsorbed on a chemically structured graphite surface. b) The DNA molecule after pulling it to the right using an AFM tip. Relaxation of the DNA molecule leads to kink-like configurations of the polymer as shown in c). [Figures with permission of N. Severin, Humboldt University, Berlin]

[150, 151]. For objects governed by bending energy, entropic interactions have been considered for the first time by Helfrich [152, 153] as "undulation forces" for fluid two-dimensional membranes. The concept of entropic or undulation forces has its limitations as can be seen in systematic treatments of *unbinding transitions* of interacting two-dimensional fluid membranes [154, 155, 156]. This unbinding transition arises from the interplay of attractive direct microscopic forces, such as van der Waals or screened electrostatic forces, and repulsive undulation forces and has been observed experimentally, e.g., for lipid bilayers in Refs. [157, 158]. For short-ranged attractive interactions decaying faster than the entropic repulsion a direct superposition of microscopic and undulation forces fails [154, 159]. Such a direct superposition neglects fluctuation effects, similar to a mean-field treatment, and suggests a first order unbinding transition, whereas a systematic study based on renormalization group techniques reveals a continuous transition with characteristic critical exponents [154].

Also the unbinding of interacting semiflexible polymers, which we discuss in detail in chapter 10, arises from the competition of the repulsive entropic forces and direct attractive interactions. Analogously to fluid membranes, the mean-field-like superposition of direct and entropic interactions gives a first order transition for short-ranged attractive potentials decaying faster than $1/|\mathbf{z}|^{2/3}$ for large separations $|\mathbf{z}|$ of the interacting semiflexible polymers. In contrast, the systematic transfer matrix treatment presented in chapter 10, reveals how the order of the unbinding transition depends on the dimensionality of the embedding space *and* the orientation of the interacting semiflexible polymers.

Novel types of single molecule manipulation experiments become possible with *adsorbed* semiflexible polymers because both visualization and manipulation are easier for adsorbed polymers [160]. In this thesis, two such single polymer manipulation techniques for adsorbed semiflexible polymers are treated in detail, the force-induced desorption in chapter 11 and the forced sliding over the adhesive substrate in chapter 12. The basis for an understanding of these manipulation experiments is provided in chapter 10, where a theoretical description

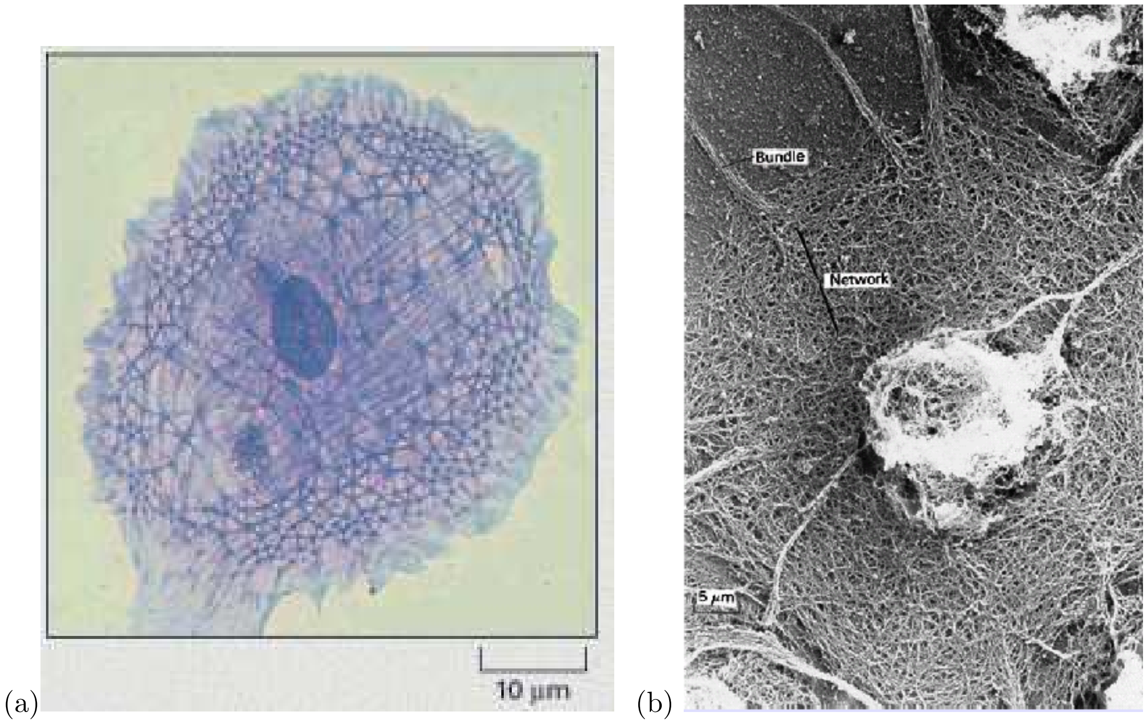

Figure 7.4: a) Filament structures in the cytoskeleton of a cell stained for proteins [129]. b) Typical filament morphologies in the cytoskeleton are networks and bundles [130].

of the adsorption transition of a single semiflexible polymer to an adhesive substrate with a short-range attraction is given. Force-induced desorption has been realized experimentally by attaching single polymers to AFM tips, which allows to measure the force exerted by the polymer as a function of the distance from the adsorbing substrate [161]. The force-induced desorption is similar to another type of single molecule manipulation experiment, the unzipping of two semiflexible polymers. Unzipping of polymers has first been studied for the unzipping of the two rather flexible strands of DNA [162] but has recently also been realized for much stiffer protein fibers [163]. Single polymers or other molecules on surfaces can be imaged using scanning tunneling microscopy (STM) [164] on metal or semiconductor surfaces or atomic force microscopy (AFM) [142]. But these techniques not only permit imaging on the surface but the microscopy tips can also be used to manipulate and position individual molecules [165] or individual semiflexible polymers such as DNA [166] on the substrate. In addition, the adsorbing substrate can be modified chemically or lithographically to present a patterned surface structure to the adsorbing polymer [128, 166], which typically leads to contrasts in adsorption strength. The spatial extension of these regular structures ranges from the micrometer scale down to nanometers. The manipulation of a single DNA molecule with an AFM tip on a chemically structured graphite surface [166] is demonstrated in Fig. 7.3.

There has been intense experimental and theoretical interest in semiflexible polymers from biological physics because cytoskeletal filaments such as F-actin, intermediate filaments, and microtubules are the main structural elements of biological cells and determine many of their mechanical and motile properties. F-actin is one of the most abundant proteins in eukaryotic cells and forms the cortex of the cytoskeleton, whereas microtubules provide the actual skeleton of the cell [129]. The microtubule network plays important roles in the internal organization of the cell, in cell locomotion, morphogenesis, and cell division. Actin filaments are versatile building blocks of the cytoskeleton, which can arrange into various different architectures such as bundles or meshworks, depending on the filament density and the concentration of actin crosslinking molecules in the surrounding liquid. The cytoskeleton of a living cell is no "passive" equilibrated structure but constantly remodeling by polymerization and depolymerization of filaments. This is a non-equilibrium process that requires hydrolysis of ATP or GTP and can be used by the cell to generate forces, e.g., for locomotion. Also small forces generated by motor proteins organize and rearrange cytoskeletal filaments and give rise to active, non-equilibrium filament dynamics, which plays an important role for cell division, motility, and force generation [131].

Structure formation by filament assemblies, either in thermal equilibrium or coupled to active processes, is one central subject of the present thesis, which will be treated in detail for two systems, filament bundles and motility assays, in chapters 10, 13, and 14. Both of these model systems are relevant for important *in vivo* processes but at the same time accessible to controlled experimental *in vitro* studies. In chapter 13, the formation of crosslinked filament bundles, which represent one important structural element of the cytoskeleton, is studied in thermal equilibrium. In chapter 14, we consider *in vitro* motility assays, in which filaments are bound to a substrate by immobilized motor proteins, which actively pull the filaments along the surface. We use motility assays to study the structure formation of interacting filaments as they are pulled by molecular motors. This provides a first step towards a theoretical understanding of motor-driven structure formation in the cytoskeleton of the living cell.

Filaments in the cytoskeleton are arranged into a variety of network-like structures. F-actin forms the cortex of the cell, where it typically occurs in two types of morphologies, dense filament meshworks or bundle-like structures, see Fig. 7.4. Bundles of actin filaments are an important structural motif which occurs, e.g., in cell protrusions (filopodia), stress fibers, or muscles. Actin filaments in the cell perform relatively large thermal fluctuations as they have persistence lengths around 30μm [132] of the same order as their typical contour lengths. Therefore, crosslinking proteins stabilize such bundles against thermal fluctuations. For a living cell, it is important to possess a flexible assembly mechanism for structural elements such as bundles. This is achieved by a relatively weak crosslinker-filament binding, which typically involves several hydrogen bonds. As will be demonstrated in chapter 13, this mechanism of a filament attraction mediated by weakly binding crosslinkers fulfills two biological functions. Firstly, it allows for a *reversible* bundle formation, i.e., bundling and unbundling and, secondly, both processes can be regulated easily by the crosslinker concentration in the surrounding solution. Experimentally, bundle formation can be studied in a more controlled way *in vitro* using F-actin solutions containing crosslinking proteins

[167, 168, 169]. Bundle formation in biological or biomimetic systems is an example of a cooperative assembly process, which gives rise to structure formation. Structure formation processes are a domain of statistical physics and the bundle formation can be successfully described as an equilibrium phase transition. An immediate consequence of this concept is that new mechanical properties can emerge in the bundled phase. One example is the bundle stiffness, which can be tuned by the number of filaments that are joined in a bundle and the filament interactions, which demonstrates that the assembly becomes more than the sum of its parts.

In order to understand the formation of such bundles using methods from statistical physics, we start in chapter 10 from a theoretical description of the conceptually simplest bundling transition, which is the binding of two semiflexible polymers in the presence of a short-range attractive potential. This binding transition is closely related to the adsorption transition of a single semiflexible polymer. As it turns out, this phase transition still allows for an analytical solution using transfer matrix techniques and, thus, for a complete classification of critical exponents and universality classes as well as a closed expression for the scaling functions governing the filament segment distribution. In particular, we find that the bundling of filaments is a discontinuous transition in three spatial dimensions, which is markedly different from the corresponding continuous binding transition of strings or flexible polymers in three dimensions. Building on these results for the bundling of two filaments, we address the more complicated assembly processes involved in the bundling of N filaments in the presence of attractive filament interactions mediated by adhesive crosslinkers in chapter 13. Using a combination of Monte Carlo simulations and analytical arguments based on the binding of two sub-bundles, we study filament bundles containing up to $N = 20$ filaments and find that such bundles form in a single discontinuous phase transition. Depending on the initial conditions of the bundling process, the bundling transition can be kinetically trapped resulting in the segregation of smaller sub-bundles for strong filament attractions. This rich scenario of structure formation is in agreement with experimental observations on F-actin solutions containing crosslinking proteins [167, 168, 169].

Structure formation in the living cell cannot rely exclusively on equilibrium processes. One way of dynamically restructuring the cytoskeleton is via active processes such as ATP- or GTP-driven polymerization and depolymerization of filaments, which gives rise to a constant turnover of monomers within each filament, the so-called “treadmilling”. Another active ATP-driven process is the rearrangement of filaments by molecular motors, which is an important dynamical process involved, e.g., in cell division. The resulting non-equilibrium dynamics driven by such active processes is a new paradigm in polymer physics, which leads to new dynamic phenomena such as pattern formation. This has been demonstrated in a number of recent experiments on “active polymer gels”, i.e., filament solutions containing multi-headed motors [170, 171, 172, 173], where the formation of dynamic patterns such as asters or vortices have been observed. Theoretical studies of such patterns [174, 175, 176, 177, 178, 179] have used a coarse-grained continuum description with kinetic equations for filament density and orientation fields and a motor density field. In these approaches it is inherently difficult to relate the macroscopic transport coefficients of such descriptions to the experimentally accessible microscopic parameters of the system.

Therefore, it is desirable to have biomimetic model systems, where the underlying principles of this new type of non-equilibrium polymer dynamics can be studied both experimentally and theoretically in more detail. One such system are motility or gliding assays, where motor proteins are immobilized on a solid substrate [180] and which will be the topic of chapter 14. The immobilized molecular motors bind filaments and actively pull them over the substrate. In these systems filaments are essentially confined to two dimensions by their binding to motor proteins and the areal motor density on the substrate becomes a quenched degree of freedom because motors are adsorbed and immobilized. These two simplifications allow for a complete description of the stochastic motion of single, non-interacting filaments, which has been studied theoretically for the first time in Ref. [181]. In a gliding assay with many rod-like filaments interacting by a hard-core potential, the filaments can undergo a phase transition from an isotropic to a nematic phase upon increasing the filament density. In the absence of motor activity, this phase transition is the well-known Onsager transition of a two-dimensional hard-rod fluid. Building on the description of the active dynamics of a single filament we can apply concepts from liquid crystal theory to study the cooperative behavior of many filaments and find an extension of the equilibrium Onsager theory to the actively driven non-equilibrium system. This theory predicts that nematic ordering can be induced by increasing the motor activity, i.e., increasing the density of immobilized motors, which is confirmed by Langevin dynamics simulations of the motility assay. Furthermore, we can make predictions about the locus of the isotropic-nematic transition in terms of the microscopic model parameters such as a function of the motor density. Such a nematic ordering is maybe the most simple pattern formation that an active filament system can exhibit and, thus, can serve as a model system for future studies of more complex active filament systems.

This part of the thesis is structured as follows. We start by studying fluctuations of single semiflexible polymers confined to microchannels in chapter 8, where we can perform a detailed comparison of analytical calculations, simulation results, and experiments, see Ref. [182]. Ref. [183] is the basis of the following chapter 9, where we discuss the detailed theoretical description of stretching experiments on semiflexible polymers, which includes effects from a discrete chain structure, extensibility effects, and finite size effects. In chapter 10, which is based on Refs. [184, 185], an analytical treatment of the unbinding transition of two semiflexible polymers and the adsorption transition of a single semiflexible polymer is presented using transfer matrix methods. In these transitions polymers bind or adsorb against thermal fluctuations. In chapters 11 and 12, we focus on the manipulation of single adsorbed filaments by external forces. In chapter 11, based on Ref. [186], the force-induced desorption or the unzipping by a localized external force is considered, i.e., the combined effect of thermal fluctuations *and* an external point force on the adsorption transition. In chapter 12, which is based on Refs. [187, 188, 189], the thermally activated dynamics of a semiflexible polymer that is adsorbed on a *structured* substrate and pushed by an external force is discussed. We consider diffusional relaxation, a homogeneous driving force, and point driving forces. In the final chapters 13 and 14, we move from single filaments to filament assemblies and focus on their cooperative behavior. In chapter 13, which is based on Ref. [190], the unbundling transition of a bundle containing N filaments is studied analytically and by Monte-Carlo simulations. In chapter 14, based on Ref. [191], we consider the active filament dynamics in a motility assay, where we find the generalization of the two-dimensional Onsager isotropic-nematic transition to the actively driven system.

Chapter 8

Confined Filaments

We study thermal fluctuations of individual semiflexible polymers or filaments, which are confined to translationally invariant channels. Tangent correlations of confined filaments depend both on their bending rigidity and the channel geometry. The tangent correlation function is calculated both analytically using the concept of undulation forces and by Monte Carlo simulations. Long filaments confined to channels exhibit enhanced tangent correlations. The tangent correlation function shows a characteristic minimum, which is governed by the deflection length. The theoretical results are used to experimentally determine persistence and deflection lengths of actin filaments, which are confined to microchannels and studied by fluorescence microscopy. This is achieved by including corrections for finite size and image analysis effects into the theoretical result for the tangent correlation function.

8.1 Introduction

Filamentous (F-) actin is one of the most important building blocks of the cytoskeleton of eukaryotic cells [129]. The cortex of the cytoskeleton consists of a dense meshwork of F-actin with a typical meshsize of the order of micrometers [134]. F-actin filaments in the cytoskeleton are strongly confined within this meshwork. Furthermore, various other macromolecules, predominantly proteins, are contained in the cytoplasm. This typically leads to *crowding* and, thus, confinement of polymers within the cell body [192].

Confinement has important consequences both for static and dynamic properties of semiflexible polymers and is often pre-requisite for experimental investigations by optical microscopy. Fluorescence microscopy studies of F-actin have to be performed on single filaments confined to a two-dimensional plane [132]. The reptation dynamics of a single actin filament confined in the meshwork of an actin solution has been visualized in Ref. [134] for the first time. Recently, also the confinement and imaging of DNA in channels with widths in the nm regime has been achieved [193, 194].

In the following, we consider a semiflexible polymer that is confined between two rigid and planar walls. The effect of such a transverse confinement on a thermally fluctuating object like a semiflexible polymer gives rise to an increase of its free energy due to the entropy cost of collisions with the confining walls. This free energy of confinement can also be interpreted as a steric repulsion between the confining walls and the polymer. For objects governed by bending energy, entropic interactions have been considered for the first time by Helfrich [152, 153] as "undulation forces" for fluid two-dimensional membranes but the concept of entropic forces is much older. Entropic interactions are well-known for an ideal gas that is confined to a container and exerts pressure on the container walls and for confined flexible polymers [147, 148, 122, 123], which are governed by entropic tension. For strings governed by tension, entropic interactions are well-known since the seminal work of Prokovski and Talapov on incommensurate two-dimensional crystals [149], and they also play an important role for flux line lattices in confined geometries. For a two-dimensional flux line lattice in a planar superconductor with parallel magnetic field and point disorder, the entropic interactions lead to a stabilization of the vortex glass phase at *all* temperatures [150, 151]. Moreover, entropic interactions are relevant in the dislocation theory of vortex lattice melting presented in chapter 4, where the steric repulsion stabilizes the dislocation ensemble at high densities. Recently, Zaanen applied Helfrich's theory of entropic interactions also to quantum stripe excitations [195], as they are found in strongly correlated cuprate systems [196], to show that a gas of quantum stripes always solidifies due to the entropic repulsion.

For semiflexible polymers confinement effects have been considered first in the context of nematic ordering in semiflexible polymer liquid crystals [197, 198]. Odijk introduced the important concept of a *deflection length* along the semiflexible polymer. On scales larger than the deflection length fluctuations are affected by the confined geometry [199]. Helfrich applied the concept of undulation forces, which corresponds to replacing the confining potential by a parabolic confining potential, also to confined semiflexible polymers or tubular vesicles [200]. Odijk showed that results for confinement free energies based on the liquid crystal approaches and the undulation force approach are essentially equivalent [201]. A semiflexible polymer in a confining parabolic potential has been treated by a transfer matrix approach in Ref. [202].

In recent years much theoretical effort was directed towards an exact determination of the free energy of confinement for various geometries and semiflexible chain variants, see Refs. [203, 204, 205, 206, 207]. Whereas it is not easily possible to obtain such free energies experimentally, we focus in this chapter on conformational fluctuations, which are measured by fluorescence microscopy of suitably confined, fluctuating filaments. Such a biomimetic model system is ideal to explore the physical concepts of confined semiflexible polymers, both experimentally and theoretically. We calculate analytically the tangent correlation function of a confined semiflexible polymer employing Helfrich's undulation force concept. The results are compared to Monte Carlo (MC) simulations for a worm-like chain in a quasi two-dimensional rectangular channel, similar to the experimental system. We find that the simulation data agrees well with the analytical results. Then the theoretical results are used to determine persistence and deflection length from experimental fluorescence microscopy image data by including corrections for finite size and image analysis effects.

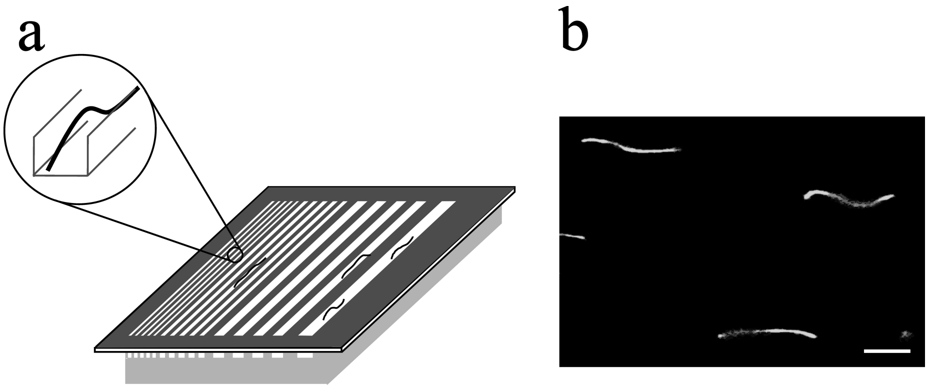

Figure 8.1: Experimental Setup. a) Sketch of the microchannel chamber with different channel widths, actin filaments are fluctuating in rectangular channels. b) Fluorescence micrograph (10 μm scale bar). [Figure with permission of S. Köster, Max Planck Institute for Dynamics and Self-Organization, Göttingen]

8.2 Experimental methods

The experimental setup has been described in detail in Ref. [208]. An array of microchannels is fabricated by soft lithography with channel widths ranging from $\ell \simeq 1.5\mu$m to $\ell \simeq 10\mu$m and a channel height $\ell_z \simeq 1.4\mu$m, see Fig. 8.1. To avoid sticking of actin filaments to the channel walls, the channel surfaces were coated with BSA (bovine serum albumin). Phalloidin-stabilized and fluorescently labeled actin filaments are brought into microchannels with rectangular cross sections as schematically shown in Fig. 8.1. Contour fluctuations are observed by fluorescence microscopy. The details of the image analysis are described below.

8.3 Model

For the theoretical description, we consider a semiflexible polymer in three spatial dimensions in a channel with rectangular cross-section as shown schematically in Fig. 8.2. The channel is translationally invariant along the x-axis. Using the worm-like chain model and parameterizing the polymer with contour length L_c by arc length $0 < s < L_c$ and unit tangent vectors $\mathbf{t}(s)$, the Hamiltonian is given by the sum of bending and potential energy,

$$\mathcal{H}_{WLC}[\mathbf{t}(s)] = \int_0^{L_c} ds \left[\frac{\kappa}{2} (\partial_s \mathbf{t})^2 + V_{ch}(\mathbf{r}(s)) \right] . \tag{8.1}$$

Here, $\mathbf{r}(s) = \int_0^s d\tilde{s} \mathbf{t}(\tilde{s})$ is the three-dimensional position vector of the chain at arc length s. The purely repulsive confining potential $V_{ch}(\mathbf{r})$ from the translationally invariant channel

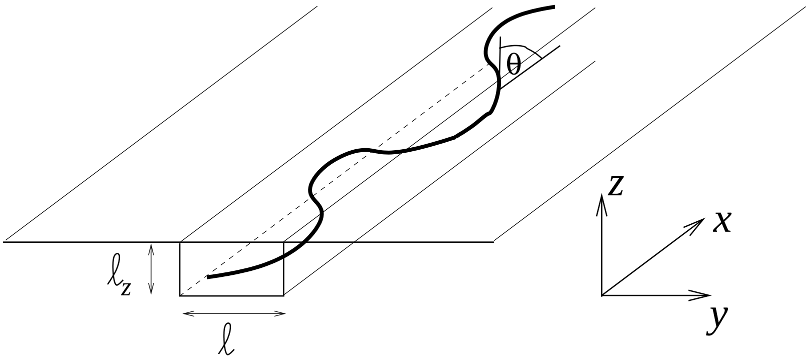

Figure 8.2: Semiflexible polymer confined to a rectangular channel. The channel width is ℓ, the channel height is ℓ_z. θ is the angle between the two-dimensional projection of the tangent vector into the xy-plane and the x-direction.

walls only depends on the last two components of $\mathbf{r} = (x, y, z)$,

$$V_{ch}(\mathbf{r}) = V_\ell(y) + V_{\ell_z}(z) \quad \text{with} \quad V_\ell(y) \equiv \begin{cases} 0 & \text{for } |y| < \ell/2 \\ \infty & \text{else} \end{cases} . \tag{8.2}$$

We focus on the regime where the confinement is sufficiently strong and the bending rigidity or persistence length is sufficiently large that U-turns of the polymer within the channel are suppressed. Then the semiflexible polymer is oriented along the x-axis and can be parameterized by two-dimensional displacements $\mathbf{z}(x) = (y(x), z(x))$ perpendicular to the x-axis with $0 < x < L$, where L is the projected length of polymer. In this Monge parameterization, the effective Hamiltonian of the semiflexible polymer is given by

$$\mathcal{H}[\mathbf{z}(x)] = \int_0^L dx \left[\frac{\kappa}{2}\left(\partial_x^2 \mathbf{z}\right)^2 + V_\ell(y(x)) + V_{\ell_z}(z(x))\right] \tag{8.3}$$

with the confining channel potentials V_ℓ as defined in eq. (8.2). In (8.3) we neglected terms of fourth or higher order in derivatives of $\mathbf{z}$, which is justified for small gradients $\langle(\partial_x \mathbf{z})^2\rangle$. Then, also the difference between arc and projected length is small, $s(x) \approx x$. We focus on the limit $\ell_z \ll \ell$ of a quasi two-dimensional system, which is the typical situation in the experimental realization, where values for ℓ/ℓ_z range from approximately 1 to 10. In the experiment fluorescent microscopy allows to image the two-dimensional projection $(x, y(x))$ such that we consider only fluctuation of the single component $y(x)$ governed by the confining channel potential $V_\ell(y)$ in the following.

8.4 Tangent correlations

The deflection length λ is defined as the length scale where the channel boundaries start to influence tangent correlation functions [199]. In the absence of the confining potential

$V_\ell(y)$ in (8.3) the fluctuations are given by $\langle y^2\rangle \sim L^3/L_p$ where $L_p = 2\kappa/T$ is the *persistence length*[1] (T is the temperature in energy units). The condition $\langle y^2\rangle \sim \ell^2$ defines the *deflection length* [199]

$$\lambda \sim \ell^{2/3} L_p^{1/3}. \tag{8.4}$$

Typical displacement gradients are of the order of $\langle(\partial_x y)^2\rangle \sim \lambda/L_p \sim (d/L_p)^{2/3}$ and, thus, the Hamiltonian (8.3) is applicable for narrow channels $\ell \ll L_p$ – regardless of the length L of the semiflexible polymer. Using the deflection length concept the free energy cost ΔF_w of confining polymer configurations in the y-coordinate can be estimated by assuming that each collision with the confining walls costs entropy of the order of k_B, or free energy of the order of T (temperature in energy units), which leads to $\Delta F_w \sim L/\lambda$.

Although it predicts the correct free energy of confinement, the scaling argument for the deflection length is slightly misleading because it is based on a simplified collision picture, which suggests that there is exactly one collision per deflection length and that the probability of contact with the wall $\mathcal{P}_w$ decays as $\mathcal{P}_w \sim 1/\lambda \sim \ell^{-2/3}$, which is, however, not correct [209, 210]. For a semiflexible polymer in two dimensions, which is confined to a half-plane by a single wall, an exact transfer matrix treatment shows that the contact probability $\mathcal{P}_w \sim \lambda^{-\chi_r}$ is given by a characteristic exponent $\chi_r = 5/2$ [211], which is larger than one, i.e., not every correlated segment of length λ undergoes a collision with the wall.

In principle, also the Hamiltonian (8.3) can be studied starting from a differential transfer matrix equation for the restricted partition sum, see Ref. [204] [similar to what we will use in chapter 10 for attractive external potentials, cf. eq. (10.4)]. In a transfer matrix treatment, we expect a discrete set of eigenstates of the corresponding stationary transfer matrix equation for exponentially decaying solutions $Z \sim \exp(-E_n L/T)$ with a corresponding energy eigenvalue E_n. Then the free energy of confinement is given by the ground state $\Delta F_w = E_0 L$ and the deflection length λ is given by the correlation length, i.e., by the difference $\lambda = T/(E_1 - E_0)$. We expect the value of the ground state to show the same parameter dependence as higher levels, $E_0 = \mathrm{const} E_1$, which confirms the scaling relation $\Delta F_w \sim T/\lambda$.

The transfer matrix approach and the above scaling arguments also suggest that gradient-correlations for the Hamiltonian (8.3) in the two-dimensional xy-plane fulfill a scaling relation

$$C_{2D}(x,x') \equiv \langle(\partial_x y(x) - \partial_x y(x'))^2\rangle = \frac{\lambda}{L_p}\mathcal{C}\left(\frac{|x-x'|}{\lambda}\right) \tag{8.5}$$

in the limit of large $L \gg \lambda$. The scaling function $\mathcal{C}(x)$ has to approach $\mathcal{C}(x) \approx 2x$ in the limit of small x corresponding to the limit of a free semiflexible polymer in two dimensions where $\langle(\partial_x y(x) - \partial y(x'))^2\rangle = 2|x-x'|/L_p$. For large x, we must have $\mathcal{C}(x) \approx 2c_{ms}$, where the constant c_{ms} gives the thermal mean-square fluctuations $\langle(\partial_x y(x))^2\rangle = c_{ms}\lambda/L_p$ of tangents. The scaling (8.5) also gives rise to a corresponding relation for the two-dimensional tangent correlations

$$T_{2D}(s,s') \equiv \langle\cos(\theta(s) - \theta(s'))\rangle \approx 1 - \frac{1}{2}C_{2D}(s,s') \tag{8.6}$$

---

[1] Note that this definition differs by a factor of 2 from the definition used in Ref. [208], where we used κ/T as persistence length, cf. eq. (7.1).

where $\theta(s)$ is the angle between the two-dimensional projection of the tangent vector $\mathbf{t}(s)$ into the xy-plane and the x-direction, $\theta(s) \approx \partial_x y(s)$.

In order to further quantify the scaling function we use the concept of undulation forces introduced by Helfrich [152, 153, 200], which is equivalent to assuming that the confining channel potential $V_\ell(y)$ can be approximated by a *parabolic* confining potential $V_p(y) \approx \frac{1}{2}Ky^2$. For the resulting quadratic Hamiltonian, we can calculate the gradient correlations in (8.5) analytically in Fourier space. In the limit of large L with periodic boundary conditions, we find $C_{2D}(x, x') = C_p(x - x')$ with

$$\begin{aligned} C_p(x) &= \int_{-\infty}^{\infty} \frac{dq}{2\pi} \frac{q^2 T}{\kappa q^4 + K} 2(1 - \cos(qx)) \\ &= \sqrt{2}\frac{\lambda_p}{L_p}\left[\cos\left(\frac{\pi}{4}\right) - \cos\left(\frac{\pi}{4} + \frac{|x|}{\lambda_p}\right)\exp\left(-\frac{|x|}{\lambda_p}\right)\right] \end{aligned} \tag{8.7}$$

and

$$\lambda_p \equiv \sqrt{2}\left(\frac{\kappa}{K}\right)^{1/4}. \tag{8.8}$$

Thus, for a parabolic confining potential $C_{2D}(x, x')$ obeys the above scaling form (8.5) with a scaling function

$$\mathcal{C}(x) = \mathcal{C}_p(x) \equiv \sqrt{2}\left[\cos(\pi/4) - \cos(\pi/4 + x)\, e^{-x}\right] = 1 - (\cos x - \sin x)e^{-x} \tag{8.9}$$

and $\lambda = \lambda_p$. The mean-square fluctuations are $\langle (\partial_x y(x))^2 \rangle = \lambda_p / 2L_p$, i.e., $c_{ms} = 1/2$.

The scaling function has a characteristic shape with a pronounced first local *minimum* at $x = \pi/2$ and further local extrema at $x = \pi/2 + n\pi$ with $n > 1$. The first minimum corresponds to a minimum in the tangent correlation function $\langle \cos(\theta(s) - \theta(s')) \rangle = 1 - \frac{1}{2}C_p((s - s')/\lambda_p)$ for segment distances comparable to the deflection length, $s - s' = \frac{\pi}{2}\lambda_p$. This reflects the first encounter with the confining potential resulting in the re-correlation of tangents. The minimum in the tangent correlations $\langle \cos(\theta(s) - \theta(s')) \rangle$ for $s - s' \sim \lambda$ is a very robust feature, which is present also in all experimental and Monte Carlo data for sufficiently long polymers in confining channel potentials V_ℓ with hard walls.

For the parabolic confining potential, it is also possible to systematically calculate finite size corrections for $C_{2D}(x, x')$, which become relevant whenever x or x' are within a distance comparable to λ of the polymer ends. In the experiments filaments are relatively short, $L \lesssim 30\mu\text{m}$, and finite size corrections due to end effects are often large if the whole polymer length is used for a tangent correlation analysis. The experimental situation corresponds to *free* filaments ends, i.e., boundary conditions $\partial_x^2 y(0) = \partial_x^2 y(L) = 0$ and $\partial_x^3 y(0) = \partial_x^3 y(L) = 0$ for the Hamiltonian $\mathcal{H}[y(x)] = \int_0^L dx[\frac{\kappa}{2}\left(\partial_x^2 y\right)^2 + V_p(y)]$. The normal modes for this Hamiltonian with free boundary conditions are given by the set of functions [212]

$$\begin{aligned} q_l(x) &\equiv \sqrt{\frac{2}{L}} \frac{\cosh(k_l L/2)\cos(k_l(x - L/2)) + \cos(k_l L/2)\cosh(k_l(x - L/2))}{(\cos^2(k_l L/2) + \cosh^2(k_l L/2))^{1/2}} \quad \text{for } l > 0 \text{ odd} \\ q_l(x) &\equiv \sqrt{\frac{2}{L}} \frac{\sinh(k_l L/2)\sin(k_l(x - L/2)) + \sin(k_l L/2)\sinh(k_l(x - L/2))}{(\sin^2(k_l L/2) + \sinh^2(k_l L/2))^{1/2}} \quad \text{for } l > 0 \text{ even} \end{aligned} \tag{8.10}$$

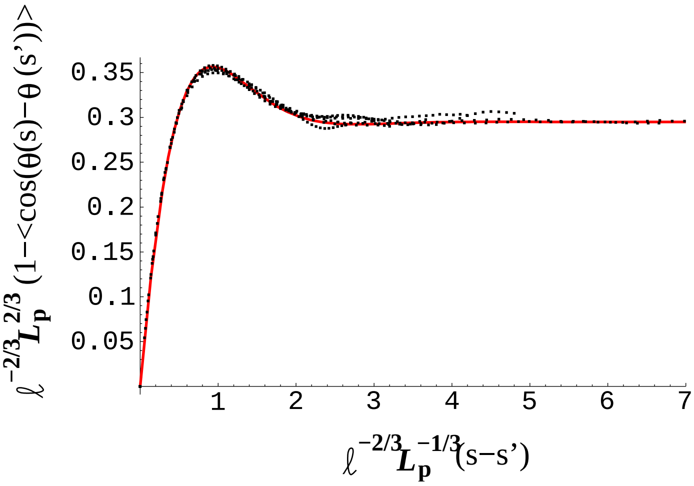

Figure 8.3: Collapse of the MC data for a two-dimensional worm-like chain in the confining channel potential $V_\ell(y)$. The rescaled tangent correlation function $\ell^{-2/3} L_p^{2/3}(1 - \langle\cos(\theta(s) - \theta(s'))\rangle)$ is plotted as a function of the rescaled arc length difference $\ell^{-2/3} L_p^{-1/3}(s - s')$. The plot contains MC data for long filaments with contour length $L_c = 100\mu$m and s and s' far away from the polymer ends. Persistence lengths are $L_p = 2\kappa/T = 40\mu$m and $L_p = 60\mu$m, and channel widths $\ell = 2.5, 5.0, 7.5, 10.0\mu$m. All data collapse on the red Master curve given by the scaling function $a\mathcal{C}_p(x/a)/2$, cf. eq. (8.9), with a numerical constant $a \simeq 0.59$.

where wave vectors k_l are determined by $\tanh(k_l L/2) = (+/-)\tan(k_l L/2)$ for l even/odd (the $l = 0$ modes are not needed in the following). The functions are orthonormal with $\int_0^L dx q_l(x) q_{l'}(x) = \delta_{ll'}$. Using these functions to introduce appropriate decoupled normal modes we find for the gradient correlation function the sum

$$C_{2D}(x, x') = \sum_{l>0} \frac{T}{\kappa k_l^4 + K}[\partial_x q_l(x)\partial_x q_l(x) + \partial_x q_l(x')\partial_x q_l(x') - 2\partial_x q_l(x)\partial_x q_l(x')], \qquad (8.11)$$

which can be evaluated only numerically.

8.5 Monte Carlo simulations

It is tempting to assume that the same scaling function (8.9) for a long filament in a parabolic confining potential can also be used to describe tangent correlations in the presence of the original confining channel potential $V_\ell(y)$. For this type of potential analytic calculations are not possible, therefore, we performed MC simulations to check this hypothesis.

The MC simulations were performed using the worm-like chain Hamiltonian (8.1) with a rectangular channel potential with $\ell_z \ll \ell$ such that the fluctuations are quasi-two-dimensional. The filament was discretized into 100 segments in the simulation. Parameters

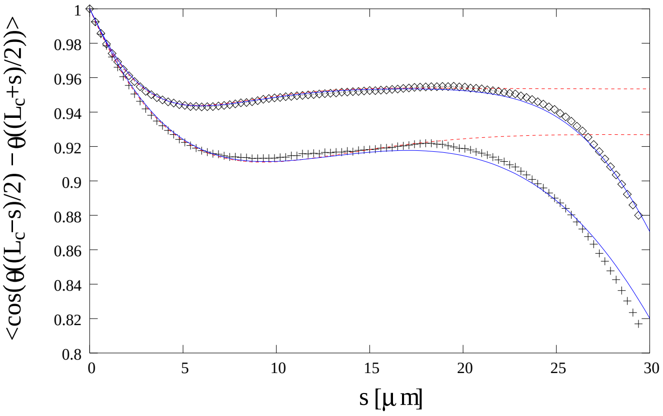

Figure 8.4: MC data for a two-dimensional worm-like chain of length $L_c = 30\mu$m and persistence length $L_p = 40\mu$m in a confining channel potential $V_\ell(y)$ with widths $\ell = 2.5$, μm ($\diamond$) and $\ell = 5.0$, μm ($+$). The tangent correlation function $\langle\cos(\theta((L_c - s)/2) - \theta((L_c + s)/2))\rangle$ is plotted as a function of the segment distance s. Blue lines are plots of $1 - \frac{1}{2}C_{2D}((L - s)/2), (L + s)/2)$ according to eq. (8.11) with $L = 32.5\mu$m for $\ell = 2.5$, μm and $L = 35.0\mu$m for $\ell = 5.0$, μm. The dashed red lines are plots of $1 - \frac{1}{2}C_p(s)$ according to eq. (8.7) for an infinitely long polymer.

were chosen comparable to the experiments in [208], i.e., a channel height of $\ell_z = 1.4\mu$m as in the experiment and channel widths up to $\ell = 10.0\mu$m. We simulated filaments with $L_p = 2\kappa/T = 40\mu$m comparable to F-actin and $L_p = 60\mu$m.

The MC results for the tangent correlation function $1 - T_{2D}(s, s') = 1 - \langle\cos(\theta(s) - \theta(s'))\rangle$ for a long filament with $L = 100\mu$m with s and s' far away form the polymer ends are shown in Fig. 8.3. The rescaled values $\ell^{-2/3}L_p^{2/3}(1 - T_{2D}(s, s'))$ as a function of the rescaled arc length difference $\ell^{-2/3}L_p^{-1/3}(s - s')$ collapse onto a master curve given by the scaling function $a\mathcal{C}_p(x/a)/2$ for a *parabolic* confining potential, cf. eq. (8.9), with a numerical constant $a \simeq 0.59$. This shows that the scaling function (8.9) for a parabolic confining potential $V_p(y)$ indeed agrees well with the scaling function for the rectangular channel with the hard wall potential $V_\ell(y)$. This is a remarkable finding because the undulation force concept is an *ad hoc* approximation. From the data collapse we find the result

$$\lambda \simeq 0.59\ell^{2/3}L_p^{1/3} \tag{8.12}$$

for the deflection length.

Next we consider finite size effects from the polymer ends. The MC results for the correlation function $T_{2D}((L_c - s)/2, (L_c + s)/2) = \langle\cos(\theta((L_c - s)/2) - \theta((L_c + s)/2))\rangle$ between two segments a distance $0 < s < L_c$ apart are shown in Fig. 8.4 for a polymer length $L_c = 30\mu$m and a persistence length $L_p = 40\mu$m. The finite size effects are substantial as comparison with the result $1 - \frac{1}{2}C_p(s)$ for an infinitely long polymer shows. The results can be fitted well using the formula (8.11) for a parabolic confining potential $V_p(y)$ if the polymer length L in (8.11) is chosen somewhat larger than the actual contour length. This effect is due to an increased mobility of free ends in the parabolic potential as compared to a channel with hard walls.

8.6 Data analysis and simulation

Our MC simulation results show that we can analyze experimental data for the tangent correlation function in a rectangular confining channel using the formulae (8.7) or (8.11) obtained via the undulation force approximation, i.e., for a parabolic confining potential. These formulae can be used to determine the persistence and deflection length of the filaments from the fluorescence microscopy images.

In the experiment the tangent correlations have to be extracted by image analysis from the fluorescence microscopy images. The image analysis techniques are similar to what has been used in Ref. [132]. The greyscale images are first transformed into a black-and-white image of a filament by applying a threshold criterion. The resulting image of a filament has a typical thickness of $1\mu m$ corresponding to the size of about 16 pixels. These images are reduced to a one-pixel skeleton by a contraction algorithm as it is described in Ref. [132]. The resulting one-pixel line is interpolated by a natural cubic spline and, finally, tangent vectors are reconstructed by constructing points with equal spacing of $\sim 0.3\mu m$ corresponding to the size of 5 pixels along the spline.

In order to improve the statistics it is advantageous to spatially average the tangent correlation along the polymer contour, i.e., to measure $\overline{\langle\cos(\theta(s))\rangle} \equiv \frac{1}{L_c-s}\int_0^{L_c-s} ds_0 \langle\cos(\theta(s_0+s)-\theta(s_0))\rangle$. For a long polymer, end effects can be neglected and the formula (8.7) should describe the data, $\overline{\langle\cos(\theta(s))\rangle} = 1-\frac{1}{2}C_p(s)$. The corresponding fit to the experimental data for three different channel widths is shown in Fig. 8.5 a,b,c (dashed lines), where we used a fixed persistence length $L_p = 2\kappa/T = 38\mu\text{m}$ and the deflection length λ as only fit parameter in (8.7).

These fits show deviations, which have three main reasons: (i) Finite size effects from the polymer ends, (ii) an effective averaging over small distances stemming from the contraction algorithm in the image analysis, and (iii) a pronounced decorrelation of neighboring segments due to the discretization of the filament contour image into pixels. All three corrections have to be taken into account in the data analysis.

(i) Finite size effects can be avoided by excluding the polymer ends from the spatial averaging of the tangent correlations. We excluded a length of $5\mu\text{m}$ (comparable to λ) at each polymer end from the spatial averaging. Alternatively, the formula (8.11) which includes such end effects explicitly can be used to fit the data.

(ii) In the experimental images filaments have an effective thickness D_f of typically $D_f \sim 1\mu m$ from thermal fluctuations during exposure time and from the intensity profile of fluorescent labels. In the subsequent image analysis the contraction algorithm then gives rise to a local averaging of data over arc length distances $\Delta s \sim D_f$ comparable to the filament thickness. This correction becomes particularly important for narrow channels

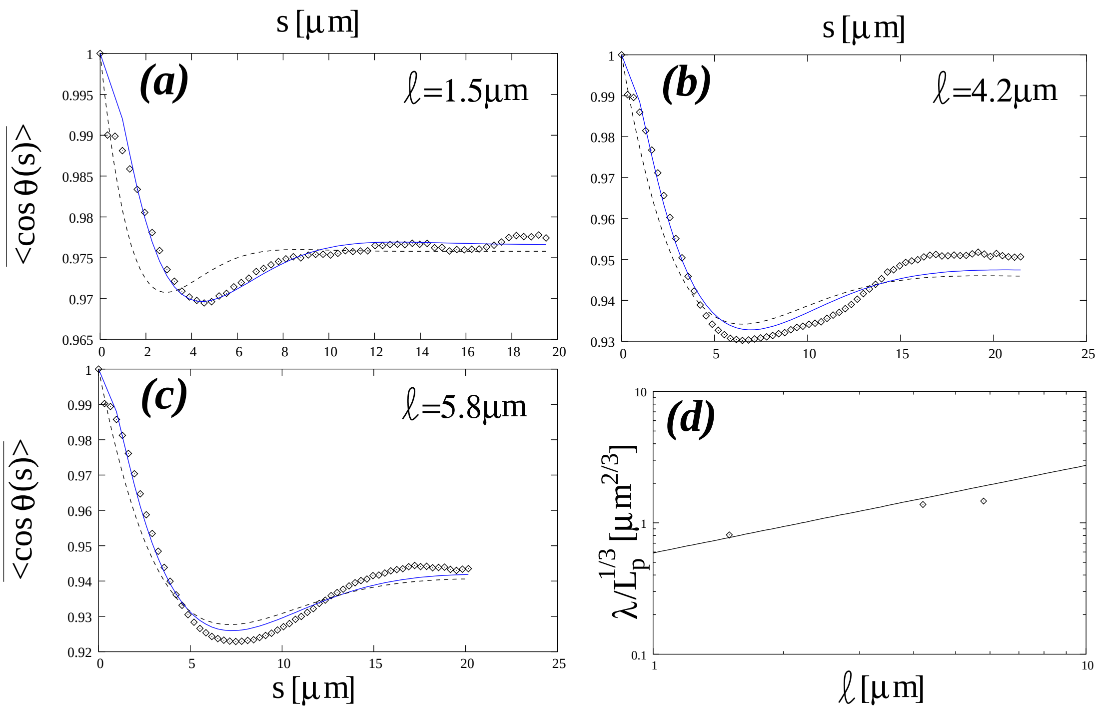

Figure 8.5: (a,b,c): Fits of the experimental data ($\diamond$) for the averaged tangent correlation $\overline{\langle \cos(\theta(s))\rangle}$ as a function of the segment distance s for filaments of length $L \simeq 30\mu$m and channel widths $\ell \simeq 2,\, 4,\, 6\mu$m. The dashed lines are fits using eq. (8.7) for a long polymer, i.e., $\langle \cos(\theta(l))\rangle = 1 - \frac{1}{2}C_p(l)$ with $L_p \simeq 38\mu$m and λ as the only fit parameter without further corrections, which gives $\lambda \simeq 1.84,\, 4.14,\, 4.55\mu$m. The blue lines are fits using the procedure outlined in the text (with $D_f = 0.5\mu$m) and give $L_p \simeq 37.73,\, 31.40,\, 30.18\mu$m and $\lambda \simeq 2.71,\, 4.35,\, 4.56\mu$m for $\ell \simeq 1.5,\, 4.2,\, 5.8\mu$m, respectively. (d): Double-logarithmic plot of the deflection lengths $\lambda/L_p^{1/3}$ resulting from the fits including corrections (blue lines) as a function of the channel width ℓ. The solid line represents the result (8.12) from MC simulations.

with ℓ only slightly large than D_f. The effective local averaging by the skeleton algorithm gives rise to increased correlations between tangents at large distances.

This effect can be taken into account in formula (8.7) or (8.11) by modifying the correlation function of Fourier or normal modes, $G(q) = Tq^2/(\kappa q^4 + K)$, which appears both in (8.7) and (8.11) to $G_D(q) \equiv G(q)e^{-q^2 D_f^2}$. This includes a convolution with a Gaussian of width $\sim D_f$, which approximates the averaging effect. For the data analysis we used a value $D_f = 0.5\mu$m, which should be similar to the experimental value.

(iii) The discretization and thresholding of the filament contour in the pixelized black-and-white image leads to an effective decorrelation of neighboring segments. Polymer contours parallel to the pixel grid tend to become rotated to a 45° angle by discretization and

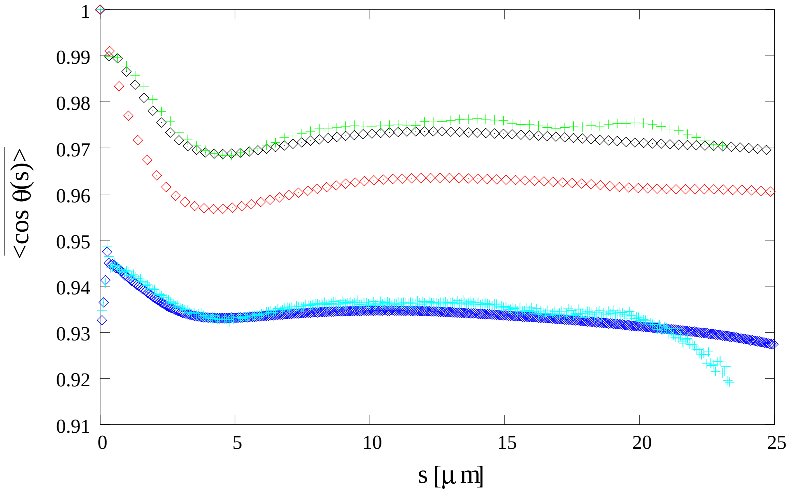

Figure 8.6: Comparison of experimental (+) and MC simulated (◇) data for the averaged tangent correlation $\overline{\langle\cos(\theta(s))\rangle}$ as a function of the segment distance s for filaments of length $L \simeq 30\mu$m, persistence length $L_p \simeq 38\mu$m, and a channel width $\ell \simeq 1.5\mu$m (cf. Fig. 8.5 a). The lower blue points represent data after thresholding before contour reconstruction, the upper black and green points data after contour reconstruction, and the red points represent the original MC data before simulating the imaging process.

thresholding. This mechanism for deviations is effective only for points a few pixels apart, i.e., on length scales comparable to the pixel size. This effect is hard to quantify in (8.7) or (8.11), therefore we simply exclude the first two data points from the analysis.

Including the corrections (i)–(iii) into the fitting procedure based on eq. (8.7), the fits to the experimental data can be improved as demonstrated in Fig. 8.5 a,b,c (blue lines). For these fits we also used the persistence length as additional fit parameter. Persistence lengths can indeed vary as different actin filaments are used in the experiment. The results for the persistence lengths are in the range $30-40\mu$m in agreement with other experiments [132]. The fitting results for the deflection length and the persistence length are shown in Fig. 8.5 d, together with the result (8.12) from the MC simulations. The agreement is remarkable for narrow channels with $\ell \simeq 1.5\mu$m, whereas deflection lengths for the wider channels are somewhat smaller. Wider channels are harder to sample, therefore the statistics of experimental data is worse for these channels (in Fig. 8.5 a,b,c we represent data from around 200 experimental images for each channel width).

In order to achieve a more detailed comparison between simulation and experiment, we MC simulated the experimental data acquisition by introducing a pixel grid with the same pixel size as in the experiment and generating “microscopy images” by illuminating each pixel that is touched by the polymer contour. Then we also introduce a finite exposure time and a finite filament thickness to obtain simulated image data. We applied the same image analysis steps described above also to the simulated data to reconstruct the filament contour.

As opposed to the experiment, we have both the filament contour reconstructed from the image data *and* the original filament contour available in the MC simulation. Fig. 8.6 shows both the experimental data and the MC simulated data for the spatially averaged tangent correlations of the thresholded contour before reconstruction, the reconstructed contour, and the simulation data for the tangent correlations of the original filament contour for narrow channels with $\ell \simeq 1.5\mu\mathrm{m}$. The MC simulated data and the experimental data agree remarkably well.

This allows us to check that the above points (i)–(iii) are indeed the main sources of deviations by systematically changing exposure time and filament thickness in the data simulation. It can be verified that for small exposure time and small filament thickness ($D_f \approx 0$) the MC data for the original contour is recovered except for the decorrelation of neighboring tangents. We also observe that this decorrelation effect is even more pronounced before reconstructing the contour, which suggests that it is due to the initial discretization procedure when the image is acquired.

8.7 Conclusion

In conclusion we have demonstrated that the concept of undulation forces as originally introduced by Helfrich [152, 153] can be successfully applied to the tangent correlation functions of a semiflexible polymer confined to a rectangular microchannel. The concept allows for a description not only of the mean-square fluctuations of tangents but also of the full shape of the tangent correlation function as it is given by eq. (8.7) for long polymers and (8.11) in the presence of finite size effects from free polymer ends. MC simulations show that the deflection length is given by (8.12). These theoretical results are used to obtain the persistence and deflection length from experimental fluorescence microscopy images of fluctuating actin filaments confined to microchannels of different widths. The results for the persistence and deflection length as well as the direct MC simulation of the experimental data show good agreement between experiment and simulation for narrow channels. The techniques introduced in this chapter can be useful to analyze fluctuations of individual confined filaments also in less well-defined environments, such as in entangled solutions [134] or the living cell. This is achieved by including corrections for finite size effects and image analysis effects into the theoretical result for the tangent correlation function.

Chapter 9

Stretching of Semiflexible Polymers with Elastic Bonds

A semiflexible harmonic chain model with extensible bonds is introduced and applied to the stretching of semiflexible polymers or filaments. The semiflexible harmonic chain model allows to study effects from bending rigidity, bond extension, discrete chain structure, and finite length of a semiflexible polymer in a unified manner. The interplay between bond extension and external force can be described by an effective inextensible chain with increased stretching force, which leads to apparently reduced persistence lengths in force–extension relations. We obtain force–extension relations for strong and weak stretching regimes which include the effects of extensible bonds, discrete chain structure, and finite polymer length. We discuss the associated characteristic force scales and calculate the crossover behavior of the force–extension curves. Strong stretching is governed by the discrete chain structure and the bond extensibility. The linear response for weak stretching depends on the relative size of the contour length and the persistence length which affects the behavior of very rigid filaments such as F–actin.

9.1 Introduction

The Kratky-Porod or worm-like chain [139, 213, 214, 215, 216] describes inextensible polymers with positional fluctuations that are not purely entropic but governed by their bending energy and characterized by their bending modulus κ or the persistence length. The worm-like chain model has been successfully applied to stretching experiments on the single-molecule level in order to interpret force–extension relations for single polymer chains. Experimental progress in manipulating single polymeric molecules has been rapid over the past decade and stretching experiments have become possible for a number of bio- and synthetic polymers such as DNA [145, 217], polysaccharides [218], polyelectrolytes [219], proteins like titin [218, 220] and actin filaments [221]. In all of these experiments the force–extension relation obtained by Marko and Siggia in [146] for a worm-like chain has been used to interpret the results. The main characteristic of this relation for an inextensible worm-like chain of contour length L is an end-to-end extension L_f in the direction of the stretching force $\mathbf{f}$ that is saturating as $1 - L_f/L \propto 1/\sqrt{f}$ for large stretching forces $f = |\mathbf{f}|$ [146].

One assumption underlying the original worm-like chain model is the inextensibility of the polymer chain. This assumption is clearly violated in the limit of a large tensile force when the elasticity of molecular bonds is probed as it is also seen in experiments on DNA [222], polyelectrolytes [219] and F–actin [221] where L_f exceeds L and a *linear* force–extension relation $L_f/L - 1 \propto f$ is seen at larger forces as compared to the characteristic $f^{-1/2}$-saturation of the inextensible worm-like chain. In Refs. [214, 223, 224, 225] the extensibility of the polymer has been accounted for by correcting the overall relative extension L_f/L by an additional term f/k where k is the stretching modulus of the polymer. In Ref. [226] microscopic degrees of freedom for stretchable bond lengths have been included into a worm-like chain model to allow for a systematic statistical mechanics treatment of the finite extensibility.

In this chapter, we introduce a description of extensible semiflexible polymers by a *semiflexible harmonic chain* (SHC) model which incorporates elastic bonds with non-zero equilibrium bond length as microscopic degrees of freedom into a discrete version of the worm-like chain. The SHC model allows us to study effects of bending rigidity, bond extension, discrete chain structure, and finite length of a semiflexible polymer on the force–extension behavior in a unified manner. In calculating the work done by the stretching force we take into account the thermal fluctuations of the variable bond length. The resulting force–extension relations for the SHC can be calculated for large tensile forces by expanding around the stretched configuration, for small forces by an expansion in powers of f. We find that the coupling between external force and bond extension gives rise to an effectively increased stretching force. If experimental force–extension curves are analyzed using the standard model of an inextensible worm-like chain this leads to an apparently reduced persistence length. The corrections calculated within this chapter for the SHC model can be used to extract the actual rather than the apparent bending rigidity or persistence length from experimental force–extension curves. At very large stretching forces the correlation length is decreased below the bond length and we find a different force–extension relation with a f^{-1}-saturation as for a freely jointed chain due to the discrete chain structure [227]. Furthermore, we calculate finite size corrections at small forces which are relevant for experiments on biopolymers such as F–actin [221] with contour length comparable to the persistence length. Effects from the extensibility, corrections due to the discrete chain structure, and finite size corrections can all be included in interpolation formulae for the force–extension curves of the SHC that are accurate within 10% [183].

9.2 The semiflexible harmonic chain model

A semiflexible polymer or filament can be modeled by a discrete chain of N bonds of length b_0 with directions described by unit tangent vectors $\mathbf{t}(n)$ with $|\mathbf{t}(n)| = 1$ ($n = 1, \ldots, N$), see Figure 9.1. The contour length of the polymer is $L = Nb_0$. The bonds can represent either actual chemical bonds in a polymer or larger segments of a filament, for example a helical repeat unit in F–actin. The bonds or segments can be tilted against each other and eventually stretched. The bond vectors connect $N + 1$ "particles" at positions $\mathbf{r}(i) =$

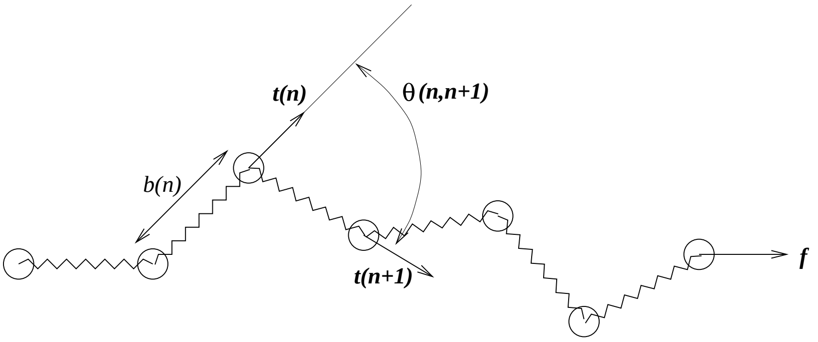

Figure 9.1: The semiflexible harmonic chain (SHC) model. $\mathbf{t}(n)$ are bond directions with $|\mathbf{t}(n)| = 1$, $b(n)$ the bond lengths, and $\mathbf{f}$ the external force applied to one end of the polymer. The other end is fixed.

$\mathbf{r}(0) + \sum_{n=1}^{i} b_0 \mathbf{t}(n)$ $(i = 0, \ldots, N)$, where $\mathbf{r}(0)$ is the position of the particle at the fixed end of the polymer. In the following, we will discuss the general case of d spatial dimensions. Experimentally relevant are the cases $d = 2$ corresponding to semiflexible polymers which adhere to a substrate [228] or are confined in a slab-like geometry, and $d = 3$.

Discrete model

In order to describe an *extensible* semiflexible chain we introduce harmonic bonds of variable length $b(n)$ with a stretching energy $E_s = \sum_{n=1}^{N} \frac{1}{2} k(n) b_0^2 \epsilon^2(n)$, where each bond has the equilibrium length b_0 and $\epsilon(n) \equiv (b(n) - b_0)/b_0$ are the relative bond extensions. The bonds act as harmonic elastic springs characterized by bond stretching moduli $k(n)$, which we can allow to depend on the bond index n to model spatial heterogeneity.

For an extensible chain the work done by the external force $\mathbf{f}$ applied to one end $\mathbf{r}(N)$ of the chain with the other end $\mathbf{r}(0)$ fixed is $E_f = -\mathbf{f} \cdot (\mathbf{r}(N) - \mathbf{r}(0)) = -\sum_{n=1}^{N} b_0 (1 + \epsilon(n)) \mathbf{f} \cdot \mathbf{t}(n)$. In a semiflexible chain the tilting of neighboring bonds costs a bending energy [213, 215, 216] $E_b = \sum_{n=1}^{N-1} (\kappa/2b_0) \left(\mathbf{t}(n+1)) - \mathbf{t}(n)\right)^2$, which only depends on the angles $\theta(n, n+1) = \arccos(\mathbf{t}(n) \cdot \mathbf{t}(n+1))$ enclosed by unit tangent vectors, see Figure 9.1, and one material parameter, the bending rigidity κ. The bending potential is periodic in the tilt angles $\theta(n, n+1)$ and quadratic for small tilt angles.

The sum of bending and stretching energies together with the work of the external force gives the Hamiltonian for the discrete *semiflexible harmonic chain* (SHC)

$$\mathcal{H}[\mathbf{t}(n), \epsilon(n)] = \sum_{n=1}^{N-1} \frac{\kappa}{2b_0} \left(\mathbf{t}(n+1)) - \mathbf{t}(n)\right)^2 + \sum_{n=1}^{N} \left(\frac{k(n) b_0^2}{2} \epsilon^2(n) - b_0 (1 + \epsilon(n)) \mathbf{f} \cdot \mathbf{t}(n) \right). \tag{9.1}$$

Note that in the absence of a stretching force $f = 0$ there is no direct coupling between the bond directions $\mathbf{t}(n)$ and the relative bond extensions $\epsilon(n)$.

In the SHC model we use harmonic bonds as we assume that stretching forces or thermal fluctuations are not sufficient to probe the regime of anharmonic bond stretching potentials [226]. We expect the characteristic force scales needed to probe such anharmonicities to be comparable to forces that induce structural transitions (such as overstretching of DNA) or even rupture of the semiflexible polymer.

In order to study force–extension behavior, discrete models of semiflexible polymers have also been used in Refs. [227] or [229], and bond extension has been taken into account in Refs. [223] and [226]. The SHC model (9.1) includes a discrete chain structure of finite length with bending energy and extensible bonds within a single model.

In single-molecule stretching experiments two kinds of boundary conditions can be realized. We can consider clamped ends with fixed tangents $\mathbf{t}(1)$ and $\mathbf{t}(N)$ as in [230] or free ends where $\mathbf{t}(1)$ and $\mathbf{t}(N)$ can fluctuate. In the partition function of the discrete SHC (9.1) we sum over all tangent configurations $\mathbf{t}(n)$ according to the boundary conditions of clamped or free ends and subject to the local constraint $|\mathbf{t}(n)| = 1$ and also over all possible bond lengths $b(n)$ or relative bond extensions $\epsilon(n)$. In contrast to [230], we focus on single-molecule stretching experiments with *free* ends where *all* bond directions fluctuate.

The integrations over bond extensions $\epsilon(n)$ are Gaussian and can be readily performed to obtain an effective Hamiltonian only depending on the tangent configurations $\mathbf{t}(n)$

$$\begin{aligned}\mathcal{H}_{\text{eff}}[\mathbf{t}(n)] &= -T\ln\left[\prod_{n=1}^{N}\int d\epsilon(n)e^{-\mathcal{H}[\mathbf{t}(n),\epsilon(n)]/T}\right]\\ &= \sum_{n=1}^{N-1}\frac{\kappa}{2b_0}\left(\mathbf{t}(n+1))-\mathbf{t}(n)\right)^2-\sum_{n=1}^{N}b_0\mathbf{f}\cdot\mathbf{t}(n)-\sum_{n=1}^{N}\frac{1}{2k(n)}\left(\mathbf{f}\cdot\mathbf{t}(n)\right)^2\\ &\equiv \mathcal{H}_i[\mathbf{t}(n)]-\sum_{n=1}^{N}\frac{1}{2k(n)}\left(\mathbf{f}\cdot\mathbf{t}(n)\right)^2\ . \end{aligned} \tag{9.2}$$

The last term in (9.2) stems from the coupling of fluctuating elastic bonds to the external force and is absent for an *inextensible* discrete worm-like chain with Hamiltonian $\mathcal{H}_i[\mathbf{t}(n)]$ that is obtained in the limit of large stretching moduli $k(n)$. Inspecting the signs in (9.2) shows that this term leads to an effectively increased stretching force.

Continuum model

In the limit of small bond lengths b_0 we can switch to a continuous description using a parameterization by arc length $s = nb_0$ of the *unstretched* configuration. The continuous version of the SHC Hamiltonian (9.1) becomes [214]

$$\mathcal{H}[\mathbf{t}(s),\epsilon(s)] = \int_0^L ds\left[\frac{\kappa}{2}(\partial_s\mathbf{t})^2+\frac{k(s)b_0}{2}\epsilon^2(s)-(1+\epsilon(s))\mathbf{f}\cdot\mathbf{t}(s)\right]. \tag{9.3}$$

In the inextensible limit of large stretching moduli $k(s)$ fluctuations in the bond length can be neglected ($\epsilon(s) = 0$) and the continuous SHC Hamiltonian (9.3) reduces to the inextensible worm-like chain Hamiltonian [139, 213]

$$\mathcal{H}_i[\mathbf{t}(s)] = \int_0^L ds \left[\frac{\kappa}{2}(\partial_s \mathbf{t})^2 - \mathbf{f}\cdot\mathbf{t}(s)\right] . \tag{9.4}$$

In the absence of a stretching force $\mathbf{f} = 0$ the correlation function of the tangent vectors $\mathbf{t}(s)$ of the worm-like chain fall off exponentially [123, 141], $\langle \mathbf{t}(s)\cdot\mathbf{t}(0)\rangle = \frac{1}{d}\exp(-s/\tilde{L}_p)$, thereby defining a characteristic length scale, the *persistence length* L_p

$$L_p \equiv (d-1)\tilde{L}_p \equiv 2\kappa/T \ . \tag{9.5}$$

As in the discrete SHC model, the Gaussian path integral over bond extensions $\epsilon(s)$ can be performed also for the continuous SHC Hamiltonian (9.3) to give the effective continuous Hamiltonian

$$\mathcal{H}_{\text{eff}}[\mathbf{t}(s)] = \mathcal{H}_i[\mathbf{t}(s)] - \int_0^L ds \frac{1}{2k(s)b_0}\left(\mathbf{f}\cdot\mathbf{t}(s)\right)^2 \tag{9.6}$$

which is the analogon of (9.2) and has also been derived in [226].

In the following we will employ different approximate methods to obtain force–extension relations for the effective Hamiltonians (9.2) or (9.6) describing the SHC. The extension L_f in force direction is always found from the dependence of the free energy $F(f) = -T\ln Z(f)$ on the force $f = |\mathbf{f}|$ by the thermodynamic relation

$$L_f \equiv \langle(\mathbf{r}(L) - \mathbf{r}(0))\cdot\frac{\mathbf{f}}{f}\rangle = -\partial_f F(f) \ . \tag{9.7}$$

9.3 Force scales

The SHC models as introduced above contain the following dimensionful parameters: the mean bond length b_0 which represents the basic length scale; the contour length of the SHC $L = Nb_0$; the bond stretching modulus $k(n) = k$ which we will take to be position independent in this subsection and which has the dimension of energy divided by length squared; the bending rigidity κ which has the dimension energy times length; and the temperature T which has the dimension of energy (in the units used here). These parameters define four different force scales

$$f_{cr} \equiv T^2/\kappa\,, \qquad f_L \equiv \kappa/L^2\,, \qquad f_\kappa \equiv 4\kappa/b_0^2\,, \qquad \text{and} \quad f_k \equiv kb_0, \tag{9.8}$$

that govern the stretching of the SHC.

Crossover force scale f_{cr}

First we consider the limiting case of an inextensible chain ($f \ll f_k$) and further consider the continuum limit of small segment sizes b_0 ($f \ll f_\kappa$) corresponding to the simplest model (9.4) describing an inextensible worm-like chain. In the thermodynamic limit of an infinite chain ($f_L = 0$) we are left with only two parameters, namely T and κ, which define a single

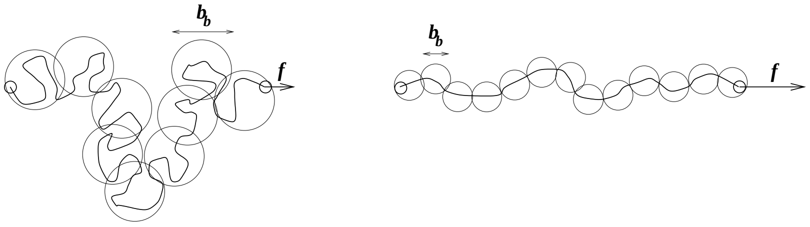

Figure 9.2: Left: Weak stretching of a semiflexible polymer for $f < f_{cr}$ or $\xi_f > L_p$. Right: Strong stretching for $f > f_{cr}$ or $\xi_f > L_p$.

force scale, $f_{cr} \equiv T^2/\kappa = 2T/L_p = 4\kappa/L_p^2$. To elucidate the significance of f_{cr} as a crossover force scale from weak to strong stretching we introduce a "blob" picture of the stretched inextensible worm-like chain.

To introduce the characteristic size of a blob we consider an initially straight segment of length ℓ. Bending the segment to an angle $\Delta\theta$ costs an energy $\Delta E_b \simeq \kappa\Delta\theta^2/\ell$. Additionally, work $\Delta E_f \simeq f\ell\Delta\theta^2$ has to be performed to bend the segment against the external force f. Balancing both energies sets a blob length $\ell = \xi_f$ with

$$\xi_f \simeq \sqrt{\kappa/f} \simeq L_p\sqrt{f_{cr}/f} \ . \tag{9.9}$$

On small scales $\ell < \xi_f$ inside each blob, we find an essentially unstretched ($f = 0$), thermally fluctuating inextensible SHC. On larger scales $\ell > \xi_f$, the blobs form an effective freely jointed chain of blobs with effective bonds length b_b and stretched by the external force f, see Figure 9.2.

The blob size b_b is given by the mean end-to-end distance calculated with respect to the continuum worm-like chain Hamiltonian (9.4) in the absence of an external force $f = 0$:

$$b_b = \xi_f \mathcal{L}_b^{1/2}\left(\tilde{L}_p/\xi_f\right) \approx \begin{cases} (2\xi_f\tilde{L}_p)^{1/2}, & \text{for } \xi_f \gg \tilde{L}_p \\ \xi_f, & \text{for } \xi_f \ll \tilde{L}_p \end{cases} \tag{9.10}$$

with a scaling function $\mathcal{L}_b(x) \equiv 2x\left(1 - x + xe^{-1/x}\right)$.

The blobs form an effective freely jointed chain under tension by the external force f containing L/ξ_f blobs of size b_b. The force–extension relation of a freely jointed chain is well-known [231], and we expect a force–extension relation that is of the form

$$\frac{L_f}{N_b b_b} = \mathcal{F}_d\left(\frac{f b_b}{T}\right) \ , \tag{9.11}$$

where $\mathcal{F}_d(x)$ is a scaling function that depends only on the dimensionality d and is similar to the corresponding scaling functions $\mathcal{F}_d^{\mathrm{FJC}}(x)$ for a freely jointed chain. The effective freely jointed chain shows a characteristic crossover from weak to strong stretching at forces $f \simeq T/b_b$.

The result (9.11), together with the relation (9.10) for the effective bond length, gives the scaling form for the force–extension relation of an inextensible SHC:

$$\frac{L_f}{L} = \frac{b_b}{\xi_f}\mathcal{F}_d\left(\frac{fb_b}{T}\right) = \mathcal{G}_d\left(\frac{f}{f_{cr}}\right) \ , \tag{9.12}$$

where $\mathcal{G}_d(x^2) = \mathcal{L}_b^{1/2}(x/(d-1))\mathcal{F}_d\left[2x\mathcal{L}_b^{1/2}(x/(d-1))\right]$. The scaling form (9.12) is governed by the force-dependent ratios $L_p/\xi_f \simeq (f/f_{cr})^{1/2}$, see (9.10), and $f\xi_f/T \simeq (f/f_{cr})^{1/2}$. Thus f_{cr} is crossover force scale between weak and strong stretching of the inextensible SHC. For $f \simeq f_{cr}$, the blob size $b_b \simeq \xi_f \simeq L_p$ matches both the persistence length L_p and the crossover length ξ_f. The force scale f_{cr} itself then matches $f_{cr} \simeq T/\xi_f \simeq T/b_b$, and the effective freely jointed chain of blobs undergoes a crossover from weak to strong stretching.

For strong stretching forces $f \gg f_{cr}$ with $\xi_f \ll L_p$ rigid polymer segments of blob length $b_b \simeq \xi_f$ form an effective freely jointed chain that is strongly aligned by the stretching force $\mathbf{f}$, see Figure 9.2. Using the asymptotic behavior $\mathcal{F}_d(x) \approx 1 - (d-1)x/2$ and $\mathcal{L}_b(x) \approx 1$ for large x, we find the well-known result $1 - L_f/L \simeq \sqrt{f_{cr}/f}$ for a worm-like chain close to full stretching [146]. For weak stretching forces $f \ll f_{cr}$ with $\xi_f \gg L_p$, on the other hand, the blob length ξ_f exceeds the persistence length L_p such that the chain starts to become flexible within each blob. Furthermore, the freely jointed chain of blobs is only weakly aligned, see Figure 9.2. Using $\mathcal{F}_d(x) \simeq x$ and $\mathcal{L}_b(x) \simeq x$ for small x we obtain linear response behavior $L_f/L \simeq f/f_{cr}$ as expected at low tensile forces.

The force scale f_{cr} is solely determined by the rigidity of the semiflexible polymer. For a rather stiff filament such as F–actin with a persistence length of $\tilde{L}_p \simeq 10\mu$m [132] or $L_p \simeq 20\mu$m the crossover force $f_{cr} = T^2/\kappa = 2T/L_p$ between weak and strong stretching is estimated as $f_{cr} = 2T/L_p \sim 4\times10^{-4}$pN. Such small forces are not experimentally accessible as optical traps or tweezers can be used in order to study forces in the regime of 1pN and magnetic tweezers down to 0.01pN. For less rigid semiflexible biopolymers such as DNA with $L_p \simeq 100$nm [135] one finds $f_{cr} = 2T/L_p \sim 8 \times 10^{-2}$pN and the force regime of weak stretching is accessible by magnetic tweezers [145].

Discrete chains and force scale f_κ

The discrete chain structure of the SHC model (9.2) with a bond length b_0 introduces the force scale $f_\kappa \equiv 4\kappa/b_0^2$. Effects from the segment size b_0 can be neglected for small forces $f \ll f_\kappa$ or $\xi_f \gg b_0$ where we can use the continuous model (9.6). For large forces $f \gg f_\kappa$ the crossover length ξ_f becomes smaller than the size b_0 of individual segments of the SHC, and the discrete structure of the SHC becomes relevant. Within the blob scaling picture, the blob length ξ_f has to be replaced then by the segment length b_0 in the scaling result (9.12) for the force–extension relation.

The force scale f_κ is related to the force scale f_{cr} by

$$f_\kappa/f_{cr} = (L_p/b_0)^2 \gg 1 \tag{9.13}$$

as we will focus on semiflexible polymers, for which the persistence length L_p is large compared to the bond length b_0. Thus, f_κ is always within the strong stretching regime.

$L_p \gg b_0$ is generally fulfilled for semiflexible biopolymers such as DNA or actin but might be violated for synthetic polyelectrolytes at sufficiently high salt concentration [219]. For typical semiflexible filaments such as F–actin we find $f_\kappa/f_{cr} = (L_p/b_0)^2 \sim 4 \times 10^6$ with $L_p \simeq 20\mu$m [132] and a segment size $b_0 \simeq 10$nm [232] that we estimate by the the size of a G–actin monomer. This gives rise to large values $f_\kappa \sim 1.6$nN. For DNA at high salt concentrations one finds values $f_\kappa/f_{cr} = (L_p/b_0)^2 \sim 10^5$ with $L_p \simeq 100$nm [135] and a segment size $b_0 \simeq 0.34$nm set by the distance between base pairs. Accordingly we find an even higher value $f_\kappa \sim 7$nN.

Finite chains and force scale f_L

The contour length L of the semiflexible polymer introduces another force $f_L \equiv \kappa/L^2$. So far we have considered the thermodynamic limit of a long chain such that $f \gg f_L$ or $\xi_f \ll L$ and we can neglect finite size effects. If $L < \xi_f$, corresponding to small forces $f < f_L$, we expect finite size effects and a crossover in the force–extension relation. Within the blob picture these finite size effects can be taken into account by replacing ξ_f by L in the scaling result (9.12) for the force–extension relation.

The force scale f_L is related to the crossover force scale f_{cr} by $f_L/f_{cr} = L_p/2L$. For $L > L_p/2$ or $f_L < f_{cr}$ finite size effects will occur only in the weak stretching regime for $f < f_L < f_{cr}$ whereas for semiflexible polymers with a short contour length, $L < L_p/2$ or $f_L > f_{cr}$, e.g. typical actin filaments, finite size effects will also affect the strong stretching regime within the force window $f_{cr} < f < f_L$.

The force scale f_L is related to the force scale f_κ by

$$f_L/f_\kappa = (b_0/4L)^2 \gg 1 \tag{9.14}$$

as the contour length L is always large compared to the segment size b_0.

Extensibility and force scale f_k

In the SHC model (9.2) we also allow for extensible segments or bonds with stretching modulus k which introduces the force scale $f_k \equiv kb_0$. Individual bonds of the discrete SHC can be considered inextensible for small forces $f \ll f_k$. By definition this force scale also depends on the segment size b_0 which is a consequence of the fact that the introduction of extensible bonds requires a discrete chain structure. Within the model (9.2), this force scale is independent of the other scales since we can choose an arbitrary value of k. However, we can consider the SHC as a “discretized elastic rod” consisting of circular segments of length b_0 and radius a. For such a model we find $kb_0 \simeq Ea^2$, i.e., the force scale f_k is determined by the Young's modulus modulus of the material and the radius a of the rod and thus independent of b_0. This implies that $k \propto b_0^{-1}$ depends on the segment size, and the force scale f_k does not necessarily vanish in the continuum limit of small b_0.

If we consider the SHC as a discretized elastic rod, also the bending rigidity κ and the stretching modulus k are no longer independent but related by elasticity theory according to $kb_0/\kappa \simeq 1/a^2$, and thus $f_k/f_\kappa \simeq (b_0/a)^2$. This suggests that for long elongated segments with $b_0 \gg a$ we have $f_k \gg f_\kappa$ whereas disc-like segments with $b_0 \ll a$ lead to $f_k \ll f_\kappa$. Experimental values for the force scale f_k have been obtained for F–actin in Ref. [221] where $f_k \sim 35\text{nN}$ is found such that $f_k \gg f_\kappa$.

Using the discretized elastic rod model we also find

$$f_k/f_{cr} \simeq (L_p/a)^2 \gg 1 \quad \text{and} \quad f_k/f_L \simeq (L/a)^2 \gg 1 \tag{9.15}$$

(which holds regardless of the value of b_0 within the discretized elastic rod model) as we can assume $L_p \gg a$ and $L \gg a$ in general, which is well fulfilled for F–actin with $a \simeq 4\text{nm}$ or DNA with $a \simeq 0.8\text{nm}$. Therefore, f_k represents a force scale that lies always within the strong stretching regime. Also, the relative extension of the SHC is insensitive to finite size effects.

9.4 Strong stretching

For large stretching forces $f \gg f_{cr}$, the tangent vectors $\mathbf{t}$ deviate only little from the direction set by the force. Therefore we choose the x-direction such that $\mathbf{f} = f\mathbf{e}_x$ and decompose tangent vectors according to $\mathbf{t} = (t_x, \mathbf{t}_\perp)$ into one component t_x parallel to the force and a $d_\perp = (d-1)$-dimensional vector $\mathbf{t}_\perp$ describing the perpendicular deviations [146]. The local constraint $|\mathbf{t}(n| = 1$ eliminates $t_x(n)$ as a degree of freedom by using $t_x = (1 - \mathbf{t}_\perp^2)^{1/2}$. For strong stretching $\langle t_\perp^2 \rangle \ll 1$ is small, and we can expand the effective Hamiltonian (9.2) of the weakly bent SHC up to second order terms in $\mathbf{t}_\perp$:

$$\begin{aligned} \mathcal{H}_{\text{eff}}[\mathbf{t}_\perp(n)] &= \sum_{n=1}^{N-1} \frac{\kappa}{2b_0} (\mathbf{t}_\perp(n) - \mathbf{t}_\perp(n+1))^2 \\ &\quad + \sum_{n=1}^{N} \frac{fb_0}{2} \left(1 + \frac{f}{k(n)b_0}\right) \mathbf{t}_\perp^2(n) - Nfb_0 - \sum_{n=1}^{N} \frac{f^2}{2k(n)} \ . \end{aligned} \tag{9.16}$$

$-Nfb_0$ is the potential energy of the fully stretched chain and the last term in (9.16) represents the overall elastic energy of the bonds [223].

However, we find further effects from extensional fluctuations of elastic bonds that couple both to the external force and the bond directions. Comparing the second term in (9.16) with the corresponding term in the expansion for the Hamiltonian (9.4) of the inextensible worm-like chain we read off that corrections due to the coupling of elastic bonds with the external force term lead to an effectively increased force [226]

$$f_{\text{eff}}(n) = f\left(1 + \frac{f}{k(n)b_0}\right) = f\left(1 + \frac{f}{f_k}\right) \ , \tag{9.17}$$

where the last equality holds for homogeneous bonds $k(n) = k$.

The partition sum of the effective Hamiltonian (9.16) for free ends is obtained by performing the path integral over the remaining degrees of freedom $\mathbf{t}_\perp(n)$ [233]

$$Z(f) = \prod_{n=1}^{N} \int d\mathbf{t}_\perp(n) e^{-\mathcal{H}_{\text{eff}}[\mathbf{t}_\perp(n)]/T} \ . \tag{9.18}$$

For the case of homogeneous bonds $k(n) = k$, this path integral can be directly evaluated. We first perform the path integral for boundary conditions of clamped ends, i.e., with fixed $\mathbf{t}_\perp(1)$ and $\mathbf{t}_\perp(N)$ before we integrate in the end over $\mathbf{t}_\perp(1)$ and $\mathbf{t}_\perp(N)$ to obtain the result for free ends. In order to perform the path integral for clamped ends we consider the "classical path" $\mathbf{t}_\perp^0(n)$ that minimizes the Hamiltonian (9.16) for boundary conditions $\mathbf{t}_\perp^0(1) = \mathbf{t}_\perp(1)$ and $\mathbf{t}_\perp^0(N) = \mathbf{t}_\perp(N)$ and integrate over fluctuations $\delta\mathbf{t}_\perp(n) = \mathbf{t}_\perp(n) - \mathbf{t}_\perp^0(n)$, which then fulfill boundary conditions $\delta\mathbf{t}_\perp(1) = \delta\mathbf{t}_\perp(N) = 0$. As the Hamiltonian (9.16) is quadratic, contributions from the classical path $\mathbf{t}_\perp^0(n)$ and fluctuations $\delta\mathbf{t}_\perp(n)$ separate exactly, and the partition function factorizes into $Z(f) = Z_0(f) Z_\delta(f) e^{Lf/T + Lf^2/2Tf_k}$,

$$Z_0(f) \equiv \prod_{n=1,N} \int d\mathbf{t}_\perp(n) e^{-\tilde{\mathcal{H}}_{\rm eff}[\mathbf{t}_\perp^0(n)]/T}\ , Z_\delta(f) \equiv \prod_{n=2}^{N-1} \int d\delta\mathbf{t}_\perp(n) e^{-\tilde{\mathcal{H}}_{\rm eff}[\delta\mathbf{t}_\perp(n)]/T}, \tag{9.19}$$

where we split off the last two terms of (9.16) and used $\tilde{\mathcal{H}}_{\rm eff}[\mathbf{t}_\perp(n)] \equiv \mathcal{H}_{\rm eff}[\mathbf{t}_\perp(n)] + Lf + Lf^2/2f_k$.

The path integral in the fluctuation contribution $Z_\delta(f)$ can be calculated by using Fourier modes. For the corresponding contribution $F_\delta(f) = -T \ln Z_\delta(f)$ to the free energy we find

$$\begin{aligned} \frac{1}{L}\left[F_\delta(f) - F_\delta(0)\right] &\approx d_\perp T \int_0^{\pi/b_0} \frac{dq}{2\pi} \ln\left(\frac{1-\cos(qb_0) + f_{\rm eff} b_0^2/2\kappa}{1-\cos(qb_0)}\right) \\ &= \frac{d_\perp T}{b_0} \text{arcsinh}\left[\left(\frac{f_{\rm eff}}{f_\kappa}\right)^{1/2}\right] , \end{aligned} \tag{9.20}$$

where we approximated the discrete sum over Fourier modes by an integral as $N \gg 1$.

To calculate the classical path we can use the continuum approximation $x = nb_0$ for small b_0 and find that $\mathbf{t}_\perp^0(x)$ fulfills the equation $\partial_x^2 \mathbf{t}_\perp^0 = \xi_f^{-2}\mathbf{t}_\perp^0$ with the crossover length $\xi_f \equiv \sqrt{\kappa/f_{\rm eff}}$ set by the stretching force, cf. (9.9). In the limit $L \gg \xi_f$ or $f \gg f_L$ the classic solution is approximately $\mathbf{t}_\perp^0(x) \approx \mathbf{t}_\perp(1)e^{-x/\xi_f} + \mathbf{t}_\perp(N)e^{-(L-x)/\xi_f}$, and approaches the straight, force-aligned configuration $\mathbf{t}_\perp^0(x) = 0$ over the characteristic distance ξ_f away from the ends. In the opposite limit $L \ll \xi_f$ or $f \ll f_L$, the classic solution is approximately linear $\mathbf{t}_\perp^0(x) \approx \mathbf{t}_\perp(1) + \frac{x}{L}\Delta\mathbf{t}_\perp$, where $\Delta\mathbf{t}_\perp \equiv \mathbf{t}_\perp(N) - \mathbf{t}_\perp(1)$. In both cases the resulting energy $tilde\mathcal{H}_{\rm eff}[\mathbf{t}_\perp^0(n)]$ is quadratic in $\mathbf{t}_\perp(1)$ and $\mathbf{t}_\perp(N)$, and performing the remaining Gaussian integrals in the expression for $Z_0(f)$, we finally obtain identical results

$$\frac{1}{L}F_0(f) = \frac{d_\perp T}{2L} \ln\left[4\pi^2 \frac{f_{\rm eff}}{f_{cr}}\right] \tag{9.21}$$

for the corresponding free energy contribution $F_0(f) = -T \ln Z_0(f)$ in both cases. Together with (9.20), this gives the free energy at strong stretching

$$\begin{aligned} \frac{1}{L}\left[F(f) - F(0)\right] &= -f - \frac{f^2}{2f_k} + \frac{d_\perp}{2}\left(f_{cr} f_\kappa\right)^{1/2} \text{arcsinh}\left[\left(\frac{f_{\rm eff}}{f_\kappa}\right)^{1/2}\right] \\ &\quad + \frac{d_\perp}{2}\left(f_{cr} f_L\right)^{1/2} \ln\left[\frac{f_{\rm eff}}{f_{cr}}\right] , \end{aligned} \tag{9.22}$$

where we used $2T/b_0 = (f_{cr}f_\kappa)^{1/2}$ and $T/L = (f_{cr}f_L)^{1/2}$. Effects from the extensibility enter this result through the force scale f_k which also occurs in the expression (9.17) for the effective stretching force f_{eff}; effects from the discrete chain structure and the finite chain length enter through the force scales f_κ and f_L, respectively.

Using the thermodynamic relation (9.7), we arrive at the main result of this section, the force–extension relation for strong stretching

$$\begin{aligned}\frac{L_f}{L} &= \frac{f}{f_k} + 1 - \frac{d_\perp}{4}\left(\frac{f_{cr}}{f}\right)^{1/2} \frac{1+2f/f_k}{(1+f/f_k)^{1/2}} \frac{1}{(1+f_{\mathrm{eff}}/f_\kappa)^{1/2}} \\ &\quad - \frac{d_\perp}{2}\frac{(f_{cr}f_L)^{1/2}}{f}\frac{1+2f/f_k}{1+f/f_k} \ . \end{aligned} \tag{9.23}$$

This strong stretching result with its limiting cases will be discussed in detail in section 9.6.

The expansion in $\mathbf{t}_\perp$ for a weakly bent SHC is valid as long as $\langle \mathbf{t}_\perp^2\rangle \ll 1$. It can be shown that this condition is fulfilled for the force regime $f_{\mathrm{eff}} \gg f_{cr}$ above the crossover force scale f_{cr}, which confirms the blob scaling picture.

9.5 Weak stretching

For small stretching forces $f \ll f_{cr}$, we can obtain the free energy for the effective Hamiltonian (9.2) of the SHC by expanding the free energy in the force $\mathbf{f}$ up to second order. In the absence of an external force, the correlation function of the tangent vectors $\mathbf{t}(n)$ can be calculated using angular representations of the Boltzmann weights that have been obtained in the context of path integrals for a quantum particle on the unit sphere in d dimensions in [141]:

$$\langle t_i(n)t_j(n')\rangle_0 = d^{-1}\left[A\left(L_p/b_0\right)\right]^{|n-n'|}\delta_{ij} \approx \begin{cases} d^{-1}e^{-|n-n'|b_0/\tilde{L}_p}\delta_{ij}, & \text{for } L_p \gg b_0 \ , \\ d^{-1}(L_p/4b_0)^{|n-n'|}\delta_{ij}, & \text{for } L_p \ll b_0 \end{cases} \tag{9.24}$$

with a function

$$A(x) \equiv \frac{I_{d/2}(x/2)}{I_{d/2-1}(x/2)} \approx \begin{cases} \exp\left(-(d-1)/x\right), & \text{for } x \gg 1 \ , \\ x/4, & \text{for } x \ll 1 \ , \end{cases} \tag{9.25}$$

where $I_\nu(x)$ is the Bessel function of order ν [234] and $\tilde{L}_p$ is defined in (9.5). The brackets $\langle \ldots \rangle_0$ indicate an expectation value with respect to the SHC Hamiltonian at $f = 0$ given by the bending energy, $\mathcal{H}_0 = E_b$. In the presence of the external force f, the effective Hamiltonian (9.2) is divided up according to $\mathcal{H}_{\mathrm{eff}} = \mathcal{H}_0 + \mathcal{H}_f$, and the free energy satisfies the relation $F(f) - F(0) = -T\ln\langle e^{-\mathcal{H}_f/T}\rangle_0$. Performing a cumulant expansion up to second order in $\mathcal{H}_f$ for homogeneous bonds $k(n) = k$ and keeping only terms up to second order in $\mathbf{f}$ leads to

$$\frac{1}{L}\left[F(f) - F(0)\right] \approx -\frac{1}{N}\sum_{n=1}^{N}\frac{1}{2kb_0}\langle(\mathbf{f}\cdot\mathbf{t}(n))^2\rangle_0 - \frac{b_0}{2NT}\sum_{n=1}^{N}\sum_{n'=1}^{N}\langle(\mathbf{f}\cdot\mathbf{t}(n))(\mathbf{f}\cdot\mathbf{t}(n'))\rangle_0. \tag{9.26}$$

In deriving (9.26) we used that $\langle \mathbf{f}\cdot\mathbf{t}(n)\rangle_0 = 0$ as we consider free ends and have to integrate over rotations of $\mathbf{t}(0)$ giving rise to rotations of the entire polymer, in contrast to the situation of clamped ends studied in Ref. [230]. Both expectation values in the right hand side of this equation involve the correlation function of the tangent vectors $\mathbf{t}$ as given by (9.24). If the latter expression is inserted, the sums can be performed, and one obtains

$$\frac{1}{L}\left[F(f)-F(0)\right] \approx -\frac{f^2}{2dkb_0} - \frac{f^2 b_0}{2dT}\left(\frac{1+A}{1-A} - \frac{2A}{N}\frac{1-A^{N+1}}{(1-A)^2}\right) \tag{9.27}$$

with $A \equiv A(L_p/b_0)$.

Focusing on the limit $L_p \gg b_0$ or $f_\kappa \gg f_{cr}$, see (9.13), we insert the asymptotic expression $A \approx \exp(-b_0/\tilde{L}_p)$, see (9.25), to obtain

$$\frac{1}{L}\left[F(f)-F(0)\right] \approx -\frac{f^2}{2df_k} - \frac{2}{d(d-1)}\frac{f^2}{f_{cr}}\mathcal{L}\left(\frac{\tilde{L}_p}{L}\right) \tag{9.28}$$

and the function $\mathcal{L}(x) \equiv \mathcal{L}_b(x)/2x$ or

$$\mathcal{L}(x) \equiv 1 - x + xe^{-1/x} \approx \begin{cases} 1-x, & \text{for small } x \\ 1/2x, & \text{for large } x \end{cases} . \tag{9.29}$$

This function describes finite size corrections in the free energy which have to be taken into account for polymer contour lengths $L \leq \tilde{L}_p$ comparable or smaller than the persistence length. Using the thermodynamic relation (9.7), the free energy for weak stretching as given by (9.28) leads to the force–extension relation

$$\frac{L_f}{L} \approx \left[\frac{1}{df_k} + \frac{4}{d(d-1)}\frac{1}{f_{cr}}\mathcal{L}\left(\frac{\tilde{L}_p}{L}\right)\right] f , \tag{9.30}$$

which is the main result of this section, limiting cases of which will be discussed in section 9.6. The extension exhibits a linear response behavior as expected for low tensile forces. The first term in (9.30) represents the effect from the response of the thermally fluctuating extensible bonds and differs by the factor $1/d$ from what has been suggested in Ref. [224]. The second term represents the contribution from entropic elasticity and bending energy. Relation (9.30) shows that semiflexible polymers exhibit strong finite size effects at weak stretching depending on the ratio $\tilde{L}_p/L = (2/(d-1))(f_L/f_{cr})^{1/2}$. As already mentioned the force scale f_κ does not occur in (9.30) as we work in the continuum limit $f \ll f_\kappa$ assuming that f_κ is inaccessible. Therefore we implicitly assumed $f_k \ll f_\kappa$ in (9.30).

For vanishing κ, the SHC model (9.2) reduces to an extensible freely jointed chain. This limit corresponds to $L_p \ll b_0$ or $A \ll 1$ according to (9.25).

9.6 Discussion and limiting cases

In this section we will discuss our main results, the force–extension relations (9.23) for strong stretching $f \gg f_{cr}$ and (9.30) for weak stretching $f \ll f_{cr}$, and consider various limiting cases along with finite size effects. These results can also be used to obtain useful interpolation formulae for the whole force range (see Appendix in Ref. [183]).

Extensibility crossover force $f_{k,cr}$

The force–extension relation (9.23) for strong stretching includes various effects from the bond extensibility of the SHC model (9.2). Individual bonds of the discrete SHC have relative extensions $\langle\epsilon\rangle = f/f_k$ which give rise to the first term in (9.23). In the force regime $f \gg f_k$ they are the leading contribution to L_f/L and the SHC is clearly extensible.

In the regime $f \ll f_k$ individual bonds can be considered inextensible, and the first term can be neglected against the second term in (9.23), which represents the extension of the fully stretched inextensible chain, $L_f/L = 1$. However, the extension of the entire SHC is also governed by much smaller entropic contributions, which give rise to the last two terms in (9.23). Therefore, the extensibility of the SHC can become already relevant if the bond extension contribution f/f_k exceeds the entropic terms in (9.23). This happens for forces $f_{k,cr} \ll f \ll f_k$ where the new force scale $f_{k,cr}$ is defined by the condition $L_f/L = 1$ in (9.23). The force scale $f_{k,cr}$ describes the crossover from an inextensible to an extensible chain within the regime $f \ll f_k$.

Depending on the bond stiffness and thus f_k three different situations (a–c) are possible.

(a) For $f_L \ll f_{k,cr} \ll f_\kappa$ [note that $f_L \ll f_\kappa$, see (9.14)], effects from the discrete chain structure and finite size effects can be neglected, and we find [223]

$$f_{k,cr} = \left(\frac{d_\perp}{4}\right)^{2/3} \left(f_k^2 f_{cr}\right)^{1/3}, \text{ for } f_L \ll f_{k,cr} \ll f_\kappa \; . \tag{9.31}$$

As we want to consider the situation $f_{cr} \ll f_k$, see (9.15), this force scale is indeed much smaller than f_k, i.e., $f_{k,cr} \ll f_k$.

(b) If the bond stiffness is increased such that $f_L \ll f_\kappa \ll f_{k,cr}$, the discrete chain structure becomes relevant, and we obtain

$$f_{k,cr} = \left(\frac{d_\perp}{4}\right)^{1/2} \left(f_k^2 f_{cr} f_\kappa\right)^{1/4}, \text{ for } f_L \ll f_\kappa \ll f_{k,cr} \ll f_k, \tag{9.32}$$

which is again much smaller than f_k because we consider $f_\kappa \ll f_k$ and $f_{cr} \ll f_k$.

(c) Finally, for a very small bond stiffness or very short polymers with $f_{k,cr} \ll f_L \ll f_\kappa$, we find

$$f_{k,cr} = \left(\frac{d_\perp}{2}\right)^{1/2} \left(f_k^2 f_{cr} f_L\right)^{1/4}, \text{ for } f_{k,cr} \ll f_L \; . \tag{9.33}$$

Also this result for $f_{k,cr}$ is much smaller than f_k as $f_L \ll f_k$, see (9.15), and $f_{cr} \ll f_k$.

The discrete SHC as described by (9.2) can be considered inextensible only for small forces $f \ll f_{k,cr} \ll f_k$. The continuous model (9.6) applies to forces $f \ll f_\kappa$, and thus describes an extensible continuous chain for $f_{k,cr} \ll f \ll f_\kappa$ but an inextensible continuous chain for $f \ll f_{k,cr}$ and $f \ll f_\kappa$. For the inextensible continuous chain we can use the simplest model (9.4) of an inextensible worm-like chain. For very stiff bonds with $f_\kappa \ll f_{k,cr}$ we thus have to use the discrete SHC model if we want to consider effects from the extensibility, i.e., the force range $f \gg f_{k,cr}$ or even $f \gg f_k$.

In logarithmic plots of force–extension curves for the extensible SHC, i.e., plots of $\ln(f/f_{cr})$ as function of L_f/L, there is a point of inversion around $L_f/L \sim 1$ or $f \sim f_{k,cr}$ within the strong stretching regime, which signals the onset of extensibility effects.

Inextensible, continuous SHC (worm-like chain)

In the limit of $f \ll f_{k,cr} \ll f_k$ and $f \ll f_\kappa$ we are left with an inextensible, continuous SHC described by the worm-like chain model (9.4). In this limit our result (9.23) for *strong stretching* $f \gg f_{cr}$ reduces to

$$\frac{L_f}{L} \;=\; 1 - \frac{d_\perp}{4}\left(\frac{f_{cr}}{f}\right)^{1/2} - \frac{d_\perp}{2}\frac{(f_{cr}f_L)^{1/2}}{f}\ . \tag{9.34}$$

For $f \gg f_L$, finite size effects are irrelevant, the last term can be neglected, and it remains the well-known result of Marko and Siggia [146]

$$\frac{L_f}{L} \;\approx\; 1 - \frac{d_\perp}{4}\frac{T}{\sqrt{f\kappa}},\ \text{for}\ \ f \gg f_L\ . \tag{9.35}$$

For $f_L > f_{cr}$ or contour lengths small compared to the persistence length $L < L_p/2$, however, there are also pronounced finite size effects for strong stretching in the force range $f_{cr} < f < f_L$.

For *weak stretching* $f \ll f_{cr}$ we find from (9.30) a linear response behavior

$$\frac{L_f}{L} \;\approx\; \frac{4}{d(d-1)}\mathcal{L}\left(\frac{\tilde{L}_p}{L}\right)\frac{f}{f_{cr}}\ , \tag{9.36}$$

which has also pronounced finite size effects as described by the function $\mathcal{L}(x)$, see eq. (9.29), and depending on the ratio $\tilde{L}_p/L = (2/(d-1))(f_L/f_{cr})^{1/2}$. This might explain difficulties in fitting experimental results for actin filaments [221], which typically have contour lengths comparable to or smaller than the persistence length L_p.

Inextensible SHC

Next we take into account effects from the discrete structure of the SHC, i.e., the force scale f_κ becomes accessible but we still consider an inextensible chain with $f \ll f_{k,cr} \ll f_k$. In particular this implies $f_\kappa \ll f_{k,cr}$ and thus $f_{k,cr}$ is given by (9.32). Then we can use the SHC model (9.2) without the last term. For *strong stretching* $f \gg f_{cr}$ the result (9.23) gives additional corrections leading to

$$\frac{L_f}{L} = 1 - \frac{d_\perp}{4}\left(\frac{f_{cr}}{f}\right)^{1/2}\frac{1}{(1+f/f_\kappa)^{1/2}} - \frac{d_\perp}{2}\frac{(f_{cr}f_L)^{1/2}}{f}. \tag{9.37}$$

In the limit $f \ll f_\kappa$ the result reduces to the above formula (9.34) for the inextensible, continuous SHC but for $f \gg f_\kappa$ the behavior changes, and we find

$$\frac{L_f}{L} = 1 - \frac{d_\perp}{4}\frac{(f_{cr}f_\kappa)^{1/2}}{f} = 1 - \frac{d_\perp}{2}\frac{T}{fb_0},\quad \text{for}\ \ f \gg f_\kappa, \tag{9.38}$$

where we can neglect finite size effects as $f \gg f_\kappa$ entails $f \gg f_L$ according to (9.14). Thus we obtain $1 - L_f/L \propto 1/f$ for large f which is reminiscent of force–extension relations for freely jointed chain models. The limit $f \gg f_\kappa$ can be realized for small bending rigidities κ. For vanishing κ, it is obvious that the inextensible SHC model (9.2) without the last term indeed reduces to a freely jointed chain. Note that (9.38) is identical to the strong stretching limit of the corresponding force–extension relation for a freely jointed chain. In terms of the blob picture, this is due to the fact that for $f \gg f_\kappa$ the crossover or blob length becomes smaller than the bond length $\xi_f \ll b_0$ such that the force effectively stretches *independent* discrete bonds as in a freely jointed chain model [227].

As effects from the discrete chain structure are only relevant for $f \gg f_\kappa$, but we consider the situation $L_p \gg b_0$ or $f_\kappa \gg f_{cr}$, see (9.13), the *weak stretching* regime $f \ll f_{cr}$ displays the same behavior as for the inextensible, continuous SHC that we discussed in the previous section.

Extensible SHC

Now we want to consider the situation where the extensibility of the SHC becomes relevant, i.e., the force range $f \gg f_{k,cr}$ or even $f \gg f_k$. Then we use the full Hamiltonian (9.2) of the extensible SHC. For *strong stretching* $f_{\text{eff}} \gg f_{cr}$ (or $f \gg f_{cr}$ if $f_k \gg f_{cr}$, see (9.15), holds), we then have to use the full result (9.23) for the force–extension relation as well. The full result (9.23) has various limits depending on the relative size of f_κ, f_k, and the stretching force f or f_{eff}. They all have in common that for $f_{k,cr} \ll f \ll f_k$ the elastic response of the stretched bonds can no longer be neglected and for $f \gg f_k$ it becomes the leading term, $L_f/L \simeq f/f_k$. The subleading terms can display different behavior.

In the previous section we have already discussed the inextensible limit of a discrete chain in the force regime $f_\kappa \ll f \ll f_{k,cr}$, where we found a crossover to a freely jointed chain behavior resulting in (9.38). If the chain is extensible and f/f_k is no longer a small parameter, a freely jointed chain behavior sets in already for $f_{\text{eff}} \gg f_\kappa$, which is equivalent to $f \gg (f_\kappa f_k)^{1/2}$ if $f \gg f_k$, and relation (9.38) becomes modified to

$$\frac{L_f}{L} = \frac{f}{f_k} + 1 - \frac{d_\perp}{4}\frac{(f_{cr} f_\kappa)^{1/2}}{f}\frac{1 + 2f/f_k}{1 + f/f_k}, \text{ for } f_{\text{eff}} \gg f_\kappa \ . \tag{9.39}$$

The subleading terms $f/f_k + 1 - L_f/L \propto 1/f$ still show force–extension behavior reminiscent of freely jointed chain models but with a modified prefactor. The modification of the prefactor leads to an apparently reduced bond length

$$b_{\text{app}} = b_0 \frac{1 + f/f_k}{1 + 2f/f_k} \approx b_0 \left(1 - \frac{f}{f_k}\right) \tag{9.40}$$

of the freely jointed chain as compared to the inextensible case. The force–extension curve as described by (9.39) has a point of inversion if plotted logarithmically, i.e., $\ln (f/f_{cr})$ as function of L_f/L. The point of inversion is located at a force $f \approx f_{k,cr}$, where $f_{k,cr}$ is given by (9.32) in this force regime.

Also in the *weak stretching* regime $f \ll f_{cr}$ we have to use the full result (9.30) for an extensible SHC. However, the differences to the results for inextensible chains are small if $f_{cr} \ll f_k$, see (9.15), as for weak stretching we consider forces $f \ll f_{cr}$ and thus $f \ll f_k$.

Extensible, continuous SHC

Finally, we want to consider the extensible, continuous limit of the SHC. This means we consider forces $f_{\text{eff}} \ll f_\kappa$ but $f/f_{k,cr}$ or even f/f_k are no longer small. Then we can use the continuous SHC model (9.6). In particular, we will consider the situation $f \gg f_{k,cr}$, otherwise the chain becomes effectively inextensible again, and our above results for the worm-like chain apply. For *strong stretching* $f_{\text{eff}} \gg f_{cr}$ [or $f \gg f_{cr}$ if $f_k \gg f_{cr}$, see (9.15), holds], our result (9.23) becomes

$$\frac{L_f}{L} = \frac{f}{f_k} + 1 - \frac{d_\perp}{4}\left(\frac{f_{cr}}{f}\right)^{1/2} \frac{1+2f/f_k}{(1+f/f_k)^{1/2}}, \text{ for } \; f \gg f_{k,cr}, f_L, \tag{9.41}$$

where we have also neglected finite size corrections as we want to focus on forces $f \gg f_L$. This limiting case has also been obtained in Ref. [226] and has to be compared to the force–extension relation (9.35) of Marko and Siggia [146] for the worm-like chain. The first term in (9.41) is equivalent to the correction introduced already by Odijk [223] and describes the overall elastic response of a chain with stretch modulus k. However, there is an additional correction due to the extensibility in the third term, which gives an apparently reduced bending rigidity

$$\kappa_{\text{app}} = \kappa \frac{1+f/f_k}{(1+2f/f_k)^2} \approx \kappa\left(1 - \frac{3f}{f_k}\right) \tag{9.42}$$

as compared to the inextensible worm-like chain. The apparent reduction of κ stems from the coupling of thermally fluctuating bond extensions to both the external force and the bond directions. Fits of experimental force–extension curves using the inextensible worm-like chain model result (9.35) will thus measure the apparent parameter κ_{app} rather than the actual parameter κ.

Only in the force range $f_{k,cr} \ll f \ll f_k$, we can neglect the correction terms such that $\kappa_{\text{app}} \approx \kappa$ and we find the force–extension relation proposed by Odijk [223]

$$\frac{L_f}{L} = \frac{f}{f_k} + 1 - \frac{d_\perp}{4}\left(\frac{f_{cr}}{f}\right)^{1/2}, \text{ for } \; f_k \gg f \gg f_{k,cr}, f_L. \tag{9.43}$$

In the absence of finite size effects, i.e., focusing on forces $f \gg f_L$, the force–extension curves as described by (9.41) or (9.43) have a point of inversion if plotted logarithmically, i.e., $\ln(f/f_{cr})$ as function of L_f/L. The point of inversion is located at a force $f \approx 4^{-2/3} f_{k,cr}$ [223] where $f_{k,cr}$ is given by (9.31) and $f_{k,cr} \ll f_k$.

Application: F–actin

In Ref. [183], we have derived interpolation formulae which interpolate between the weak stretching and strong stretching results, which are accurate within 10%. The interpolation

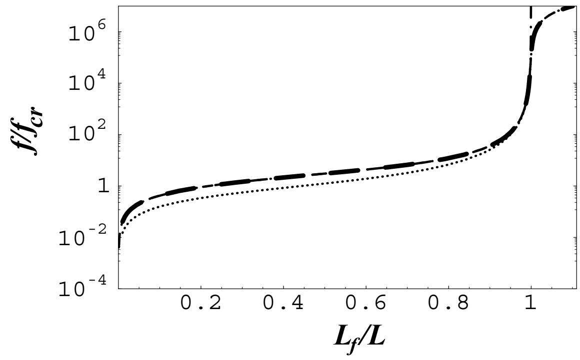

Figure 9.3: Logarithmic plots of the force–extension relations (f/f_{cr} as function of L_f/L) for SHCs in $d = 3$. The thick dashed curve shows an interpolation formulae from Ref. [183] for an *extensible* SHC with parameters $B \equiv f_{cr}/f_\kappa = (b_0/L_p)^2 = 10^{-6}$, $\tilde{L}_p/L = 1$, and $f_k/f_{cr} = 10^8$ appropriate for F–actin. The dashed and dotted curves show the limiting cases $B = 0$, $\tilde{L}_p/L = 1$ and $B = \tilde{L}_p/L = 0$, respectively. The dashed dotted curve shows an *inextensible* SHC ($f/f_k = 0$) for the same parameters $B = 10^{-6}$, $\tilde{L}_p/L = 1$.

formulae can be used to illustrate and apply our results to F–actin (see Fig. 9.3) whose force–extension relation has been experimentally studied in [221] in $d = 3$.

With a measured persistence length of $L_p \simeq 20\mu$m [221], the crossover force $f_{cr} = 2T/L_p$ between weak and strong stretching is estimated as $f_{cr} = 2T/L_p \sim 4 \times 10^{-5}$pN for F–actin. In the experiments in [221] stretching was performed with forces up to $f \sim 300$pN, corresponding to $f/f_{cr} \sim 10^6$. The bond length b_0 for actin can be estimated by the size of a G–actin monomer as $b_0 \simeq 10$nm [232] such that $b_0/L_p \sim 10^{-3}$ or $f_\kappa/f_{cr} \sim 10^6$. For the characteristic stretching force $f_k = kb_0$ a value $f_k \sim 35$nN has been obtained in Ref. [221] corresponding to $f_k/f_{cr} \sim 10^8$. This leads to an extensibility crossover force scale $f_{k,cr} \simeq (f_k^2 f_{cr})^{1/3} \sim 40$pN or $f_{k,cr}/f_{cr} \sim 10^5$, which determines the point of inversion in the logarithmic plots in Figure 9.3 at $f \approx 4^{-2/3} f_{k,cr}$. In Ref. [221] the persistence length of F–actin is comparable to the contour length, $L \sim \tilde{L}_p$. This leads to rather large corrections at low forces with $\mathcal{L}(\tilde{L}_p/L) \approx 0.4$. For $L \sim \tilde{L}_p$, the force scale f_L is comparable to f_{cr}, i.e., $f_L \sim f_{cr}$.

In Figure 9.3 we visualize the effects from extensibility, discrete chain structure, and finite size effects. We show the full interpolation formula derived in Ref. [183] that includes all three effects in comparison to limiting cases that neglect one of these effects. It is clearly seen that for F–actin finite size effects have a more pronounced effect on the force-extension curve than effects from the discrete chain structure. Also effects from the extensibility are noticeable at the highest forces [221]. In particular, the point of inversion is well observable in the experiment, although the relative bond extensions are rather small with $\langle\epsilon\rangle = f/f_k \sim 10^{-2}$ for high stretching forces of $f \sim 300$pN.

9.7 Conclusion

We have studied the stretching of extensible semiflexible polymers using the discrete extensible SHC model that additionally contains microscopic degrees of freedom describing elastic bonds. The bond stretching depends on the bond direction such that thermal fluctuations of the bonds length lead to an effectively increased stretching of the bond directions. This manifests as an additional forcing term in the effective Hamiltonian (9.2) that is obtained after performing the partial trace over thermally fluctuating extensions of the elastic bonds. We derived force–extension relations (9.23) and (9.30) for the SHC model for strong and weak stretching, respectively, which took into account effects from the extensibility and the discrete chain structure as well as finite size effects. The result can be used to discuss various important limiting cases. In the limit of strong stretching the discrete chain structure can lead to behavior reminiscent of a freely jointed chain at very large tensile forces whereas for weak stretching a continuous description is fully justified. On the other hand, we have to consider finite size corrections for weak stretching if the contour length becomes comparable to the persistence length as it is typically the case for filamentous semiflexible polymers such as F–actin. The results can be combined into interpolation formulae for the force–extension relations of extensible semiflexible polymers, which is described in detail in Ref. [183]. In Ref. [183], we also use a complementary transfer matrix treatment of the SHC model combined with a variational calculation to analyze the crossover at intermediate forces. The numerical transfer matrix diagonalization provides exact numerical force–extension curves which we used to determine the accuracy of interpolation formulae and variational calculation. For the interpolation formulae the agreement is within 10% accuracy, even in the presence of finite size corrections. The results are relevant to experiments on DNA or F–actin and we have illustrated our results with explicit estimates for F–actin using experimental results of Ref. [221].

Chapter 10

Unbinding and Desorption

A complete classification for unbundling transitions of two semiflexible polymers and for desorption transitions of such polymers at planar surfaces is presented. The interaction potentials can depend both on the polymer/polymer (or polymer/surface) separation and on the orientation of the polymers. Using analytical transfer matrix methods and scaling arguments, the order of the transitions and the corresponding critical exponents are obtained for all types of interaction potentials in arbitrary spatial dimension $d = 1 + d_\perp$. We also establish a duality mapping between the restricted partition sums in the absence and the presence of a short-range attraction, which allows us to obtain exact results for the critical exponents related to the unbinding transition, the transition point and transition order. Our results are applicable to biopolymers or polyelectrolytes with large persistence lengths such as actin filaments, microtubules, or DNA.

10.1 Introduction

Semiflexible polymers such as DNA or actin filaments have a large bending stiffness and, thus, a large persistence length, L_p. On scales which exceed L_p, the orientational order of the polymer segments decays exponentially, and the polymer effectively behaves as a flexible chain with the segment size set by L_p. In contrast, on length scales which are small compared to L_p, the bending energy of the semiflexible polymer plays an equally important role and strongly affects the behavior of the polymer. The persistence lengths of the most prominent biopolymers range from 100nm for DNA [135], to the μm-range for actin [132, 133, 134] or even up to the mm-range for microtubules [133].

Semiflexibility is also crucial for the bundling of such biopolymers and for their adsorption onto adhesive surfaces as schematically shown in Fig. 10.1. Important examples are bundles of F-actin which are crosslinked with various types of sticker molecules [235, 236] and the adsorption of polyelectrolytes onto oppositely charged surfaces [237]. Unbundling and desorption transitions arise from the competition between the energy gained by binding to an attractive potential well and the associated loss of configurational entropy. As one increases the bending rigidity and, thus, the persistence length, this entropy loss is reduced and the polymers bundle and adsorb more easily. One case which is particularly interesting from an experimental point of view is the adsorption of semiflexible polymers onto planar

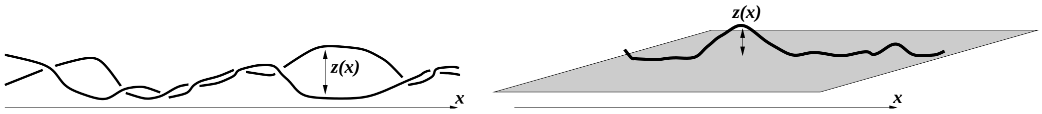

Figure 10.1: Left: Bundling of two semiflexible polymers. Right: Adsorption of a semiflexible polymer onto a planar substrate.

substrates in three dimensions. Since the shape fluctuations parallel to such a substrate are not affected by the interaction potential between polymer and substrate, this case is equivalent to bundling in two dimensions.

For bundling (or adsorption), the potential of the polymer/polymer (or polymer/surface) interactions contains both an attractive potential well and a repulsive hard wall or rod. On the one hand, all potential wells which arise from intermolecular forces are short-ranged in the sense that they decay faster than $1/|\mathbf{z}|^{2/3}$ for large separations $|\mathbf{z}|$ of the interacting objects [117, 159]. On the other hand, these attractive wells may not only depend on $|\mathbf{z}|$ but also on the orientation of the polymers. One example for the latter situation is provided by crosslinkers or stickers which bind with a preferred angle to the semiflexible polymers such as α-actinin or fimbrin which crosslink F-actin [235, 236].

For all of these potentials, the competition between bending energy and configurational entropy leads to an unbundling or desorption transition at a certain critical temperature (or potential depth). Our analytical solutions give explicit expressions for these transition points as well as for the critical exponents which characterize the corresponding critical behavior. Two exponents, χ and θ, characterize the probability distribution of the polymers. The exponent governs the contact probability which scales as $1/\xi_{\|}^{\chi}$ with the longitudinal correlation length $\xi_{\|}$, and the exponent θ governs the segment distribution close to the potential. Another critical exponent, $\nu_{\|}$, governs the longitudinal correlation length and the singular part of the free energy. This implies that $\nu_{\|}$ determines the order of the transition provided $\nu_{\|} \geq 1$.

Somewhat surprisingly, we find that the exponent $\nu_{\|}$ is changed by the orientation dependence of the interaction potentials whereas this dependence does not affect the two exponents χ and θ. Therefore, two systems, which are characterized by the same values for the exponents χ and θ, may differ in the order of their transitions. One example is provided by desorption from a planar substrate which is *second* order if the interaction potential is independent of the polymer orientation but *first* order if it is orientation-dependent. Different values for $\nu_{\|}$ are also found for symmetric potential wells in the absence of hard walls. Furthermore, the hard rod repulsion is argued to be *irrelevant* in $d \geq 3$ dimensions.

Our analytical approach starts from the differential transfer matrix equation discussed previously in [238, 239, 240]. We study the corresponding eigenvalue equation for the localized ground state and derive a general integral expression for it. In order to obtain explicit solutions, we consider attractive potential wells with potential range ℓ_a and determine the matching conditions at ℓ_a. In the limit of *small* ℓ_a, these matching conditions become analytically tractable and lead to two relations: the first relation determines the scaling form of the probability distribution and, thus, the critical exponents χ and θ; the second relation determines the transition point and the critical exponent $\nu_{\|}$. Our results for the critical exponents are expected to apply to all short-range interaction potentials, i.e., to all potentials which decay faster than $1/|\mathbf{z}|^{2/3}$ for large separations $|\mathbf{z}|$.

It is instructive to compare the unbinding transition of semiflexible polymers interacting with a short-ranged attractive and a repulsive hard rod potential to the corresponding unbinding transitions of fluid membranes, which are higher-dimensional elastic manifolds also governed by their bending rigidity [154, 155, 156]. In general, we can consider $d_{\|}$-dimensional membranes in $d = d_{\|} + 1$ spatial dimensions, and a semiflexible polymer in $d = 1 + 1$ dimension can be viewed as a one-dimensional membrane ($d_{\|} = 1$). The unbinding transition of membranes arises from the interplay of attractive intermolecular forces, such as van der Waals or screened electrostatic forces, and repulsive entropic forces, and has been observed experimentally in three spatial dimensions, e.g., for lipid bilayers in Refs. [157, 158]. The entropic repulsion of semiflexible polymers decays as $1/|\mathbf{z}|^{2/3}$ with their separation $|\mathbf{z}|$, which is a special case of the entropic repulsion law $1/|\mathbf{z}|^{2d_{\|}/(4-d_{\|})}$ for membranes [154, 117, 159]. All short-range attractive potentials decaying faster than the respective entropic repulsion are expected to be in the same universality class, which has been called "strong fluctuation regime" for membranes [154, 117, 159]. For this class of potentials a simple mean-field like superposition of microscopic potentials and entropic repulsion fails [154, 159], and more exact methods, such as renormalization group studies [154, 117] or transfer matrix methods for one-dimensional polymers, have to be applied. In Ref. [154] it has been shown that membranes with short-range attractive interactions undergo a continuous unbinding transition with characteristic critical exponents at a certain critical interaction potential strength. For semiflexible polymers, the order of the unbinding transition depends also on the codimension $d_{\perp}$ and the orientation dependence of the interaction potentials. For the case $d_{\perp} = 1$ and in the absence of an orientation dependence in the interaction potential, which corresponds to a one-dimensional membrane, we find a continuous unbinding transition in agreement with Ref. [154].

10.2 Model

We consider polymer chains (or long polymer segments) with bending rigidity κ and persistence length $L_p = 2\kappa/T$ where T is the temperature in energy units. These polymers have a contour length L_c which is comparable to or smaller than L_p. In this regime, the semiflexible polymer is oriented along one axis, say the x-axis as in Fig. 10.1, and can be parameterized by displacements $\mathbf{z}(x)$ perpendicular to the x-axis with $0 < x < L$ where L is the projected length of the polymer. We consider polymers in $d = 1 + d_{\perp}$ dimensions for which $\mathbf{z}$ is a $d_{\perp}$-dimensional vector. This parameterization is appropriate provided (i) one does not focus on the properties of the polymer ends such as the distribution of the end-to-end distance [241] and (ii) the longitudinal correlation length $\xi_{\|}$ to be defined below is small compared to L_p.

The conformations of the polymer are governed by the interplay between its bending energy $\int_0^L dx \frac{1}{2}\kappa\left(\partial_x^2 \mathbf{z}\right)^2$ and its potential energy $\int_0^L dx V(\mathbf{z}(x))$ where $V(\mathbf{z}(x))$ contains an attractive potential well of range ℓ_a which favors the straight configuration $\mathbf{z}(x)=0$. The unbundling of a pair of semiflexible polymers interacting with the potential $V(\mathbf{z}_1-\mathbf{z}_2)$ is equivalent to the unbinding of a single polymer with relative coordinate $\mathbf{z}=\mathbf{z}_1-\mathbf{z}_2$ and effective $\kappa=\kappa_1\kappa_2/(\kappa_1+\kappa_2)$ from the external potential $V(\mathbf{z}(x))$.

We model the attractive part of the interaction potentials as spherical potential wells of radius ℓ_a. Such binding potentials can arise from van der Waals forces, screened electrostatic interactions, and crosslinking molecules. In these cases, the potential range ℓ_a is comparable to the polymer thickness, the Debye-Hückel screening length, and the size of the linker molecule, respectively. For van der Waals forces and for electrostatic interactions dominated by ion-ion interactions, the attractive potential does not depend on the orientation of the polymer segments. For crosslinker-mediated adhesion, on the other hand, such an orientation-dependence arises if the linker molecules prefer to bind to polymer segments at a preferred angle as applies, e.g., to the crosslinkers α-actinin and fimbrin [235, 236] which prefer to bind to F-actin at right angles. Therefore, we will consider generalized potential wells which depend on the tangent vector $\mathbf{v}\equiv\partial_x\mathbf{z}$ and have the form

$$\begin{aligned} V_a(\mathbf{z},\mathbf{v}) &= W\Phi_\Delta(\mathbf{v}) = G_\Delta\Phi_\Delta(\mathbf{v})/c(d_\perp)\ell_a^{d_\perp} && \text{for} \quad |\mathbf{z}|<\ell_a \\ &= 0 && \text{for} \quad |\mathbf{z}|>\ell_a \end{aligned} \tag{10.1}$$

with potential strength $W \equiv G_\Delta/c(d_\perp)\ell_a^{d_\perp} < 0$, $c(d_\perp) \equiv \pi^{d_\perp/2}/\Gamma(1+d_\perp/2)$, and the dimensionless function $\Phi_\Delta(\mathbf{v})$. This potential well attains the asymptotic form $V_a(\mathbf{z},\mathbf{v}) \approx G_\Delta\Phi_\Delta(\mathbf{v})\delta(\mathbf{z})$ in the limit of small ℓ_a. It will be convenient to consider a general class of functions $\Phi_\Delta(\mathbf{v})$ which satisfy the homogeneity relation $\Phi_\Delta(b\mathbf{v}) = b^{-d_\perp\Delta}\Phi_\Delta(\mathbf{v})$. Orientation-independent interactions arising, e.g., from electrostatic forces correspond to $\Delta=0$ and $\Phi_0(\mathbf{v})=1$; linker molecules, which bind at right angles to *both* filaments, allow binding only for parallel polymer segments and correspond to $\Delta=1$ and $\Phi_1(\mathbf{v})=\delta(\mathbf{v})$.

In order to study adsorption of semiflexible polymers on planar surfaces or to take the mutual avoidance of the polymers into account, we include a repulsive potential $V_r(\mathbf{z})$ with $V_r=\infty$ for $|\mathbf{z}|<\ell_w$ with $\ell_w<\ell_a$. In $d_\perp=1$, this is equivalent to a hard wall (or a half space geometry) with $z>0$; in higher dimensions, the potential $V=V_r$ excludes the polymer from a hard rod around $|\mathbf{z}|=0$. In the following, we will study both purely attractive potentials $V=V_a$ and potential wells in front of a hard wall or rod as described by $V=V_a+V_r$.

10.3 Transfer matrix

It is convenient to measure all length scales in units of the persistence length L_p and all energies in units of T. Thus, we introduce the dimensionless quantities

$$\begin{aligned} &\bar{\mathbf{z}}=\mathbf{z}/L_p, \quad \bar{x}=x/L_p, \quad \bar{\mathbf{v}}=\mathbf{v}, \\ &\bar{V}(\bar{\mathbf{z}},\bar{\mathbf{v}}) = L_pV(\bar{\mathbf{z}}L_p,\bar{\mathbf{v}})/T \quad (\bar{\ell}_a=\ell_a/L_p \;\text{ and }\; \bar{G}_\Delta = L_p^{1-d_\perp}G_\Delta/T). \end{aligned} \tag{10.2}$$

In the following, we will use these dimensionless quantities but suppress the overbars for ease of notation. The restricted partition sum of a single semiflexible polymer is then given by

$$Z(\mathbf{z},\mathbf{v};\mathbf{z}_0,\mathbf{v}_0;L) = \int_{(\mathbf{z}_0,\mathbf{v}_0;0)}^{(\mathbf{z},\mathbf{v};L)} \mathcal{D}\mathbf{z}'(x) \exp\left\{-\int_0^L dx \left[\frac{1}{4}\left(\partial_x^2 \mathbf{z}'\right)^2 + V(\mathbf{z}',\partial_x \mathbf{z}')\right]\right\} \quad (10.3)$$

where $\mathbf{z} \equiv \mathbf{z}'(L)$ and $\mathbf{v} \equiv \partial_x \mathbf{z}'(L)$ now denote the end points and end tangents of the chain and $\mathbf{z}_0 \equiv \mathbf{z}'(0)$ and $\mathbf{v}_0 \equiv \partial_x \mathbf{z}'(0)$ specify the initial point and tangent of the chain. In the following, we will study (10.3) by transfer matrix methods. This leads to the differential equation [238, 239]

$$\partial_L Z = -\mathbf{v} \cdot \nabla_{\mathbf{z}} Z + \nabla_{\mathbf{v}}^2 Z - V(\mathbf{z},\mathbf{v}) Z \quad (10.4)$$

with the boundary condition $Z(\mathbf{z},\mathbf{v};\mathbf{z}_0,\mathbf{v}_0;0) = \delta(\mathbf{z}-\mathbf{z}_0)\delta(\mathbf{v}-\mathbf{v}_0)$. First, we focus on the case $\mathbf{z}_0 = \mathbf{0}$ and $\mathbf{v}_0 = \mathbf{0}$ and consider the quantity $Z(\mathbf{z},\mathbf{v};L) \equiv Z(\mathbf{z},\mathbf{v};\mathbf{0},\mathbf{0};L)$.

10.4 Scaling behavior

For $V = 0$, the solution of (10.4) has the scaling form

$$Z(\mathbf{z},\mathbf{v};L) = L^{-2d_\perp} \Omega_0 \left(|\mathbf{z}|/L^{3/2}, |\mathbf{v}|/L^{1/2}, \vartheta\right) \quad (10.5)$$

where ϑ is the angle enclosed by $\mathbf{z}$ and $\mathbf{v}$ (with $\vartheta = 0, \pi$ for $d_\perp = 1$). In this case, the shape function is given by [238, 240]

$$\Omega_0(y,u,\vartheta) = \left(\frac{\sqrt{3}}{2\pi}\right)^{d_\perp} \exp\left(-3y^2 + 3yu\cos\vartheta - u^2\right). \quad (10.6)$$

The expression (10.5) implies $\langle|\mathbf{v}|^2\rangle \sim L$ for the tangents and $\langle|\mathbf{z}|^2\rangle \sim L^3$ for the displacements.

If the polymer is bound to a sufficiently strong attractive potential, its partition function behaves as $Z(\mathbf{z},\mathbf{v};L) \sim Z_E(\mathbf{z},\mathbf{v})\exp(-EL)$ for large system size L where the ground state Z_E satisfies the eigenvalue equation

$$-EZ_E = -\mathbf{v} \cdot \nabla_{\mathbf{z}} Z_E + \nabla_{\mathbf{v}}^2 Z_E - V(\mathbf{z},\mathbf{v}) Z_E \quad (10.7)$$

with ground state energy $E < 0$. The normalization $\int d^{d_\perp}\mathbf{z} \int d_\perp^d \mathbf{v} Z_E(\mathbf{z},\mathbf{v}) Z_E(\mathbf{z},-\mathbf{v}) = 1$ and the boundary condition for $Z(\mathbf{z},\mathbf{v};0)$ imply the asymptotic equality $Z(\mathbf{z},\mathbf{v};L) \approx Z_E(\mathbf{z},\mathbf{v}) Z_E(0,0)\exp(-EL)$ for large L.

The attractive potential modifies the scaling result (10.5) in two ways: (i) The system is now characterized by the longitudinal correlation length $\xi_\| = 1/|E|$ parallel to the polymer which diverges upon approaching the unbinding transition at $E = 0$ and (ii) The small distance behavior at $z = 0$ is affected by the potential and we expect the more general scaling form

$$Z(\mathbf{z},\mathbf{v};L) = \xi_\|^{-\chi} |\mathbf{z}|^{\theta/2} \Omega\left(|\mathbf{z}|/\xi_\|^{3/2}, |\mathbf{v}|/|\mathbf{z}|^{1/3}, \vartheta\right) e^{L/\xi_\|} \quad (10.8)$$

where we used the relation $\langle|\mathbf{v}|^2\rangle \propto \langle|\mathbf{z}|^2\rangle^{1/3}$ to reformulate the scaling in $|\mathbf{z}|$. Furthermore, we implicitly assumed a rotationally invariant potential $V = V(|\mathbf{z}|, |\mathbf{v}|)$ for $d_\perp > 1$.

The scaling form (10.8) depends on the two exponents χ and θ, which are not independent but related by a normalization condition which gives $\chi = 2d_\perp + 3\theta/2$ for $\chi > 0$. The latter relation was first derived in [238] for $d_\perp = 1$. For $2d_\perp + 3\theta/2 < 0$, the main contributions in the normalization integral come from small scales which implies $\chi = 0$ and thus the more general exponent relation

$$\chi = \max\left(2d_\perp + \frac{3}{2}\theta, 0\right). \tag{10.9}$$

The dominance of small scales for $2d_\perp + 3\theta/2 < 0$ and $\chi = 0$ indicates that a finite fraction of polymer segments remains bound at the transition point which is analogous to the behavior of strings in $d \geq 1 + 4$ dimensions [242].

10.5 Potential well in $1 + 1$ dimensions

We first consider a purely attractive potential $V = V_a$ as defined in (10.1) in 1+1 dimensions. We start from a matching procedure at the boundary of the potential well, i.e., at $|z| = \ell_a$, from which we determine the ground state Z_E of the eigenvalue equation (10.7). In the exterior region $|z| > \ell_a$, where V vanishes, the ground state has the form

$$Z_E(z, v) = \int d\alpha \Theta(\alpha z) A_E(\alpha) e^{-\alpha z} \psi_{\alpha,E}(v) \tag{10.10}$$

where $\Theta(y)$ is the Heaviside step function. The function $\psi_{\alpha,E}(v)$ fulfills the eigenvalue equation $\left(\alpha v + \partial_v^2\right) \psi_{\alpha,E} = -E\psi_{\alpha,E}$ and has the form

$$\psi_{\alpha,E}(v) = \psi_{-\alpha,E}(-v) = \alpha^{-1/6}\, Ai\left[-\alpha^{1/3} v - \frac{E}{\alpha^{2/3}}\right] \qquad \text{for} \quad \alpha > 0 \tag{10.11}$$

where $Ai(x)$ denotes the Airy function [234]. In order to determine the coefficient function $A_E(\alpha)$, we integrate over the interior region $|z| < \ell_a$ on both sides of (10.7) which leads to the matching condition

$$v\left(Z_E(\ell_a, v) - Z_E(-\ell_a, v)\right) \approx -G_\Delta \Phi_\Delta(v) \frac{1}{2}\left(Z_E(\ell_a, v) + Z_E(-\ell_a, v)\right) \tag{10.12}$$

in the limit of small ℓ_a. We now insert the integral representation (10.10) for Z_E which leads, after some computation, to two relations. The first relation gives the explicit expression

$$A_E(\alpha) = \mathcal{N}_E\, \psi_{\alpha,E}(0) \tag{10.13}$$

for the coefficient function $A_E(\alpha)$ where $\mathcal{N}_E$ is an α-independent normalization constant. This relation determines the distribution $Z_E(\mathbf{z}, \mathbf{v})$ via (10.10) which is found to be *independent* of $\Phi_\Delta(v)$. The normalization condition for Z_E leads to $\mathcal{N}_E \sim 1/\ln^{1/2}(1/\ell_a|E|^{3/2})$.

In this way, we *derive* the scaling form (10.8) for the partition sum of the polymer with exponents

$$\theta_a = -4/3 \quad \text{and} \quad \chi_a = 0\,(\log) \tag{10.14}$$

and the shape function

$$\Omega_a(y,u) \;\;\propto\;\; \int_0^\infty d\alpha \exp(-\alpha)\alpha^{-1/3} Ai\left[\left(\frac{y}{\alpha}\right)^{2/3}\right] Ai\left[-u\alpha^{1/3} + \left(\frac{y}{\alpha}\right)^{2/3}\right] \tag{10.15}$$

as plotted in Fig. 10.2. Apart from the logarithmic singularity, the exponents as given by (10.14) have been obtained previously by field-theoretic methods [240].

The matching condition (10.12) leads to a second implicit relation $E = E(G_\Delta)$ between the ground state energy E and the strength G_Δ of the potential in (10.1). This relation determines the transition point and, thus, the critical potential depth $G_{\Delta,c}$ for binding via the implicit equation $0 = E(G_{\Delta,c})$. In contrast to the result for the segment distribution, the relation $E = E(G_\Delta)$ is non-universal in the sense that it depends on Δ and, thus, on the potential function $\Phi_\Delta(v)$.

The critical potential depth $G_{\Delta,c}$ is found to behave as $|G_{\Delta,c}| \approx |g_{\Delta,c}|\,\ell_a^{(1+\Delta)/3}$ for small potential range ℓ_a with $|g_{0,c}| = 1/\Gamma(1/3)\,Ai[0]$ for $\Delta = 0$ and $|g_{1,c}| = 1/\Gamma(2/3)\,Ai^2[0]$ for $\Delta = 1$. Furthermore, an expansion around $G_\Delta = G_{\Delta,c}$ and $E = 0$ determines the exponent $\nu_\|$ for the longitudinal correlation length $\xi_\|$ which diverges as $\xi_\| \propto |g_\Delta - g_{\Delta,c}|^{-\nu_\|} \sim |t|^{-\nu_\|}$ where t is the reduced temperature (note that the rescaled potential strength $G_\Delta \sim 1/T^2$). This gives $1/\nu_\| = \min((1+\Delta)/2, 1)$ for the correlation length exponent; for $\Delta = 0$, this implies $\nu_\| = 2$. For $\Delta = 1$, one has $\xi_\| \sim |\log t|/t$ and $\nu_\| = 1 + \log$. The free energy of the polymer is given by the ground state energy $f = E \sim 1/\xi_\|$ and we find a *second* order delocalization transition for $0 \leq \Delta \leq 1$.

10.6 Potential well with hard wall in $1+1$ dimensions

Next, we consider an attractive potential well in front of a hard wall as described by $V = V_a + V_r$ in 1+1 dimensions. Outside of the well, i.e., for $z > \ell_a$, the ground state Z_E can again be written as in (10.10), and the coefficient function $A_E(\alpha)$ can again be determined by the corresponding matching condition. The additional boundary conditions $Z_E(0,v) = 0$ for $v > 0$, which is imposed by the hard wall at $z = 0$, can be incorporated by eigenfunctions $\phi_{\alpha,E}(v)$ which have been explicitly determined in Ref. [211] for $V = V_r$, i.e., in the absence of the potential well.

In this way, we derive again the scaling form (10.8) for the partition sum of the polymer. The critical exponents now have the values

$$\theta_{a,r} = -5/3 \quad \text{and} \quad \chi_{a,r} = \max(-1/2, 0) = 0 \tag{10.16}$$

and the shape function is given by

$$\Omega_{a,r}(y,u) \;\;\propto\;\; \int_0^\infty d\alpha \exp(-\alpha)\alpha^{-1/6} \exp\left(-\frac{2}{3}\frac{y}{\alpha}\right) Ai\left[-u\alpha^{1/3} + \left(\frac{y}{\alpha}\right)^{2/3}\right] \tag{10.17}$$

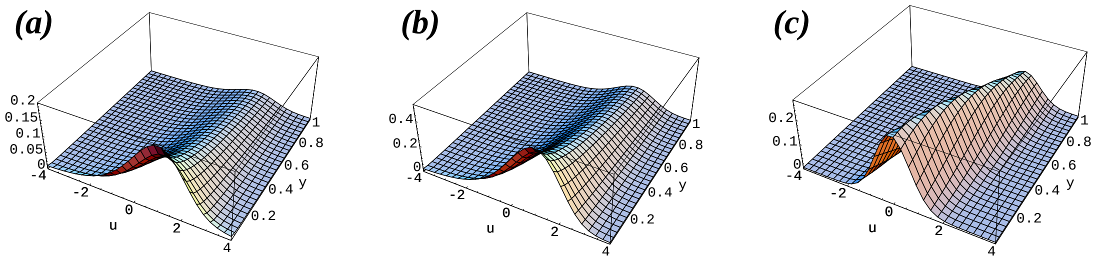

Figure 10.2: Shape functions $\Omega(y,u)$ in $1+1$ dimensions: (a), (b), and (c) exhibit the functional dependence as given by the expressions (10.15), (10.17), and (10.6) corresponding to interactions potentials $V = V_a$, $V = V_a + V_r$ and $V = 0$, respectively. [Note that $\Omega_0(y,u)$ depends on $u \equiv |\mathbf{v}|/L^{1/2}$, whereas $\Omega_a(y,u)$ and $\Omega_{a,r}(y,u)$ depend on $u \equiv |\mathbf{v}|/|\mathbf{z}|^{1/3}$.]

where we have used the asymptotic behavior $\phi_{\alpha,E}(v) \approx \pi^{-1}(3v)^{1/2}\exp\left(-2E^{3/2}/3\alpha\right)$ of the eigenfunctions for $0 < \alpha^{1/3}v \ll 1$ as obtained in [211]. As in the absence of the repulsive wall, the shape function Ω is again independent of Δ which reflects the v-dependence of the binding potential; for $E = 0$ it reduces to the special case treated in Ref. [238]. The matching condition leads again to a second relation from which we obtain the critical binding strength $|G_{\Delta,c}| \sim \ell_a^{(1+\Delta)/3}$ in the limit of small ℓ_a. For $\Delta > 0$, non-singular terms dominate in the expansion of the free energy $f = E(G_\Delta)$ around $G_\Delta = G_{\Delta,c}$, and the transition is *first* order with $\nu_{\|} = 1$ whereas it becomes *second* order with $\nu_{\|} = 1 + \log$ for $\Delta = 0$. As in the case of strings in $d \geq 1 + 4$ dimensions [242], these first order unbinding transitions are peculiar, however, since the correlation length $\xi_{\|} = 1/|E|$ diverges upon approaching the transition at $E = 0$, and polymer fluctuations exhibit scaling properties determined by the shape function $\Omega(0,u)$.

10.7 Unbundling in $1 + d_\perp$ dimensions

For $1 + d_\perp > 2$, the solution of (10.7) depends on the angle ϑ between $\mathbf{z}$ and $\mathbf{v}$ as in (10.8) which considerably complicates the analytical treatment. Progress can be made via two approximations in terms of the scaling variable $u \equiv |\mathbf{v}|/|\mathbf{z}|^{1/3}$: (i) The large-$u$-approximation which leads to $Z_E(|\mathbf{z}|,|\mathbf{v}|,\vartheta) \propto \delta(\vartheta)$, i.e., to a distribution which is localized around $\vartheta = 0$; and (ii) The small-u-approximation which leads to a spherically symmetric ground state $Z_E(|\mathbf{z}|,|\mathbf{v}|,\vartheta) = Z_E(|\mathbf{z}|,|\mathbf{v}|,0)$. For both approximations, we can construct solutions using analogous procedures as for $d_\perp = 1$. First, a solution in the region $|\mathbf{z}| > \ell_a$ is constructed and integration over the small sphere $|\mathbf{z}| < \ell_a$ on both sides of (10.7) gives matching conditions which determine the corresponding coefficient functions.

For $V = V_a$, i.e., without a hard rod, both approximations lead to the scaling form (10.8) with exponents

$$\theta_a = 4(1 - 2d_\perp)/3 \quad \text{and} \quad \chi_a = \max\left(2(1 - d_\perp), 0\right). \tag{10.18}$$

As for $d_\perp = 1$, we find that these exponents are universal and do not depend on Δ. It is interesting to note that the so-called necklace model [116] leads to the same values for θ_a and χ_a if one determines the contact probability for tangential contacts with the partition sum of the free polymer as given by (10.5). The latter values are also obtained using the field-theoretic methods in [240].

The correlation length exponent $\nu_\|$, on the other hand, is again found to depend on Δ. Both the small-u-approximation and the necklace model lead to

$$1/\nu_\| = \min\left(\frac{1}{2}(3d_\perp - 2 + d_\perp\Delta), 1\right) \tag{10.19}$$

which implies a second (or higher) order transition for $\nu_\| > 1$ and a first order transition for $0 < \nu_\| < 1$. For $d_\perp = 2$, the physically most interesting case, this implies $\nu_\| = 1$ and a *first* order unbundling transition in agreement with the Monte Carlo simulations in [240]. The critical binding strength behaves as $|G_{\Delta,c}| \sim \ell_a^{(3d_\perp-2+d_\perp\Delta)/3}$ for small ℓ_a. When expressed in terms of the original potential depth W as defined in (10.1), this implies the critical depth $|W_c| \sim (T/L_p)(L_p/\ell_a)^{(2-d_\perp\Delta)/3}$. For $\Delta = 0$, this agrees with a two-state model as in [243] when the loss of entropy is estimated by $\sim (T/L_p)(L_p/\ell_a)^{2/3}$ [199].

Finally, we want to argue that the hard rod potential $V = V_r$ is irrelevant in $d \geq 1+2$ dimensions. This is expected from the large-u-approximation for $V = V_a$ which leads to the shape function $\Omega_a(0, u, \vartheta) \sim \exp\left(-u^3/9\right)$ at the transition point with $u = |\mathbf{v}|/|\mathbf{z}|^{1/3}$ as before. In $d = 1+1$, essentially the same behavior of $\Omega_{a,r}(0, u)$ is found for $V = V_a + V_r$, i.e., for a potential well in the *presence* of a hard wall, whereas $\Omega_a(0, u)$ decays as an inverse power in u for $V = V_a$. Thus, the insertion of the hard rod in $d \geq 1+2$ should not change the critical behavior of the polymers, and the critical exponents given above should also apply for $V = V_a + V_r$. We have confirmed this expectation by Monte Carlo simulations in $d = 1+2$ dimensions as will be described elsewhere. For strings in $1 + d_\perp$ dimensions, the hard rod becomes irrelevant precisely in $d = 1+2$ dimensions as follows by extending the results of [242].

10.8 Duality mapping

The results obtained by direct transfer matrix calculations can be complemented and corroborated by a duality mapping based on the transfer matrix equations for the restricted partition sums in the absence and the presence of a short-range attraction. This duality mapping provides an independent method to obtain the unbinding and desorption transition point, the order of the transition, and, moreover, a set of scaling relations for the critical exponents of bound and unbound filaments. Furthermore this method can be easily extended to the unbinding of strings governed by tension [185].

The restricted partition sum $Z(\mathbf{z}, \mathbf{v}; \mathbf{z}_0, \mathbf{v}_0; L)$ fulfills the transfer matrix equation (10.4) with the boundary condition $Z(\mathbf{z}, \mathbf{v}; \mathbf{z}_0, \mathbf{v}_0; 0) = \delta(\mathbf{z} - \mathbf{z}_0)\delta(\mathbf{v} - \mathbf{v}_0)$ at $L = 0$. Then, the Laplace transform of $Z(\mathbf{z}, \mathbf{v}; \mathbf{z}_0, \mathbf{v}_0; L)$ with respect to L,

$$\tilde{Z}_s(\mathbf{z}, \mathbf{v}; bz_0, \mathbf{v}_0) = \int_0^\infty dL e^{-sL} Z(\mathbf{z}, \mathbf{v}; \mathbf{z}_0, \mathbf{v}_0; L), \tag{10.20}$$

fulfills a slightly different transfer matrix equation

$$s\tilde{Z}_s = -\mathbf{v}\cdot\nabla_{\mathbf{z}}\tilde{Z}_s + \nabla^2_{\mathbf{v}}\tilde{Z}_s - V(\mathbf{z},\mathbf{v})\tilde{Z}_s + \delta(\mathbf{z}-\mathbf{z}_0)\delta(\mathbf{v}-\mathbf{v}_0) \tag{10.21}$$

where the last term on the right hand side stems from the boundary condition at $L = 0$.

In the following we exploit the formal similarity of the transfer matrix equation (10.21) and the stationary eigenvalue equation (10.7) for the eigenstate $Z_E(\mathbf{z},\mathbf{v})$ to an energy eigenvalue E if we identify $s = -E$: a short-range attractive potential $V_a(\mathbf{z},\mathbf{v}) \propto -\delta(\mathbf{z}-\mathbf{z}_0)\delta(\mathbf{v}-\mathbf{v}_0)$ in the stationary transfer matrix equation (10.7) plays the role of the initial condition in the Laplace transformed transfer matrix equation (10.21) for a potential $V-V_a$, i.e., in the absence of the short-range attraction V_a. This will allow us to establish a duality mapping between the stationary transfer matrix equation for *bound* states (characterized by the set of exponents θ_b and χ_b) in a potential $V = V_r + V_a$ (where $\theta_b = \theta_{a,r}$ and $\chi_b = \chi_{a,r}$) or $V = V_a$ (where $\theta_b = \theta_a$ and $\chi_b = \chi_a$) and the Laplace transformed transfer matrix equation for *unbound* states (characterized by the set of exponents θ_u and χ_u) in a corresponding potential $V - V_a = V_r$ (where $\theta_u = \theta_r$ and $\chi_u = \chi_r$) or $V - V_a = 0$ (where $\theta_u = \theta_0 = 0$ and $\chi_u = \chi_0 = 2d_\perp$, cf. (10.5)) lacking the short-range attractive part.

We first consider the case $\Delta = 1$. A semiflexible polymer in a bound state $Z^V_E(\mathbf{z},\mathbf{v})$ fulfills the stationary transfer matrix equation (10.7) for a potential V containing the short-range attraction $V_a(\mathbf{z},\mathbf{v}) = G_1\delta(\mathbf{z}-\mathbf{z}_0)\delta(\mathbf{v}-\mathbf{v}_0)$, where we will consider the limit of small $|\mathbf{z}_0|$ and $|\mathbf{v}_0|$. We compare the stationary transfer matrix equation (10.7) with the Laplace transformed transfer matrix equation (10.21) for $\tilde{Z}^{V-V_a}_s(\mathbf{z},\mathbf{v};\mathbf{z}_0,\mathbf{v}_0)$ with $s = -E$ and for a potential $V - V_a$ without short-range attraction. If we rewrite $\delta(\mathbf{z}-\mathbf{z}_0)\delta(\mathbf{v}-\mathbf{v}_0) = \delta(\mathbf{z}-\mathbf{z}_0)\delta(\mathbf{v}-\mathbf{v}_0)\tilde{Z}^{V-V_a}_s(\mathbf{z},\mathbf{v};\mathbf{z}_0,\mathbf{v}_0)/\tilde{Z}^{V-V_a}_s(\mathbf{z}_0,\mathbf{v}_0;\mathbf{z}_0,\mathbf{v}_0)$ we find that both equations are equivalent and solutions have the same normalization if the following two conditions are fulfilled:

$$\begin{aligned} Z^V_E(\mathbf{z},\mathbf{v}) &= \mathcal{N}_E\tilde{Z}^{V-V_a}_{-E}(\mathbf{z},\mathbf{v};\mathbf{z}_0,\mathbf{v}_0) \\ &\qquad \text{with } \mathcal{N}_E^{-2} = \int_{\mathbf{z}}\int_{\mathbf{v}} \tilde{Z}^{V-V_a}_{-E}(\mathbf{z},\mathbf{v}|\mathbf{z}_0,\mathbf{v}_0)\tilde{Z}^{V-V_a}_{-E}(\mathbf{z},-\mathbf{v}|\mathbf{z}_0,\mathbf{v}_0) &(10.22)\\ -G_1^{-1} &= \tilde{Z}^{V-V_a}_{-E}(\mathbf{z}_0,\mathbf{v}_0;\mathbf{z}_0,\mathbf{v}_0) = Z^V_E(\mathbf{z}_0,\mathbf{v}_0)/\mathcal{N}_E\ . &(10.23)\end{aligned}$$

These two conditions define the duality mapping for semiflexible polymers between transfer matrix equations for potentials V and $V-V_a$ for the case $\Delta = 1$. This exact mapping can be generalized to arbitrary Δ if we use the additional assumption that $\tilde{Z}^{V-V_a}_{-E}(\mathbf{z}_0,\mathbf{v}_0;\mathbf{z}_0,0) \sim \delta(\mathbf{v}_0)$ is a strongly localized function of $\mathbf{v}_0$ in the limit $\mathbf{z}_0 \approx 0$. This assumption is justified if the scaling function $\Omega_a(y,u)$ is exponentially decaying for $u \gg 1$ such that $\tilde{Z}^{V-V_a}_{-E}(\mathbf{z}_0,\mathbf{v}_0;\mathbf{z}_0,0) \approx 0$ for tangents $|\mathbf{v}_0| \gg |\mathbf{z}_0|^{1/3}$. Then we can integrate both sides of (10.21) with a kernel $\int_{\mathbf{v}_0}\Phi_\Delta(\mathbf{v}_0)\tilde{Z}^{V-V_a}_s(\mathbf{z}_0,\mathbf{v}_0;\mathbf{z}_0,0)\ldots$, which finally leads to a generalized duality mapping

$$\begin{align} Z_E^V(\mathbf{z},\mathbf{v}) &= \mathcal{N}_E \tilde{Z}_{-E}^{V-V_a}(\mathbf{z},\mathbf{v};\mathbf{z}_0,0) \notag \\ &\quad \text{with } \mathcal{N}_E^{-2} = \int_{\mathbf{z}}\int_{\mathbf{v}} \tilde{Z}_{-E}^{V-V_a}(\mathbf{z},\mathbf{v};\mathbf{z}_0,0)\tilde{Z}_{-E}^{V-V_a}(\mathbf{z},-\mathbf{v};\mathbf{z}_0,0) \tag{10.24} \\ -G_\Delta^{-1} &= \int_{\mathbf{v}_0} \Phi_\Delta(\mathbf{v}_0)\tilde{Z}_{-E}^{V-V_a}(\mathbf{z}_0,\mathbf{v}_0|\mathbf{z}_0,0) = \int_{\mathbf{v}_0}\Phi_\Delta(\mathbf{v}_0) Z_E^V(\mathbf{z}_0,\mathbf{v}_0)/\mathcal{N}_E\ , \tag{10.25} \end{align}$$

which is valid in the limit $\mathbf{z}_0 \approx 0$.

The mapping allows us to obtain results for the full potential V by solving the Laplace transformed problem for the simpler potential $V - V_a$ and give direct information on the partition sums Z_E^V and $\tilde{Z}_s^{V-V_a}$ and thus the segment distributions. Without working out explicit solutions of the transfer matrix equations, we can use the duality mapping to derive various exact exponent relations between exponents χ_u and θ_u for unbound semiflexible polymers and their respective counterparts χ_b and θ_b for bound semiflexible polymers in the presence of the short-range attraction V_a.

To derive the exponent relation for χ_u and χ_b we study the limit of small $|E|$ in (10.22) or (10.24). The scaling form for the unbound string [see eq. (10.5) for $V = 0$] determines the s-dependence of the singular part of $\tilde{Z}_s^{V-V_a}$ for small s according to $\tilde{Z}_{s,\text{sing}}^{V-V_a} \sim s^{\chi_u - 1}$. For $\chi_u < 1$ the singular part is the leading order contribution; for $\chi_u > 1$ the leading order contribution is finite, $\tilde{Z}_s^{V-V_a} \sim$ const. Using the Chapman-Kolmogorov relation, we find from (10.22) or (10.24) the singular behavior $\mathcal{N}_E \sim |E|^{1-\chi_u/2}$ for $\chi_u < 2$ for small $|E|$ and $\mathcal{N}_E \sim$ const for $\chi_u > 2$. Furthermore, $Z_E^V \sim |E|^{\chi_b/2}$ for small $|E|$ according to the scaling form (10.8). Equating powers of $|E|$ in (10.22) we arrive at the general exponent relation

$$\chi_b = \begin{cases} \max(2-\chi_u, 0) & \text{for } \chi_u > 1 \\ \chi_u & \text{for } \chi_u < 1 \end{cases} \tag{10.26}$$

This relation agrees with our direct transfer matrix calculations. For potentials $V = V_a$, for example, we can compare (10.18) and the corresponding result $\chi_0 = 2d_\perp$ for $V = 0$. The same exponent relation also holds for strings [185]. This exponent relation has been formulated in Ref. [240] based on a mapping between the renormalization group equations for strings and semiflexible polymers of different dimensionality. An equivalent exponent relation has been confirmed numerically in Ref. [238].

In order to derive the corresponding exponent relation for θ_u and θ_b, we analyze the scaling behavior of the Laplace transform $\tilde{Z}_s^{V-V_a}$ of the unbound polymer for small $|\mathbf{z}|$ in (10.22) or (10.24). We finally arrive at the exponent relation [185]

$$\theta_b = \begin{cases} \theta_u + 2(1-\chi_u)/\zeta & \text{for } \chi_u > 1 \\ \theta_u & \text{for } \chi_u < 1 \end{cases} \tag{10.27}$$

which holds both for semiflexible polymers with a roughness exponent $\zeta = 3/2$ and $\chi_u = 2d_\perp + 3\theta_u/2$ [according to the scaling law (10.9)] and for strings with a roughness exponent $\zeta = 1/2$ and $\chi_u = d_\perp/2 + \theta_u/2$. Also this relation agrees with our direct transfer matrix calculations.

Now we address the transition point, transition order, and the correlation length exponent $\nu_\|$ by analyzing the dependence of the bound state energy E on the potential strength G_Δ in relation (10.23) for $\Delta = 1$ or relation (10.25) for arbitrary Δ. We start with the case $\Delta = 1$. Setting $E = 0$ on the right hand side of (10.23) we find the transition point $G_{1,c}$. As the singular part of $\tilde{Z}_s^{V-V_a}$ for small s is $\tilde{Z}_{s,\text{sing}}^{V-V_a} \sim s^{\chi_u - 1}$, we find $G_{1,c} = 0$ for $\chi_u < 1$; thus, there is no unbinding transition for $\chi_u < 1$ and the semiflexible polymer is always in a bound state. Expanding around $E = 0$ for $\chi_u > 1$ gives $|G_{1,c}^{-1} - G_1^{-1}| \propto |E|^{1/\nu_\|} = \xi_\|^{-1/\nu_\|}$ with [1]

$$1/\nu_\| = \min(\chi_u - 1, 1) \quad \text{for} \quad \chi_u > 1 \ . \tag{10.28}$$

We also used that the linear order dominates the singular contribution to $\tilde{Z}_s^{V-V_a}$ for $\chi_u > 2$ such that the transition becomes *first order* with $\nu_\| = 1$. For $1 < \chi_u < 2$, we find $\nu_\| > 1$ and a *continuous* transition. The result (10.28) agrees with those of the necklace model [116], and it also applies to strings [185]. Relation (10.28) can be generalized to arbitrary Δ. Performing the analogous expansion in (10.25) we find

$$1/\nu_\| = \min(\tilde{\chi}_u - 1, 1) \quad \text{for} \quad \tilde{\chi}_u > 1 \ , \quad \text{where} \quad \tilde{\chi}_u \equiv \chi_u - d_\perp(1-\Delta)/2 \ . \tag{10.29}$$

For this class of potentials there is no transition for $\tilde{\chi}_u < 1$, a first order transition for $\tilde{\chi}_u > 2$ and a continuous transition for $1 < \tilde{\chi}_u < 2$. The result (10.28) is recovered for $\Delta = 1$ and $\Phi_1(\mathbf{v}) = \delta(\mathbf{v})$.

The exponent relations (10.26) and (10.28) or (10.29), together with the scaling law (10.9), allow us to calculate all critical exponents of the unbinding problem if only one exponent (χ_u or θ_u) of the unbound semiflexible polymer (or string) in the absence of the short-range attractive potential is known. These exponents are often known analytically, or can be easily obtained numerically. For $V = 0$, we have $\theta_u = \theta_0 = 0$. For $V = V_r$ and $d_\perp = 1$, we can make use of another exponent relation, $\chi_u = \chi_r = 1 + \zeta$ [209], which is also valid for both strings and filaments.

10.9 Conclusion

We have studied unbundling and desorption transitions of semiflexible polymers by analytical methods starting from the differential transfer matrix equation (10.7) for the ground state. We considered attractive potential wells, which can depend on the polymer orientation as described by the function $G_\Delta \Phi_\Delta(v)$, see (10.1), with scaling index $0 \leq \Delta \leq 1$. The distribution functions for the polymer displacements and orientations are shown to have the scaling form (10.8) and to be *independent* of Δ. In contrast, the critical exponent $\nu_\|$ for the longitudinal correlation length $\xi_\|$ is found to depend explicitly on Δ. This leads to a singular part of the free energy $\sim 1/\xi_\|$ which determines the order of the transition provided $\nu_\| \geq 1$. Therefore, two potentials which differ in Δ can lead to transitions of different order even though the distribution functions have the same scaling form. This happens in $d = 1 + 1$ dimensions in the presence of a hard wall which is equivalent to the

---

[1] This corrects two typographic errors in the corresponding eq. (20) in Ref. [185].

experimentally accessible case of desorption transitions from a planar substrate in $d = 1 + 2$ dimensions.

Using the transfer matrix approach we also derived a duality mapping between bound and unbound states of semiflexible polymers, which complements and corroborates direct transfer matrix calculations. This mapping allows us to determine the transition point and the order of unbinding and desorption transitions. We derived exponent relations for the return probability exponents χ, the segment distribution exponents θ and the correlation length exponent $\nu_\|$ from the mapping. These relations also apply to strings and allow us to determine *all critical exponents related to the unbinding and desorption transitions of both semiflexible polymers and strings from a single exponent characterizing the unbound string or filament.*

Chapter 11

Force-induced Desorption and Unzipping

The thermally assisted force-induced desorption of semiflexible polymers from an adhesive surface or the unzipping of two bound semiflexible polymers by a localized force are investigated. The phase diagram in the force-temperature plane is calculated both analytically and by Monte Carlo simulations. Force-induced desorption and unzipping of semiflexible polymers are first order phase transitions. A characteristic energy barrier for desorption is predicted, which scales with the square root of the polymer bending rigidity and governs the initial separation process before a plateau of constant separation force is reached. This leads to activated desorption and unzipping kinetics accessible in single molecule experiments.

11.1 Introduction

Peeling an adhesive fiber from a surface or separating two adhesive fibers are two basic experimental tests of elastic and adhesive fiber properties. Over the past decade, experimental force spectroscopy techniques such as atomic force microscopy (AFM) [142, 244, 220, 245], optical [143, 217] or magnetic tweezers [144, 246] have been developed, which allow to perform analogous manipulation experiments on *individual polymers* with spatial resolution in the nm-range and force resolution in the pN-range. Particularly suited for single polymer manipulation experiments are large rod-like polymers, e.g., biopolymers such as DNA or protein fibers, dendronized or charged polymers. These polymers are *semiflexible*, i.e., governed by their bending energy with typical persistence lengths L_p in the nm- or μm-regime. Quantitative analysis of force spectroscopy experiments on semiflexible polymers requires theoretical models that take into account the *combined* effects of external force, temperature, and polymer bending energy. In this chapter, we present a theory and simulations for the force-induced desorption and unzipping of semiflexible polymers. Force-induced desorption experiments with single semiflexible polymers have recently been realized by attaching adsorbed polyelectrolytes to an AFM tip [247, 248, 219, 161, 249, 250]. The most recent experiments [161, 249, 250] give access to the *single* polymer force-distance curve. Force-induced desorption is assisted by thermal fluctuations and, thus, also gives additional insight into the fundamental problem of polymer adsorption [251, 252], which has been studied intensively both analytically [253, 239, 238, 254, 255, 256, 237, 257, 258, 259, 260, 184] and by simulations [261, 262] for semiflexible polymers.

A closely related problem is the force-induced unzipping of two semiflexible polymers, e.g., the unzipping of stiff protein fibers [163]. The unzipping of DNA [162, 263], where single strands are usually modeled as *flexible* polymers, has been extensively studied theoretically [264, 265, 266, 267, 268, 269]. Two types of barrier effects have been reported previously in the context of unzipping of flexible polymers. It has been found that any *finite* polymer can unzip or desorb below the critical force by overcoming a free energy barrier, which is proportional to its total length [264]. This effect is also present for semiflexible polymers, but we will consider the thermodynamic limit of long polymers such that the bound state becomes thermodynamically stable below the critical force. Furthermore, in the unzipping of DNA another free energy barrier arises from the enhanced stiffness of double stranded DNA [267]. In this chapter, I rather focus on the situation where each of the unzipping polymers is semiflexible, and point out a generic barrier effect governed by their *intrinsic* bending rigidity.

We show that the desorption and unzipping of semiflexible polymers by localized forces are first order transitions and obtain the full phase diagram in the force-temperature plane both analytically and by Monte Carlo simulations. For semiflexible polymers, force-induced desorption or unzipping require thermal activation over a characteristic *energy barrier* that scales with the square root of the bending rigidity and is absent for fully flexible polymers. This energy barrier governs the initial separation process before a plateau of constant desorption or unzipping force is reached and has important consequences for desorption and unzipping experiments. The energy barrier is a generic bending rigidity effect and gives rise to an enhanced stability against external forces. It plays a role for the unzipping and desorption of stiff biopolymers such as DNA [162, 265, 263], protein fibers [163], or cytoskeletal filaments and in numerous materials science applications such as the delamination of thin adhesive sheets or fibers [270].

11.2 Force-induced desorption at zero temperature

First, we will focus on force-induced desorption and discuss the related problem of unzipping of two bound semiflexible polymers in the end. In the absence of thermal fluctuations ($T = 0$), a semiflexible polymer is only governed by its bending energy, and we recover a classical mechanics problem, similar to the fracture mechanics problem of splitting a thin elastic beam from a solid surface [271]. At $T = 0$, polymer excursions parallel to the adhesive surface at $z = 0$ are suppressed, and the configuration of a polymer segment of contour length L_c can be parameterized by tangent angles $\phi(s)$ with respect to the adhesive surface, where s is the arc length ($0 < s < L_c$), see Fig. 11.1a. The bending energy is given by $E_b = (\kappa/2)\int_0^{L_c} ds(\partial_s\phi)^2$, where κ is the bending rigidity of the semiflexible polymer. The adsorption energy is $E_a = \int_0^{L_c} dsV(z(s))$, where $z(s)$ is the distance of polymer segments from the adsorbing surface at $z = 0$ and $V(z)$ is a generic square well adhesion potential of small range ℓ_a with $V(z) = W < 0$ for $z < \ell_a$, $V(z) = 0$ for $z > \ell_a$, and $V(z) = \infty$ for $z < 0$ due to the hard wall. For van der Waals forces or screened electrostatic interactions the potential range ℓ_a is comparable to the polymer thickness or the Debye-Hückel screening length, respectively. For the discussion at $T = 0$ we consider a contact potential, i.e., the limit of small ℓ_a. In the absence of a desorbing force the polymer lies flat on the adhesive surface ($\phi(s) = 0$ for all s) gaining an energy $-|W|L_c$. The semiflexible polymer is peeled from the adhesive surface by a localized desorbing force $\mathbf{F}_d$ that is applied in z-direction at the end point $s = 0$. Under the influence of the force, a polymer segment $0 < s < L_d$ desorbs, which costs a potential energy $|W|L_d$. In order to map out the energy landscape of the desorption process, we consider a *constrained* equilibrium with a prescribed height h of the polymer end at $s = 0$. Then we have to minimize the sum of bending and potential energy of the polymer, $E = |W|(L_d - L_c) + E_b$ under the constraint of a fixed height $h = \int_0^{L_d} ds \sin\phi(s)$ of the end point. Minimizing with respect to L_d gives the transversality condition $\partial_s\phi(L_d) = (2|W|/\kappa)^{1/2} \equiv 1/R_{co}$ which determines the contact curvature radius R_{co}; the boundary condition at $s = L_d$ is $\phi(L_d) = 0$. We take the point $s = 0$ to be a polymer tail resulting in a boundary condition $\partial_s\phi(0) = 0$ corresponding to a free tangent. Solving the shape equation in the presence of the height constraint, we find the scaling form $\Delta E(h) \equiv E(h) - E(0) = (\kappa|W|)^{1/2}\,\mathcal{F}_E\,(h/R_{co})$ for the total energy with the two limits

$$\Delta E(h) \approx \begin{cases} 2^{7/4}3^{-1/2}h^{1/2}\kappa^{1/4}|W|^{3/4} & \text{for } h \ll R_{co} \\ |W|[h + 4(\sqrt{2}-1)R_{co}] & \text{for } h \gg R_{co} \end{cases} . \tag{11.1}$$

For the desorbed polymer length we obtain the scaling result $L_d(h) = R_{co}\mathcal{F}_L\,(h/R_{co})$ with the limits

$$L_d \approx \begin{cases} \sqrt{3}h^{1/2}R_{co}^{1/2} & \text{for } h \ll R_{co} \\ h + 2(\sqrt{2}-1)R_{co} & \text{for } h \gg R_{co} \end{cases} . \tag{11.2}$$

For $h \ll R_{co}$, the bending energy dominates, whereas for $h \gg R_{co}$, essentially the whole desorbed length L_d is lifted straight and perpendicular to the substrate except for a curved segment of length $\sim R_{co}$ around the contact point. Including the energy gain for a constant desorbing force f_d, we obtain the energy landscape $\Delta G(h) \equiv \Delta E(h) - f_d h$ at $T = 0$ as a function the height h from the result (11.1), see Fig. 11.1c. The result for $\Delta G(h)$ shows that force-induced desorption is a *first order* transition which takes place above the threshold force $f_{d,c} = |W|$; then the global energy minimum of $\Delta G(h)$ is at infinite h. For *all* force values ${}_d > f_{d,c} = |W|$, the local minimum at $h = 0$ corresponding to the firmly adsorbed state is separated by an *energy barrier* ΔG_b from the minimum at infinite h. For large forces $f_d \gg |W|$, the energy barrier $\Delta G_b \sim \kappa^{1/2}|W|^{3/2}/f_d$ scales with the square root of κ and, hence, is a consequence of the bending rigidity of the polymer. Due to this energy barrier, force-induced desorption requires either assisting thermal fluctuations or an h-dependent force $f_d(h) = \partial_h\Delta E(h)$ diverging as $h^{-1/2}$ for small h.

11.3 Thermal desorption

In the absence of a desorbing force ($f_d = 0$), the semiflexible polymer can undergo thermal desorption which we want to describe using a model connecting length scales below and above the persistence length $L_p \equiv 2\kappa/T$ ($k_b \equiv 1$). On length scales comparable or smaller than L_p, the thermally fluctuating semiflexible polymer is only weakly bent and stays oriented, say along the x-axis. Desorption can then be described by the one-dimensional distance field $z(x)$, where $0 < x < L$ and $L < L_c$ is the projected polymer length, see Fig. 11.1a. Bending and adhesion energy of the weakly bent semiflexible polymer give a Hamiltonian

$$\mathcal{H}_{\rm SF}[z(x)] = \int_0^L dx \left[\frac{\kappa}{2}(\partial_x^2 z)^2 + V(z(x))\right] \,. \tag{11.3}$$

The desorption transition for the model (11.3) has been studied by transfer matrix techniques in Ref. [184]. The critical potential strength for desorption is $W_{c,\rm SF} = -c_{\rm SF}T/\ell_a^{2/3}L_p^{1/3}$, where $c_{\rm SF} \approx \sqrt{3\pi}/2 \approx 1.5$. The transfer matrix treatment shows that the free energy difference between adsorbed and free state vanishes as

$$|f_{W,\rm SF}| \approx |W_{c,\rm SF}||w_{\rm SF}|/\ln|w_{\rm SF}|^{-1}, \tag{11.4}$$

where $w_{\rm SF} \equiv (W–W_{c,\rm SF})/W_{c,\rm SF}$. Therefore, the correlation length $\xi_\| = T/|f_{W,\rm SF}| \propto |w_{\rm SF}|^{-\nu}$ diverges with an exponent $\nu = 1 + \log$. The weak bending approximation is valid as long as tangents are small, i.e., $\langle(\partial_x z)^2\rangle \sim \xi_\|/L_p \lesssim 1$, which is fulfilled outside a window of adhesion strengths, $|W - W_{c,\rm SF}| \gtrsim T/L_p$, around the critical value $W_{c,\rm SF}$.

For $\xi_\| \gg L_p$, i.e., inside the window $|W - W_{c,\rm SF}| \ll T/L_p$, the semiflexible polymer is described as effectively flexible Gaussian polymer with $N = L_c/L_p$ Kuhn segments of length $b = L_p$ and a Hamiltonian

$$\mathcal{H}_F[z(s)] = \int_0^{L_c} ds[(3T/2L_p)(\partial_s z)^2 + V_{\rm eff}(z(s))]. \tag{11.5}$$

Each adsorbed Kuhn segment of length $b \equiv L_p$ is weakly bent and performs small scale fluctuations according to the model (11.3), which gives rise to the *effective* adsorption potential $V_{\rm eff}(z)$ of the same form as the bare potential but with an effective binding energy $W_{\rm eff} = f_{W,\rm SF} \sim W - W_{c,\rm SF}$ renormalized by entropic small scale contributions and a width $\ell_{a,\rm eff} = L_p$ set by the thermal fluctuations $\langle z^2\rangle \sim b^3/L_p = L_p^2$ of each Kuhn segment.

The standard transfer matrix approach for Gaussian polymers [122] shows that the critical effective potential for thermal desorption is $W_{{\rm eff},c} = -c_{\rm F}T/L_p$ where $c_{\rm F} \approx \pi^2/24$, which is equivalent to $W_c \approx W_{c,\rm SF}[1 + c_{\rm F}(\ell_a/L_p)^{2/3}]$. Because $W_c < W_{c,\rm SF}$, the polymer indeed desorbs in the flexible regime, which describes the large scale behavior. The free energy of adsorption in the effective flexible polymer model is given by

$$f_W \approx 3W_{\rm eff}^2 L_p/T \sim 3(W - W_{c,SF})^2 L_p/2T \tag{11.6}$$

The critical properties of the desorption transition at $W = W_c$ are described by the *flexible* polymer model $\mathcal{H}_F$, i.e., thermal desorption is of *second order* with $\nu = 2$. On the other hand, the transition point $W_c \sim W_{c,\mathrm{SF}}$ and apparent critical properties in the entire region $|W-W_c| \gtrsim T/L_p$ are governed by the *semiflexible* model (11.3) with $\nu = 1 + \log$.

Connecting length scales below and above L_p we finally obtain the following free energy of adsorption

$$|f_W| \approx \begin{cases} 3(W-W_c)^2 L_p/2T & \text{for } |W-W_c| \ll T/L_p \\ |f_{W,\mathrm{SF}}| \sim |W-W_c| & \text{for } |W-W_c| \gtrsim T/L_p \end{cases} \tag{11.7}$$

The free energy f_W is related to the correlation length by $|f_W| = T/\xi_{\|}$. The first line in (11.7) is the free energy of adsorption in the flexible regime; the second line is the free energy of adsorption in the semiflexible regime, which holds for $|f_W| \gtrsim T/L_p$, outside a window of adhesion strengths of width T/L_p around the critical value W_c.

11.4 Thermally assisted force-induced desorption.

In the presence of thermal fluctuations the free energy of adsorption f_W replaces the bare potential strength W and the free energy per length $g(f_d)$ of a thermally fluctuating, stretched semiflexible polymer replaces the force $-f_d$. For small stretching forces $f_d \ll T/L_p$, the polymer is effectively flexible and entropic elasticity gives $g(f_d) \approx -f_d^2 L_p/6T$, whereas for strong stretching $f_d \gg T/L_p$, we have $g(f_d) \approx -f_d + (2Tf_d/L_p)^{1/2}$, where the square root contribution is typical for semiflexible behavior [146, 183]. The polymer desorbs if the stretching free energy $g(f_d)$ compensates for the free energy cost of desorption, i.e., for $|g(f_d)| > |f_W|$. This gives a first order force-induced desorption transition (similar to DNA unzipping [265, 268, 269], where the single strands are flexible polymers), at a critical force

$$f_{d,c} \approx \begin{cases} (6T|f_W|/L_p)^{1/2} & \text{for } |f_W| \ll 2T/L_p \\ |f_W| + (2T|f_W|/L_p)^{1/2} & \text{for } |f_W| \gg 2T/L_p \end{cases} \tag{11.8}$$

and, thus, the phase boundary of the adsorbed phase in the f_d-$|W|$ or f_d-T plane. The line of first order force-induced desorption transitions ends in the critical point of thermal desorption at zero force.

11.5 Simulations

The results for the phase diagram were confirmed by Monte Carlo (MC) simulations of a discretized semiflexible polymer consisting of $N = L_c/\Delta s$ beads with heights z_i (i.e., $h = z_N$) and $N-1$ connecting segments of length Δs with unit tangent vectors $\mathbf{t}_i$ using the Hamiltonian $\mathcal{H} = E_b + \sum_{i=1}^{N} \Delta s V(z_i) - f_d h$, where $E_b = (\kappa/2)\sum_{i=1}^{N-1}(\mathbf{t}_{i+1} - \mathbf{t}_i)^2/\Delta s$ is the bending energy. The MC simulation uses the Metropolis algorithm with a combination of local displacement, pivot, and reptation moves. The resulting MC phase diagrams in the f_d-T plane are shown in Fig. 11.1(b). The analytical result (11.8) correctly describes three main features of the simulation results: (i) A characteristic square-root dependence $f_{d,c} \sim |f_{W,\mathrm{SF}}|^{1/2} \sim |T-T_c|^{1/2}$ close to the thermal desorption transition typical for flexible behavior. (ii) A broad *linear* regime $f_{d,c} \approx |f_W| \sim |T-T_c|$ at lower temperatures, which is absent for flexible polymers and due to the bending rigidity effects. (iii) At low temperatures

$T < |W|\ell^{2/3}L_p^{1/3}$, we find $f_{d,c} \sim |W| - T^{4/3}/\ell^{2/3}\kappa^{1/3} + T|W|^{1/2}/\kappa^{1/2}$, which gives a small *reentrant* region of the desorbed phase because thermal fluctuations weaken the adhesion strength less than the pulling force. Such "cold desorption/unzipping" has been reported previously for flexible polymers like DNA [268, 269].

11.6 Free energy landscape

The energy landscape of the desorption process can be mapped by calculating the constrained free energy $\Delta F(h) = -T\ln[Z(h)/Z(0)]$ where $Z(h)$ is the restricted partition sum over all polymer configurations with a given height h of the end point. The transfer matrix treatment of the weakly bent semiflexible polymer (11.3) in Ref. [184] (see also chapter 10) gives the scaling form

$$Z(h) = (h/L_p)^{\theta_{a,r}/2+1/3}\Omega(L_p^{1/2}h/\xi_{\parallel}^{3/2})e^{L/\xi_{\parallel}} \tag{11.9}$$

with an explicit result for the shape function

$$\Omega(y) = \int du\Omega_{a,r}(y,u) \propto \int_0^\infty d\alpha\alpha^{-1/2}e^{-\alpha-2y/3\alpha} = \sqrt{\pi}e^{-(8y/3)^{1/2}} \tag{11.10}$$

and an exponent $\theta_{a,r} = -5/3$, see also (10.16). The resulting constrained free energy

$$\Delta F(h) = -\frac{T}{2}\ln\left(\frac{h}{L_p}\right) + \sqrt{\frac{8}{3}}h^{1/2}T^{1/4}L_p^{1/4}|f_W|^{3/4} \tag{11.11}$$

for the semiflexible regime $|f_W| \gtrsim T/L_p$ is the exact generalization of the $T = 0$ result (11.1) for $h \ll R_{co}$ to finite temperatures, where the free energy of adsorption of a semiflexible polymer f_W replaces the bare contact potential W and a logarithmic entropic repulsion from the hard wall occurs. The result (11.11) can be corroborated by a scaling argument starting from the estimate $\Delta F(h, L_d) \sim \kappa h^2/L_d^3 + |f_W|L_d$ of the free energy cost to desorb a segment of length L_d at a given height h of the end point. Minimizing with respect to L_d gives $L_d \sim h^{1/2}T^{1/4}L_p^{1/4}|f_W|^{-1/4}$ and a free energy cost $\propto h^{1/2}$ as in (11.11). For large h, the free energy cost (11.11) is *always* exceeded by the linear energy gain $-f_d h$ from the desorbing force, which suggests a desorption instability even for small forces f_d [260].

However, the weak bending approximation breaks down upon increasing h if typical tangent angles $h/L_d > 1$ become large for $h > R_{co} \equiv (\kappa/2|f_W|)^{1/2}$. Then the whole desorbed tail of length L_d becomes lifted perpendicular to the substrate except for a curved segment of length $\sim R_{co}$, i.e., $L_d \approx h + \mathcal{O}(R_{co})$. In this limit the full free energy $\Delta G(h) = \Delta F(h) - hf_d$ in the presence of the desorbing force can be written as

$$\Delta G(h) \approx h(|\Delta f_W| + g(f_d)) + cR_{co}, |f_W| \tag{11.12}$$

where $g(f_d)$ is the free energy gain per length of the desorbed semiflexible polymer segment stretched by a force f_d. c is a numerical constant of order unity with $c = 4(\sqrt{2}-1)$ at

$T = 0$, see (11.1). Equation (11.12) is in accordance with our above free energy criterion $|g(f_d)| = |f_W|$ for the desorption transition.

Therefore, also for $T > 0$, the free energy landscape $\Delta G(h) = \Delta F(h) - hf_d$, as given by (11.11) for $h \lesssim R_{co}$ and (11.12) for $h \gg R_{co}$, exhibits a *barrier* for $f_d > f_{d,c}$, which arises from the bending rigidity although the microscopic adhesion potential is purely attractive. In the MC simulation, $\Delta G(h)$ can be calculated from the logarithm of the end point distribution function, which clearly confirms the existence of a barrier, see Fig. 11.1(c). In the semiflexible regime for $|f_W| \gtrsim T/L_p$, we find an energy barrier $\Delta G_b \sim \kappa^{1/2}|f_W|^{3/2}/f_d$ for all forces $f_d > f_{d,c} \approx |f_W|$. The barrier scales with $\kappa^{1/2}$ and decreases as $1/f_d$ starting from $\Delta G_b \sim (\kappa|f_W|)^{1/2}$. The barrier is attained for a height $h \sim \Delta G_b/f_d$, which approaches $h \sim R_{co}$ for $f_d = |f_W|$. In the semiflexible regime $|f_W| \gtrsim T/L_p$, we have $\Delta G_b \gtrsim T$ and $R_{co} \lesssim L_p$. Upon entering the flexible regime the barrier becomes smaller than the thermal energy T and can thus be overcome quasi-spontaneously by thermal activation; the contact radius becomes larger than the Kuhn segment length L_p.

11.7 Desorption kinetics and experiments

The existence of the barrier has important consequences for single polymer desorption experiments. If the experiment is performed in equilibrium the necessary desorption force $f_d(h) = \partial_h \Delta F(h) \sim h^{-1/2}\kappa^{1/4}|W - W_{c,\mathrm{SF}}|^{3/4}$ *diverges* for small h, before a plateau of constant separation force $f_d = f_{d,c}$ is reached at large h. This is indeed often observed in experimental force-distance curves [219, 161, 249, 250]. Measurements of the shape of the $h^{-1/2}$-divergence together with the plateau force $f_{d,c}$ allow to determine the bending rigidity κ and the free energy of adsorption f_W of the semiflexible polymer using the results (11.11) and (11.8).

If the desorption experiment is performed out of equilibrium at constant desorption force larger than the threshold force, $f_d > f_{d,c}$, the energy barrier ΔG_b has to be overcome by thermal activation with an Arrhenius-type desorption rate

$$k_d \sim \tau^{-1} e^{-\Delta G/T} \sim \tau^{-1} e^{-f_0/f_d} \tag{11.13}$$

where $f_0 \equiv L_p^{1/2}|W - W_{c,\mathrm{SF}}|^{3/2}/T^{1/2}$ is a characteristic force and τ a microscopic time. The force-dependence of k_d is qualitatively different from other thermally activated single molecule processes such as bond dissociation[272]. For a time-ramped desorption force $f_d(t) = r_d t$ with a sufficiently slow constant loading rate $r_d \ll f_0/\tau$ the dynamics is thermally activated, and we find $t_d^* \sim (f_0/r_d)/\ln(f_0/r_d\tau)$ and $f_d^* \sim r_d t_d^* \sim f_0/\ln(f_0/r_d\tau)$ for the most frequent desorption time and force, respectively.

11.8 Unzipping

The unzipping of two bound semiflexible polymers by a force $\mathbf{f_d}$ pulling apart the polymer ends (see Fig. 11.1a) can be studied in the same way as force-induced desorption. The component $\mathbf{f_d} \cdot \mathbf{z}$ of the three-dimensional separation vector $\mathbf{z}$ of polymers plays an analogous role as the height coordinate z for desorption. The systems differ in the attractive potential which is a function of the absolute value $|\mathbf{z}|$, $V = V(|\mathbf{z}|)$ for unzipping. This results in a different criticality of the thermal desorption transition of a weakly bent semiflexible polymer which becomes first order with $\nu = 1$ and $\theta = -4$ [184], whereas the thermal unzipping of the flexible Gaussian polymer is second order with $\nu = 2$ as for the desorption. Apart from numerical prefactors, our main results (11.1,11.7,11.11,11.12,11.8) remain unchanged.

11.9 Conclusion

In summary, we found that the force-induced desorption and unzipping of semiflexible polymers are first order phase transitions. We predict the existence of a characteristic energy barrier which is a consequence of the bending rigidity and absent for flexible polymers. The results for the phase diagram and the energy barrier are confirmed by Monte Carlo simulations. The energy barrier gives rise to activated desorption or unzipping kinetics and leads to an enhanced dynamic stability of the bound state of stiff adhesive polymers or fibers under force. This effect plays a role for biological polymers under force, e.g., in DNA, protein, or filament unzipping and desorption as well as for materials science applications ranging from the delamination of thin sheets to the peeling of adhesive hairs, e.g., wet hair [270]. The results can also shed new light on the zipping or adsorption dynamics of semiflexible filaments, which plays an important role in cytoskeletal networks [273].

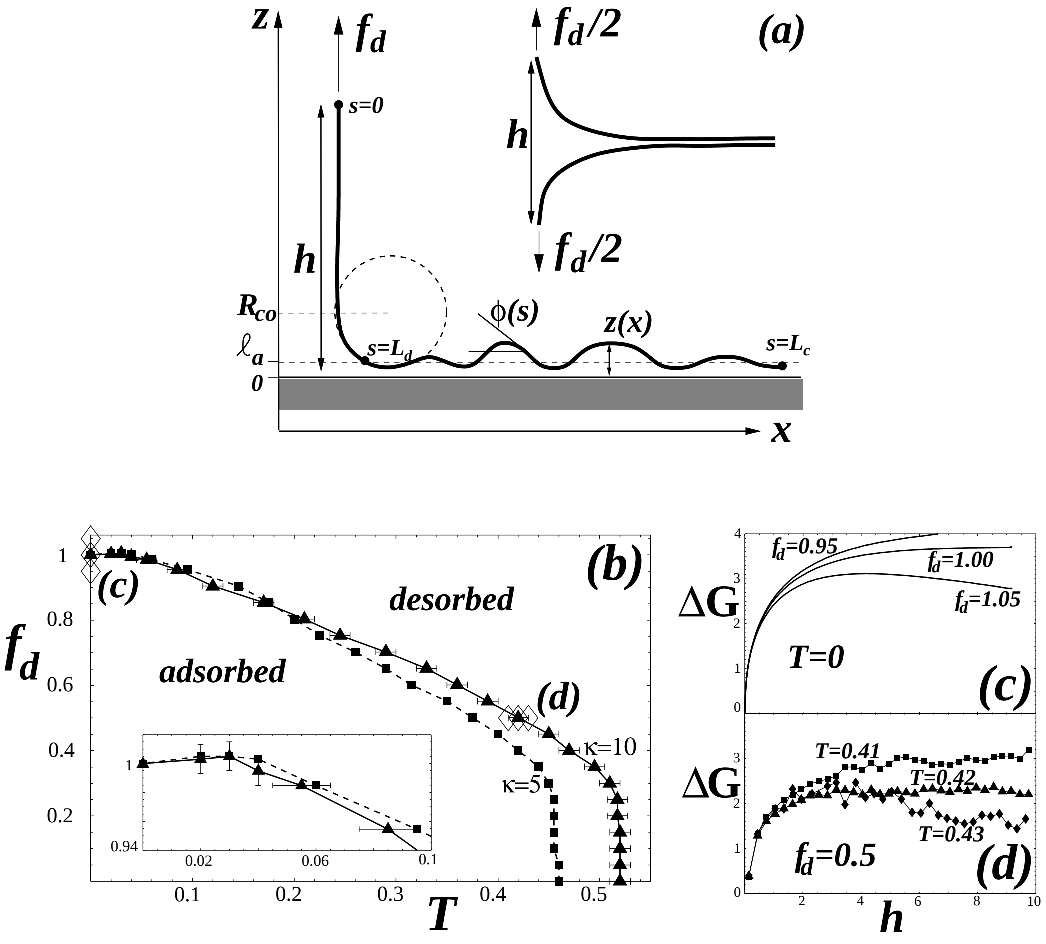

Figure 11.1: (a) Force-induced desorption and unzipping of semiflexible polymers (inset); f_d is the desorbing (unzipping) force and h the height (separation) at the end point. (b) Phase diagrams in the plane of desorbing force f_d and temperature T from Monte Carlo simulations for bending rigidities $\kappa = 10$ (triangles) and $\kappa = 5$ (squares), adsorption potential range $\ell_a = 0.1$, and contour length $L_c = 100$ (all lengths in units of Δs, energies in units of the adhesion energy $|W|\Delta s = 1$; lines are guides to the eye). Inset shows the reentrance region at low temperatures. (c),(d) Free energy landscapes $\Delta G(h)$ for $\kappa = 10$ and forces and temperatures as indicated by diamonds in the phase diagram b. (c) at $T = 0$ according to the analytical result, see eq. (11.1). (d) for $f_d = 0.5$ from Monte Carlo simulations in agreement with eqs. (11.11) and (11.12). In the desorbed phase $\Delta G(h)$ exhibits an energy barrier.

Chapter 12

Dynamics and Manipulation on Structured Substrates

We study the activated motion of adsorbed polymers which are driven over a structured substrate by either a uniform *or a localized* point force. *The lateral surface structure is represented by double-well or periodic potentials. We calculate shape, energy, and effective diffusion constant of kink excitations, and in particular their dependence on the bending rigidity of the semiflexible polymer. For symmetric potentials, the kink motion is purely diffusive whereas kink motion becomes directed in the presence of a uniform driving force on the polymer. The Kramers escape over the potential barriers proceeds by nucleation and diffusive motion of kink-antikink pairs, the relaxation to the straight configuration by annihilation of kink-antikink pairs. We determine the average velocity of the semiflexible polymer based on the collective kink dynamics in the stationary state. For a point driving force, the collective kink dynamics can be described by an one-dimensional symmetric simple exclusion process. Our results apply to the activated motion of biopolymers such as DNA and actin filaments or synthetic polyelectrolytes on structured substrates and to experiments with single polymers using, for example, tips of scanning force microscopes to drag the polymer.*

12.1 Introduction

The Kramers problem [274] of thermally activated escape of an object over a potential barrier is one of the central problems of stochastic dynamics. It has been extensively studied not only for point particles [275] but also for extended objects such as elastic strings, i.e., lines under tension such as flux lines in type-II superconductors [7] or dislocations in crystals [96]. Elastic strings activate over potential barriers by nucleation and subsequent separation of soliton-antisoliton pairs which are localized kink excitations [276, 277]. An analogous problem is the activated motion of a flexible polymer over a potential barrier [278, 279].

However, the thermally activated escape of a semiflexible polymer, which is a filament governed by its bending energy rather than entropic elasticity or tension, remained an open question that we want to address in this chapter. Semiflexible polymers such as DNA or actin filaments have a large bending stiffness and, thus, a large persistence length, L_p. On scales exceeding L_p, the orientational order of the polymer segments decays exponentially, and the polymer effectively behaves as a flexible chain with a segment size set by L_p. In contrast, on length scales which are small compared to L_p, the bending energy of the semiflexible polymer strongly affects the behavior of the polymer. The persistence lengths of the most prominent biopolymers range from 100nm for DNA [135], to the 30μm-range for actin [133, 134] or even up to the mm-range for microtubules [133] and becomes comparable to typical contour lengths of these polymers. Whereas the adsorption of such semiflexible polymers onto homogeneous adhesive surfaces has been studied previously in [237, 238, 184], much less is known about the behavior of a semiflexible polymer adsorbed on a *structured* surface.

In this chapter we focus on the escape of a semiflexible polymer over a translationally invariant potential barrier as shown in Fig. 12.1, which can be realized on chemically or lithographically structured surfaces. The behavior of semiflexible biopolymers on such structured substrates is of interest, e.g., for electrophoresis applications [280]. Another important class of semiflexible polymers are synthetic polyelectrolytes, whose self-assembly and dynamic behavior on structured substrates has only been studied recently [128]. We consider two types of driving forces: Homogeneous or *uniform* driving forces across the potential barriers can be easily realized on structured substrates by electric fields for charged polymers as in electrophoresis or by hydrodynamic flow. *Point* driving forces acts only locally on the polymer and can be realized in single molecule manipulation by AFM tips [166].

Our theoretical study is motivated by experimental advances in the manipulation and visualization of single polymers using optical [143] and magnetic [246] tweezers, or scanning force microscopy [166]. In Refs. [166, 125] it has been demonstrated that these techniques allow to experimentally apply localized point forces to a polymer adsorbed on a substrate. Polymers that are strongly adsorbed onto crystalline substrates such as graphite or mica experience a spatially modulated adsorption potential reflecting the underlying crystal lattice structure and giving rise to preferred orientations of the adsorbed polymer. For such systems, the dynamics of the adsorbed polymer is governed by thermal activation over the potential barriers of the surface potential.

One example of polymers adsorbed on a structured surface are self-assembling polymer chains consisting of long-chain alkanes and alkylated small molecules on crystalline substrates such as the basal plane of graphite [281]. The alkyl chains orient along the substrate axes thereby providing an effective periodic adsorption potential. Also biopolymers such as DNA or polyelectrolytes, or dendronized polymers can be oriented on the basal plane of graphite by using long chain alkanes as an oriented template layer [128, 166]. It has been demonstrated experimentally that these polymers can be manipulated individually on the structured surface by applying point forces using the tip of a scanning force microscope [166, 125].

Our main results are as follows. As for flexible polymers, the activated dynamics of semiflexible polymers at low forces is governed by the nucleation of localized kink-like excitations shown in Fig. 12.1. We find, however, that the activated dynamics of semiflexible polymers is different from that of flexible polymers as kink properties are not governed by

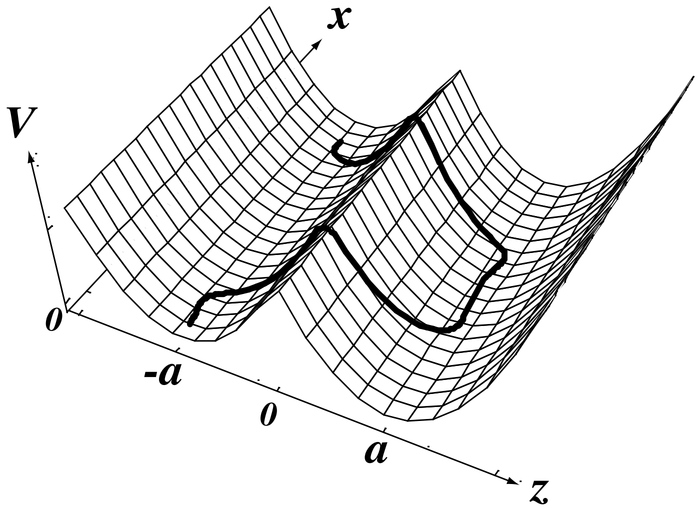

Figure 12.1: Typical conformation of a semiflexible polymer (thick line) with a kink-antikink pair in a double-well potential V which depends on the coordinate z and is independent of the coordinate x.

entropic elasticity of the polymer chain but rather by the bending energy of the semiflexible polymer. This enables us to determine the persistence length from kink-properties. Furthermore, we calculate time scales for barrier crossing and the mean velocity of the semiflexible polymer for all regimes of homogeneous driving forces: (i) nucleation and purely diffusive motion of single kinks (ii) nucleation and driven diffusive motion of single kinks and (iii) for large driving force dynamic equilibrium between nucleation and recombination in a kink ensemble.

Also for low point driving forces, the dynamics of the polymer is governed by thermal activation and nucleation of localized kink-like excitations as shown in Fig. 12.2. We calculate the critical point force below which the polymer moves by thermal activation over the barriers of the adsorption potential. The steady state of this activated motion determines the profile and velocity of the moving polymer and is governed by the (collective) driven motion of the kink excitations which can be described as a one-dimensional symmetric simple exclusion process of these excitations. Our results for the critical point force, the velocity, and the profile of the moving polymer are accessible in manipulation experiments on adsorbed polymers and allow to extract material parameters of the polymer and the substrate structure from such experiments.

12.2 Equation of motion

We consider the dynamics of a semiflexible polymer in 1+1 dimensions in a double-well potential that is translationally invariant in one direction, say the x-axis as in Fig. 12.1. The semiflexible polymer has a bending rigidity κ and persistence length $L_p = 2\kappa/T$ where T

is the temperature in energy units. We focus on the regime where the potential is sufficiently strong that the semiflexible polymer is oriented along the x-axis and can be parameterized by displacements $z(x)$ perpendicular to the x-axis with $-L/2 < x < L/2$, where L is the projected length of polymer. The Hamiltonian of the semiflexible polymer is given by

$$\mathcal{H} = \int_{-L/2}^{L/2} dx \left[\frac{\kappa}{2} \left(\partial_x^2 z\right)^2 + V(z) \right] , \tag{12.1}$$

i.e., the sum of its bending and potential energy.

Our assumption of an oriented polymer is valid if U-turns of the polymer within a single potential well are suppressed by the bending energy. This is the case if the size $2a$ of each potential well in the z-direction is smaller than the persistence length L_p. This condition is typically fulfilled for adsorbing substrates structured on the nm-scale [281]. Furthermore, the polymer should be strongly adsorbed, which corresponds to a small density of thermally induced kink excitations, i.e., $E_k \gg T$ where E_k is the kink energy, see eq. (12.7) below.

Uniform force

For a uniform force we consider a piecewise harmonic double-well potential

$$V(z) = \frac{1}{2} V_0 (|z| - a)^2 - Fz \tag{12.2}$$

that is independent of x and thus translationally invariant in the x-direction, where V_0 is the depth of the potential, $2a$ the distance between potential minima, and F the external driving force density. Below the critical force $F_c \equiv aV_0$ the potential has two minima at $z^{\pm}_{min} = \pm a + F/V_0$. The Hamiltonian (12.1) can be made dimensionless by measuring energies in units of a characteristic energy $E_{sc} = a^2 \kappa^{1/4} V_0^{3/4}$, the x-coordinate in units of a characteristic length $x_{sc} = (\kappa/V_0)^{1/4}$ and the z-coordinate in units of a.

We consider an overdamped, Rouse-like dynamics of the semiflexible polymer with an equation of motion

$$\gamma \partial_t z = -\frac{\delta \mathcal{H}}{\delta z} + \zeta(x,t) = -\kappa \partial_x^4 z - V'(z) + \zeta(x,t) \tag{12.3}$$

where γ is the friction constant and $\zeta(x,t)$ is a Gaussian distributed thermal random force with $\langle \zeta \rangle = 0$ and $\langle \zeta(x,t)\zeta(x',t') \rangle = 2\gamma T \delta(x-x')\delta(t-t')$. We neglect longitudinal motion of polymer segments (see Ref. [188] for a discussion) and do not study the effects of an external tension or compression. For $V = 0$, tension and compression have been considered, for example, in [282].

Point force

For a point force the potential is given by

$$V_p(x,z) \equiv \frac{1}{2} V_0 (|z| - a)^2 - F_p \delta(x - x_p) z \; . \tag{12.4}$$

The potential (12.4) contains the action of a point force pulling the polymer at the point $x = x_p$ with a force F_p in the z-direction. For zero point force $F_p = 0$, the potential is symmetric, translationally invariant in the x-direction, has a barrier height $V_0 a^2/2$, and the distance between minima is $2a$. For $F_p > 0$, the point force in (12.4) breaks the translational invariance of the system.

The overdamped motion of the polymer is then described by

$$\gamma\partial_t z = -\frac{\delta\mathcal{H}}{\delta z} + \zeta(x,t) = -\kappa\partial_x^4 z - V_0'(z) + F_p\delta(x - x_p) + \zeta(x,t) \ , \qquad (12.5)$$

with $V_0(z) \equiv \frac{1}{2}V_0(|z| - a)^2$ and γ and $\zeta(x,t)$ as above.

12.3 Static kink

No force

At first we construct the static kink for $F = 0$ and $F_p = 0$, which is a localized metastable excitation. The static kink $z_k(x)$ is defined as the configuration that minimizes the energy (12.1), i.e., is a time-independent solution of (12.3) in the absence of thermal noise ($\zeta = 0$) for boundary conditions $z_k(\pm L/2) = \pm a$ and $\partial_x z_k|_{\pm L/2} = 0$. For $F = 0$ the potential is symmetric and $V(z) = V(-z)$ such that the kink configuration is anti-symmetric with $z_k(x) = -z_k(-x)$ and centered at $x = 0$ (i.e. $z_k(0) = 0$). For our piecewise defined potential we have to fulfill five matching conditions at $x = 0$ which connect the two parts $x < 0$ and $x > 0$ of the kink: $z_k(-0) = z_k(+0) = 0$, $\partial_x^n z_k|_{-0} = \partial_x^n z_k|_{+0}$ for $n = 1, 2, 3$. Both parts $z_k(x) + a$ for $x < 0$ and $z_k(x) - a$ for $x > 0$ of the static kink are linear combinations of the four functions $e^{\pm x/w_k} e^{\pm ix/w_k}$ where the eight linear expansion coefficients are determined from the boundary and matching conditions. The width w_k of the kink and the energy E_k of a single static kink in the thermodynamic limit of large L are given by

$$w_k = \sqrt{2}x_{sc} = \sqrt{2}(\kappa/V_0)^{1/4} \quad \text{and} \qquad (12.6)$$

$$E_k = E_{sc}/\sqrt{2} = a^2\kappa^{1/4}V_0^{3/4}/\sqrt{2} \ . \qquad (12.7)$$

We expect our results for the kink energy $E_k{\sim}E_{sc}$ and width $w_k{\sim}x_{sc}$ to hold for all potentials with a barrier height $\sim V_0 a^2$ and potential minima separation $\sim a$ independent of the particular potential form; only numerical prefactors will differ. We want to point out that measurements of the kink width w_k and the critical force density F_c or the kink energy E_k are sufficient to determine the bending rigidity $\kappa = F_c w_k^4/4a = E_k w_k^3/2a^2$ and thus the persistence length $L_p = 2\kappa/T$ if the distance $2a$ between potential minima is known.

A static single kink in a polymer of length L is equivalent to one half of a symmetric kink-antikink pair configuration with kink-antikink separation $d = L$ in a polymer of length $2L$, as shown in Fig. 12.1. The kink-antikink interaction energy $E_{int}(d) = 2(E_k(d) - E_k(\infty))$ can thus be found by determining the single kink energy in a polymer of length $L = d$. For large separation $d/w_k \gg 1$ we find an exponential decay $E_{int}(d) \sim \exp(-d/w_k)$.

We also studied numerically the stability of a kink-antikink pair at small separations and find that it becomes unstable with respect to spontaneous annihilation for $d/w_k < 2.55$.

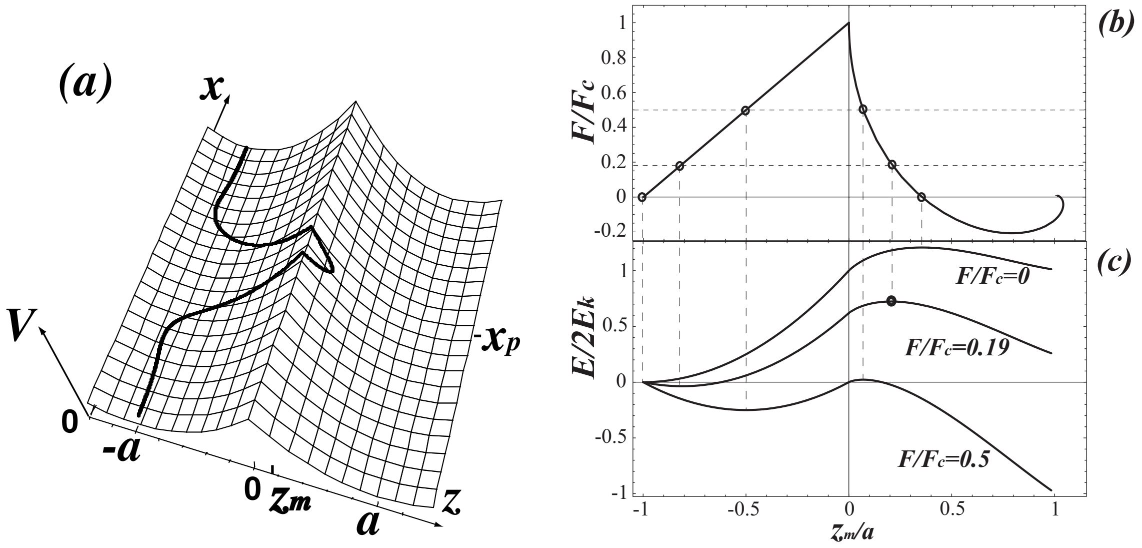

Figure 12.2: (a) Kink-antikink configuration of a semiflexible polymer in a double-well potential V under the action of a point force F_p displacing the midpoint in the z-direction to a value z_m. The configuration $z_k(x)$ is calculated for $F_p/F_c = 0.19$, $z_m/a = 0.21$ ($L_2/w_k = 1.1$, $L_1/w_k = 15$) and has an energy $E/2E_k = 0.72$. (b) The midpoint z_m (in units of a) as a function of the external force (in units of critical force $4E_k/a$). (c) Energy $E(z_m)$ (in units of $2E_k$) of a kink-antikink pair as a function of the midpoint z_m (in units of a) for different forces $F_p/F_c = 0, 0.19, 0.5$.

A semiflexible polymer will stay localized to the potential wells even if we set $V(z) = 0$ for $|z| > 2a$ as long as $V_0 > V_{0,c}$ with $V_{0,c}a^2 \simeq (T/L_p)(L_p/a)^{2/3}$ according to the results of chapter 10. This condition is equivalent to $E_k \gg T$ and thus a small density of thermally induced kink excitations. A small kink density in combination with the condition $L_p \gg a$ also ensures that the semiflexible polymer stays oriented along the x-axis such that the Hamiltonian (12.1) stays valid. The condition $E_k \gg T$ of a small kink density is equivalent to $L_p \gg w_k^3/a^2$. For sufficiently strong substrate potentials this gives a much wider range of applicability of the Hamiltonian (12.1) than in the absence of a potential where the condition $L_p > L$ of weak bending has to be fulfilled for a semiflexible polymer to be oriented.

Point force

First, we calculate the stationary shape of the semiflexible polymer that is deformed by a point force acting at its midpoint into a kink-antikink configuration $z_k(x)$ as shown in fig. 12.2a. This configuration is obtained by displacing the polymer at the midpoint where the point force acts to a prescribed position z_m and letting the rest of the polymer equilibrate. Therefore, we have to solve the saddle-point equation $\delta\mathcal{H}/\delta z = 0$ for the energy (12.1), i.e., eq. (12.5) for the time-independent case and in the absence of noise ($\zeta = 0$), with appropriate boundary conditions *and* a prescribed position $z_k(x_p) = z_m$. For $z_m > 0$ the kink configuration crosses the barrier at two points, see fig. 12.2a; we choose the origin

$x = 0$ and the length L_2 such that these points are $z_k(0) = 0$ and $z_k(L_2) = 0$. The polymer has a total length $L = L_1 + L_2$ and extends from $x = -L_1/2$ to $x = L_1/2 + L_2$, and the force acts at the midpoint $x_p = L_2/2$. The kink-like configuration has to fulfill four boundary conditions, $z_k(-L_1/2) = z_k(-L_1/2 + L_2) = -a$ and $z_k'|_{-L_1/2} = z_k'|_{-L_1/2+L_2} = 0$. At the midpoint $x_p = L_2/2$, we fix the displacement z_m of the polymer $z_k(x_p) = z_m$, and the point force causes a discontinuity in the third derivative, $z_k'''(x_p+) - z_k'''(x_p-) = F_p/\kappa$. In addition, $z_k(x)$ and its first two derivatives have to be continuous at the midpoint, and $z_k(x)$ and its first three derivatives have to be continuous at each crossing point $x_0 = 0, L_2$.

Away from the point force, i.e., for $x \neq x_p$ the saddle point solutions are linear combinations of the four functions $\exp(\pm x/w_k)\exp(\pm ix/w_k)$ where $w_k \equiv \sqrt{2}(\kappa/V_0)^{1/4}$ is the kink width. Construction of the solution through the four regions separated by the crossing points and the midpoint then requires to determine 16 linear expansion coefficients and the two parameters L_2 and z_m as a function of the system size L and the remaining model parameters including the point force from the boundary and matching conditions. The resulting shapes of the kink-like polymer configurations are shown in fig. 12.2a. fig. 12.2c shows the energies $E(z_m)$ of the kink-like configuration as a function of z_m for different point forces F_p. For low forces the energies $E(z_m)$ in fig. 12.2c have two stationary points, a stable minimum at $z_m = z_{m,min} < 0$ (the midpoint does not cross the barrier) and an unstable maximum at $z_m = z_{m,nuc} > 0$. This maximum is unstable with respect to further displacement of the midpoint and represents the critical nucleus configuration. For $F_p = 0$, we obtain another stable minimum at $z_m = a$ (the midpoint reaches the next potential well) which is the static kink-antikink solution calculated before, with width w_k and energy E_k given by eq. (12.6) and eq. (12.7), respectively. In the limit of large L, we can find analytic expressions for the resulting stationary positions $z_{m,min}$ and $z_{m,nuc}$ as a function of the applied force F_p, see fig. 12.2b. We find that there are no stationary positions if the point force F_p exceeds a critical value F_c given by

$$F_c = 4E_k/a = 2\sqrt{2}a\kappa^{1/4}V_0^{3/4}. \tag{12.8}$$

The midpoint displacement $z_{m,min} < 0$ in the stationary minimum is a linear function of the external force, $z_{m,min} = -a\,(1 - F_p/F_c)$ and reaches the barrier at $z_{m,min} = 0$ for $F_p = F_c$, see fig. 12.2b. This force-displacement relation describes the linear response of the polymer before crossing the barrier. For the midpoint displacement in the unstable nucleus configuration $z_{m,nuc} > 0$, on the other hand, we obtain the following set of two equations for $z_{m,nuc}$ and L_2,

$$\begin{aligned} F_p/F_c &= (\cos x - \sin x)e^{-x}\Big|_{x=L_2/2w_k}, \\ z_{m,nuc}/a &= 1 - (\sin x + \cos x)e^{-x}\Big|_{x=L_2/2w_k}. \end{aligned} \tag{12.9}$$

As shown in fig. 12.2b, F_p is decreasing for increasing $z_{m,nuc}$ as the critical nucleus configuration widens for small point forces. The negative values of F_p for large $z_{m,nuc}$ indicate that for a semiflexible polymer the kink-antikink configuration reached for $z_m = a$ is stabilized by an energy barrier. Only below a negative threshold force $F_c^- \equiv -F_c e^{-\pi/2} < 0$ the kink-antikink configuration becomes unstable.

12.4 Moving kink

A driving uniform force density F leads to an asymmetry in the potential and an effective force on kinks. Moving a kink by $-\Delta x$ increases the polymer length in the lower potential minimum by Δx and leads to an energy gain $-2aF\Delta x$ and thus a constant force $\mathcal{F}_k = -2aF$ on a kink. As argued above deviations from kink interactions are exponentially small for separations $d \gg w_k$. The force $\mathcal{F}_k$ leads to kink motion such that we also have to consider moving kink solutions. For constant kink velocity v the kink configuration assumes a form $z_k(x,t) = z_k(x - vt)$ that solves (12.3) for $\zeta = 0$. Introducing the coordinate $y \equiv x - vt$ for the comoving frame, equation (12.3) reduces to

$$\kappa \partial_y^4 z_k - v\gamma \partial_y z_k + V'(z_k) = 0 \tag{12.10}$$

which has to be solved with boundary conditions analogously to the static kink. However, in the asymmetric potential the kink is no longer symmetric but centered at $y_0 \neq 0$ with $z_k(y_0) = 0$ where we also have to evaluate the matching conditions. Eq. (12.10) can be made dimensionless by measuring time in units of a characteristic time $t_{sc} = \gamma/V_0$ and velocities in units of $v_{sc} = x_{sc}/t_{sc} = \kappa^{1/4}V_0^{3/4}/\gamma$. For a moving kink both parts $z_k(y) - z_{min}^-$ for $y < 0$ and $z_k(y) - z_{min}^+$ for $y > 0$ are linear combinations of four functions $e^{K_n y}$ where K_n $(n = 1, ...4)$ are the four roots of the equation $\kappa K_n^4 - v\gamma K_n + V_0 = 0$ that real part of which determine the width of the kink $w_k(v) \sim 1/|Re(K_n)|$. We find

$$K_n w_k = \pm H^{1/2}(\bar{v}) \pm (-H(\bar{v}) \pm 2^{3/2} 3^{-3/4} \bar{v} H^{-1/2}(\bar{v}))^{1/2} \tag{12.11}$$

(the first and third sign have to be identical) where $\bar{v} = 3^{3/4}v/4v_{sc}$ is a dimensionless velocity and $H(\bar{v}) = 3^{-1/2}((\bar{v}^2 + \sqrt{\bar{v}^4 - 1})^{1/3} + (\bar{v}^2 + \sqrt{\bar{v}^4 - 1})^{-1/3})$ an increasing, real function with $H(\bar{v}) \geq H(0) = 1$ and $H(\bar{v}) \sim \bar{v}^{2/3}$ for $\bar{v} \gg 1$. The width of the moving kink decreases with velocity as $w_k(\bar{v}) = w_k H^{-1/2}(\bar{v})$ (for $\bar{v} < 1$). In the limit of large polymer length $L \gg w_k(v)$ a moving kink solution, fulfilling all boundary and matching conditions, must satisfy the force-velocity relation

$$F(\bar{v}) = -F_c \bar{v} \frac{3^{1/4} 2^{-1/2} H^{3/2}(\bar{v})}{H^3(\bar{v}) + 3^{-3/2}\bar{v}^2} \ . \tag{12.12}$$

For small force densities, we find a linear relation $F \approx -3^{1/4}2^{-1/2}F_c\bar{v}$, close to the critical force density F_c the velocity diverges as $-\bar{v} \sim (1 - F/F_c)^{-3/2}$, see Fig. 12.3.

The result (12.12) can also be used to obtain the friction constant η_k of a moving kink by equating the friction force $v\eta_k$ with the driving force $\mathcal{F}_k = -2aF$ which gives the relation $\eta_k = 2a|F(v)|/v$, see Fig. 12.3. η_k is also related to the energy dissipation rate dE/dt due to kink motion which is defined as the product of the friction force $-v\eta_k$ and velocity: $dE/dt = -v^2\eta_k$. On the other hand, dE/dt can be calculated directly using the equations of motion (12.3) and (12.10) in the limit of large L

$$\frac{dE}{dt} = \int_{-\infty}^{+\infty} dx \frac{\delta \mathcal{H}}{\delta z_k} \partial_t z_k = -\gamma v^2 \int_{-\infty}^{+\infty} dy \, (\partial_y z_k)^2 \ , \tag{12.13}$$

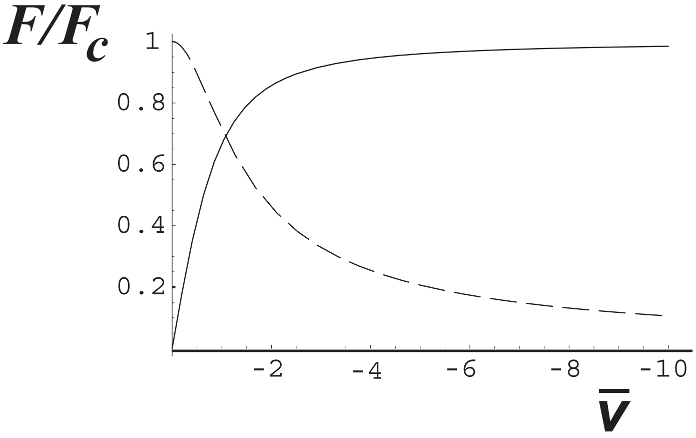

Figure 12.3: Force density F (in units of F_c, solid line) and friction constant η_k (in units of $3F_c a/2^{3/2}v_{sc} = 3a^2\gamma/w_k$, dashed line) as function of velocity $\bar{v} = 3^{3/4}v/4v_{sc}$ for a moving kink.

and we read off a kink friction constant $\eta_k = \gamma \int_{-\infty}^{+\infty} dy\, (\partial_y z_k)^2$. Integration in the limit of small driving forces gives $\eta_k \approx 3\gamma a^2/2w_k$ and equating the friction force with the driving force $-2aF = v\eta_k$ gives a linear relation $v = -4Fw_k/3\gamma a$ which agrees to leading order with our above result (12.12), see also Fig. 12.3.

12.5 Thermal noise and kink motion

For a more detailed analysis of the effect of noise on the kink motion we consider noise-induced perturbations of shape and velocity of a kink moving with constant velocity v. For a time-dependent kink center at $x_k(t)$ the comoving frame coordinate is given by $\bar{y} \equiv x - x_k(t)$. Adding shape perturbations to the corresponding kink solution $z_k(\bar{y})$ of (12.10), we arrive at the decomposition

$$z(x,t) = z_k(x - x_k(t)) + \sum_{p=1}^{\infty} X_p(t)\phi_p(x - x_k(t), t). \tag{12.14}$$

ϕ_p are normal modes of the kinked polymer which we will determine below and $X_p(t)$ are expansion coefficients; the zero mode of kink translation is explicitly taken into account by positioning the kink center at $x_k(t)$. Substituting (12.14) into the equation of motion (12.3) and expanding about the kink, we obtain

$$\gamma(v - \dot{x}_k)\left(\partial_{\bar{y}} z + \sum_{p=1}^{\infty} X_p \partial_{\bar{y}}\phi_p\right) + \gamma \sum_{p=1}^{\infty} \dot{X}_p\phi_p = \zeta \tag{12.15}$$

if the normal modes $\phi_p(\bar{y},t) = f_p(\bar{y})e^{-\omega_p t}$ fulfill the eigenvalue equation

$$\kappa\partial_{\bar{y}}^4 f_p - \gamma v \partial_{\bar{y}} f_p + V''(z_k(\bar{y}))f_p = \omega_p \gamma f_p \tag{12.16}$$

where $V''(z) = V_0(1-2a\delta(z))$. (12.16) has to be solved with boundary conditions $f_p(-L/2) = f_p(L/2) = 0$ and $f'_p(-L/2) = f'_p(L/2) = 0$ where we consider the limit $L/2 \gg x_k(t)$ and neglect the shift of boundaries in the comoving frame. Eq. (12.16) has a set of eigenvalues ω_p with orthonormal eigenfunctions $f_p(\bar{y})$ (with respect to the scalar product $\langle f|g\rangle \equiv \int d\bar{y} f(\bar{y})g(\bar{y})$). The translation mode $f_0 = \partial_{\bar{y}} z_k(\bar{y})/C$ of the kink has zero eigenvalue $\omega_0 = 0$. C is a normalization constant determined by $C^2 = \langle \partial_{\bar{y}} z_k | \partial_{\bar{y}} z_k\rangle$. Multiplying eq. (12.15) with the translation mode f_0 and integrating yields an equation of motion for the kink

$$\dot{x}_k = v + \zeta_k \left[1 + C^{-1}\sum_{p=1}^{\infty} X_p e^{-\omega_p t}\langle f_0|\partial_{\bar{y}} f_p\rangle\right]^{-1} \tag{12.17}$$

where $\zeta_k(t) = -(C\gamma)^{-1}\int d\bar{y} f_0(\bar{y})\zeta(\bar{y}+x_k(t),t)$ is an effective Gaussian thermal noise for the kink with correlations $\langle\zeta_k(t)\zeta_k(t')\rangle = \delta(t-t')(2T/C^2\gamma)$ (where we used $\langle f_0|f_0\rangle = 1$). The sum in (12.17) represents terms from kink-phonon scattering neglecting of which leads to an overdamped Langevin equation $\dot{x}_k(t) = v + \zeta_k(t)$ describing Brownian motion with drift. From the noise correlations we can read off the corresponding diffusion constant of the kink as $D_k = T/C^2\gamma$. Note that the corresponding kink friction constant $\eta_k = T/D_k$ is identical to our above result (12.13) obtained from complementary energetic considerations.

If kink-phonon scattering is neglected, the kink is performing a Brownian motion with drift. The polymer crosses the potential barrier by moving a kink over the entire length L of the polymer. Thus, the average crossing time is $t_{cr} \sim L/v$ for the case of directed diffusion with $v > 0$ under the influence of a driving force density F. For $F = 0$ and $v = 0$ the kink performs an unbiased random walk with $\langle x_k^2\rangle \sim D_k t$ from which we estimate the average crossing time as $t_{cr} \sim L^2\eta_k/T \sim L^2\gamma a^2/Tw_k$. For $F = 0$ and at low temperatures t_{cr} gives the relaxation time from a kinked state as in Fig. 12.1 to a kinkless state. The diffusive part of the kink motion can be neglected for forces $F \gg 2T/La$.

12.6 Kink nucleation and collective kink dynamics

Uniform force

For sufficiently large uniform force F, thermally activated barrier crossing proceeds by the nucleation and subsequent separation of a kink-antikink pair, see Fig. 12.4. Each passing kink or antikink increases the polymer position by $\Delta z = 2a$. For an ensemble of ρL kinks and ρL antikinks with kink density $\rho \ll 1/w_k$ as in Fig. 12.4, the fraction of moving polymer segments is given by $2\rho L\, w_k/L = 2\rho w_k$. These polymer segments move with velocity $2av/w_k$ in the z-direction which leads to the average velocity $v_z \equiv \langle\partial_t z\rangle = 4av\rho$. The kink density ρ is determined by the dynamical equilibrium of kink nucleation with rate j (per length) that we will calculate below, see (12.18), and kink-antikink recombination with rate $2\rho^2 v$ [276].

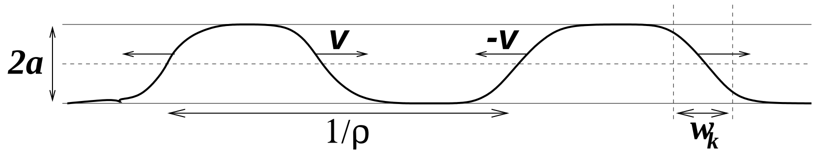

Figure 12.4: An ensemble of well-separated kinks and antikinks which move with velocity v and $-v$, respectively.

Equating both rates gives a steady-state density $\rho^2 = j/2v$ and thus an average polymer velocity $v_z = 2a(2vj)^{1/2}$.

In order to find the nucleation rate j, we use Kramers theory. In the following, we only give the main results of this calculation, details will be described elsewhere. As for flexible strings [276], the dynamics of the nucleation is governed by the critical nucleus representing the saddle point in the multi-dimensional energy landscape. The critical nucleus configuration $z_n(x)$ is the analogon of the static kink-antikink pair for $F > 0$ and fulfills the same saddle-point equation $\delta\mathcal{H}/\delta z = 0$, see (12.3). For the critical nucleus we obtain an excess energy $\Delta E_n \approx 2E_k(1 - F/F_c)^2$ that enters the nucleation current $j \sim \exp(-\Delta E_n/T)$. The prefactor depends on the corresponding attempt frequencies and, thus, the spectra $\omega_{n,p}$ and $\omega_{s,p}$ of fluctuations around the the critical nucleus and the straight polymer, respectively. For the straight polymer we find a spectrum of stable phononic modes $\omega_{s,0} = V_0/\gamma$ and $\omega_{s,p} \approx V_0/\gamma + \kappa((\pi/2 + p\pi)/L)^4/\gamma$ $(p \geq 1)$. For the critical nucleus, the spectrum consists of an unstable mode $\omega_{n,0} < 0$ representing the collective coordinate along which the nucleation proceeds, a zero mode $\omega_{n,1} = 0$ corresponding to the translation of the nucleus, and a sequence of stable phononic modes $\omega_{n,2} = V_0/\gamma$ and $\omega_{n,p} \approx V_0/\gamma + \kappa((b + p\pi)/L)^4/\gamma$ $(p \geq 3)$, where b is a numerical constant. Using Kramers theory in the regime $F > T/2aw_k$ [283], we finally obtain the nucleation rate

$$j = (2\pi)^{-3/2}\gamma^{1/2}GT^{-1/2}Q_n \exp\left(-\Delta E_n/T\right) \tag{12.18}$$

where $Q_n^2 \equiv |\omega_{n,0}|\omega_{s,0}\omega_{s,1}\prod_{p>1}\omega_{s,p}/\omega_{n,p} \approx |1 - 2^{4/3}(1 - F/F_c)^{-8/3}|(V_0/\gamma)^3$ contains all attempt frequencies, and $G \equiv L^{-1}\int dx_n[\int dx\,(\partial_x z_n(x))^2]^{1/2} \approx a(1 - F/F_c)/\sqrt{w_k}$ is the Jacobian for the change of coordinates from the amplitude of the translational mode $\partial_x z_n$ to the nucleus position x_n.

For small driving force densities $F \ll 2\rho T/a$, the kink motion is diffusive, and the above approach breaks down as kink-antikink pairs cannot separate but tend to recombine. For $E_k \gg T$, the system reaches thermodynamic equilibrium with a low kink density $\rho_{eq} \sim \exp(-E_k/T)$ given by the Boltzmann distribution and with $v_z = 4av\rho_{eq}$. For intermediate driving forces $2\rho T/a \ll F < F/2aw_k$, the critical nucleus is in quasi-equilibrium [283], and we find again $j \sim \exp(-\Delta E_n/T)$ as in the high-force expression (12.18) but with a different parameter dependence of the prefactor.

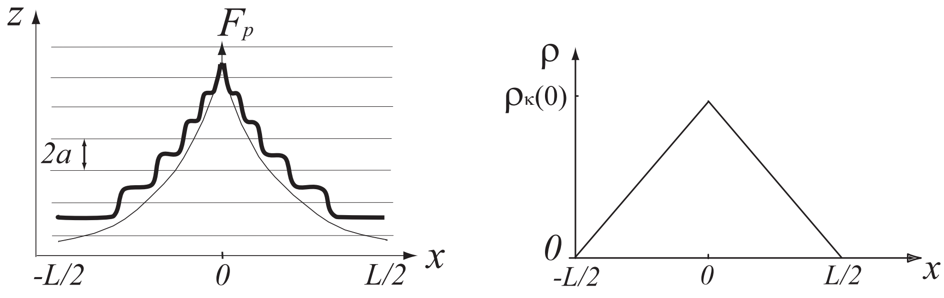

Figure 12.5: (Left) The shape of a semiflexible polymer pulled over a periodically structured surface by a point force acting at the midpoint. The horizontal lines indicate the position of potential barriers. The thick solid line shows a typical polymer configuration $z(x)$, the thin line the average shape $\langle z(x)\rangle$. (Right) The stationary kink density $\rho_k(x)$ as a function of the distance from the point x_p where the force is acting on the polymer.

Point force

Now we turn to the activated kink nucleation in the presence of a point force pushing the polymer over the potential barrier. The point force breaks the translational invariance in x-direction and kink-antikink pairs are only nucleated at $x = x_p$ with a rate J per unit time. This thermally activated process is governed by an energy barrier which is given by the excess energy ΔE_n of the critical nucleus configuration. The energy of the critical nucleus can be obtained from the energy profiles $E(z_m)$ shown in fig. 12.2c as the difference $\Delta E_n \equiv E(z_{m,nuc}) - E(z_{m,min})$ between minimum and maximum values of the energy $E(z_m)$ of the kink-like configuration. We find $\Delta E_n \sim 2E_k\,(1 - F_p/F_c)^2$, which vanishes as the force approaches the critical value F_c. The activation energy enters the nucleation current

$$J = (Q_n/2\pi)\exp(-\Delta E_n/T) \qquad \text{with} \quad Q_n^2 \equiv |\omega_{n,0}|\omega_{s,0}\prod_{p>0}(\omega_{s,p}/\omega_{n,p})\ , \tag{12.19}$$

which shows Arrhenius-type behavior. The prefactor Q_n includes the spectrum of attempt frequencies $\omega_{n,p}$ and $\omega_{s,p}$ ($p = 0, 1, ...$) for phononic fluctuations around the critical nucleus configuration and the straight configuration $z_m = -a$, respectively. We find one unstable negative mode $\omega_{n,0} \leq 0$, which diverges as $\omega_{n,0} = (V_0/\gamma)[1 - 2^{4/3}(1 - F_p/F_{c,\kappa})^{-4/3}]$ upon approaching the critical force $F_p \approx F_c$, a bound state with $0 < \omega_{n,1} \leq V_0/\gamma$, and a set of positive modes $\omega_{n,p} > V_0/\gamma$ with the same level spacing as the modes of the straight configuration. It is important to note that two translational modes (for kink and antikink) only exist if the point force is zero because the point force breaks the translation invariance. Close to the critical force $F_p \simeq F_c$, we obtain $Q_n^2 \approx (V_0/\gamma)^2[1 - 2^{4/3}(1 - F_p/F_c)^{-4/3}]$.

After nucleation of a kink-antikink pair at $x = x_p$ by thermal activation, kink and antikink are driven apart by a small force $\sim E_k/w_k e^{-L_2/w_k}$, which decays exponentially with the distance $L_2 > w_k$ between kink and antikink. This exponential decay is characteristic for a point driving force which interacts only over a distance $\sim w_k$ with the kink and very different from the case of a spatially uniform force, where also kinks experience a spatially uniform driving force. For separations $L_2 > w_k$ the kink diffuses essentially freely with a diffusion constant $D_k = 2Tw_k/3\gamma a^2$ as derived above.

A spatially localized driving force also leads to a distinct steady state motion of the polymer in a periodically continued potential, see fig. 12.5. This motion can be described in terms of the collective dynamics of an ensemble of kinks and antikinks which are generated at the *single* point $x = x_p$ by the point force and subsequently separated by the exponentially decaying force. For the following discussion we choose coordinates such that $x_p = 0$, and the polymer extends from $-L/2 < x < L/2$. Because a point force creates kink-antikink pairs only at $x = 0$, we find an ensemble consisting only of kinks in the region $x > 0$ and an ensemble consisting only of antikinks in $x < 0$. As two (anti-)kinks have a mutual short-range repulsion of range w_k, we have an ensemble of diffusing kinks (antikinks) with a hard-core repulsion on the interval $L/2 > x > 0$ ($-L/2 < x < 0$). In order to treat the non-equilibrium dynamics of these ensembles, we introduce a discrete one-dimensional lattice of possible kink positions with spacing $\Delta x = w_k$ which allows to map the dynamics of each ensemble onto the *symmetric simple exclusion process* (SSEP) with open boundaries [284, 285]. In the following we consider the kink ensemble ($x > 0$); the antikink ensemble ($x < 0$) can be treated analogously. In the kink ensemble, the kink particles are freely diffusing, i.e., they have *symmetric* rates $D \equiv D_k/w_k^2$ for hopping to the right and left on the lattice $x_i = iw_k$ ($i = 1, ..., N$ with $N = L/2w_k$); they interact through their hard-core repulsion. In the SSEP, boundary conditions are specified by rates α and δ for particles to enter the system at the left ($i = 1$) and right ($i = N$), respectively, if that site is empty. For the kink ensemble we have $\alpha = J$, as kinks are nucleated at $i = 1$ with the Kramers rate (12.19), and $\delta = 0$ as no kinks enter the system at $i = N$. Furthermore, kinks leave the system diffusively, at $i = 1$ by annihilation with an antikink and at $i = N$ by relaxation of the free polymer end.

Despite the hard-core interaction the stationary density profile $\rho_k(x)$ of kinks in the SSEP fulfills the stationary diffusion equation, $\partial_x^2 \rho_k = 0$ [284, 285]. Furthermore, our boundary conditions are equivalent to boundary conditions $\rho_k(0) = w_k^{-1} \min(\alpha/D, 1)$ and $\rho_k(L/2) = 0$ for the stationary kink density at the ends of the system. For $\alpha > D$ the system reaches its maximal kink density w_k^{-1} at $x = 0$. The resulting linear density profile $\rho_k(x)$ is

$$\begin{aligned} \rho_k(x) &= \rho_k(0)(1 - 2|x|/L) \quad \text{with} \\ \rho_k(0) &= w_k^{-1} \min(\alpha/D, 1) = \min(Jw_k/D_k, 1/w_k) \end{aligned} \tag{12.20}$$

as shown in fig. 12.5 (right). The average distance between kinks is $1/\rho_k(x)$ and at each kink the polymer position changes by $\Delta z = -2a$ leading to a characteristic *parabolic* polymer shape $\langle z(x)\rangle - z_m = -2a \int_0^{|x|} d\tilde{x} \rho_k(\tilde{x}) = -2(a/w_k) \min(Jw_k^2/D_k, 1)|x|(1 - |x|/L)$ in the stationary state as shown in fig. 12.5 (left). The average velocity $v_z \equiv \langle \partial_t z\rangle$ of the polymer in the z-direction is determined by the stationary current $J_{\text{SSEP}} = -D_k \partial_x \rho_k = \min(J, D_k/w_k^2) w_k/L$ of the SSEP. Only for small nucleation rates $J \ll D_k/w_k^2$ the kink interaction can be neglected and the current is directly given by the Kramers rate (12.19),

$J_{\mathrm{SSEP}} \approx J w_k/L$. During the time $1/J_{\mathrm{SSEP}}$ the polymer advances by a distance $2a$ leading to $v_z = 2aJ_{\mathrm{SSEP}} \approx 2a \min(J, D_k/w_k^2) w_k/L$.

12.7 Conclusion

In summary, we described the activated motion of single adsorbed polymers on a structured substrate, which are either displaced by a *uniform* force, which can be realized, e.g., by hydrodynamic flows or by electric fields in case of charged polymers, or displaced by localized *point* forces, which can be realized experimentally using, e.g., scanning force microscopy tips. The static kink has the energy E_k and the width w_k as given by (12.6). Both kink properties are governed by the bending rigidity of the semiflexible polymer.

In the presence of a uniform driving force density F, there is a force $\mathcal{F}_k$ acting on the kink that leads to moving kink solutions which satisfy the force-velocity relation (12.12). In the absence of kink-phonon scattering the kink performs Brownian motion with drift for which we have calculated the friction constant η_k and the diffusion constant D_k. This leads to estimates for the crossing times $t_{cr} \sim L/v$ for large forces $F \gg 2T/La$ and $t_{cr} \sim L^2\eta_k/T$ for small forces $F \ll 2T/La$. For large forces, the nucleation of kinks proceeds by activation over the saddle point which represents the critical nucleus. Application of Kramers theory leads to the nucleation rates (12.18) which determine the average velocity $\langle \partial_t z \rangle$ of the polymer. Our results are not only relevant to the dynamics of semiflexible polymers but can be extended to kink excitations in fluid membranes [286].

Also for point forces, the dynamics is governed by kink-like excitations. Kink and antikink pairs are *locally* nucleated by the point force and then undergo a separation which is diffusive on separations larger than the kink width w_k. We have calculated the nucleation rate (12.19) using Kramers theory. The collective kink dynamics can be mapped onto a one-dimensional symmetric simple exclusion process (SSEP). Using this mapping we find the average polymer velocity and a characteristic average parabolic shape for a driven semiflexible polymer.

Chapter 13

Unbinding of Filament Bundles

Bundles of semiflexible polymers such as actin filaments are studied theoretically. The bundle formation is governed by attractive filament interactions mediated by cross-linking sticker molecules. Using a combination of analytical arguments and Monte Carlo simulations, it is shown that the formation of bundles of parallel filaments requires a threshold concentration of linkers which becomes independent of the filament number for large bundles. The unbinding of bundles happens in a single, discontinuous transition. We discuss the behavior of the bundle thickness at and below the transition. In the bound phase, large bundles tend to segregate into sub-bundles due to slow kinetics. Our results are in qualitative agreement with experiments on F–actin in the presence of the cross-linking protein α-actinin.

13.1 Introduction

Biological cells and chemical synthesis provide a large variety of rod-like filaments. These filaments are semiflexible polymers with a large persistence length L_p and can assemble into different morphologies. Actin filaments, e.g., are characterized by $L_p \simeq 17\mu$m [132, 133, 134] and form both bundles [287] and meshworks depending on the presence of different actin-binding linker molecules [235, 236, 287]. Since the inter-filament attraction is mediated by crosslinkers with weak bonds, the formation of F–actin bundles is reversible and can be controlled by the crosslinker concentration [167, 168, 169]. Bundle formation has also been studied in the context of polyelectrolytes, for which charge correlations of polyvalent counterions [288, 289] or counterion aggregation [290] are possible bundling mechanisms. The formation of filament meshworks has been addressed in Ref. [291], focusing on the meshwork topology rather than on the elastic properties of the filaments.

In this Letter, we theoretically study bundle formation and unbinding of N essentially parallel filaments in the presence of cross-linking molecules with two adhesive end groups. It is convenient to confine these filaments within a tubular compartment of length L and diameter $L_\perp$. As shown below, this system exhibits a critical crosslinker concentration, $X_1 = X_{1,c}$, which separates two different concentration regimes. For $X_1 < X_{1,c}$, the filaments are unbound and uniformly distributed within the compartment. For $X_1 > X_{1,c}$, the filaments form either a single bundle, which represents the true ground state of the system as in

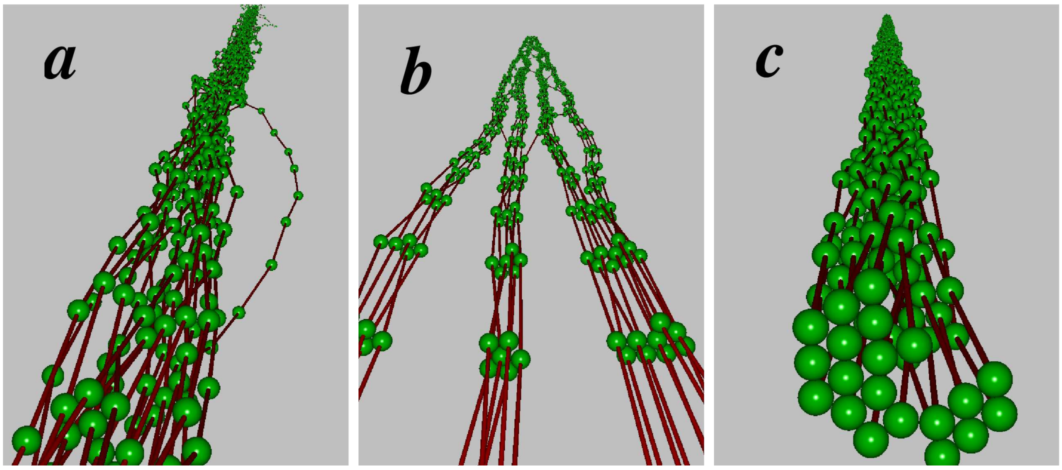

Figure 13.1: Monte Carlo snapshots of bundles with $N = 20$ filaments. (a) Close to the unbinding transition in the bundled phase. (b) Deep in the bound phase, the bundle tends to segregate due to slow kinetics and filament entanglement. (c) The equilibrium shape of the bundle is roughly cylindrical.

Fig. 13.1(a) and (c) , or several sub-bundles, which represent metastable, kinetically trapped states as in Fig. 13.1(b). Furthermore, as we decrease the crosslinker concentration from a value above $X_{1,c}$ towards a value below $X_{1,c}$, the bundles undergo a discontinuous unbinding transition at $X_1 = X_{1,c}$.

We explicitly derive this behavior for filaments of fixed length L but filaments of variable length and/or growing filaments should behave in the same way provided the width of the length distribution is small compared to its mean value. Our results are in qualitative agreement with recent experimental observations that bundles of F-actin filaments form above a threshold concentration of cross-linking proteins [167, 168, 169]. In these experiments, a stable and narrow length distribution is achieved by adding the protein phalloidin, which inhibits depolymerization, as well as capping proteins such as gelsolin [167, 168, 169]. Our theoretical predictions also apply to bundles of microtubules [292] or carbon nanotubes [293].

13.2 Model

In order to model a single bundle we consider N parallel filamentous polymers with bending rigidities κ_i $(i = 1, .., N)$, persistence lengths $L_{p,i} = 2\kappa_i/T$ where T is the temperature in energy units, and contour lengths comparable to or smaller than $L_{p,i}$. The filaments are oriented along one axis, say the x-axis, and can be parametrized by two-dimensional displacements $\mathbf{z}_i(x)$ perpendicular to the x-axis, see Fig. 13.2, with $0 < x < L$, where L is the projected length of the polymer. Our parametrization is appropriate provided the longitudinal correlation length is small compared to $L_{p,i}$. Since we will focus on the unbinding or disassembly process, we can put $L_\perp = \infty$ and, in this way, eliminate one model parameter.

The filament interaction is mediated by cross-linking sticker molecules that adsorb from the surrounding solution. Each linker consists of a short polymer with adhesive end groups, see Fig. 13.2. In order to describe the linker degrees of freedom we discretize the filament into segments of length $a_\|$, i.e., $x_k = ka_\|$ and $\mathbf{z}_{i,k} = \mathbf{z}_i(x_k)$, and introduce occupation numbers $n_{i,k} = n_i(x_k) = 0, 1$ for linkers at segment k of filament i. The segment length $a_\|$ is given by the size of the crosslinker end group. The Hamiltonian for the filament-linker system has the form

$$\mathcal{H} = \sum_i \left[\mathcal{H}_{b,i}\{\mathbf{z}_i\} + \mathcal{H}_1\{n_i\}\right] + \sum_{i,j} \mathcal{H}_2\{\mathbf{z}_i - \mathbf{z}_j, n_i, n_j\} \ , \tag{13.1}$$

where the first contribution $\mathcal{H}_{b,i} = \int_0^L dx \frac{1}{2}\kappa_i \left(\partial_x^2 \mathbf{z}_i\right)^2$ contains the bending energies of the filaments with bending rigidities κ_i. The term $\mathcal{H}_1$ describes the intrafilament interactions of linkers. We consider a lattice gas of linkers with hard-core repulsion adsorbing on a filament with $\mathcal{H}_1 = \sum_k a_\| W_1 n_{i,k}$ where $W_1 < 0$ is the adhesive energy (per length) of one linker end group. The third contribution $\mathcal{H}_2$ describes the pairwise interactions between filaments i and j and is given by

$$\mathcal{H}_2 \ = \ \sum_k a_\| \left[V_r(\Delta \mathbf{z}_{ij,k}) + \frac{1}{2}(n_{i,k} + n_{j,k} - 2n_{i,k}n_{j,k}) V_a(\Delta \mathbf{z}_{ij,k})\right] \tag{13.2}$$

where $\Delta \mathbf{z}_{ij,k} \equiv \mathbf{z}_{i,k} - \mathbf{z}_{j,k}$. The first term is the hard-core repulsion of filaments that is independent of the linker occupation with a potential $V_r(\mathbf{z}) = \infty$ for $|\mathbf{z}| < \ell_r$ and $V_r(\mathbf{z}) = 0$ otherwise where ℓ_r is of the order of the filament diameter. The second term is the linker-mediated attraction and is non-zero if one of the filaments carries a linker. Then the other filament is attracted by a linker-mediated potential $V_a(\mathbf{z})$. The filament can gain an additional energy $|W_1|$ if it is in a range ℓ_a of the order of the linker size, which we model by a potential well [1]

$$\begin{aligned} V_a(\mathbf{z}) &= W_1 \text{ for } 0 < |\mathbf{z}| - \ell_r < \ell_a \ , \\ V_a(\mathbf{z}) &= 0 \ \text{ otherwise.} \end{aligned} \tag{13.3}$$

The filament interaction (13.2) depends only on the coordinate differences $\Delta \mathbf{z}_{ij,k}$. Therefore, the center of mass $\bar{\mathbf{z}}_k \equiv \sum_i \mathbf{z}_{i,k}$ of the filament ensemble decouples and performs free diffusion. Bundle formation depends only on $N-1$ $\bar{\mathbf{z}}_k$-independent displacement fields such as, e.g., $\Delta \mathbf{z}_{1i,k}$ with $i = 2, \ldots, N$.

Now we can trace over the linkers in the grand-canonical ensemble and obtain an effective interaction Hamiltonian $\bar{\mathcal{H}}_2$ [294]. In the limit of low linker densities we find

$$e^{-\bar{\mathcal{H}}_2/T} \ = \ \prod_i \left[(1 - X_1) + X_1 e^{-\sum_{j(\neq i)} \sum_l a_\| (V_r + V_a)/T}\right] \tag{13.4}$$

---

[1] This potential corresponds to the case $\Delta = 0$ in chapter 10.

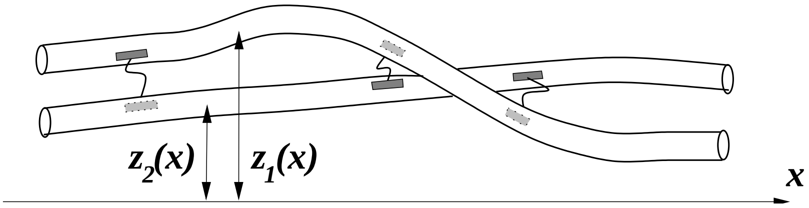

Figure 13.2: crosslinkers connecting two filaments. Each crosslinker consists of two adhesive endgroups and a short flexible linker polymer.

with the linker concentration per site, $X_1 \equiv \langle n_{i,k}, \rangle_1$ where the average is taken with the Hamiltonian $\mathcal{H}_1$. X_1 is determined by the concentration of linkers in solution by

$$X_1 \equiv \langle n_{i,k} \rangle_1 = Kc_x/(1+Kc_x) \ , \tag{13.5}$$

where K is the equilibrium constant of the association reaction of the crosslinker with the filament and c_x is the crosslinker concentration in solution. For weakly bound linkers $|W_1| \ll T/a_\|$, we can expand and end up with effective pairwise linker-mediated filament interactions, i.e., $\bar{\mathcal{H}}_2 \approx \frac{1}{2}\sum_k a_\|[V_r(\Delta\mathbf{z}_{ij,k}) + \bar{V}_a(\Delta\mathbf{z}_{ij,k})]$, which have the same functional form as the bare interactions; the short-range attractive part $\bar{V}_a$ is of the form (13.3) with a strength $\bar{W} \approx 2X_1W_1$ proportional to the linker concentration on the filament. For strongly bound linkers $|W_1| \gtrsim T/a_\|$, the strength of the short-range attractive part of the effective pair interaction is given by $e^{-a_\|\bar{W}/T} = (1-X_1)+X_1e^{-a_\|\bar{W}/T}$, but higher-order non-pairwise interactions are also generated. Pairwise filament interactions with potentials of the form (13.3) can also arise from van-der-Waals, electrostatic, or depletion forces.

13.3 Unbinding of two filaments

The unbinding of two semiflexible polymers with interaction $V_r + \bar{V}_a$ has been studied in detail by transfer matrix methods in Ref. [184]. The unbinding of two filaments was shown to occur at a critical potential strength

$$|\bar{W}_c| \ \sim \ (T/L_p)(L_p/\ell_a)^{2/3} \tag{13.6}$$

(for $\ell_a \gg \ell_r$) where $L_p = 2\kappa_{12}^r/T$ is associated with the reduced bending rigidity $\kappa_{12}^r \equiv \kappa_1\kappa_2/(\kappa_1+\kappa_2)$ for the relative coordinate $\Delta\mathbf{z}_{12}$. For $|\bar{W}| < |\bar{W}_c|$ filaments are unbound with infinite mean separation $\langle|\Delta\mathbf{z}_{12}|\rangle$, for $|\bar{W}| > |\bar{W}_c|$ they form a tightly bound state with $\langle|\Delta\mathbf{z}_{12}|\rangle < \ell_a+\ell_r$. The detailed transfer matrix treatment [184] shows that the transition is *discontinuous* in three dimensions. Furthermore, the mean filament separation stays *finite* at the transition, $\langle|\Delta\mathbf{z}_{12}|\rangle \sim \ell_a+\ell_r$, before it jumps to infinity in the unbound phase, whereas the second moment *diverges* as $\langle(|\Delta\mathbf{z}_{12}|-\ell_r)^2\rangle \sim |\bar{W}-\bar{W}_c|^{-1}$ upon approaching the transition. A filament pair thus exhibits pronounced fluctuations close to the unbinding transition even though the transition is first order. These results are confirmed by MC

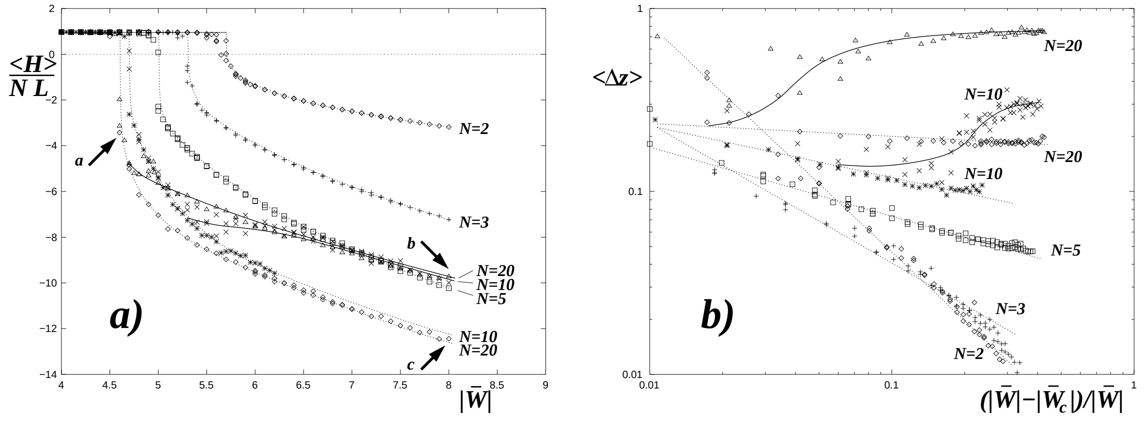

Figure 13.3: MC data for $N = 2, 3, 5, 10, 20$ identical filaments (with persistence length $L_p = 200$, contour length $L = 100$, potential range $\ell_a = 0.001$, and hard core radius $\ell_r = 0.1$; all lengths are in units of Δx; lines are guides to the eye). For $N = 10, 20$ two branches of data are shown corresponding to two different initial conditions; in the lower branch we prepared a compact cylindrical configuration, in the upper branch (thick lines) we arranged filaments initially in a plane. (a) Mean energy $\langle \mathcal{H} \rangle / NL$ per filament (in units of T) as a function of the effective potential strength $|\bar{W}|$. Arrows correspond to the snapshots in Fig. 13.1. (b) Logarithmic plot of the mean filament separation $\langle \Delta z \rangle \equiv \langle |\Delta \mathbf{z}_{ij}| - \ell_r \rangle$ (in units of Δx) as a function of the reduced potential strength $(|\bar{W}| - |\bar{W}_c|)/|\bar{W}|$.

simulations which also show that the critical exponents do not depend on the presence or absence of the hard-core V_r.

13.4 Unbundling of three filaments

Whereas the critical behavior of two unbinding filaments can be obtained from the exact transfer matrix treatment, this is no longer possible for three or more filaments. Therefore we use an effective 2-polymer model to approach the question whether bundling happens in a single transition. For filaments with very heterogeneous bending rigidities we expect a cascade of two pairwise binding transitions. According to (13.6) the pair with the highest reduced κ^r_{ij} [say $(ij) = (12)$ assuming that $\kappa_1 \geq \kappa_2 \geq \kappa_3$] binds in a first transition, before the third filament joins the resulting pair bundle in a second transition. Fluctuations of the center of mass of the pair bundle are governed by a rigidity $\kappa^c_{12} \equiv \kappa_1 + \kappa_2$. The binding transition of the third filament is then governed by a reduced rigidity $\kappa_{123} \equiv \kappa^c_{12}\kappa_3/(\kappa^c_{12}+\kappa_3)$ and a potential strength $\bar{W}_{123} = 2\bar{W}$. For both transitions we can calculate the critical potential strength $\bar{W}_c$ using (13.6). If $|\bar{W}_c|$ is smaller for the second transition, our assumption of a transition cascade is inconsistent. This leads to the criterion $8\kappa_{123} > \kappa^r_{12}$ for the existence of a *single* transition, which is remarkably robust against bending rigidity heterogeneity. For $\kappa_1 = \kappa_2 > \kappa_3$, a single transition exists as long as $\kappa_3 > 0.06\kappa_1$.

13.5 Unbundling of N filaments

For N identical ($\kappa_i = \kappa$) parallel filaments, we proceed similarly and consider the unbinding of two sub-bundles consisting of M and $N - M$ filaments. A sub-bundle of M filaments has a rigidity $\kappa_M^c = M\kappa$, and the unbinding of the two sub-bundles is governed by the reduced rigidity $\kappa_M^r = M(N - M)\kappa/N$. The effective sub-bundle attraction $\bar{W}_M$ is the product of the pair attraction $\bar{W}$ and the difference Δn_{nn} in the number of interacting filament pairs upon separating the sub-bundles, i.e., $\bar{W}_M \sim \bar{W}\Delta n_{nn}$. Applying the result (13.6) to the two sub-bundles, we find that they unbind at a critical potential strength $\bar{W}_c(M) \sim \bar{W}_c^{\text{pair}} M^{-1/3}/\Delta n_{nn}(M)$ for $N \gg M$, where $\bar{W}_c^{\text{pair}}$ is the critical potential strength for a filament pair. In deriving this result we used that due to the repulsive part of their interaction, filaments in large bundles only interact with a limited number q of nearest neighbors for short-range attractions as mediated by crosslinkers (this is not the case for sufficiently long-range interactions). We find that $|\bar{W}_c(M)|$ decreases with M such that there is a *single* unbundling transition, which takes place if a single filament losing $\Delta n_{nn} \approx q/2$ nearest neighbors unbinds from the bundle. For large N, this leads to the N-independent result $\bar{W}_c \approx \bar{W}_c(M = 1) \sim 2\bar{W}_c^{\text{pair}}/q$. For small N, $|\bar{W}_c|$ decreases monotonically from the pair value $|\bar{W}_c^{\text{pair}}|$. In the absence of a hard-core repulsion, on the other hand, we expect $|\bar{W}_c|$ to *vanish* as $\sim 1/N$ for large N since all filaments attract each other.

13.6 Monte Carlo simulations

To gain further insight into bundle formation we have performed extensive MC simulations for bundles containing up to $N = 20$ filaments using the effective Hamiltonian $\mathcal{H} = \sum_i \mathcal{H}_{b,i} + \sum_{i,j} \bar{\mathcal{H}}_2$ which is obtained after integrating out cross-linking stickers. Filaments are discretized into $L/\Delta x$ points along the x-direction, in which we apply periodic boundary conditions. In each MC step we attempt a random perpendicular displacement in the z-direction. These MC simulations can be used to determine the locus and order of the unbinding transitions since the mean energy $\langle \mathcal{H} \rangle$, see Fig. 13.3a, exhibits a discontinuity across a first order transition. To gain further insight into bundle morphologies we also measure the mean segment separation $\langle |\Delta \mathbf{z}_{ij}| - \ell_r \rangle$, see Fig. 13.3b, which is directly proportional to the mean bundle thickness that can be determined by optical microscopy in experiments.

Our MC simulations confirm that for bundles containing up to $N = 20$ filaments there is a single, *discontinuous* unbinding transition, see Fig. 13.3a. In the presence of a hard-core repulsion, we also observe saturation of the critical potential strength $\bar{W}_c$ to a N-independent limiting value for large N as predicted analytically. As can be seen in Fig. 13.1a typical bundle morphologies close to the transition are governed by pair contacts of filaments. The bundle thickness, as given by the mean segment separation $\langle |\Delta \mathbf{z}_{ij}| - \ell_r \rangle$, stays *finite* up to the transition, see MC data in Fig. 13.3b. For increasing N, an increasing number of higher moments $\langle (|\Delta \mathbf{z}_{ij}| - \ell_r)^m \rangle$ remains finite at the transition showing that the critical thickness fluctuations of large bundles become small [it can be shown that all moments with $m < 2(N - 1)(3N - 4)/3$ remain finite at the transition].

Deep in the bundled phase, i.e., for large $|\bar{W}|$, our MC simulations show that bundles do not always reach their equilibrium shape. Small sub-bundles containing typically $N \sim 5$ filaments form easily, start to entangle, and further equilibration is kinetically arrested suggesting that the bundle is in a "glass" phase. Fig. 13.1b shows the segregation into sub-bundles in a typical configuration and Fig. 13.3a shows the corresponding rise in the mean bundle energy per filament which approaches the $N = 5$ result. In Fig. 13.3b the pronounced rise of the mean separation for $N > 5$ with increasing potential strength and with increasing N is due to the segregation. This behavior is reminiscent of the experimentally observed F–actin structures consisting of networks of small bundles [168]. Only when starting from a sufficiently compact initial state, bundles relax towards the equilibrium form in the MC simulation, which is a roughly cylindrical bundle with a hexagonal filament arrangement ($q = 6$) as shown in Fig. 13.1c. In contrast to the segregated form, the bundle thickness and the mean energy per filament of the equilibrium form decrease with increasing N, as can be seen in Fig. 13.3. Both types of bundles swell as one increases the hard core ℓ_r.

13.7 Discussion and Conclusion

The critical potential strength $\bar{W}_c$ corresponds to a critical crosslinker concentration $X_{1,c}$. For weakly bound linkers $|W_1| \ll T/a_{\|}$, we have a simple linear relation $\bar{W} \approx 2X_1W_1$ such that $X_{1,c} \approx \bar{W}_c/2W_1$. The corresponding relation for strongly bound linkers is more complicated. Unbundling can be studied experimentally by (i) isolating a bundle of N filaments from a system at high crosslinker concentration using, e.g., a micropipette and (ii) transferring the bundle to crosslinker solutions of lower concentration, where it eventually unbinds for $X_1 < X_{1,c}$.

We have shown that long parallel filaments in a finite compartment distribute evenly for $|\bar{W}| < |\bar{W}_c|$, whereas they bind into a single bundle for $|\bar{W}| > |\bar{W}_c|$. In the parallel filament model, we neglect the translational entropy $S_{\text{tr}} \sim (N-1)\ln(ND^2/L_\perp^2)$ where D and $L_\perp$ are the diameter of a single filament and the system's extension perpendicular to the filaments, respectively. This entropic contribution is indeed negligible compared to the binding free energy in the limit of large L provided $L_\perp \ll DN^{1/2}e^{LJq/4T}$. The phase with homogeneously distributed parallel filaments for $|\bar{W}| < |\bar{W}_c|$ can be interpreted as a low-density nematic phase, whereas the bundle that forms for $|\bar{W}| > |\bar{W}_c|$ resembles a domain of a high-density nematic phase which coexists with a phase of small filament density.

In order to include translational and rotational entropy we can map the ensemble of semiflexible filaments considered here onto an ensemble of rigid rods of length L and diameter D at a certain concentration c [295, 296]. The effective pairwise attraction (per length) J is given by the bundling free energy of the filaments, which arises from the competition of configurational entropy and short-range attraction and is given by $J \sim \bar{W}_c - \bar{W} > 0$ for $|\bar{W}| > |\bar{W}_c|$ and by $J = 0$ for $|\bar{W}| < |\bar{W}_c|$. As shown in Refs. [295, 296], the hard rod system separates into a high-density nematic phase and a low-density nematic or isotropic phase above a critical attraction, i.e., for $J > J^* = J^*(c, L)$. The critical value J^* behaves as $J^* \sim 1/L$ [295] in the limit of large L which is consistent with our result that, in the same limit, N parallel filaments form a bundle for $|\bar{W}| > |\bar{W}_c|$ or $J > 0$ corresponding to $J^* = 0$. The phase separation for $J > J^*$ is in qualitative agreement with the experimental results in Refs. [167, 168, 169]. An intermediate gel phase as observed in Ref. [167] is absent in the rigid rod model since this phase is presumably governed by entanglement effects.

In conclusion, we have shown that bundles of long, parallel filaments which adhere via molecular crosslinkers, undergo a single, discontinuous unbinding transition at a finite crosslinker concentration. Therefore, bundle assembly and disassembly can be controlled by varying the crosslinker concentration in the surrounding solution. Large bundles can be kinetically trapped in glass-like states consisting of several subbundles.

Chapter 14

Active Nematic Ordering in Motility Assays

We theoretically study the cooperative behavior of cytoskeletal filaments in motility assays in which immobilized motor proteins bind the filaments to substrate surfaces and actively pull them along these surfaces. Because of the mutual exclusion of the filaments, the coupled dynamics of filaments, motor heads, and motor tails leads to a nonequilibrium phase transition which generalizes the nematic-isotropic phase transition of the corresponding equilibrium system, the hard-rod fluid. Langevin dynamics simulations show that the motor activity enhances the tendency for nematic ordering. We develop a quantitative theory for the location of the phase boundary as a function of motor density. At high detachment forces of motors, we also observe filament clusters arising from blocking effects.

14.1 Introduction

In biological cells, small forces generated by motor proteins organize and rearrange cytoskeletal filaments and give rise to active, non-equilibrium filament dynamics, which plays an important role for cell division, motility, and force generation [131]. Whereas conventional "passive" polymer dynamics is driven by thermal fluctuations [123], active filament dynamics is characterized by a constant supply of mechanical energy by motor proteins, which hydrolyze adenine triphosphate (ATP). Active filament dynamics has been studied *in vitro* using solutions of microtubules and two-headed kinesin motor proteins [170, 171, 172] or , where the formation of patterns such as asters and vortices is observed. Theoretical studies of such patterns [174, 175, 176, 177, 178, 179] have used a coarse-grained continuum description with kinetic equations for filament density and orientation fields and a motor density field. In these approaches it is inherently difficult to relate the macroscopic transport coefficients of such descriptions to the experimentally accessible microscopic parameters of the system. Based on experimental work on actin solutions containing myosin motor minifilaments [297] it has been suggested that the effect of motor activity can be described by an increased effective temperature in the non-equilibrium system [298]. Theoretical work on solutions of polymerizing filaments shows that also active polymerization

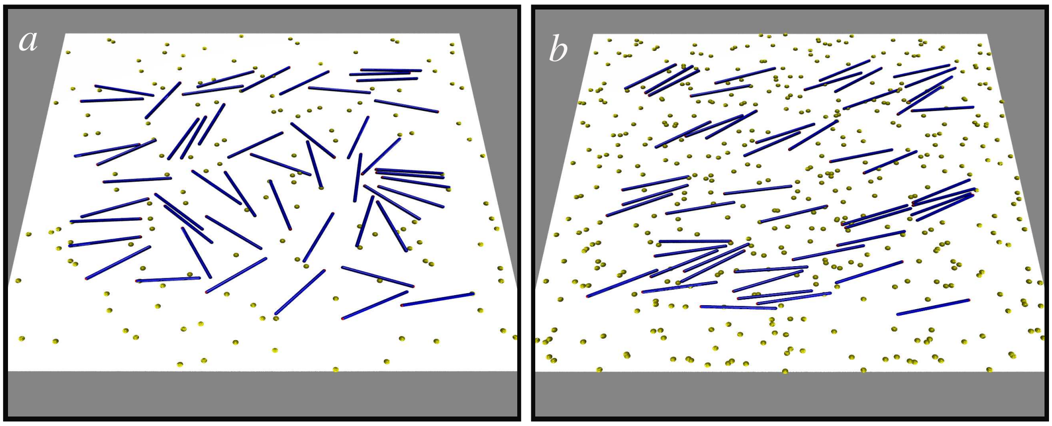

Figure 14.1: Snapshots of rodlike filaments on a motor coated substrate with randomly distributed motors and periodic boundary conditions. The filament concentration is $\rho = 2/L^2$, i.e., below the critical concentration of the equilibrium nematic-isotropic transition. For detachment forces $F_{de} = F_{st}$, we find (a) an isotropic phase at low motor surface density $\sigma wL = 0.03$ and (b) active nematic ordering at high motor surface density $\sigma wL = 0.09$.

dynamics can give rise to pattern formation [299].

In this chapter, we study dynamics and pattern formation of many filaments in motility assays, where filaments glide over a planar substrate driven by motor proteins whose tails are anchored to the substrate. Motility or gliding assays are by now a standard tool to characterize motor proteins by analyzing the transport velocities of *single* filaments gliding over the substrate. In this work, we focus on the *cooperative* behavior of many filaments, which are transported in a confined two-dimensional assay such that a hard-core repulsion is effective. This system has been considered previously by a mapping to a coarse-grained spin model [300], which raises again the problem of relating the effective model parameters to experimentally accessible microscopic system parameters. The equilibrium system corresponding to the motility assay in the absence of motors is the two-dimensional hard-rod fluid, which exhibits an isotropic-nematic ordering transition above a critical density of filaments [301, 302]. In the absence of motors, the theory of the passive dynamics of the hard-rod fluid has been established in Refs. [305, 306, 307]. In this Letter, we show both numerically using a microscopic simulation model and analytically that the nematic ordering is enhanced by the presence of motor activity due to the combined effect of hard-core filament interactions and active forces exerted by the motors. Using previous results for the persistent motion of single filaments [181, 303, 304] we extend the dynamic mean-field theory for nematic ordering [305, 306, 307] to active systems. From the theoretical treatment, we derive the concept of an increased effective length, which successfully explains our simulation data and allows to obtain the phase behavior in terms of the experimentally accessible microscopic model parameters.

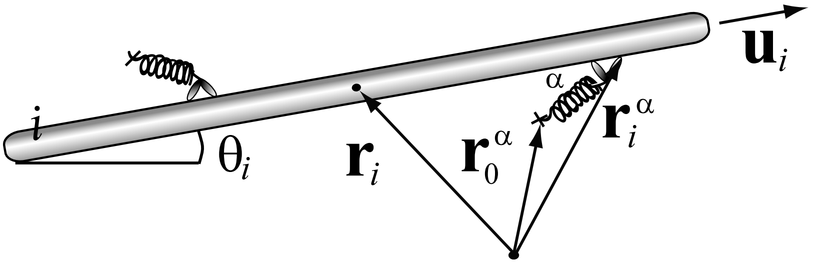

Figure 14.2: Schematic top view of a filament in the motility assay with two motors attached. The configuration of filament i is specified by the position $\mathbf{r}_i$ of its center of mass and its orientation angle θ_i or its orientational unit vector $\mathbf{u}_i = (\cos\theta_i, \sin\theta_i)$. The attached motor α is anchored at $\mathbf{r}_0^\alpha$ and its head is positioned at $\mathbf{r}_i^\alpha$.

14.2 Model

Our microscopic model for motility assays describes filament configurations, motor heads, and polymeric motor tails as separate degrees of freedom. One end of the motor tail is anchored to the substrate, and the motor head on the other end can bind to a filament in the correct orientation due to the tail flexibility. Once bound the motor head moves along the filament thereby stretching the polymeric tail, which gives rise to a loading force acting both on the motor head and the attached filament. This force feeds back onto the motion of the bound motor head, which moves with a load-dependent motor velocity [308, 309]. Filaments follow an overdamped dynamics with external forces from the stretched motor tails and the repulsive filament-filament interaction.

To proceed, let us consider N rigid filaments of length L (with index $i = 1, ..., N$) on a planar substrate.[1] The configuration of filament i can then be specified by the two-dimensional vector $\mathbf{r}_i$ for its center of mass and by the angle θ_i for its orientation, see Fig. 14.2. The orientational unit vector of the filament is $\mathbf{u}_i = (\cos\theta_i, \sin\theta_i)$. The filament is subject to forces $\mathbf{F}_i^\alpha$ from N_i attached motors (with index $\alpha = 1, ..., N_i$). Each such force arises from the polymeric tail of motor α, which is stretched by the directed motion of the motor head on the filament, which will be described below. The end-to-end vector of the polymeric tail is $\Delta\mathbf{r}^\alpha \equiv \mathbf{r}_i^\alpha - \mathbf{r}_0^\alpha$, where the motor tail is anchored at $\mathbf{r}_0^\alpha$ and the head position is $\mathbf{r}_i^\alpha$. We model the polymeric tail as a freely jointed chain, which is stretched by the force $-\mathbf{F}_i^\alpha$ pointing in the direction $\Delta\mathbf{r}^\alpha$. The absolute value $|\mathbf{F}_i^\alpha|$ is obtained by inverting the force-extension relation of a freely jointed chain, $|\Delta\mathbf{r}^\alpha|/L_m = f_{\mathrm{FJC}}(|\mathbf{F}_i^\alpha| b_m/T)$, where L_m and b_m are the total contour length and monomer length of the polymeric motor tail, respectively, and $f_{\mathrm{FJC}}(x) \equiv 1/\tanh x - 1/x$, see [183]. In addition to motor forces, the filaments are subject to interaction forces $\mathbf{F}_{ij}$ due to the purely repulsive interactions between filaments i and j corresponding to a hard-rod interaction for filaments of diameter

---

[1] Deformable filaments can be modeled by introducing segments connected by elastic springs and hinges [P. Kraikivski, Ph.D. thesis, Universität Potsdam, 2005].

D.

Under the influence of the motor forces $\mathbf{F}_i^\alpha$ and the interaction forces $\mathbf{F}_{ij}$ each filament i performs an overdamped translational motion, which is described by the stochastic Langevin-type equation of motion

$$\mathbf{\Gamma} \cdot \partial_t \mathbf{r}_i = \sum\nolimits_{\alpha=1}^{N_i} \mathbf{F}_i^\alpha + \sum\nolimits_{j=1}^{N} \mathbf{F}_{ij} + \boldsymbol{\zeta}_i \ , \tag{14.1}$$

where $\mathbf{\Gamma}$ is the matrix of translational friction coefficients, which is given by friction coefficients $\Gamma_\parallel$ and $\Gamma_\perp$ for motion parallel and perpendicular to the filament orientation $\mathbf{u}_i$, respectively, $\mathbf{\Gamma} = \Gamma_\parallel \mathbf{u}_i \otimes \mathbf{u}_i + \Gamma_\perp(\mathbf{I} - \mathbf{u}_i \otimes \mathbf{u}_i)$ [123], where $\mathbf{I}$ is the unit matrix and $\otimes$ the dyadic vector product. $\boldsymbol{\zeta}_i(t)$ are the Gaussian distributed thermal random forces with correlations $\langle \boldsymbol{\zeta}_i(t) \otimes \boldsymbol{\zeta}_j(t') \rangle = 2T\mathbf{\Gamma}\delta_{ij}\delta(t-t')$.

In addition to filament translation motor and interaction forces give also rise to the torques $M_i^\alpha = |(\mathbf{r}_i^\alpha - \mathbf{r}_i) \times \mathbf{F}_i^\alpha|$ and M_{ij}, respectively. These torques lead to an overdamped rotational dynamics, which is described by

$$\Gamma_\theta \partial_t \theta_i = \sum\nolimits_{\alpha=1}^{N_i} M_i^\alpha + \sum\nolimits_{j=1}^{N} M_{ij} + \zeta_{\theta,i} \ , \tag{14.2}$$

where Γ_θ is the rotational friction coefficient and $\zeta_{\theta,i}(t)$ is a Gaussian distributed thermal random torque with correlations $\langle \zeta_{\theta,i}(t)\zeta_{\theta,j}(t') \rangle = 2T\Gamma_\theta \delta_{ij}\delta(t-t')$. Note that all friction coefficients $\Gamma_\parallel$, $\Gamma_\perp$ and Γ_θ are known from the passive filament dynamics.

The dynamics of motor heads is described by a deterministic equation of motion

$$\partial_t x_i^\alpha = v(\mathbf{F}_i^\alpha) \ , \tag{14.3}$$

where $|x_i^\alpha| \leq L/2$ defines the position of the motor α along the rod i, i.e., $\mathbf{r}_i^\alpha = \mathbf{r}_i + x_i^\alpha \mathbf{u}_i$, i.e., the filament polarity is such that the motor head moves in the direction $\mathbf{u}_i$. The motor velocity v is a function of the loading force $\mathbf{F}_i^\alpha$ which builds up due to stretching of the motor tail. We use a force-velocity relation with a maximum value $v_{\max}$ for forces $\mathbf{F}_i^\alpha \cdot \mathbf{u}_i \geq 0$ pulling the motor forward, a linear decrease for forces $\mathbf{F}_i^\alpha \cdot \mathbf{u}_i < 0$ pulling the motor backwards, and $v = 0$ for $\mathbf{F}_i^\alpha \cdot \mathbf{u}_i < -F_{st}$, where F_{st} is the stall force [308, 309].

We assume that the motor binds to the filament when the distance between the position of the fixed end of the motor tail at $\mathbf{r}_0^\alpha$ and the filament is smaller than a capture radius w. Apart from the stall force F_{st} the motor is also characterized by its detachment force F_{de}, above which the unbinding rate of the motor head becomes large. For simplicity we assume in our model that the motor head detaches whenever the force F_i^α exceeds a threshold value F_{de}. We consider the case of processive motors with a high duty ratio close to unity, i.e., motors detach from a filament only if they reach the filament end or if the total force becomes larger than the detachment force F_{de}.

14.3 Simulation

Using the above model we performed simulations of gliding assays for a random distribution of motors with a surface density σ and periodic boundary conditions. At each time step Δt

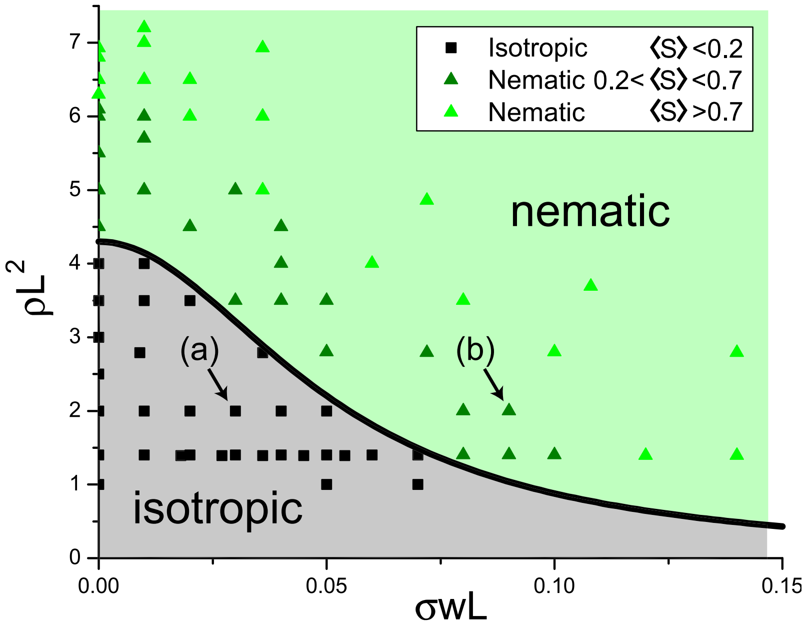

Figure 14.3: The phase diagram of the gliding assay as a function of the dimensionless filament density ρL^2 and dimensionless surface motor density $\sigma L w$ for a detachment force $F_{de} = F_{st}$. Each simulation run corresponds to one data point; arrows correspond to the snapshots in Fig. 14.1. If the average order parameter $\langle S \rangle < 0.2$, the system is in the isotropic phase (black squares, grey area), if $\langle S \rangle > 0.2$ it is in the nematic phase (green triangles, green area). Simulation parameters are explained in the text. The solid line represents the analytical result (14.7).

we update the motor head position x_i^α and filament position by using the discrete version of the equations of motion (14.1), (14.2), and (14.3). The parameter values that we choose for the simulations are comparable with experimental data on assays for conventional kinesin. The simulation results presented in Figs. 14.1 and 14.3 have been obtained for assays with quadratic geometry and size $25\mu\text{m}^2$ with rigid filaments of length $L = 1\mu\text{m}$ and diameter $D = L/40$ at room temperature $T = 4 \times 10^{-3}\text{pN}\,\mu\text{m}$. Friction coefficients are $\Gamma_\perp = 2\Gamma_\| = 4\pi\eta L/\ln(L/D)$ and $\Gamma_\theta = \Gamma_\| L^2/6$, where η is the viscosity of the surrounding liquid. We use a value $\eta = 0.5\text{pN}\,\text{s}/\mu\text{m}^2$ much higher than the viscosity of water, $\eta_{\text{water}} \sim 10^{-3}\text{pN}\,\text{s}/\mu\text{m}^2$, which allows to take larger time steps and decreases the simulation time. We checked that this does not affect results. We use a maximum motor speed of $v_{\max} = 1\mu\text{m}\,\text{s}^{-1}$ and a stall force of $F_{st} = 5\text{pN}$. The capture radius for motor proteins is $w = 10^{-2}\mu\text{m}$ and the length of the fully stretched motor tail $L_m = 5 \times 10^{-2}\mu\text{m}$.

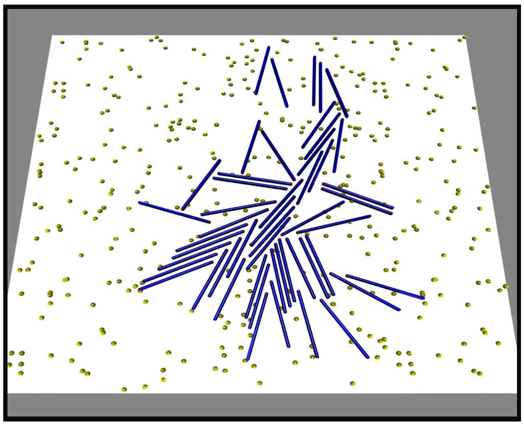

Figure 14.4: Snapshot of a cluster of mutually blocking filaments for large detachment force $F_{de} = 10F_{st}$ using otherwise the same parameters as in Fig. 14.1(b) [$\rho = 2/L^2$, $\sigma w L = 0.09$].

14.4 Phase behavior

Motor activity strongly modifies the nematic ordering of rigid filaments of length L and diameter D in a motility assay. Therefore, both the rod density ρ and the motor density σ are essential in order to determine the phase behavior of the non-equilibrium motility assay, which can be described in the plane of the two dimensionless parameters ρL^2 and $\sigma w L$. Nematic ordering in a system of N filaments can be characterized by the time averages of the order parameter $S \equiv \sum_{i \neq j} \cos(2(\theta_i - \theta_j))/N(N-1)$. In an infinite system, we expect $\langle S \rangle = 0$ in the isotropic phase and $\langle S \rangle = 1$ for perfect nematic order. In equilibrium, i.e., in the absence of motors ($\sigma = 0$) we find a continuous nematic-isotropic transition at a critical density $\rho_{c,0} \simeq 4.3/L^2$ in the simulation, which is in good agreement with the analytic result $\rho_c = 3\pi/2L^2$ based on Onsager's theory [302]. The equilibrium transition is found numerically from the inversion point of the curve $\langle S \rangle = \langle S \rangle(\rho)$ for a value $\langle S \rangle \simeq 0.2$, which we also use as the threshold value for active nematic ordering if motors are present ($\sigma > 0$). Snapshots of the actively driven system in the isotropic and nematic phase are shown in Figs. 14.1a and b, respectively. In the resulting phase diagram Fig. 14.3, the critical density ρ_c for active nematic ordering *decreases* with increasing motor density, i.e., nematic ordering is favored if more mechanical energy is fed into the system. The transition is continuous also for non-zero motor-density. Note that in the presence of motor activity, there is a non-vanishing filament current in the nematic phase, which is characteristic for a non-equilibrium phase.

Mutual blocking of filaments can lead to kinetically arrested filament clusters as shown in Fig. 14.4. We find that stable arrested clusters appear if the detachment force F_{de} is large compared to the stall force F_{st} such that the maximal force transmitted to a filament through collisions does not lead to detachment of the filament and dissolution of the cluster. Because collisions between filaments are exceptional in the isotropic phase, clusters occur primarily in the nematic phase region.

14.5 Theory

The motion of a filament with contour length L is characterized by stochastic switching between rotational and translational diffusion if no motors are attached, directed translation in rotationally diffusing directions if one motor is attached, and directed translation in one direction if two or more motors are attached. The relative frequency of these types of motion depends on the mean number of motors attached to the filament or the mean distance $\langle d_m \rangle$ between bound motors and, thus, on the surface motor concentration σ [181]. In the limit of high motor concentration a filament has two or more bound motors on average and $\langle d_m \rangle \sim 1/\sigma w$. The single filament performs a persistent walk with a persistence length [181]

$$\xi_p = \frac{L + 2\langle d_m \rangle}{L + 3\langle d_m \rangle} \frac{\langle d_m \rangle^2}{L} \left(e^{L/\langle d_m \rangle} - 1 - \frac{L}{\langle d_m \rangle} \right) \tag{14.4}$$

corresponding to a persistence time $t_p = \xi_p / v_F$, where v_F is the mean filament velocity. This velocity can be obtained by simultaneously equating the filament friction force with the total motor driving force and the filament velocity with the motor velocity in the steady state, which gives $v_F = v_{\max}(1 + \Gamma_{\|} v_{\max} \langle d_m \rangle / L F_{st})^{-1}$. A coarse-graining in time by averaging over time intervals of one persistence time t_p leads to an effective random walk of a single filament. On time scales larger than t_p the dynamics of a filament is again described by a diffusion equation as for passive dynamics. In the mean-field approximation the average number density of rod-like filaments $f(\mathbf{r}, \mathbf{u}, t)$ in the configuration $(\mathbf{r}, \mathbf{u})$ satisfies the following Smoluchowski equation [123, 305, 306, 307]:

$$\partial_t f \;=\; T\nabla_{\mathbf{r}} \cdot \mathbf{\Gamma}^{-1} \cdot \left(\nabla_{\mathbf{r}} f + f \nabla_{\mathbf{r}} \bar{W} \right) + T\Gamma_\theta^{-1} \mathcal{R}_{\mathbf{u}} [\mathcal{R}_{\mathbf{u}} f + f \mathcal{R}_{\mathbf{u}} \bar{W}], \tag{14.5}$$

where $\mathcal{R}_{\mathbf{u}} \equiv \mathbf{u} \times \partial_{\mathbf{u}}$ is the rotational operator. $T\bar{W} \equiv \int d\mathbf{r}' d\mathbf{u}' W(\mathbf{r} - \mathbf{r}', \mathbf{u}, \mathbf{u}') f(\mathbf{r}', \mathbf{u}', t)$ is a steric mean-field interaction, while $TW(\mathbf{r} - \mathbf{r}', \mathbf{u}, \mathbf{u}')$ represents the steric interaction potential between two filaments with center of masses and orientations $(\mathbf{r}, \mathbf{u})$ and $(\mathbf{r}', \mathbf{u}')$. The directed motion due to motors increases the number of collisions between filaments and, thus, the length scale over which filaments interact with each other. During a persistence time interval t_p two filaments in configuration $(\mathbf{r}, \mathbf{u})$ and $(\mathbf{r}', \mathbf{u}')$ collide if the connection vector $\mathbf{r} - \mathbf{r}'$ can be constructed as a linear combination $\mathbf{u}\xi + \mathbf{u}'\eta$ of the rod orientations with $-L/2 < \xi, \eta < L/2 + \xi_p$ and $|\xi - \eta| < L/2$. Therefore, we obtain a steric interaction potential

$$W = |\mathbf{u} \times \mathbf{u}'| \int\int_{-L/2}^{L/2+\xi_p} d\xi d\eta \Theta_L(\xi - \eta) \delta(\mathbf{r} - \mathbf{r}' + \mathbf{u}\xi + \mathbf{u}'\eta), \tag{14.6}$$

where $\Theta_L(\xi - \eta)$ equals one if $|\xi - \eta| < L/2$ and zero otherwise. Performing an analogous stability analysis as in Refs. [305, 306, 307] using the modified interaction potential (14.6) we finally obtain the critical filament density of the active isotropic-nematic transition,

$$\rho_c = c/L[L + \xi_p(\langle d_m \rangle, L)] \tag{14.7}$$

with $c = 3\pi/2$ from the analytical mean-field calculation. In the absence of motors we have $\xi_p = 0$ and the result (14.7) reduces to the equilibrium result of Ref. [302]. Using the result (14.4) for the persistence length $\xi_p = \xi_p(\langle d_m \rangle, L)$, we obtain an explicit expression of the nematic-isotropic phase boundary in the active system in terms of the microscopic model parameters, which is in good agreement with all simulation results, see Fig. 5.2. Beyond mean-field, we expect an increased numerical prefactor c in (14.7) but the same parameter dependence.

The result (14.7) corresponds to an *effectively increased filament length* $L_{\text{eff}} = \sqrt{L(L+\xi_p)}$ as compared to the equilibrium system, which explains that motor activity actually favors nematic ordering. In deriving (14.6), we have established a mapping of the non-equilibrium driven system onto an equilibrium system with larger effective filament length. This mapping only applies within the isotropic phase as it is based on the statistical properties of the motion of a *single* filament (or *non-interacting* filaments) but can be used to calculate the stability boundary (14.7) of the isotropic phase. The motor-activity also increases the effective diffusion constant of single filaments to $D_{\text{eff}} \sim D_T + \xi_p v_F$ [181, 303, 304]. Thus, using the Einstein relation $D_T = T(\Gamma_{\|}^{-1} + 2\Gamma_{\perp}^{-1})/3$ [123] for the thermal diffusion constant we might define an increased effective temperature $T_{\text{eff}} \sim T + 3\xi_p v_F/(\Gamma_{\|}^{-1} + 2\Gamma_{\perp}^{-1})$ for the isotropic phase. For steric filament interactions, however, this effective temperature does *not* influence the phase behavior.

14.6 Experimental realization

Confinement of filaments to strictly two dimensions is hard to realize experimentally but it has been observed that microtubules in a dynein motility assay exhibit hard-core interactions also in the absence of such a confinement [310]. Alternatively, we propose to consider a three-dimensional filament solution that is confined between two plates with anchored motors. The motor activity can induce an active *surface* nematic ordering of the filaments, which eventually propagates into the bulk if the filament density is sufficiently close to the critical density of the equilibrium Onsager transition in three dimensions.

14.7 Conclusion

We have presented simulations and a theoretical description of the phase behavior of filaments in a two-dimensional motility assay. The corresponding equilibrium system is the two-dimensional hard-rod fluid, which exhibits a nematic-isotropic phase transition. We have found that actively driven systems undergo an analogous phase transition and the motor activity *enhances* the tendency for nematic ordering. A similar enhancement is found in three-dimensional active filament solutions [175]. For the two-dimensional motility assays we have determined the phase boundary (14.7) for active nematic ordering by motors in terms of experimentally accessible microscopic model parameters. For high motor detachment forces $F_{de} \gg F_{st}$, we also find kinetically arrested filament clusters within the nematic phase region.

Chapter 15

Conclusion and Outlook

In conclusion, we have presented theoretical results for a number of cooperative phenomena displayed by fluctuating semiflexible polymers or biological filaments.

We presented theoretical descriptions for several single polymer manipulation experiments. The manipulation techniques ranged from simply confining filaments in chapter 8, the stretching of semiflexible chains in chapter 9 to force-induced desorption of the unzipping of filaments in chapter 11 and the forced sliding over an adhesive structured substrate in chapter 10. The theoretical results show how all of these manipulation techniques allow to extract information from the experiment about (i) the material properties of the filament, in particular its persistence length, and (ii) the properties of filament interactions such as the width of the confining channel, the strength of the adsorbing potential, or the effective potential barriers of the structured adhesive substrate.

Then we went on to study the formation of biologically relevant filament structures through equilibrium phase transitions, in particular, the bundling of filaments. In order to understand the formation of such complex structures, we started from conceptually simple association transitions of single filaments in chapter 10. Using transfer matrix techniques we were able to obtain a complete analytical description of the bundling of two filaments or the adsorption of a single filament on an adhesive substrate. Building on these results and combining the analytical arguments with Monte Carlo simulations we studied the formation of filament bundles containing up to $N = 20$ filaments in the presence of filament attractions mediated by crosslinking proteins in chapter 13. In agreement with experimental results, we find a single discontinuous bundling transition and the tendency of large bundles to segregate into small sub-bundles due to slow kinetics for strong filament attraction.

Finally, we addressed cooperative structure formation in an active filament system far away from thermal equilibrium in chapter 14. In the living cell, filaments of the cytoskeleton are actively rearranged by motor proteins and polymerization and de-polymerization, which are both ATP- (or GTP-) driven processes. We studied the underlying principles of this conceptually new type of polymer dynamics in motility assays, where motor proteins are immobilized on a solid substrate. They bind filaments and actively pull the filaments over the substrate. We found that the interplay between repulsive filament interactions and the active forcing by motor proteins leads to an enhanced nematic ordering of filaments as compared to the equilibrium situation in the absence of motor activity. This principle of structure or pattern formation is likely to play a role in other active filament assemblies.

I want to conclude this part of the thesis by an outlook for possible future extensions of the theoretical work presented in this thesis. In statistical physics, we have witnessed a growing interest in the quantification of non-equilibrium fluctuations in recent years. One prominent example is Jarzynski's non-equilibrium equality [311]. Experiments on single polymers, such as the unzipping of RNA [312], have provided the first quantitative tests of such relations. Due to their advantages in single molecule manipulation, stiff, semiflexible polymers appear to be ideal for further experiments, which would involve the description of the interplay of thermal fluctuations and bending rigidity on the theoretical side.

Regarding assemblies of filaments, there are many open questions concerning their non-equilibrium active dynamics. One interesting aspect – both for biological systems and for novel applications of synthetic semiflexible polymers – is force generation, either by polymerization forces or by zipping mechanisms in the presence of attractive interactions. Polymerizing filament bundles are particular interesting structures in this respect because they represent versatile modules for force generation in the cell. The force that can be generated by a bundle will depend on the number of filaments in the bundle, the filament stiffness, and the degree of crosslinking of the bundle. Because a relatively large number of firmly crosslinked filaments can build an effectively much more rigid structure, which can generate stronger forces, polymerizing bundles built from many, relatively flexible actin filaments provide a more versatile and tunable force-generating structure than single stiff microtubules. Preliminary results also show that the zipping of attractive filaments in a bundle can also provide an efficient mechanism for force generation, which does not rely on ATP-hydrolysis. Similar zipping mechanisms play an important role for the adsorption kinetics of synthetic semiflexible polymers [313], which suggests to exploit them for force generation in synthetically built nanosystems.

Another important aspect yet to be investigated theoretically are rheological properties of bundles, in particular, at forces larger than thermal forces which are present in the cell through active processes. Isotropic filament solutions and networks have been studied intensively by various rheological techniques [314] but also for isotropic networks their response to large forces as they can be generated, for example, by molecular motors in the cytoskeleton is not understood from a theoretical point of view.

The works presented in this thesis might also have applications or implications with respect to materials science. From a materials science point of view, the filament meshwork in the cytoskeleton of a cell can be described as a fibrous material. The physics of such materials is not only relevant to biology but also important for many applications throughout materials science, where cellulose or paper represents the technologically most relevant material. In such materials fiber length are typically in the mm-range and fiber diameters in the μm-range, which gives rise to a much higher bending rigidity as for typical biological filaments. Therefore, thermal fluctuations are less important in these materials but adhesive interactions play an equally important role and can be compared to the crosslinks in the biological filament network.

Finally, I want to point out some important parallels between both parts of the thesis, which treat seemingly very different physical systems, the ensemble of vortex lines from condensed matter theory at low temperatures and fluctuating biological filament ensembles. In both systems, we are interested in structure formation based on the ordering of line-like objects, which can be described using the theory of phase transitions. In both systems, different phases occur due to the flexibility of strings and filaments which makes them susceptible to fluctuations. Upon increasing thermal fluctuations the vortex lattice melts and a filament bundle unbinds. However, there is a crucial difference concerning the microscopic interactions in these systems: Vortex lines have a purely repulsive interaction and are hold together by a “pressure” exerted by the external magnetic field, whereas filament bundles are hold together by attractive filaments interactions. But filaments also have a short-range hard-core repulsion, which suggests that a “solid” bundle phase could exist with hexagonal order, which melts into a liquid bundle phase prior to the unbundling transition. It will be interesting to study such bundle melting scenarios experimentally and theoretically, for example, using Lindemann criteria as for the vortex lattice.

Appendix A

Part I

A.1 List of Symbols, Part I

The notation is mostly adapted from Ref. [7].

a	FLL spacing
a_z	basic length scale in z-dir.
B	magnetic induction
$\mathbf{b}$	Burger's vector
$b = B/B_{c2}$	reduced magnetic induction
b_{cd}	cylindrical pinning potential radius, (5.2)
b_{dc}	decoupling transition field
b_m	thermal melting field
b_{sv}	single-vortex pinning field, (3.31), (3.32)
b_t	order-disorder or amorphization transition field
b_x	intersection field of b_m and b_t
b_{2D}	2D crossover field, (3.15)
γ	pinning strength parameter, (3.20)
γ_D	dislocation anisotropy, (4.3)
c_L	Lindemann number, (3.1)
$c_{44}(K, q)$	(dispersive) FLL tilt modulus
c_{66}	FLL shear modulus
d	layer spacing
$d_\perp$	transversal dimensionality
δ	pinning strength parameter, (3.21), (3.23), (3.24)
δ_d	layered pinning strength parameter, (3.22)

E_D	dislocation core energy
E_{ex}	exchange energy (5.7)
E_s	dislocation self-energy, (4.2)
E_0	pancake ground state energy, (3.34)
E_1	vortex binding energy, (5.4)
E_r	collision repulsion energy, (5.6)
ε	anisotropy ratio, (3.9)
ϵ_D	dislocation stiffness, (4.8)
ε_d	layered anisotropy, (3.12)
ε_l	line tension
$\varepsilon_l(q)$	(dispersive) single-vortex line tension
ε_0	characteristic line energy
F_D	single dislocation free energy
$f(\rho)$	dislocation ensemble free energy
G_A, G_B	necklace partition sums
Gi	Ginzburg number
Gi_{2D}	2D Ginzburg number
$G(z)$	grand-canonical partition sum
$\mathbf{g}(\mathbf{r})$	effective dislocation random potential
$\mathbf{H}$	magnetic field
$\mathcal{H}_D$	single dislocation Hamiltonian
j_c	single-vortex critical current
j_{pl}	critical plastic current
j_0	depairing current
K	isotropized elastic constant, (4.6)
K_x	dislocation bundle compression modulus
K_z	dislocation bundle tilt modulus
κ	Ginzburg-Landau parameter
L	vortex length
L_c	collective pinning or Larkin length, (3.25), (3.29)
L_d	dispersion length scale, (3.11)
L_{pl}	plastic pinning length, (4.27)
L_0	single-vortex length, (3.6)
λ_{ab}	magnetic penetration depth
$\tilde{\lambda}_{ab}$	effective magnetic penetration depth
μ	creep exponent
μ_{pl}	plastic creep exponent
N	vortex number
$P(z)$	generating function of p_n
P_r	modified generating function, (5.9)
p_n	return probability
R_a	positional correlation length
R_D	dislocation spacing

ρ	(areal) dislocation density
$\sigma(\mathbf{r})$	random stress field
$\Sigma(\mathbf{r})$	σ-correlations
T	temperature (in energy units, i.e., $k_B \equiv 1$)
T_d	crossover temperature to strong Josephson coupling, (3.13)
T_{de}	delocalization temperature
T_{dp}	depinning temperature, (3.28)
T_k	dislocation kink temperature, (4.10)
T_m	thermal melting temperature
T_m^{2D}	2D melting temperature
T_x	intersection temperature of b_m and b_t
T^*	crossover energy, (5.4)
$t = T/T_c$	reduced temperature
U_{cd}	cylindrical pinning potential depth, (5.2)
$u_D(z)$	single dislocation displacement
$u_D(x,z)$	dislocation bundle displacement
U_p	pancake pinning energy
U_{pl}	plastic creep energy barrier
U^*	pancake energy barrier, (3.35)
$\mathbf{u}(\mathbf{R},z)$	vortex displacement
V_{cd}	cylindrical pinning potential, (5.2)
V_r	repulsive vortex interaction, (5.5)
v_{ex}	exchange Boltzmann-factor
v_r	collision Boltzmann-factor
W_p	Peierls barrier
ξ_{ab}	coherence length
ζ_D	dislocation roughness
ζ_{RM}	vortex roughness in RM regime

A.2 Material parameters of type-II superconductors

For the low-T_c compound NbSe we use the following set of material parameters:

$$\begin{aligned} T_c &\approx 6\,\mathrm{K}\,, \\ \varepsilon &\approx 1/3\,, \\ \xi_{ab} &\approx 100\,\text{Å}\,, \\ \lambda_{ab} &\approx 2000\,\text{Å}\,, \end{aligned} \tag{A.1}$$

which leads to $\kappa \approx 20$, $\mathrm{Gi} \approx 1.7 \times 10^{-6}$. NbSe has no layered structure which can be formally considered as the limit $\varepsilon_d \approx 0$. Pinning is typically weak with $\delta/\varepsilon \approx 10^{-9}$.

For the moderately anisotropic high-T_c compound YBCO we use

$$\begin{aligned} T_c &\approx 90\,\mathrm{K}\,, \\ \varepsilon &\approx 1/5\,, \\ \xi_{ab} &\approx 15\,\text{Å}\,, \\ \lambda_{ab} &\approx 1500\,\text{Å}\,, \\ d &\approx 12\,\text{Å}\,, \end{aligned} \tag{A.2}$$

which leads to $\kappa \approx 100$, $\mathrm{Gi} \approx 10^{-2}$, and $\varepsilon_d \approx 0.008 \ll \varepsilon$. A typical pinning strength is $\delta/\varepsilon \approx 10^{-2}$.

For the strongly layered high-T_c material BSCCO we use

$$\begin{aligned} T_c &\approx 100\,\mathrm{K}\,, \\ \varepsilon &\approx 1/200\,, \\ \xi_{ab} &\approx 100\,\text{Å}\,, \\ \lambda_{ab} &\approx 2000\,\text{Å}\,, \\ d &\approx 15\,\text{Å}\,, \end{aligned} \tag{A.3}$$

which leads to $\kappa \approx 200$, $\mathrm{Gi}_{2D} \approx 0.096$, $T_m^{2D} \approx 10$ K, $\varepsilon_d \approx 0.0075 > \varepsilon$, and $T_d \approx 55$ K. A typical value for the pinning parameter is $\delta_d \approx 10^4 \gg 1$ corresponding to $U_p \approx 10$ K.

Appendix B

Part II

B.1 List of Symbols, Part II

$A_E(\alpha)$	coefficient function, (10.10)
Ai	Airy function
a	half distance between potential minima, (12.2)
$a_\parallel$	filament segment length
α	motor index
b	bond length
b_b	blob size (9.10)
b_m	monomer length of polymeric motor tail
b_0	equilibrium bond length
$C_{2D}(x,x')$	gradient correlation function, (8.5)
$\mathcal{C}(x)$	correlation scaling function, (8.5)
$C_p(x)$, $\mathcal{C}_p(x)$	correlation functions, parabolic channel, (8.7), (8.9)
c_x	crosslinker concentration in solution, (13.5)
χ	contact probability exponent
χ_a	attractive potential well contact exponent, (10.14)
$\chi_{a,r}$	attractive potential well and hard wall contact exponent, (10.16)
D_f	filament thickness parameter
D	filament diameter
D_k	kink diffusion constant
D_{eff}	effective filament diffusion constant
D_T	thermal filament diffusion constant
d	dimensionality
d	kink separation
$d_\perp$	transversal dimensionality
$\langle d_m \rangle$	mean distance between bound motors
Δ	orientation dependence exponent, (10.1)

E_a	adsorption energy
E_b	bending energy
E_f	stretching energy
E_k	kink energy, (12.7)
E_n	transfer matrix energy eigenvalues
E_s	spring energy
E_{sc}	characteristic energy
ΔE_n	critical nucleus excess energy
ϵ	relative bond extension
η	viscosity
η_k	kink friction constant
F	driving force density, (12.2) [chapter 12]
F_c	critical driving force density
F_{de}	detachment force
$F(h)$	constrained free energy
$\mathbf{F}_i^\alpha$	force on filament i from motor α
$\mathbf{F}_{ij}$	filament interaction force
$\mathcal{F}_k$	kink force
F_p	point force, (12.4)
F_{st}	stall force
ΔF_w	free energy of confinement
$\mathbf{f}$	stretching force
f_{cr}	crossover force scale, (9.8)
f_d	desorbing (unzipping) force
f_d^*	most frequent desorption force
$f_{d,c}$	threshold force for desorption
f_{eff}	effective force, (9.17)
f_k	stretching force scale, (9.8)
$f_{k,cr}$	inextensibility force scale, (9.31), (9.32), (9.33)
f_κ	discreteness force scale, (9.8)
f_L	finite size force scale, (9.8)
f_p	fluctuation eigenfunctions, (12.16)
$f(\mathbf{r}, \mathbf{u}, t)$	average number density of filaments, (14.5)
f_W	free energy (per length) of adsorption, (11.7)
G	attempt frequency product
G_Δ	attractive potential strength, (10.1)
$\Delta G(h)$	free energy as a function of polymer height
g	free energy of stretched desorbed polymer, (11.12)
ΔG_b	energy barrier for desorption
$\mathbf{\Gamma}$	matrix of translational friction coefficients, (14.1)
$\Gamma_\parallel$	parallel friction coefficient
$\Gamma_\perp$	perpendicular friction coefficient
Γ_θ	rotational friction coefficient, (14.2)

γ	polymer friction constant, (12.3)
$\mathcal{H}_2$	filament interaction Hamiltonian, (13.1), (13.2)
$\bar{\mathcal{H}}_2$	linker-mediated filament interaction
h	height of polymer end
i	filament index
J	kink nucleation rate [chapter 12]
J	effective pairwise filament attraction (per length) [chapter 13]
J^*	critical pairwise attraction
j	kink nucleation rate (per length)
K	equilibrium constant crosslinker binding, (13.5)
K_n	roots, (12.11)
k	spring stretching modulus
k_d	desorption rate, (11.13)
κ	bending rigidity
κ^c	center of mass bending rigidity
κ^r	reduced bending rigidity
L	projected polymer/filament length
L_{eff}	effective filament length
L_c	polymer contour length
L_d	desorbed length
L_f	extension in force direction, (9.7)
L_m	length of polymeric motor tail
L_p, $\tilde{L}_p$	persistence lengths, (7.2), (7.1)
$L_\perp$	perpendicular system size
ℓ	channel width
ℓ_a	attractive potential width (10.1)
ℓ_z	channel height
λ	deflection length, (8.4)
λ_p	deflection length parabolic channel, (8.8)
M_i^α	torque on filament i from motor α
N	filament number
N_i	number of motor on filament i
n_i	crosslinker occupation number filament i, (13.1)
$\nu_\parallel$	correlation length exponent
Ω	scaling function, (10.8)
Ω_a	attractive potential well scaling function, (10.15)
Ω_0	free polymer scaling function, (10.5)
ω_p	fluctuation eigenvalues, (12.16)
Φ_Δ	orientation dependence, (10.1)
$\phi(s)$	tangent angles
ϕ_p	normal modes, (12.14)
$\psi_{\alpha,E}$	special eigenfunction, (10.11)

$q_l(x)$	normal modes, (8.10)
R_{co}	contact curvature radius
$\mathcal{R}_{\mathbf{u}}$	rotational operator
$\mathbf{r}$	positional vector
$\mathbf{r}_i$	filament center of mass position
$\mathbf{r}_i^\alpha$	position of motor head α on filament i
ρ_{eq}	equilibrium kink density
ρ	kink density
ρ	rod density
ρ_c	critical rod density, (14.7)
$\rho_k(x)$	kink density profile
s	arc length
S	nematic order parameter
σ	motor density
T	temperature (in energy units, i.e., $k_B \equiv 1$)
$T_{2D}(s, s')$	tangent correlation function
T_{eff}	effective temperature
t	time
t_{sc}	characteristic time
$\mathbf{t}$	tangent vector
t_{cr}	polymer crossing time
t_d^*	most frequent desorption time
t_p	persistence time of filament walk
t_x	x-component of tangent
$\mathbf{t}_\perp$	perpendicular component of tangent
θ	segment distribution exponent
θ_a	attractive potential well segment distribution exponent, (10.14)
$\theta_{a,r}$	attractive potential well and hard wall segment distribution exponent, (10.16)
θ_i	filament orientation angle
$\theta(s)$	tangent angle
$\mathbf{u}_i$	filament orientational unit vector
V	potential
V_0	depth of harmonic potential (12.2)
V_a	attractive potential, (10.1)
V_{ch}, V_ℓ	confining channel potentials, (8.2)
V_p	point force potential, (12.4)
V_r	repulsive hard core potential
v	kink velocity, (12.10)
$\mathbf{v}$	gradient or tangent vector
$\bar{v}$	dimensionless velocity
$v(\mathbf{F})$	motor force-velocity relation, (14.3)

v_F	mean filament velocity
$v_{\max}$	maximal motor velocity
v_{sc}	characteristic velocity
W	attractive potential strength, (10.1)
$\bar{W}$	linker-mediated attractive potential strength
$T\bar{W}$	steric mean-field interaction
W_1	adhesive energy of a linker group
W_c	critical potential strength
W_{eff}	effective potential strength, (11.5)
w	reduced potential strength
w	motor capture radius
w_k	kink width, (12.6)
X_p	expansion coefficients, (12.14)
X_1	crosslinker concentration on filament, (13.5)
$X_{1,c}$	critical crosslinker concentration
x	coordinate of preferred orientation
x_i^α	position of motor α on filament i, (14.3)
x_{sc}	characteristic length
x_k	kink position, (12.14)
x_p	point force location, (12.4)
$\xi_\parallel$	correlation length
ξ_f	blob length, (9.9)
ξ_p	filament walk persistence length, (14.4)
$\mathbf{z}$	displacement vector
$\bar{\mathbf{z}}$	filament bundle center of mass
$z_k(x)$	kink configuration
z_m	midpoint position
$z_n(x)$	nucleus configuration
Z	(restricted) partition sum
Z_E	ground state partition sum
ζ	thermal noise
$\boldsymbol{\zeta}_i$	thermal random force on filament i, (14.1)
$\zeta_{\theta,i}$	thermal random torque on filament i, (14.2)

Bibliography

[1] J.G. Bednorz and K.A. Müller, Z. Physik B **64**, 189 (1986).

[2] A.A. Abrikosov, Sov. Phys. JETP **5**, 1174 (1957).

[3] U. Essmann and H. Träuble, Physics Letters **24A**, 526 (1967).

[4] P.E. Goa, H. Hauglin, M. Baziljevich, E. Il'yashenko, P.L. Gammel, and T.H. Johansen, Supercond. Sci. technol. **14**, 729 (2001).

[5] E.H. Brandt, Phys. Stat. Sol. **35**, 1027 (1969); J. Low Temp. Phys. **26**, 709 and 735 (1977).

[6] E.H. Brandt, Rep. Prog. Phys. **58**, 1465 (1995).

[7] G. Blatter, M.V. Feigelman, V.B. Geshkenbein, A.I. Larkin, and V.M. Vinokur, Rev. Mod. Phys. **66**, 1125 (1994).

[8] T. Nattermann and S. Scheidl, Adv. Phys. **49**, 607 (2000).

[9] A.I. Larkin, Sov. Phys. JETP **31**, 784 (1970); A.I. Larkin and Y.N. Ovchinnikov, J. Low Temp. Phys. **34**, 409 (1979).

[10] M.P.A. Fisher, Phys. Rev. Lett **62**, 1415 (1989).

[11] D.S. Fisher, M.P.A. Fisher, and D.A. Huse, Phys. Rev. B **43**, 130 (1991).

[12] R.H. Koch, V. Foglietti, W.J. Gallagher, G. Koren, A. Gupta, and M.P.A. Fisher, Phys. Rev. Lett. **63**, 1511 (1989).

[13] E. Brezin, D.R. Nelson, and A. Thiaville, Phys. Rev. B **31**, 7124 (1985).

[14] D.R. Nelson, Phys. Rev. Lett. **60**, 1973 (1988).

[15] G. Eilenberger, Phys. Rev. **164**, 628 (1967).

[16] D.R. Nelson and H.S. Seung, Phys. Rev. B **39**, 9153 (1989).

[17] A. Houghton, R.A. Pelcovits, and A. Sudbø, Phys. Rev. B **40**, 6763 (1989).

[18] R. Liang, D.A. Bonn, and W.N. Hardy, Phys. Rev. Lett. **76**, 835 (1996).

[19] U. Welp, J.A. Fendrich, W.K. Kwok, G.W. Crabtree, and B.W. Veal, Phys. Rev. Lett. **76**, 4809 (1996).

[20] E. Zeldov, D. Majer, M. Konczykowski, V.B. Geshkenbein, V.M. Vinokur, and H. Shtrikman, Nature (London) **375**, 373 (1995).

[21] M. Roulin, A. Junod, and E. Walker, Science **273**, 1210 (1996).

[22] A. Schilling, R.A. Fisher, N.E. Phillips, U. Welp, D. Dasgupta, W.K. Kwok, and G.W. Crabtree, Nature **382**, 791 (1996).

[23] M.J.W. Dodgson, A.E. Koshelev, V.B. Geshkenbein, and G. Blatter, Phys. Rev. Lett. **84**, 2698 (2000).

[24] M.V. Feigelman, V.B. Geshkenbein, A.I. Larkin, and V.M. Vinokur, Phys. Rev. Lett. **63**, 2303 (1989).

[25] T. Nattermann, Phys. Rev. Lett. **64**, 2454 (1990).

[26] T. Giamarchi and P. Le Doussal, Phys. Rev. Lett. **72**, 1530 (1994); Phys. Rev. B **52**, 1242 (1995).

[27] J. Kierfeld, T. Nattermann, and T. Hwa, Phys. Rev. B **55**, 626 (1997).

[28] D.S. Fisher, Phys. Rev. Lett. **78**, 1964 (1997).

[29] R. Cubitt, E.M. Forgan, G. Yang, S.L. Lee, D.M. Paul, H.A. Mook, M. Yethiraj, P.H. Kes, T.W. Li, A.A. Menovsky, Z. Tarnawski, and K. Mortensen, Nature (London) **365**, 407 (1993).

[30] H. Safar, P.L. Gammel, D.A. Huse, D.J. Bishop, W.C. Lee, J. Giapintzakis, and D.M. Ginsberg, Phys. Rev. Lett. **70**, 3800 (1993).

[31] D. Lopez, L. Krusin-Elbaum, H. Safar, E. Righi, F. de la Cruz, S. Grigera, C. Feild, W.K. Kwok, L. Paulius, and G.W. Crabtree, Phys. Rev. Lett. **80**, 1070 (1998).

[32] T. Nishizaki, T. Naito, S. Okayasu, A. Iwase, and N. Kobayashi, Phys. Rev. B **61**, 3649 (2000).

[33] D.R. Nelson, Nature **375**, 356 (1995).

[34] N.F. Mott and E.W. Gurney, Trans. Faraday Soc. **35**, 364 (1939).

[35] D.R. Nelson in *Phase Transitions and Critical Phenomena*, edited by C. Domb and J.L. Lebowitz (Academic, New York, 1983), Vol. 7.

[36] H. Kleinert, *Gauge Fields in Condensed Matter* (World Scientific, Singapore, 1989), Vol. II.

[37] B. Joós *The role of dislocations in melting*, in *Dislocations in Solids*, edited by F.R.N. Nabarro and M.S. Duesbury (North-Holland, Amsterdam, 1996), Vol. 10, p.505.

[38] W.L. Bragg, in *Proceedings of the Symposium on Internal Stresses*, (Institute of Metals, London, 1947), p. 221.

[39] W. Shockley, in *L'Etat Solide*, Proceedings of Neuvienne-Consail de Physique, Brussels, 1952, edited by R. Stoops (Solvay Institut de Physique, Belgium, 1952), p. 431.

[40] S. Mizushima, J. Phys. Soc. Jpn **15**, 70 (1960).

[41] A. Ookawa, J. Phys. Soc. Jpn **15**, 2191 (1960).

[42] S.F. Edwards and M. Warner, Phil. Mag. A **40**, 257 (1979).

[43] T. Yamamoto and T. Izuyama, J. Phys. Soc. Jpn. **57**, 3742 (1988).

[44] L. Burakovsky, D.L. Preston, and R.R. Silbar, Phys. Rev. B **61**, 15011 (2000).

[45] R. Labusch, Phys. Lett. **22**, 9 (1966).

[46] H. Träuble and U. Essmann, Phys. Satus Solidi **25**, 373 (1968); J. Appl. Phys. **39**, 4052 (1968).

[47] F.A. Lindemann, Phys. Z. (Leipzig) **11**, 609 (1910).

[48] H. Löwen, Phys. Rep. **237**, 249 (1994).

[49] J.P. Hansen and L. Verlet, Phys. Rev. **184**, 151 (1969).

[50] L. Civale, A.D. Marwick, T.K. Worthington, M.A. Kirk, J.R. Thompson, L.Krusin-Elbaum, Y. Sun, J.R. Clem, and F. Holtzberg, Phys. Rev. Lett. **67**, 648 (1991).

[51] M. Konczykowski, F. Rullier-Albenque, E.R. Yacoby, A. Shaulov, Y. Yeshurun, and P. Lejay, Phys. Rev. B **44**, 7167 (1991).

[52] D.R. Nelson and V.M. Vinokur, Phys. Rev. Lett. **68**, 2398 (1992).

[53] D.R. Nelson and V.M. Vinokur, Phys. Rev. B **48**, 13060 (1993).

[54] J. Kierfeld and V. Vinokur, Phys. Rev. B **69**, 024501 (2004).

[55] J. Kierfeld, Phys. Rev. B **69**, 144513 (2004).

[56] J. Kierfeld and V. Vinokur, Phys. Rev. B **61**, R14928 (2000).

[57] J. Kierfeld, H. Nordborg, and V.M. Vinokur, Phys. Rev. Lett. **85**, 4948 (2000).

[58] J. Kierfeld and V.M. Vinokur, Phys. Rev. Lett. **94**, 077005 (2005).

[59] G. Blatter, V. Geshkenbein, A. Larkin, and H. Nordborg, Phys. Rev. B **54**, 72 (1996).

[60] B. Khaykovich, E. Zeldov, D. Majer, T.W. Li, P.H. Kes, and M. Konczykowski, Phys. Rev. Lett. **76**, 2555 (1996).

[61] S. Kokkaliaris, P.A.J. de Groot, S.N. Gordeev, A.A. Zhukov, R. Gagnon, and L. Taillefer, Phys. Rev. Lett. **82**, 5116 (1999).

[62] Y. Paltiel, E. Zeldov, Y. Myasoedov, M.L. Rappaport, G. Jung, S. Bhattacharya, M.J. Higgins, Z.L. Xiao, E.Y. Andrei, P.L. Gammel, and D.J. Bishop, Phys. Rev. Lett. **85**, 3712 (2000).

[63] D. Ertaş and D.R. Nelson, Physica C **272**, 79 (1996).

[64] Y.Y. Goldschmidt, Phys. Rev. B **56**, 2800 (1997).

[65] T. Giamarchi and P. Le Doussal, Phys. Rev. B **55**, 6577 (1997).

[66] A.E. Koshelev and V.M. Vinokur, Phys. Rev. B **57**, 8026 (1998).

[67] V. Vinokur, B. Khaykovich, E. Zeldov, M. Konczykowski, R.A. Doyle, and P.H. Kes, Physica C **295**, 209 (1998).

[68] J. Kierfeld, Physica C **300**, 171 (1998).

[69] G.P. Mikitik and E.H. Brandt, Phys. Rev. B **64**, 184514 (2001).

[70] Y. Radzyner, A. Shaulov, Y. Yeshurun, I. Felner, K. Kishio, and J. Shimoyama, Phys. Rev. B **65**, 100503 (2002); Y. Radzyner, A. Shaulov, Y. Yeshurun, *ibid.* **65**, 100513 (2002).

[71] S. Ryu, S. Doniach, G. Deutscher, and A. Kapitulnik, Phys. Rev. Lett. **68**, 710 (1992).

[72] H. Nordborg and G. Blatter, Phys. Rev. Lett. **79**, 1925 (1997).

[73] X. Hu, S. Miyashita, and M. Tachiki, Phys. Rev. B **58**, 3438 (1998).

[74] D.S. Fisher, M.P.A. Fisher, and D.A. Huse, Phys. Rev. B **43**, 130 (1991).

[75] T. Hwa and D.S. Fisher, Phys. Rev. B **49**, 3136 (1994).

[76] J.R. Clem, Phys. Rev. **43**, 7837 (1991).

[77] C. Zeng, P.L. Leath, and D.S. Fisher, Phys. Rev. Lett **82**, 1935 (1999); P. Le Doussal and T. Giamarchi, Physica C **331**, 233 (2000).

[78] L.I. Glazman and A.E. Koshelev, Phys. Rev. B **43**, 2835 (1991).

[79] S.S. Banerjee, N.G. Patil, S. Saha, S. Ramakrishnan, A.K. Grover, S. Bhattacharya, G. Ravikumar, P.K. Mishra, T.V. Chandrasekhar Rao, V.C. Sahni, M.J. Higgins, E. Yamamoto, Y. Haga, M. Hedo, Y. Inada, and Y. Onuki, Phys. Rev. B **58**, 995 (1998).

[80] J.M. Kim and J.M. Kosterlitz, Phys. Rev. Lett. **62**, 2289 (1989).

[81] T. Halpin-Healy and Y.C. Zhang, Phys. Rep. **254**, 215 (1995).

[82] M. Müller, D.A. Gorokhov, and G. Blatter, Phys. Rev. B **64**, 134523 (2001).

[83] D.A. Gorokhov and G. Blatter, Phys. Rev. B **62**, 14032 (2000).

[84] A.E. Koshelev, L.I. Glazman, and A.I. Larkin, Phys. Rev. B **53**, 2786 (1996).

[85] O.S. Wagner, G. Burkard, V.B. Geshkenbein, and G. Blatter, Phys. Rev. Lett. **81**, 906 (1998).

[86] N. Avraham, B. Khaykovich, Y. Myasoedov, M. Rappaport, H. Shtrikman, D.E. Feldman, T. Tamegai, P.H. Kes, M. Li, M. Konczykowski, K. van der Beek, and E. Zeldov, Nature (London) **411**, 451 (2001).

[87] L. B. Ioffe and V. M. Vinokur, J. Phys. C **20**, 6149 (1987).

[88] S. Lemerle, J. Ferré, C. Chappert, V. Mathet, T. Giamarchi, P. Le Doussal, Phys. Rev. Lett. **80**, 849 (1998).

[89] V.N. Kopylov, I.F. Schegolev, and T.G. Togonidze, Physica C **162-164**, 1143 (1989).

[90] V.N. Kopylov, A.E. Koshelev, I.F. Schegolev, and T.G. Togonidze, Physica C **170**, 291 (1990).

[91] M. Daeumling, J.M. Seuntjens, and D.C. Larbalestier, Nature (London) **346**, 332 (1990).

[92] N. Chikumoto, M. Konczykowski, N. Motohira, K. Kishio, and K. Kitazawa, Physica C **185-189**, 2201 (1991).

[93] N. Chikumoto, M. Konczykowski, N. Motohira, and A.P. Malozemoff, Phys. Rev. Lett. **69**, 1260 (1992).

[94] M. Konczykowski, C.J. van der Beek, S. Colson, M.V. Indenbom, P.H. Kes, Y. Paltiel, and E. Zeldov, Physica C **341**, 1317 (2000).

[95] C.J. van der Beek, S. Colson, M.V. Indenbom, and M. Konczykowski, Phys. Rev. Lett. **84**, 4196 (2000).

[96] J.P. Hirth and J. Lothe, *Theory of Dislocations* (McGraw-Hill, New York, 1968).

[97] M.C. Marchetti and D.R. Nelson , Phys. Rev. B **41**, 1910 (1990).

[98] E.H. Brandt, Phys. Stat. Sol. **35**, 1027 (1969); J. Low Temp. Phys. **26**, 709 and 735 (1977).

[99] F.R.N. Nabarro and A.T. Quintanilha, in *Dislocations in Solids*, edited by F.R.N. Nabarro (North-Holland, Amsterdam, 1980), Vol. 5.

[100] M.-C. Miguel and M. Kardar, Phys. Rev. B **56**, 11903 (1997).

[101] S.R. Shenoy, Phys. Rev. B **40**, 5056 (1989); F. Lund, Phys. Rev. Lett. **69**, 3084 (1992).

[102] J.L. Cardy and S. Ostlund, Phys. Rev. B **25**, 6899 (1982).

[103] C. Zheng, P.L. Leath, and D.S. Fisher, Phys. Rev. Lett. **82**, 1935 (1999).

[104] T. Emig, S. Bogner, and T. Nattermann , Phys. Rev. Lett. **83**, 400 (1999).

[105] T. Emig, Ph.D. thesis, Cologne University, 1998.

[106] M.S. Li, T. Nattermann, H. Rieger, and M. Schwartz, Phys. Rev. B **54**, 16024 (1996).

[107] D.W. Braun, G.W. Crabtree, H.G. Kaper, A.E. Koshelev, G.K. Leaf, D.M. Levine, and V.M. Vinokur, Phys. Rev. Lett. **76**, 831 (1996).

[108] S.S. Banerjee, A. Soibel, Y. Myasoedov, M. Rappaport, E. Zeldov, M. Menghini, Y. Fasano, F. de la Cruz, C.J. van der Beek, and M. Konczykowski, Phys. Rev. Lett. **90**, 087004 (2003).

[109] R.J. Olsson, W.-K. Kwok, L.M. Paulius, A.M. Petrean, D.J. Hofman, and G.W. Crabtree, Phys. Rev. B **65**, 104520 (2002).

[110] L. Krusin-Elbaum, L. Civale, G. Blatter, A.D. Marwick, F. Holtzberg, and C. Feild, Phys. Rev. Lett. **72**, 1914 (1994).

[111] C.J. van der Beek, M. Konczykowski, R.J. Drost, P.H. Kes, N. Chikumoto, S. Bouffard, Phys. Rev. B **61**, 4259 (2000).

[112] A.V. Lopatin and V.M. Vinokur, Phys. Rev. Lett. **92**, 067008 (2004).

[113] O. Entin-Wohlman, A. Aharony, Y. Imry, and Y. Levinson, Europhys. Lett. **50**, 354 (2000).

[114] H. Nordborg and V.M. Vinokur, Phys. Rev. B **62**, 12408 (2000).

[115] R.A. Suris, Sov. Phys. JETP **20**, 961 (1965).

[116] M.E. Fisher, J. Stat. Phys. **34**, 667 (1984).

[117] R. Lipowsky, Phys. Rev. Lett. **62**, 704 (1989).

[118] E. Frey, D.R. Nelson, D.S. Fisher, Phys. Rev. B **49**, 9723 (1994).

[119] M.V. Indenbom, C.J. van der Beek, V. Berseth, W. Benoit, G. D'Anna, A. Erb E. Walker, R. Flükiger, Nature **385**, 702 (1997); D. Nelson, Nature **385**, 675 (1997).

[120] R. Besseling, P.H. Kes, T. Dröse, and V.M. Vinokur, New J. Phys. **7**, 71 (2005).

[121] E.M. Lifshitz and L.D. Landau, *Theory of Elasticity* (Pergamon Press, New York, 1986).

[122] P.G. de Gennes, *Scaling Concepts in Polymer Physics* (Cornell University Press, Ithaca, 1979).

[123] M. Doi and S.F. Edwards, *The Theory of Polymer Dynamics* (Clarendon, Oxford, 1986).

[124] A.Y. Grosberg and A.R. Khokhlov, *Statistical Physics of Macromolecules* (American Institute of Physics Press, New York, 1994).

[125] C. Ecker, N. Severin, L. Shu, A.D. Schlüter, and J.P. Rabe, Macromolecules **37**, 2484 (2004).

[126] P. Samori, C. Ecker, I. Gössl, P.A.J. de Witte, J.J.L.M. Cornelissen, G.A. Metselaar, M.B.J. Otten, A.E. Rowan, R.J.M. Nolte, and J.P. Rabe, Macromolecules **35**, 5290.

[127] J.-M. Lehn, *Supramolecular Chemistry* (VCH, Weinheim, 1995).

[128] D.G. Kurth, N. Severin, and J.P. Rabe, Angew. Chem. **114**, 3833 (2002).

[129] B. Alberts, D. Bray, J. Lewis, M. Raff, K. Roberts, J.D. Watson, *Molecular Biology of the Cell* (Garland Publishing, New York, 1994).

[130] H. Lodish, A. Berk, L.S. Zipursky, P. Matsudaira, D. Baltimore, and J. Darnell, *Molecular Cell Biology* (W.H. Freeman, New York, 2000).

[131] J. Howard, *Mechanics of Motor Proteins and the Cytoskeleton* (Sinauer Associates, Inc., Sunderland, 2001).

[132] A. Ott, M. Magnasco, A. Simon, and A. Libchaber, Phys. Rev. E, **48**, R1642 (1993).

[133] F. Gittes, B. Mickey, J. Nettleton, and J. Howard, J. Cell Biol. **120**, 923 (1993).

[134] J. Käs, H. Strey, and E. Sackmann, Nature **368**, 226 (1994).

[135] W.H. Taylor and P.J. Hagerman, J. Mol. Biol. **212**, 363 (1990).

[136] J.-L. Barrat and J.-F. Joanny, *Advances in Chemical Physics, Vol. XCIV*, edited by I. Prigogine and S.A. Rice (John Wiley & Sons, New York, 1996).

[137] T. Odijk, J. Polym. Sci. **15**, 477 (1977).

[138] J. Skolnick and M. Fixman, Macromolecules **10**, 944 (1977).

[139] O. Kratky and G. Porod, Recl. Trav. Chim. Pays-Bas **68**, 1106 (1949).

[140] E.M. Lifshitz and L.D. Landau, *Statistical Physics, Part 1* (Pergamon Press, New York, 1969).

[141] H. Kleinert, *Path Integrals in Quantum Mechanics, Statistics, and Polymer Physics, and Financial Markets* (World Scientific, Singapore, 2004).

[142] G. Binnig, C.F. Quate, and C. Gerber, Phys. Rev. Lett. **56**, 930 (1986).

[143] A. Ashkin, Science **210**, 1081 (1980).

[144] S.B. Smith, L. Finzi, C. Bustamante, Science **258**, 1122 (1992).

[145] C. Bustamante, J.F. Marko, E.D. Siggia, and S. Smith, Science **265**, 1599 (1995).

[146] J.F. Marko and E.D. Siggia, Macromolecules **28**, 8759 (1995).

[147] P.-G. de Gennes, J. Chem. Phys. **48**, 2257 (1968).

[148] P.-G. de Gennes, J. Phys. (Paris) **37**, 1445 (1976).

[149] V.L. Pokrovsky and A.L. Talapov, Phys. Rev. Lett. **42**, 65 (1979).

[150] J. Kierfeld, PhD thesis, University of Cologne (1996).

[151] T. Emig and S. Bogner, Phys. Rev. Lett. **90**, 185701 (2003).

[152] W. Helfrich, Z. Naturforsch. A **33**, 305 (1978).

[153] W. Helfrich and R.-M. Servuss, Nuovo Cimento D **3**, 137 (1984).

[154] R. Lipowsky and S. Leibler, Phys. Rev. Lett. **56**, 2541 (1986).

[155] R. Lipowsky, in *Handbook of Biological Physics, Vol. 1*, edited by R. Lipowsky and E. Sackmann (Elsevier, Amsterdam, 1995).

[156] R. Lipowsky, in *Encyclopedia of Applied Physics, Vol. 23* (VCH Publishers, Weinheim and New York 1998).

[157] M. Mutz and W. Helfrich, Phys. Rev. Lett. **62**, 2881 (1989).

[158] B. Pozo-Navas, V.A. Ragunathan, J. Katsaras, M. Rappolt, K. Lohner, and G. Pabst, Phys. Rev. Lett. **91**, 028101 (2003).

[159] R. Lipowsky, Physica Scripta **T29**, 259 (1989).

[160] S.S. Sheiko and M. Möller, Chem. Rev. **101**, 4099 (2001).

[161] M. Seitz, C. Friedsam, W. Jöstl, T. Hugel, and H.E. Gaub, Chem. Phys. Chem. **4**, 986 (2003).

[162] B. Essevaz-Roulet, U. Bockelmann, and F. Heslot, Proc. Natl. Acad. Sci. USA **94**, 11935 (1997).

[163] C.W. Jones, J.C. Wang, R.W. Briehl, and M.S. Turner, Biophys. J. **88**, 2433 (2005).

[164] G. Binning and H. Rohrer, Rev. Mod. Phys. **59**, 615 (1987).

[165] T.A. Jung, R.R. Schlittler, J.K. Gimzewski, H. Tang, C. Joachim, Science **271**, 181 (1996).

[166] N. Severin, J. Barner, A.A. Kalachev and J.P. Rabe, Nano Lett. **4**, 577 (2004).

[167] M. Tempel, G. Isenberg, and E. Sackmann, Phys. Rev. E **54**, 1802 (1996).

[168] O. Pelletier, E. Pokidyshevam L.S. Hirst, N. Bouxsein, Y. Li, and C.R. Safinya, Phys. Rev. Lett. **91**, 148102 (2003).

[169] M.L. Gardel, J.H. Shin, F.C. MacKintosh, L. Mahadevan, P. Matsudaira, and D.A. Weitz, Science **304**, 1301 (2004).

[170] F.J. Nédélec, T. Surrey, A.C. Maggs, and S. Leibler, Nature **389**, 305 (1997).

[171] T. Surrey, M.B. Elowitz, P.-E. Wolf, F. Yang, F. Nédélec, K. Shokat, and S. Leibler, Proc. Natl. Acad. Sci. USA **95**, 4293 (1998).

[172] T. Surrey, F. Nédélec, S. Leibler, and E. Karsenti, Science **292**, 1167 (2001).

[173] D. Humphrey, C. Duggan, D. Saha, D. Smith, and J. Käs, Nature **416**, 413 (2002).

[174] H.Y. Lee and M. Kardar, Phys. Rev. E **64**, 056113 (2001).

[175] T.B. Liverpool and M.C. Marchetti, Phys. Rev. Lett. **90**, 138102 (2003).

[176] F. Ziebert and W. Zimmermann, Phys. Rev. Lett. **93**, 159801 (2004).

[177] T.B. Liverpool and M.C. Marchetti, Phys. Rev. Lett. **93**, 159802 (2004).

[178] K. Kruse, J.F. Joanny, F. Jülicher, J. Prost, and K. Sekimoto, Phys. Rev. Lett. **92**, 078101 (2004).

[179] I.S. Aranson and L.S. Tsimring, Phys. Rev. E **71**, 050901(R) (2005).

[180] J. Scholey, *Motility assays for motor proteins*, Meth. Cell Biology **39**, (Academic Press, New York, 1993).

[181] T. Duke, T.E. Holy, and S. Leibler, Phys. Rev. Lett. **74**, 330 (1995).

[182] S. Köster, H. Stark, T. Pfohl, and J. Kierfeld, Biophys. Rev. Lett. (2007), in press.

[183] J. Kierfeld, O. Niamploy, V. Sa-yakanit, and R. Lipowsky, Eur. Phys. J. E **14**, 17 (2004).

[184] J. Kierfeld and R. Lipowsky, Europhys. Lett. **62**, 285 (2003).

[185] J. Kierfeld and R. Lipowsky, J. Phys. A: Math. Gen. **38**, L155 (2005).

[186] J. Kierfeld, Phys. Rev. Lett. **97**, 058302 (2006).

[187] P. Kraikivski, R. Lipowsky, and J. Kierfeld, Europhys. Lett. **66**, 763 (2004).

[188] P. Kraikivski, R. Lipowsky, and J. Kierfeld, Eur. Phys. J. E **16**, 319 (2005).

[189] P. Kraikivski, R. Lipowsky, and J. Kierfeld, Europhys. Lett. **71**, 138 (2005).

[190] J. Kierfeld, T. Kühne, and R. Lipowsky, Phys. Rev. Lett. **95**, 038102 (2005),

[191] P. Kraikivski, R. Lipowsky, and J. Kierfeld, Phys. Rev. Lett. **96**, 258103 (2006)

[192] R.J. Ellis, Curr. Opin. Struc. Biol. **11**, 114 (2001).

[193] J.O. Tegenfeldt, C. Prinz, H. Cao, S. Chou, W.W. Reisner, R. Riehn, Y.W. Wang, E.C. Cos, J.C. Sturm, P. Silberzan, and R.H. Austin, Proc. Natl. Acad. Sci. USA **101**, 10979 (2004).

[194] W. Reisner, K.J. Morton, R. Riehn, Y.W. Wang, Z. Yu, M. Rosen, J.C. Sturm, S.Y. Chu, E. Frey, and R. Austin, Phys. Rev. Lett. **94**, 196101 (2005).

[195] J. Zaanen, Phys. Rev. Lett. **84**, 753 (2000).

[196] E. Dagotto, Science **309**, 257 (2005).

[197] A.R. Khokhlov and A.N. Semenov, Physica A **108**, 546 (1981).

[198] A.R. Khokhlov and A.N. Semenov, Physica A **112**, 605 (1982).

[199] T. Odijk, Macromolecules **16**, 1340 (1983).

[200] W. Helfrich and W. Harbich, Chem. Scr. **25**, 32 (1985).

[201] T. Odijk, Macromolecules **19**, 2313 (1986).

[202] T.W. Burkhardt, J. Phys. A: Math. Gen. **28**, L629 (1995).

[203] M. Dijkstra, D. Frenkel, and H.N.W. Lekkerkerker, Physica A **193**, 374 (1993).

[204] T.W. Burkhardt, J. Phys. A: Math. Gen. **30**, L167 (1997).

[205] D.J. Bicout and T.W. Burkhardt, J. Phys. A: Math. Gen. **34**, 5745 (2001).

[206] A. Lamura, T.W. Burkhardt, and G. Gompper, Phys. Rev. E **70**, 051804 (2004).

[207] J. Wang and H. Gao, J. Chem. Phys. **123**, 084906 (2005).

[208] S. Köster, D. Steinhauser and T. Pfohl, J. Phys.: Condens. Matter **17** S4091 (2005).

[209] R. Lipowsky, Z. Phys. B **97**, 193 (1995).

[210] C. Hiergeist and R. Lipowsky, Physica A **244**, 164 (1997).

[211] T.W. Burkhardt, J. Phys. A: Math. Gen. **26**, L1157 (1993).

[212] S.R. Aragón S and R. Pecora, Macromolecules **18**, 1868 (1985).

[213] R.A. Harris and J.E. Hearst, J. Chem. Phys. **44**, 2595 (1966).

[214] N. Saito, K. Takahashi, and Y. Yunoki, J. Phys. Soc. Jpn. **22**, 219 (1967).

[215] M. Fixman and J. Kovac, J. Chem. Phys. **58**, 1564 (1973).

[216] J. Kovac and C.C. Crabb, Macromolecules **15**, 537 (1982).

[217] S. Smith, Y. Cui, and C. Bustamante, Science **271**, 795 (1996).

[218] M. Rief, J.M. Fernandez, and H.E. Gaub, Phys. Rev. Lett. **81**, 4764 (1998).

[219] T. Hugel, M. Grosholz, H. Clausen-Schaumann, A. Pfau, H. Gaub, and M. Seitz, Macromolecules **34**, 1039 (2001).

[220] M. Rief, M. Gautel, F. Oesterhelt, J.M. Fernandez, H.E. Gaub, Science **276**, 1109 (1997).

[221] X. Liu and G.H. Pollack, Biophys. J. **83**, 2705 (2002).

[222] P. Cluzel, A. Lebrun, R. Lavery, J.-L. Viovy, D. Chatenay, F. Caron, Science **271**, 792 (1996).

[223] T. Odijk, Macromolecules **28**, 7016 (1995).

[224] M.D. Wang, H. Yin, R. Landick, J. Gelles, and S.M. Block, Biophys. J. **72**, 1335 (1997).

[225] C. Bouchiat, M.D. Wang, J.-F. Allemand, T. Strick, M. Block, and V. Croquette, Biophys. J. **76**, 409 (1999).

[226] R.R. Netz, Macromolecules **34**, 7522 (2001).

[227] L. Livadaru, R.R. Netz, and H.J. Kreuzer, Macromolecules **36**, 3732 (2003).

[228] B. Maier, U. Seifert, and J.O. Rädler, Europhys. Lett. **60**, 622 (2002).

[229] A. Lamura, T.W. Burkhardt, and G. Gompper, Phys. Rev. E **64**, 061801 (2001).

[230] K. Kroy and E. Frey, Phys. Rev. Lett. **77**, 306 (1996).

[231] P.J. Flory, *Statistical Mechanics of Chain Molecules* (Interscience, New York, 1969).

[232] P. Janmey, J.X. Tang, and C.F. Schmidt, *Actin filaments* in *Biophysics Textbook online*, `http://www.biophysics.org/btol/`.

[233] R.P Feynman and A.R. Hibbs, *Quantum Mechanics and Path Integrals* (McGraw-Hill, 1995).

[234] M. Abramowitz and A.I. Stegun, *Handbook of Mathematical functions* (Natl. Bur. Stand., Washington, 1965).

[235] K.R. Ayscough, Curr. Opin. Cell Biol. **10**, 102 (1998).

[236] S.J. Winder, Curr. Opin. Cell Biol. **15**, 14 (2003).

[237] R.R. Netz and J.-F. Joanny, Macromolecules **32**, 9013 (1999).

[238] G. Gompper and T. Burkhardt, Phys. Rev. A **40**, 6124 (1989).

[239] A.C. Maggs, D.A. Huse, and S. Leibler, Europhys. Lett. **8**, 615 (1989).

[240] R. Bundschuh, M. Lässig, and R. Lipowsky, Eur. Phys. J. E **3**, 295 (2000).

[241] J. Wilhelm and E. Frey, Phys. Rev. Lett. **77**, 2581 (1996).

[242] R. Lipowsky, Europhys. Lett. **15**, 704 (1991).

[243] R. Lipowsky, J. Phys.: Cond. Mat. **6**, A409 (1994).

[244] O.M. Leung, M.C. Groh, Science **255**, 64 (1992).

[245] M. Rief and H. Grubmüller, Chem. Phys. Chem. **3**, 255 (2002).

[246] Strick T. R., Allemand J.-F., Bensimon D., Bensimon A., Croquette V., Science **271**, 1835 (1996).

[247] T.J. Senden, J.-M. di Meglio, and P. Auroy, Eur. Phys. J. B **3**, 211 (1998).

[248] X. Chatellier, T.J. Senden, J.-F. Joanny, and J.-M. Di Meglio, Europhys. Lett. **41**, 303 (1998).

[249] S. Cui, C. Liu, and X. Zhang, Nano Lett. **3**, 245 (2003).

[250] C. Friedsam, A. Del Campo Becares, U. Jonas, M. Seitz, and H.E. Gaub, New J. Phys. **6**, 9 (2004).

[251] G.J. Fleer, M.A. Cohen Stuart, J.M.H.M. Scheutjens, T. Cosgrove, B. Vincent, *Polymers at interfaces* (Chapman & Hall, London, 1983);

[252] R.R. Netz and D. Andelman, Physics Reports **380**, 1 (2003).

[253] T.M. Birshtein, E.B. Zhulina, and A.M. Skvortsov, Biopolymers **18**, 1171 (1979); E.B. Zhulina, T.M. Birshtein, and A.M. Skvortsov, Biopolymers **19**, 805 (1980).

[254] D.C. Morse and G.H. Frederickson, Phys. Rev. Lett. **73**, 3235 (1994).

[255] C.C. van der Linden, F.A.M. Leermakers, and G.J. Fleer, Macromolecules **29**, 1172 (1996).

[256] D.V. Kuznetsov and W. Sung, J. Chem Phys. **107**, 4729 (1997).

[257] S. Stepanow, J. Chem. Phys. **115**, 1565 (2001).

[258] A.N. Semenov, Eur. Phys. J. E **9**, 353 (2002).

[259] P.K. Mishra, S. Kumar, and Y. Singh, Physica A **323**, 453 (2003).

[260] P. Benetatos and E. Frey, Phys. Rev. E **67**, 051108 (2003).

[261] E.Y. Kramarenko, R.G. Winkler, P.G. Khalatur, A.R. Khoklov, and P. Reineker, J. Chem. Phys. **104**, 4806 (1996).

[262] T. Sintes, K. Sumithra, and E. Straube, Macromolecules **34**, 1352 (2001).

[263] U. Bockelmann, P. Thomen, B. Essevaz-Roulet, V. Viasnoff, and F. Heslot, Biophys. J **82**, 1537 (2002).

[264] K.L. Sebastian, Phys. Rev. E **62**, 1128 (2000).

[265] D.K. Lubensky and D.R. Nelson Phys. Rev. Lett. **85**, 1572 (2000).

[266] S.M. Bhattacharjee, J. Phys. A: Math. Gen. **33**, L423 (2000).

[267] S. Cocco, R. Monasson, and J.F. Marko, Proc. Natl. Acad. Sci. USA **98**, 8608 (2001).

[268] D. Marenduzzo, A. Trovato, and A. Maritan, Phys. Rev. E **64**, 031901 (2001).

[269] D. Marenduzzo, S.M. Bhattacharya, A. Maritan, E. Orlandini, and F. Seno, Phys. Rev. Lett. **88**, 028102 (2002).

[270] J. Bico, B. Roman, L. Moulin, A. Boudaoud, Nature **432**, 690 (2004).

[271] B.R. Lawn and T.R. Wilshaw, *Fracture of britte solids* (Cambridge University Press, Cambridge, 1975).

[272] G.I. Bell, Science **200**, 618 (1978).

[273] J. Uhde, M. Keller, E. Sackmann, A. Parmeggiani, and E. Frey, Phys. Rev. Lett. **93**, 268101 (2004).

[274] H.A. Kramers, Physica (Utrecht) **7**, 284 (1940).

[275] P. Hänggi,P. Talkner, and M. Borkovec M., Rev. Mod. Phys. **62**, 251 (1990).

[276] M. Büttiker M. and R. Landauer, Phys. Rev. Lett. **43**, 1453 (1979); Phys. Rev. A **23**, 1397 (1981).

[277] J.F. Currie, J.A. Krumhansl, A.R. Bishop, and S.E. Trullinger, Phys. Rev. B **22**, 477 (1980).

[278] K.L. Sebastian, Phys. Rev. E **61**, 3245 (2000).

[279] K.L. Sebastian and A.K.R. Paul, Phys. Rev. E **62**, 927 (2000).

[280] J. Han, S.W. Turner, and H.G. Craighead, Phys. Rev. Lett. **83**, 1688 (1999).

[281] J.P. Rabe and S. Buchholz, Science **253**, 424 (1991).

[282] U. Seifert, W. Wintz W., and Nelson P., Phys. Rev. Lett. **77**, 5389 (1996).

[283] P. Hänggi, F. Marchesoni, and P. Sodano, Phys. Rev. Lett. **60**, 2563 (1988).

[284] H. Spohn, J. Phys. A: Math. Gen. **16**, 4275 (1983).

[285] G.M. Schütz, in *Phase Transitions and Critical Phenomena, Vol. 19*, edited by C. Domb and J.L. Lebowitz (Academic Press, San Diego, 2001).

[286] A. Ammann and R. Lipowsky, J. Phys. II France **6**, 255 (1996).

[287] J.R. Bartles, Curr. Opin. Cell Biol. **12**, 72 (2000).

[288] B.-Y. Ha and A.J. Liu, Phys. Rev. Lett. **81**, 1011 (1998).

[289] B.I. Shklovskii, Phys. Rev. Lett. **82**, 3268 (1999).

[290] I. Borukhov, R.F. Bruinsma, W.M. Gelbart, and A.J. Liu, Phys. Rev. Lett. **86**, 2182 (2001).

[291] A.G. Zilman and S.A. Safran, Europhys. Lett. **63**, 139 (2003).

[292] N. Hirokawa, Curr. Opin. Cell. Biol. **6**, 74 (1994).

[293] J. Coleman *et al.*, J. Phys. Chem. B **108**, 3446 (2004).

[294] R. Lipowsky, Phys. Rev. Lett. **77**, 1652 (1996).

[295] M. Warner and P.J. Flory, J. Chem. Phys. **73**, 6327 (1980).

[296] A.R. Khokhlov and A.N. Semenov, J. Stat. Phys. **38**, 161 (1985).

[297] D. Humphrey, C. Duggan, D. Saha, D. Smith, and J. Käs, Nature **416**, 413 (2002).

[298] T.B. Liverpool, A.C. Maggs, and A. Ajdari, Phys. Rev. Lett. **86**, 4171 (2001).

[299] F. Ziebert and W. Zimmermann, Phys. Rev. E **70**, 022902 (2004).

[300] B. Bassetti, M.C. Lagomarsino, and P. Jona, Eur. Phys. J. B **15**, 483 (2000).

[301] L. Onsager, Ann. N.Y. Acad. Sci. **51**, 627 (1949).

[302] R.F. Kayser and H.J. Raveché, Phys. Rev. A **17**, 2067 (1978).

[303] M.R. Faretta and B. Basetti, Europhys. Lett. **41**, 689 (1998).

[304] F. Gibbons, J.-F. Chauwin, M. Despósito, and J.V. José, Biophys. J. **80**, 2515 (2001).

[305] T. Shimada, M. Doi, and K. Okano, J. Chem. Phys. **88**, 2815 (1988).

[306] M. Doi, T. Shimada, and K. Okano, J. Chem. Phys. **88**, 4070 (1988).

[307] T. Shimada, M. Doi, and K. Okano, J. Chem. Phys. **88**, 7181 (1988).

[308] C.M. Coppin, D.W. Pierce, L. Hsu, R.D. Vale, Proc. Natl. Acad. Sci. USA **94**, 8539 (1997).

[309] S.M. Block, C.L. Asbury, J.W. Shaevitz, M.J. Lang, Proc. Natl. Acad. Sci. USA **100**, 2351 (2003).

[310] Kazuhiro Oiwa, *private communication.*

[311] C. Jarzynski, Phys. Rev. Lett. **78**, (1997) 2690.

[312] J. Liphardt, S. Dumont, S.B. Smith, I.Jr. Tinoco, and C. Bustamante, Science **296** (2002) 1832.

[313] C. Ecker, PhD thesis, Humboldt University Berlin (2005).

[314] F.C. MacKintosh, C.F. Schmidt, Curr. Opin. Colloid Interface Sci. **4**, 300 (1999).

Acknowledgements

Above all, I want to thank Reinhard Lipowsky for a very pleasant and stimulating time at the Max Planck Institute of Colloids and Interfaces. Without his continuous support and guidance this work would not have been possible.

I am also most thankful to all other academic teachers I had the privilege to work with during my career and who shaped my scientific views, Thomas Nattermann, Terence Hwa, and Valerii Vinokur. I am especially thankful to Valerii Vinokur for the enjoyable and stimulating time as as Postdoc at the Argonne National Laboratory, where part of the work for this thesis was done. I also want to thank the German Science Foundation for financial support through a Postdoctoral Stipend.

I would like to thank all my colleagues at the Max Planck Institute – Rumiana Dimova, Hans-Günther Döbereiner, Thomas Gruhn, Stefan Klumpp, Roland Netz, Christian Seidel, Udo Seifert, Ulrich Schwarz, Julian Shillcock, Angelo Valleriani, and Thomas Weikl – for numerous discussions and a pleasant working atmosphere.

Of course, I would also like to thank all the students, I had the pleasure to work with at the Max Planck Institute in Golm, Orapin Niamploy, Torsten Kühne, Pavel Kraikivski, Pedro Blecua, and Petra Gutjahr.

I also want to thank all the other collaborators and colleagues I met over the years for numerous discussions: Igor Aronson, Dan Blair, Martin Brinkmann, Sarah Köster, Alex Koshelev, Sean Ling, Henrik Nordborg, Thomas Pfohl, Ludger Santen, Jürgen Rabe, Nikolaus Rajewsky, Stefan Scheidl, Nikolai Severin, and probably many more.

Last but not least I want to thank my parents and, especially, Susi for understanding and support.

Publications used in this thesis

Strings and Vortex Phases

- *Dislocations and the critical endpoint of the melting line of vortex line lattices*,
  J. Kierfeld and V. Vinokur, Phys. Rev. B **61**, R14928-R14931 (2000), cited as [56].

- *Theory of Plastic Vortex Creep*,
  J. Kierfeld, H. Nordborg, and V.M. Vinokur, Phys. Rev. Lett. **85**, 4948-4951 (2000), cited as [57].

- *Single vortex fluctuations in type-II superconductors: Electromagnetic coupling and crossover to strong pinning*,
  J. Kierfeld, Phys. Rev. B **69**, 144513 (2004), cited as [55].

- *Lindemann criterion and vortex lattice phase transitions in Type-II Superconductors*,
  J. Kierfeld and V. Vinokur, Phys. Rev. B **69**, 024501 (2004), cited as [54].

- *Competitive localization of vortex lines and interacting bosons*,
  J. Kierfeld and V.M. Vinokur, Phys. Rev. Lett. **94**, 077005 (2005), cited as [58].

Filaments and Semiflexible Polymers

- *Unbundling and desorption of semiflexible polymers*,
  J. Kierfeld and R. Lipowsky, Europhys. Lett. **62**, 285-291 (2003), cited as [184].

- *Barrier crossing of semiflexible polymers*,
  P. Kraikivski, R. Lipowsky, and J. Kierfeld, Europhys. Lett. **66**, 763-769 (2004), cited as [187].

- *Stretching of Semiflexible Polymers with Elastic Bonds*,
  J. Kierfeld, O. Niamploy, V. Sa-yakanit, and R. Lipowsky, Eur. Phys. J. E **14**, 17-34 (2004), cited as [183].

- *Duality mapping and unbinding transitions of semiflexible and directed polymers*,
  J. Kierfeld and R. Lipowsky, J. Phys. A: Math. Gen. **38**, L155-L161 (2005), cited as [185].

- *Activated dynamics of semiflexible polymers on structured substrates*,
  P. Kraikivski, R. Lipowsky, and J. Kierfeld, Eur. Phys. J. E **16**, 319-340 (2005), cited as [188].

- *Point force manipulation and activated dynamics of polymers adsorbed on structured substrates*,
  P. Kraikivski, R. Lipowsky, and J. Kierfeld, Europhys. Lett. **71**, 138-144 (2005), cited as [189].

- *Discontinuous unbinding transitions of filament bundles*,
  J. Kierfeld, T. Kühne and R. Lipowsky, Phys. Rev. Lett. **95**, 038102 (2005), cited as [190].

- *Force-Induced Desorption and Unzipping of Semiflexible Polymers*,
  J. Kierfeld, Phys. Rev. Lett. **97**, 058302 (2006), cited as [186].

- *Enhanced Ordering of Interacting Filaments by Molecular Motors*,
  P. Kraikivski, R. Lipowsky, and J. Kierfeld, Phys. Rev. Lett. **96**, 258103 (2006), cited as [191].

- *Fluctuations of Single Confined Actin Filaments*,
  S. Köster, H. Stark, T. Pfohl, and J. Kierfeld, Biophys. Rev. Lett. (2007), in press, cited as [182].